309

MASTER

7-12-61

ORNL-3104
UC-20 – Controlled Thermonuclear Processes
TID-4500 (16th ed.)

THERMONUCLEAR DIVISION
SEMIANNUAL PROGRESS REPORT
FOR PERIOD ENDING JANUARY 31, 1961

OAK RIDGE NATIONAL LABORATORY
operated by
UNION CARBIDE CORPORATION
for the
U.S. ATOMIC ENERGY COMMISSION

DISCLAIMER

Printed in USA. Price $2.75. Available from the

Office of Technical Services
Department of Commerce
Washington 25, D.C.

ORNL-3104
UC-20 – Controlled Thermonuclear Processes
TID-4500 (16th ed.)

Contract No. W-7405-eng-26

THERMONUCLEAR DIVISION SEMIANNUAL PROGRESS REPORT

For Period Ending January 31, 1961

DATE ISSUED

MAY 31 1961

OAK RIDGE NATIONAL LABORATORY
Oak Ridge, Tennessee
operated by
UNION CARBIDE CORPORATION
for the
U. S. ATOMIC ENERGY COMMISSION

THIS PAGE

WAS INTENTIONALLY

LEFT BLANK

CONTENTS

THIS PAGE

WAS INTENTIONALLY

LEFT BLANK

THERMONUCLEAR DIVISION SEMIANNUAL PROGRESS REPORT

INTRODUCTION

A. H. Snell

The bunching of the ions in the storage ring of DCX-1, signalized in our last semiannual progress report, has been further studied (Sec 1.1.1), and the rather formal beginning of a matching theory has emerged (Sec 6.1). The theory predicts instabilities that arise from a resonant coupling of circumferential ion oscillations in the storage ring with electron oscillations along the lines of magnetic force, and suggests that the instabilities may set in at an ion density of 3×10^6 per cm^3. This is in fair agreement with what has been observed when gas breakup is used in DCX-1, but it is lower by a factor of nearly 1000 than the densities that are believed to have been reached experimentally when the carbon arc is used as a dissociator. There is an implication here that there may be ways to suppress the instabilities; indeed, they may have inherent self-limiting properties. Experimentally, the extent of radial loss of charged particles that may accompany the bunching has not yet been explicitly measured, but an input-output particle energy balance for the storage ring indicates that there is a higher rate of energy loss from particles injected at high beam currents (2.3 ma) than at lower beam current (0.1 ma). This has an equivalence in the lower observed mean containment times for particles injected at the higher beam currents. These matters are discussed in Sec 1.1.2; they obviously raise serious questions as to the particle densities that can ever be achieved in the present configuration of DCX-1, but they also suggest particular aspects that now deserve closer study. Meanwhile, the physical structure of DCX-1 has been changed by the addition of titanium pumping, which has given substantial improvements in the vacuum conditions, and by changes in the injection system (Sec 1.5). Thus we are presumably in a stronger position than in the past for investigating these finer details in the performance of DCX-1.

DCX-2 calculation and design have proceeded almost to completion during the period of this report, and procurement and construction have started. A variety of arrangements of orbits has been found to be possible (Secs 2, 2.2.2, 2.2.3, and 2.2.4), and DCX-2 emerges as an apparatus of deeply ranging capabilities. Meanwhile, although it has been found advisable to decelerate effort on DCX-EP-B (the reasons being administrative rather than technical), inflection and injection methods that have been developed for it in the Beta tanks are available for incorporation in DCX-2 (Sec 5).

In plasma physics we describe two principal developments. One concerns electron cyclotron heating; this is described somewhat sketchily (Sec 3.1) pending more satisfying measurement of the densities of hot electrons that have been produced, but if some of the present indications are sustained in further experiments, then the radio-frequency heating of plasma may be worth considerably more investigation. The second development concerns a major step in the understanding of the heretofore mysterious mode II of Neidigh's vacuum arc, in terms of ionic sound waves (Sec 3.2).

Vacuum arc research has centered principally around the deuterium and the lithium arcs. In the former, anode development has been required (Secs 1.2.1 and 4.3.2), but the main question has pertained to the mechanism of gas leakage from the arc, because this has been the limiting factor in the realization of a surrounding vacuum good enough to be of interest. In particular, the possible role of an abundance of about 1% of molecular ions (D_2^+) as a source of the neutral gas, either by dissociation into D^+ and D^0, or by dissociative recombination into $2D^0$, has been investigated (Sec 4.3.3). Lack of Doppler broadening suggests that dissociative recombination may not play a large part (Sec 4.3.4). Other determinations of interest in the deuterium arc work have been estimates of the D^+ ion temperature as about 16 ev, of the electron temperature as about 40 ev, and of the ion density as about 10^{14} D^+/cm^3 (Sec 4.3.4).

The lithium arc work has likewise led to more reliable operation through electrode development, and is proceeding along the direction of a determination of the factors that govern the relative abundances of Li^+, Li^{2+}, and Li^{3+} at various positions along the arc column (Sec 4.2.1).

The theoretical effort has continued to be partly in formal plasma theory (e.g., substantial progress in the evaluation of exact relativistic Fokker-Planck coefficients under nonrestrictive physical conditions, Sec 6.2) and partly in applied theory closely related to the experimental work. In the latter, there is a re-examination in Sec 6.6 of the effect of energy degradation upon the critical current in multiple-pass experiments such as DCX-2. This subject had been treated in a preliminary way in our last progress report. The new estimates indicate an increase by a factor of 2 to 3 in the critical current required for buildup when energy degradation is taken into account, and they indicate the nature of the variation of critical current with injection energy. In an application of the kind of theory that has been developed for orbital accelerators to the case of DCX storage rings, estimates are given in Sec 6.7 of the amount of phase space that is available within the restrictions of the Liouville theorem, for particle storage under different conditions of injection. The conclusion is reached that the Liouville theorem does not impose limitations within densities of thermonuclear interest.

Progress in the field of magnetics continues to be substantial. The following pages contain general theorems and methods concerned with mathematical field design (Sec 8.2) and with properties of particle orbits (Sec 8.3); applied calculations are also given for field synthesis and for forces between coils in particular cases of immediate interest (Secs 8.1, 8.4, and 8.5).

The efficiencies of evaporative vacuum pumping for gases of differing chemical composition have been compared, and the results of Sec 10.2.1 show quantitatively a good pumping speed under conditions of continuous evaporation for O_2, N_2, CO, and CO_2, while Ar, He, and CH_4 are hardly pumped at all. Differential titanium pumping has been tested under conditions simulating the circumstances under which an injected beam would have to pass from a region of higher pressure into a region of low pressure, and perhaps re-emerge into a second region of higher pressure (Sec 10.2.2). The effect of radiation from a carbon arc upon the pumping action of evaporating titanium has been briefly examined, with the indication that the pumping speed of the titanium may be reduced at first, but recovers in a few minutes (Sec 10.2.4). The calibration of conventional ionization gages is found to be quite constant with time, although it may vary between individual tubes (Sec 10.3.1); when, however, the gages are used without their envelopes, the results may be quite wild (Sec 10.3.2).

With the moving of DCX-EP-A, the shift of experimental equipment from the old building to the new has been completed. The adjustment of each apparatus into its new environment has been time-consuming, but we are ready now with increased strength to attack the many uncertainties and open questions that are inevitably left unanswered in a progress report.

THIS PAGE

WAS INTENTIONALLY

LEFT BLANK

X

✓

ABSTRACTING SUMMARY

1. DCX-1 OPERATION AND PERFORMANCE

Measurements have been made of the distribution in energy of the H^0 particles that escape from the storage ring in DCX. From these energy spectra, the distributions in energy of the H^+ particles within the ring are inferred. When either arc dissociation of the injected H_2^+ ions is used, or dissociation in the residual gas, the energy spectra of the H^0 particles are seen to broaden as the current of injected 600 kev H_2^+ ions is increased from about 0.1 ma to about 2.5 ma, and the mean energies characteristic of these spectra are observed to decrease by a few tens of kilovolts. In the case of arc dissociation, the mean containment time of the protons is found to decrease from 2.6 msec to 1.7 msec as the injected H_2^+ current is increased from 0.1 to 2.3 ma.

From electromagnetic pickup signals, light signals, and a time analysis of energy-selected escaping neutrals, evidence appears for a bunching or nonuniformity in the distribution of the trapped protons in the storage ring. The bunching is more pronounced at the higher injection currents. An energy balance suggests that the rate of energy loss from the stored protons is greater at the higher injection current than at the lower injection current. The cause of the bunching is not yet understood.

Sundry improvements in the vacuum technique of DCX are described, including the installation of titanium evaporative pumps that have lowered the base pressure by a factor of 10 to 3×10^{-8} mm Hg with a measured pumping speed for hydrogen of 50,000 liters/sec at 10^{-7} mm Hg, the testing of a large Vaclon pump, and the testing of a Redhead gage.

A new ion source has been installed, in which mass analysis is applied before the 600-kv acceleration, so that only the H_2^+ beam is accelerated. It is expected that this will furnish considerably higher injection currents than have so far been available.

2. DCX-2 DESIGN AND ENGINEERING

Magnet coils have been calculated as to shape, current density, and location to meet exacting requirements in DCX-2; the requirements include uniformity of the field over a region 52 in. long and 18 in. in diameter, with a properly located dip of 1.6% in field strength near the injection snout and a rise by a factor 3.3 into the mirrors at either end. Orbit calculations show that absolute containment holds for the injected H_2^+ ions. Helical orbits are calculated for both H_2^+ and H_3^+; substantial, and perhaps useful, precession can probably be found in the reflection region $43\frac{1}{2}$ in. to $45\frac{1}{2}$ in. from the midplane.

A summary of the present status of the design and construction of DCX-2 is given.

3. PLASMA PHYSICS

Cyclotron resonance heating of electrons in a microwave cavity has led to conditions in which densities exceeding 10^{10} electrons/cm^3 and mean energies of about 10 kev and maximum energies of several hundred kev are apparently established.

√

Ionic sound waves occurring in a throat region near the cathode of a vacuum arc have been found to account for oscillations, for blowup, and for other properties described by Neidigh during operation in mode I and mode II arcs. Harmonics of the oscillations are producible, and the frequencies are found to vary appropriately with ionic mass and with arc length. They also show appropriate independence of magnetic field strength, gas pressure, arc current, and arc voltage.

The ionic sound wave theory is shown to account fairly well for plasma oscillations found in certain mercury vapor discharges, as reported from Stanford.

4. VACUUM ARC RESEARCH

The Carbon Arc

An analysis of the dependence upon arc current of the rotational frequency of C^{2+} ions as evidenced by the Doppler slant of spectral lines has shown the dependence to be nonmonotonic. The ratio of the rotational frequency to the square of the half-width is empirically found to follow a linear relationship with the arc current.

The Lithium Arc

Anode development for lithium vacuum arcs is described. Anode cooling conditions have been found that yield Li^{2+} in strong admixture with Li^{+} in the arc. The current carried by positive ions is found to be 19% or more of the total arc current. Doppler shifts indicate a longitudinal drift energy of 70 ev for the Li^{+} ions, while line widths suggest an apparent temperature of about 10 ev. Ballistic measurements made in the lithium positive ion current that misses the cathode indicate a thrust force of about 2 g for a total arc current of about 100 amp.

Anomalous brightness of the 5484.8 line of Li^{+} is suggested to arise from population of the $2s(^3S)$ metastable triplet state.

The Deuterium Arc

The development work on a high-vacuum deuterium arc is reviewed. Electrodes have been developed which do not deteriorate with prolonged use and which introduce no impurities into the arc plasma. A variety of spectroscopic and microwave observations is described. The observed impurity level (CO and organic) is 0.06%. The arc column appears to be a 99%-ionized plasma with an ion temperature of 16 ev and an electron temperature somewhat higher. Its maximum density is of the order 10^{14} particles/cm^3. The ions carry approximately 25% of the arc current.

5. ION PRODUCTION, ACCELERATION, AND INJECTION

Test-stand performance of the von Ardenne ion source under development for DCX-2 has reached 70 ma continuous current of mixed hydrogen ions at 570 kv for half an hour, the test having been ended by target failure.

Initial testing of a rotating-target titanium pump shows a sticking factor of unity when pumping a deuterium ion beam at 4 kw/in.^{2}. A model is now installed on DCX-1 for testing.

Electrostatic deflection appears to offer a practical way of steering a 600-kev ion beam as it enters a magnetic field. A 50-ma, 21-kev beam is easily deflected 2 in. in a magnetic field of 2600 gauss. The successful application of such a device in DCX-EP-B would increase the radius of the volume available to the wrapped-up beam by a distance equal to the radius of the injection snout, or about 2.8 in.

Successful tests of the neutralized-beam injector prototype have been made. Ninety-five to ninety-nine per cent of the monoenergetic electron beam may be passed through the hollow reflux ion source and ion accelerating gap. Qualitative measurements on the behavior of the ion beam in the presence of the injected electron beam indicate that space-charge blowup of the ion beam is reduced. Results for various acceleration voltages from 5 to 15 kv, injected electron currents up to 150 ma, and ion currents of about 1 amp are discussed.

6. THEORY

Instabilities Due to Anisotropic Velocity Distributions

The stability of a plasma which is in the form of an infinite cylindrical shell has been considered. The ions all move with constant angular velocity (ω_{ci}) about the axis of the cylinder; the electrons are cold. The resultant behavior is very close to that of an infinite plasma with anisotropic velocity distribution. Instabilities are predicted for electron plasma frequencies which are integral multiples of ω_{ci}. The amplitude of the instability should be severely limited by nonlinear effects at low densities.

Exact Relativistic Fokker-Planck Coefficients for a Plasma

Exact coefficients have now been obtained for a plasma with an arbitrary zero-order velocity distribution, an arbitrary applied radiation field, and an arbitrary mixture of ion species.

A Kinetic Equation for a Radiation Field Oscillator

A Fokker-Planck equation for the radiation field oscillators has been deduced from the Liouville equation.

Excitation of the First Excited State of Hydrogen

The method of Gryzinski has been used to calculate the excitation of the first excited state of hydrogen. The resultant agreement with experiment is poor.

Code to Calculate Particle Energy Distributions

Several changes in a code to solve the coupled steady-state Fokker-Planck equations for ions and electrons have led to preliminary success. A test case is seen to relax to a Maxwell distribution as it should.

Effect of Energy Degradation on the Critical Current in an OGRA-Type Device

Previous calculations of the critical ion current in an OGRA-type device have been extended to include degradation of the ion energy by energy transfer to cold electrons released by the ionization of the neutral background. A typical plot, showing the extent of corrections to the "S-curve" is included.

Limitations on Particle Densities Imposed by the Liouville Theorem for Injection-and-Accumulation Devices

For injection of beams of neutral atoms with trapping by ionization, and for molecular-ion injection with trapping by dissociation, estimates of the limitations imposed by available phase space upon accumulable particle densities indicate that the limitation lies far above the region of controlled thermonuclear interest. For the injection of neutralized beams of ionized atoms on the other hand, the limitation may be of more nearly practical importance; the limitations are relaxed, however, if the neutralized beams contain molecular ions, and dissociation is again invoked as a trapping mechanism.

7. INSTRUMENTATION

The possible hazard of water flow failure in one of the numerous water paths of the coils in DCX-2 make individual over-temperature detection highly desirable. Results of tests on eight inexpensive bimetallic thermoswitches are described.

8. MAGNETICS

Design of Magnetic Mirror Fields with Extremely Homogeneous Central Zones

Codes and techniques are described, by which magnetic mirror fields with extremely homogeneous central zones have been designed. The magnetic field of DCX-EP-B, a product of these methods, is described in some detail.

Field Optimization by Superposition of Optimized Magnetic Fields

It is very difficult to synthesize magnetic fields with extremely homogeneous central zones and specified "field dips" for ion injection between the mirrors and the central zone. This task can be considerably facilitated if two theorems are used, which state that optimized magnetic fields can be obtained by superposition of appropriately optimized component fields. The first theorem applies to the case of a known flux density B_0 in the homogeneous central zone; the second considers this flux density as an unknown. The magnetic fields for DCX-2 and DCX-EP-B were determined with the use of these superposition theorems.

Some Geometrical Properties of Ion Trajectories

For the relativistic movement of a charged particle in a nonstationary electromagnetic field the radius of curvature ρ and the direction of the principal normal $\bar{e}_\rho$ of the trajectory can be calculated. These quantities uniquely determine this curve. For the nonrelativistic movement of an ion in any stationary electromagnetic field a computer code is suggested, which uses for each

Runge-Kutta procedure a new position of a cylindrical coordinate system which is determined by ρ, $\bar{e}_\rho$, and the particle velocity $\bar{v}$. Higher accuracy for a given step number is to be expected. An expression for the radius of curvature of the projection of a trajectory on a stationary plane is derived which can be applied for graphical determination of ion trajectories. Finally, the curvature of an r-z movement trajectory in a rotationally symmetrical magnetic field is discussed.

Force Calculations for Axially Symmetrical Coil Systems

An investigation of simplified methods of calculation of electromagnetic forces is reported and resulting formulas given. The application of these calculations to DCX-2 is shown. Furthermore, radial variation of forces on coils and the problem of forces on the injection snout are considered.

Applications of a Field Analog for Axially Symmetrical Coil Systems

A change in the mode of operation of the resistance network analog computer of the Engineering Science Group is described. The use of the device for determining magnetic field lines for a cusp geometry and for a DCX-EP-B "linear field" design are reported. Accessory electronics components for constant display of field lines are now under construction.

Design of an Ion Injector Snout

A design for a tubular injector for DCX-2 is presented, which is expected to give magnetic shielding for the injected beam without appreciably disturbing the main DCX-2 containment field outside.

9. CROSS-SECTION MEASUREMENTS

Apparatus has been readied for the measurement of the cross section for dissociation of H_2^+ by electrons, using crossed beams. Estimates are given for the degree to which noise and ripple must be suppressed. A suggestion is made for an experiment to measure the cross section for dissociation of H_2^+ by H^+.

10. VACUUM SYSTEMS AND TECHNIQUES

Comparative pumping speeds of evaporated titanium have been measured for H_2, CO, CO_2, N_2, O_2, He, Ar, and CH_4. The last three are found not to be pumped at all. Comparisons of several evaporated metals as adsorbers of H_2 have been made with the result that under the conditions of the experiment Ti seems better than Mo, Zr, Cr, Ta, Li, or Nb. A three-cell titanium differential pumping unit has been tested for possible use at the points at which an injected ion beam might enter or leave a low-pressure region containing accumulated plasma. Radiation from a carbon arc was found in a brief test to have an inappreciable effect upon the steady-state pumping action of titanium under evaporation. Some studies of ionization-gage calibrations are described, which indicate that the calibration of a given RG-75 gage remains constant with time, but if either RG-75 or VAC-NIG gages are used without their envelopes, they may be completely unreliable. A study is reported of isotherms around the jets of diffusion pumps.

11. BALL LIGHTNING

Some remarks are made upon a collection of reports of observations of ball lightning.

THIS PAGE
WAS INTENTIONALLY
LEFT BLANK

1. DCX-1 OPERATION AND PERFORMANCE

C. F. Barnett　G. R. Haste　W. J. Schill
J. L. Dunlap　J. A. Ray　R. M. Warner
R. S. Edwards　R. G. Reinhardt　E. R. Wells

1.1 ENERGY DISTRIBUTIONS AND RADIO-FREQUENCY OSCILLATIONS

1.1.1 Additional Particle Energy Measurements

The particle energy measurements now being reported were made much the same way as the preliminary measurements, which were described in the previous semiannual report.[1] A sample of the particles being lost from the trapped proton ring as charge-exchanged neutrals was allowed to pass from the DCX-1 vacuum chambers into a neutral particle spectrometer. Here the H^0 particles were collimated and recharged by passage through the differentially pumped argon gas cell. The resulting H^+ ions were electrostatically analyzed and the ions were detected by electron multipliers. A schematic diagram of the apparatus is shown in Fig. 1.1. Improvements in the equipment have provided for automatic scanning, recording of the detector current, and higher resolution than was available in the first measurements.

UNCLASSIFIED
ORNL-LR-DWG 52510

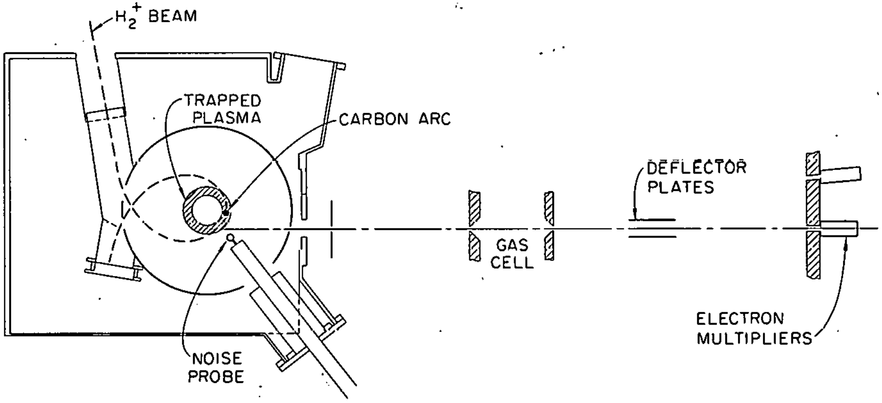

Fig. 1.1. Schematic Diagram of Spectrometer.

Corrections for the energy resolution of the spectrometer, for the energy dependences of the detector, and for the recharging cross section in the argon cell were applied to the detector current traces to obtain the energy distributions of the escaping neutrals. From these, the energy distributions of the trapped protons could be inferred by appropriate use of the known variation with energy of the charge-exchange cross section of protons with the residual gas in the DCX vacuum system. The residual gas was assumed to be nitrogen.

---

[1] *Thermonuclear Project Semiann. Rept. July 31, 1960*, ORNL-3011, sec 1.3.

Runs were made to investigate the sensitivity of the distributions to a number of parameters. The distributions were found to be strong functions of injected H_2^+ current, liner pressure, and the longitudinal displacement of the plasma volume being sampled. They were relatively insensitive to the radial location of the plasma volume (in large part due to the wide vertical acceptance angle of the spectrometer) and to slight angular orientations of the spectrometer with respect to the median plane (the range ±3° was investigated). In the remainder of the work, the axis of the spectrometer was maintained parallel to the median plane and the particles were sampled from a volume element centered at the equilibrium radius (3.25 in.). Attention was then focused on experiments in which the dependences of the energy distributions upon injected current, liner pressure, and longitudinal displacement were examined in detail.

Figure 1.2 shows a set of energy distributions of escaping particles, obtained with the spectrometer mounted in the median plane. A 10-ft-long, 300-amp carbon arc was used to dissociate the H_2^+ beam, and the pressure was maintained at 1.5×10^{-6} mm Hg (uncorrected ion gage reading) with a hydrogen leak. Figure 1.3 shows the derived set of energy distributions of the trapped protons. The average energy of each distribution is given in Table 1.1. The energy distributions of

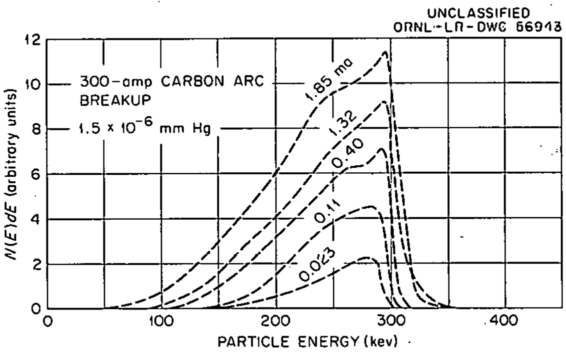

Fig. 1.2. Energy Distributions of Escaping Particles for Various H_2^+ Currents with Spectrometer on Median Plane.

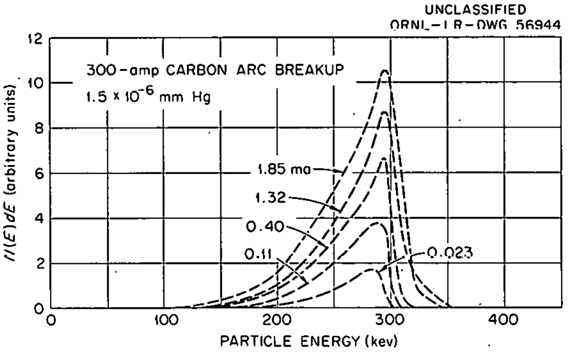

Fig. 1.3. Energy Distributions of Trapped Particles for Various H_2^+ Currents with Spectrometer on Median Plane.

Table 1.1. Variation of Mean Energy of Trapped and Escaping Hydrogen Particles with Input Current of Molecular Ions; Dissociation in Vacuum Arc

$I_{H_2^+}$ (ma)	$\bar{E}$ External (kev)	$\bar{E}$ Internal (kev)
1.85	237	265
1.32	245	269
0.40	243	261
0.11	250	262
0.023	251	263

the escaping particles broadened and shifted to lower mean energy as the injection current was increased.

Numerous scans were made with carbon arc breakup at base pressure (8×10^{-7} mm Hg) with two values of injected current (approximately 0.1 and 2.3 ma) at different longitudinal displacements. There were a number of interesting results:

1. The current dependence of the average energy (Table 1.2) is the same as that indicated in Table 1.1; the mean energies of the escaping particles are lower in the case of the higher injected current.

2. For both current values the external distributions generally shifted toward lower mean energies as the spectrometer was moved away from the median plane. At the same time the distributions became broader. Figures 1.4 and 1.5 indicate these trends.

3. The particle currents to the spectrometer detector decreased with motion away from the median plane. For 2.3 ma H_2^+, at the 2-in. position the peak current was $\frac{1}{25}$ of that at the median plane. The corresponding factor for 0.1 ma H_2^+ was $\frac{1}{300}$.

Table 1.2. Mean Energies with Arc Breakup as a Function of Input Current and Longitudinal Position

Position	High-Current Data			Low-Current Data		
	$I_{H_2^+}$ (ma)	$\bar{E}$ Escaping (kev)	$\bar{E}$ Internal (kev)	$I_{H_2^+}$ (ma)	$\bar{E}$ Escaping (kev)	$\bar{E}$ Internal (kev)
Median plane	2.27	216	260	0.10	251	272
½ in.	2.3	220	264	0.10	251	263
1 in.	2.4	175	247	0.125	225	242
1½ in.	2.3	179	254	0.10	212	238
2 in.	2.55	195	277	0.11	190	201

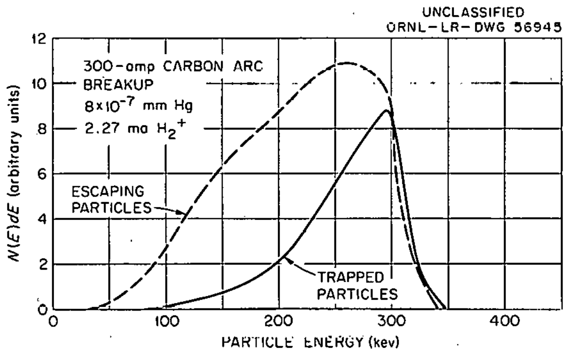

Fig. 1.4. Energy Distributions with Spectrometer on Median Plane.

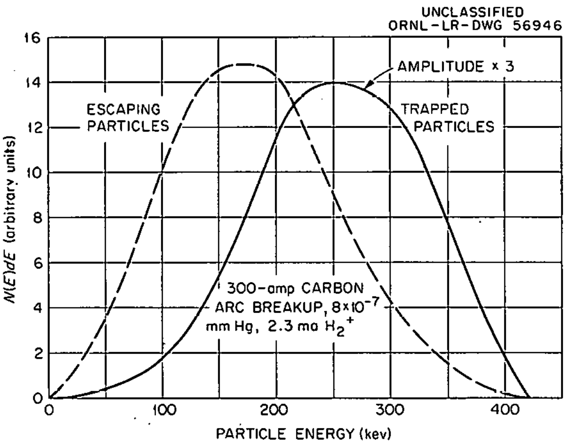

Fig. 1.5. Energy Distributions with Spectrometer 1½ in. off Median Plane.

4. The measured mean containment times for the two current values were substantially different. These were 2.6 msec for 0.1 ma and 1.7 msec for 2.3 ma.

Similar runs varying the injection current and the longitudinal position of the spectrometer were also made using hydrogen gas breakup. Data were obtained at the median plane and the ½-in. locations, but there was insufficient signal strength at positions farther from the median plane. Figures 1.6 and 1.7 are characteristic of the distributions obtained. The average energies are summarized in Table 1.3. Again the energy of the escaping particles is lower in the case of higher current injection. No differences in containment times were noted in the case of gas breakup. For each value of injected current the neutral particle detector decay traces indicated a τ of approximately 7 msec.

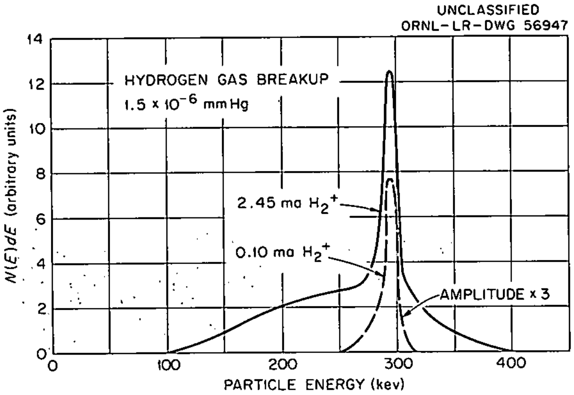

Fig. 1.6. Energy Distributions of Escaping Particles with Spectrometer on Median Plane.

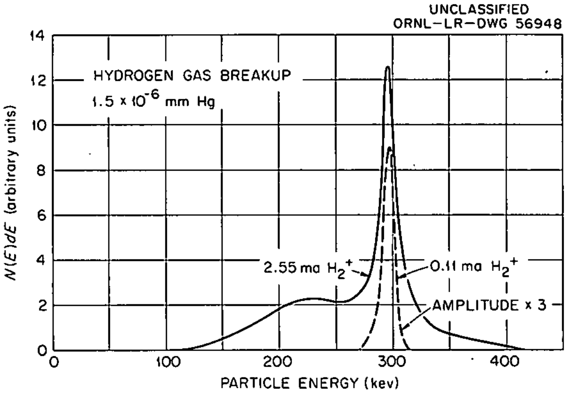

Fig. 1.7. Energy Distributions of Escaping Particles with Spectrometer ½ in. off Median Plane.

Table 1.3. Variation of Mean Energy of Trapped and Escaping Hydrogen Particles with Input Current of Molecular Ions; Dissociation in Residual Gas (No Vacuum Arc)

Position	$I_{H_2^+}$ (ma)	$\bar{E}$ Escaping (kev)	$\bar{E}$ Internal (kev)
Median plane	2.45	261	292
Median plane	0.10	291	294
½ in.	2.55	270	296
½ in.	0.11	294	299

With either carbon arc or hydrogen gas breakup, an increase in liner pressure resulted in sharper energy distributions, a shift in the mean of the escaping particle distributions toward higher energies, and, of course, a reduction in the mean proton containment time. A comparison of Figs. 1.8 and 1.9 indicates the effect of a pressure increase on the circulating proton distribution with gas breakup and with the spectrometer on the median plane.

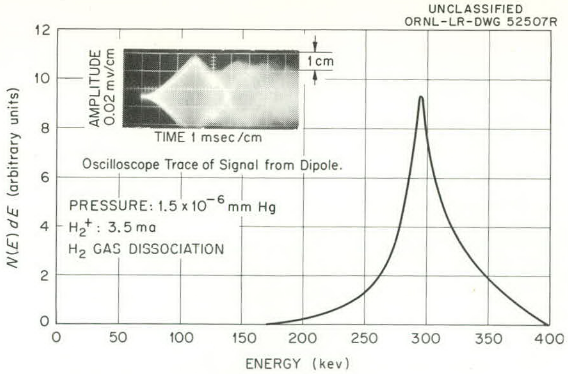

Fig. 1.8. Energy Distribution of Particles in DCX Median Plane.

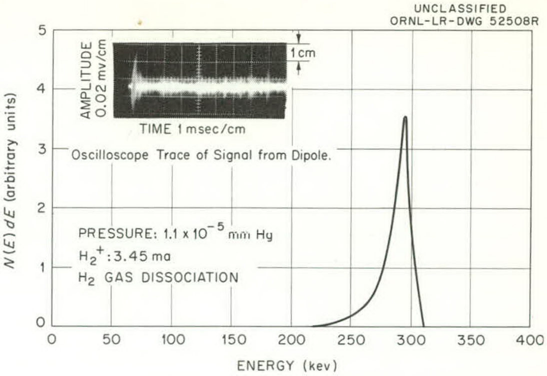

Fig. 1.9. Energy Distribution of Particles in DCX Median Plane.

Efforts were made to secure energy distributions as a function of time after the input H_2^+ was gated off. The output of the spectrometer electron multiplier was amplified in a transistor circuit and then displayed on a dual beam oscilloscope along with the signal from the central foil-covered neutral particle detector. Figure 1.10 shows oscillograms that are typical of those observed. In the upper oscillogram, the top trace is the time response of the electron multiplier signal, and the lower trace is that of the foil detector. At time $t = 0$, the H_2^+ beam was pulsed off. Note that the electron multiplier signal is a series of pulses with 50 μsec rise times and ½ msec decay times. The rise time figure is the response time of the transistor amplifier to a step function increase in signal, and the decay time is also that of the amplifier. In the lower oscillogram the time scale is compressed to show two decays and one buildup. Some time is required after the H_2^+ beam is keyed on before the electron multiplier spikes appear. This behavior suggests the existence of a critical density.

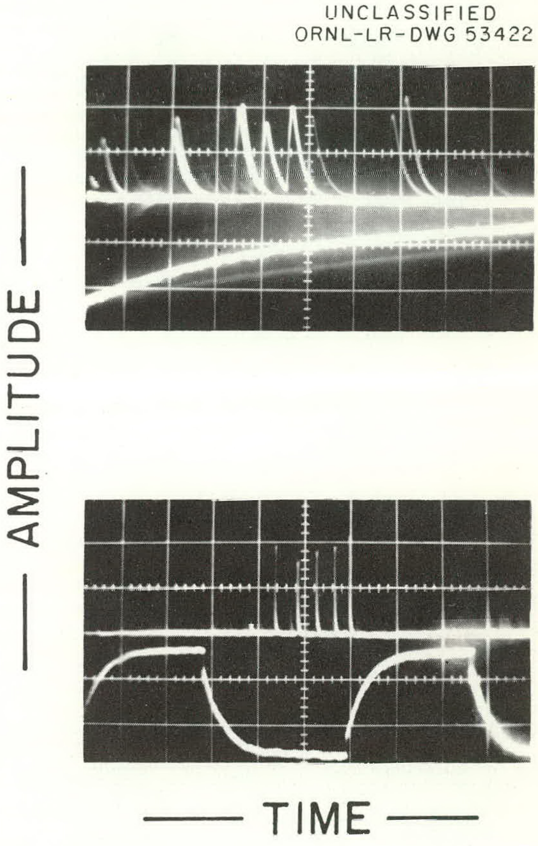

Fig. 1.10. Time Variation of Current from Electron Multiplier and Neutral-Particle Detector.

The sporadic nature of the spectrometer signal was unchanged when the electron multiplier detector was exchanged for a scintillator and photomultiplier. The general behavior shown in the oscillograms was independent of the energy selection of the spectrometer and occurred with either gas or arc dissociation.

1.1.2 Energy Balance Considerations

We consider an energy balance equation of the form:

$$I(300) = I\tau \frac{dE}{dt} + If_1 \overline{E}_1 + If_2 \overline{E}_2 + \ldots ,$$

where

I = proton trapping rate,

τ = containment time in milliseconds,

dE/dt = rate of energy loss for a trapped proton in kev per millisecond,

f_i = fraction of particles lost due to some particular loss process,

$\overline{E}_i$ = average energy of the particles lost by this process.

First let us calculate cases for arc breakup at two different values of injected current. An experiment described in a previous report[2] showed that in the geometry with the 5.3-in. radius for the proton orbit, the principal loss mechanisms were charge exchange in the arc and in the gas. This experiment indicated that at a liner pressure of 8×10^{-7} mm Hg one-half of the particles were lost by charge exchange in the gas and one-half in the arc.

The present work was done in the geometry with the 3.25-in. proton orbit radius, for which there has been no corresponding experiment. As an assumption, again let the principal loss mechanisms be charge exchange in the gas and in the arc. The size of the arc is unchanged, but since the orbit is now smaller, the charge-exchange loss in the gas now contributes relatively less. In the present geometry probably about two-thirds of the particles are lost in the arc and one-third in the gas at, again, a pressure of 8×10^{-7} mm Hg.

The energy balance equation then becomes:

$$300 = \tau \frac{dE}{dt} + \frac{\overline{E}_{\mathrm{gas\ cx}} + 2\overline{E}_{\mathrm{arc\ cx}}}{3} .$$

The $\overline{E}_{\mathrm{gcx}}$ term can be evaluated from Table 1.2. Since most of the particles are lost within an inch of the median plane, we take as $\overline{E}_{\mathrm{gcx}}$ the average of the $\overline{E}_{\mathrm{escaping}}$ values for scans on the median plane, ½ in. off, and 1 in. off.

There has been no measurement of $\overline{E}_{\mathrm{acx}}$. However, reasonable and convenient limits can be placed by assuming either that in this energy range the electron capture cross section of the arc is independent of energy, or alternatively, that it varies as the σ_{10} of the residual gas of the vacuum. In the first case the $\overline{E}_{\mathrm{acx}}$ is equal to the mean energy of the circulating protons, that is, the $\overline{E}_{\mathrm{internal}}$ of Table 1.2. In the second case the $\overline{E}_{\mathrm{acx}}$ is equivalent to the $\overline{E}_{\mathrm{gcx}}$. Again we average the results of the three scans closest to the median plane to secure the $\overline{E}_{\mathrm{acx}}$ on the basis of the two separate assumptions.

---

[2] *Thermonuclear Project Semiann. Rept. Jan. 31, 1960*, ORNL-2926, sec 1.1.1.

The values thus obtained for $\overline{E}_{gcx}$ and $\overline{E}_{acx}$, the measured containment times (each the average of numerous neutral particle detector decay curves), and the values of dE/dt derived from the energy balance equation are shown in Table 1.4. The rate of energy loss by trapped protons at the higher-current injection is found to be double the rate experienced at low-current injection.

Table 1.4. Results of Energy Balance Calculations for Arc Dissociation

$I_{H_2^+}$ (ma)	τ (msec)	$\overline{E}_{gcx}$ (kev)	$(d\sigma_{10}/dE)_{acx}$	$\overline{E}_{acx}$ (kev)	dE/dt (kev/msec)
0.1	2.6	242	$\sim E^0$	262	17
			$\sim \sigma_{10}$ gas	242	22
2.3	1.7	204	$\sim E^0$	258	35
			$\sim \sigma_{10}$ gas	204	56

The average values of dE/dt given in Table 1.4 are about 20 kev/msec for 0.1 ma H_2^+, and 45 kev/msec for 2.3 ma H_2^+. Either of these figures is reasonable for energy loss to cold electrons in the carbon arc, but if the arc is the major energy sink in both cases, it is difficult to reconcile the different dE/dt values. The arc characteristics should not change as the intercepting circulating proton current changes, because the arc density is still 10^4 or 10^5 times the circulating proton density at the higher current. The proton energy distributions are different in the two cases, but the energy loss rate to cold electrons in the arc is believed not to depend sensitively upon proton energy in the range of interest. An increased disorder in proton motion at the higher H_2^+ current would introduce additional precession by allowing particles to miss the arc, and would tend to *decrease* the dE/dt compared with that experienced by protons in the more ordered orbits at the lower current — a trend opposite to that observed.

Examine now the sensitivity of this dE/dt difference to the assumptions we have made concerning the number of particles lost in the arc relative to those lost in the gas, and to the lack of the variation with energy of the arc charge exchange cross section. The extreme corrections that can reasonably be introduced here appear when essentially all the particles are assumed lost to the arc and when the arc $d\sigma/dE$ is taken to be zero. All the particles then escape with the mean energy of the internal distribution. For both low and high injection currents, Table 1.4 shows that this is about 260 kev. The corresponding energy loss rates are found to be 15 and 24 kev/msec, the difference arising from the different measured containment times τ. The higher energy loss rate associated with the higher injected current may result from rf radiation, losses to a more dense cold plasma, plasma potential drain, ill-understood cooperative effects, or other phenomena.

The initial assumption that the sole particle loss mechanism was charge exchange must also be reconsidered. The difference in the dE/dt values would indeed be reduced if in the case of the high H_2^+ current, a loss mechanism were present which favored the loss of particles with energies above the mean of the trapped proton distribution. This could be in the form of energetic ion losses through the mirrors and/or to the walls.

Consider now the energy balance for the case of gas breakup. With the assumption that the only energetic particle loss mechanism is gas charge exchange, the energy balance equation becomes

$$300 = \tau \frac{dE}{dt} + \overline{E}_{gcx} .$$

Averaging the $\overline{E}_{escaping}$ data as given in Table 1.3 for the median plane scan and the ½-in.-west scan yields $\overline{E}_{gcx}$ values of 266 kev for 2.5-ma injection and 292 kev for 0.1-ma injection. The τ for both cases was 7 msec. The dE/dt values derived from these data are 5 kev/msec for 2.5 ma and 1 kev/msec for 0.1 ma. During a later gas breakup run with injected currents from 0.3 to 3.3 ma there was evidence that the average τ decreases at the higher H_2^+ currents, as in the case of arc breakup. This effect would increase the difference between the two dE/dt values.

As with arc breakup, the conclusion is that the mean rate of energy loss of the circulating protons for gas breakup has a tendency to increase with the injection current.

1.1.3 Measurements of Radio-Frequency Oscillations

These experiments were conducted only with gas breakup because of the large amplitude of the rf noise signals generated by the arc.

An electrostatically shielded dipole antenna was inserted in the median plane outside the plasma ring. Figure 1.11 indicates the construction of this antenna, and Fig. 1.1 shows the position of the rf probe relative to the circulating protons.

Initially the antenna signal was fed to an Empire frequency analyzer, and the frequency range 150 kc to 1000 Mc was scanned. Strong proton cyclotron radiation was observed in a band centered at 14.65 Mc. Harmonics of this radiation through the seventh were also detected, with each even harmonic weaker than the following odd harmonic. The amplitude of these signals was dependent on the input current, and the frequencies were of course dependent on the magnetic field. The amplitudes were essentially independent of the plane of orientation of the dipole. A number of other signals were found with frequencies which were independent of the magnetic field and with amplitudes independent of beam strength except that the signals disappeared when the H_2^+ beam was gated off. The more prominent of these signals were ones at 215, 285, 292, 460, and 960 Mc. It is supposed that this radiation might have been due to cavity resonances which were excited by the beam.

A series of gas breakup runs was made in which the DCX apparatus was operated at a constant pressure (1.5×10^{-6} mm Hg, hydrogen leak) and with a number of different H_2^+ currents. For each value of injected current an oscilloscope display of the rf probe output was photographed as a function of time after the H_2^+ beam was gated on, and the steady-state energy distribution was obtained. Figures 1.8 and 1.12 show the rf signal traces and the circulating proton energy distributions for the lowest and highest values of injected current. The rf signal envelope characteristically showed a quiescent interval followed by an amplitude buildup and then chaotic modulation. This behavior

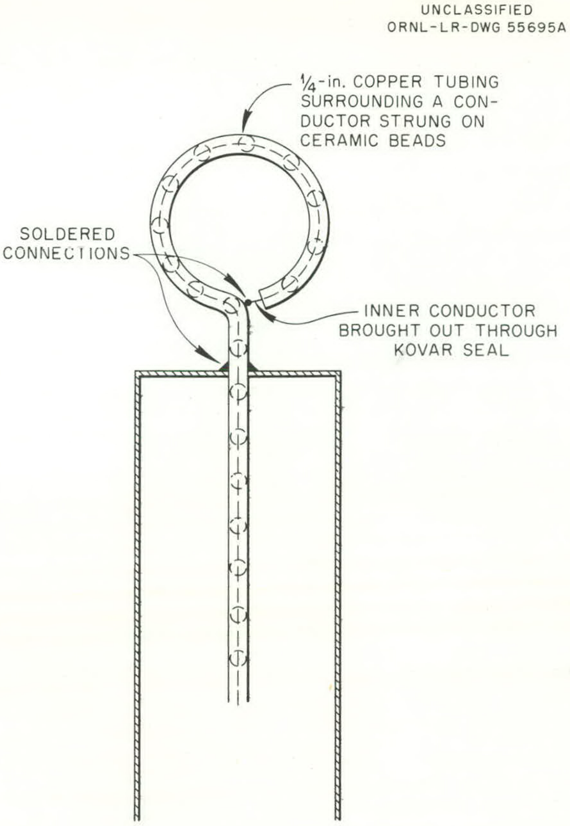

Fig. 1.11. Electrostatically Shielded RF Probe.

was essentially independent of the probe orientation. Figure 1.13 shows the variation of the quiescent time with input current, and Fig. 1.14 shows the variation of the peak amplitude of the rf signal envelope. Figure 1.9 indicates the effect of a pressure increase on the probe signal.

Excitation of the residual gas in DCX by the circulating protons produces visible light from the plasma region. Periodic fluctuations in the amplitude of this light were investigated using a photomultiplier mounted at the end of a 15-ft-long, 2-in.-diam tube which was inserted through the cathode-end face plate. The strongest fluctuations occurred in a broad band about the proton cyclotron frequency. With the photomultiplier no multiples of the cyclotron frequency were noted.

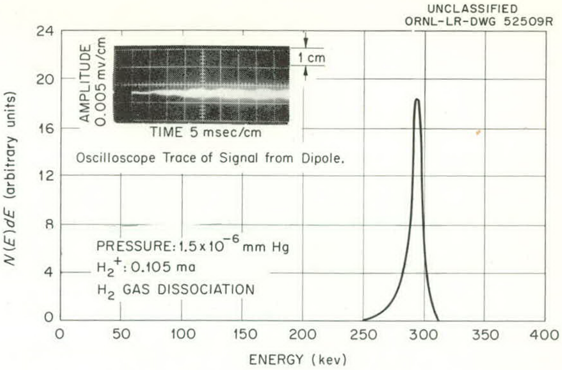

Fig. 1.12. Energy Distribution of Particles in DCX Median Plane.

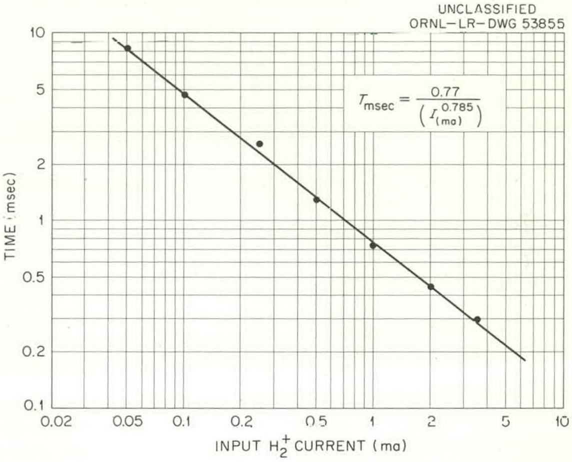

Fig. 1.13. Onset Time for Oscillations as a Function of Input Current.

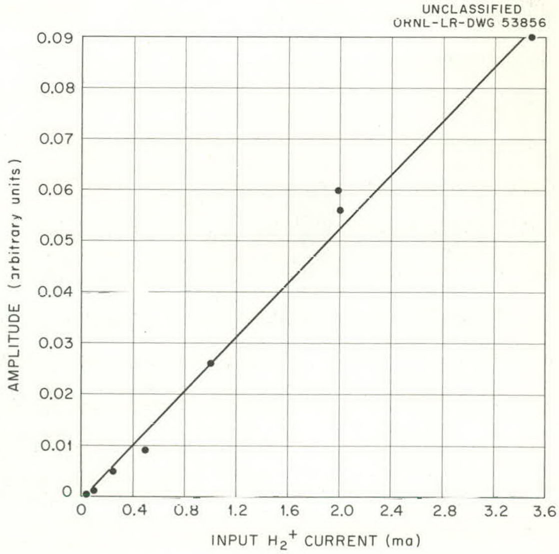

Fig. 1.14. Peak-to-Peak Amplitude of Oscillation as a Function of Input Current.

However, several other frequencies were observed, none of which corresponded to frequencies found with the rf dipole and none of which could be shifted by changes in the magnetic field or beam current. The more prominent of these were 540 kc and 2.1 and 5.4 Mc.

1.1.4 Conclusions

The interpretations of these experiments are as yet only qualitative. The sporadic nature of the spectrometer detector signal and the modulation of the excitation light from the plasma region indicate that particle "bunching" is taking place in the trapped ring. The oscilloscope displays of the spectrometer detector and the rf probe signals during the plasma buildup period suggest that there may be a form of critical density associated with the phenomenon. The changes in energy distributions and containment times with injected current indicate considerable dependence of these steady-state parameters upon the density of the stored particles, and in addition suggest that losses of energetic ions may be significant.

1.2 ARC DEVELOPMENT

1.2.1 Gas Arcs

The motivation for gas arc development work in DCX-1 is the desire to secure a hydrogen or deuterium arc that will dissociate a significant portion of the H_2^+ beam, and that at the same time will be characterized by no charge exchange with the circulating protons and a low rate of proton energy loss to the arc electrons. An additional requirement is that the arc operate at low pressures in the DCX-1 inner vacuum region.

The initial gas arc runs in DCX-1 were made using electrode and baffle geometries that had been developed by the Exploratory Physics and the Arc and Ion Pumping Groups. These experiments were described in the previous report.[3] The APIG configuration appeared the more promising, but in DCX these arcs were characterized by higher operating voltages (160 v at 200 amp) which produced anode erosion and contaminating ions. In addition, the anode gas flow rate could not be reduced much below 4 atmospheric cc/sec without resulting in an immediate anode failure. The liner ion gage pressure with 4 to 5 atmospheric cc/sec flow rates was about 1×10^{-5} mm Hg.

After attempts to provide more efficient cooling of the anode failed to materially improve any of the above characteristics, experiments were begun to develop a rotating anode structure. The configuration shown in Fig. 1.15 gradually evolved. The anode gas is bled into a stationary gas box which surrounds the anode. The only conductance from the box to the outer regions is a 2-in.-diam tubular channel through which the arc runs. The channel and gas box are of copper with water-cooling lines to dissipate the heat. The rotating anode is situated so that the arc impinges off the rotation axis upon a metal plate which has high-velocity water flow across the reverse side. Several different anode plates were tested, but ½-in.-thick copper appeared to have the best characteristics.

---

[3] *Thermonuclear Project Semiann. Rept. July 31, 1960*, ORNL-3011, sec 1.2.

UNCLASSIFIED
ORNL-LR-DWG 55694

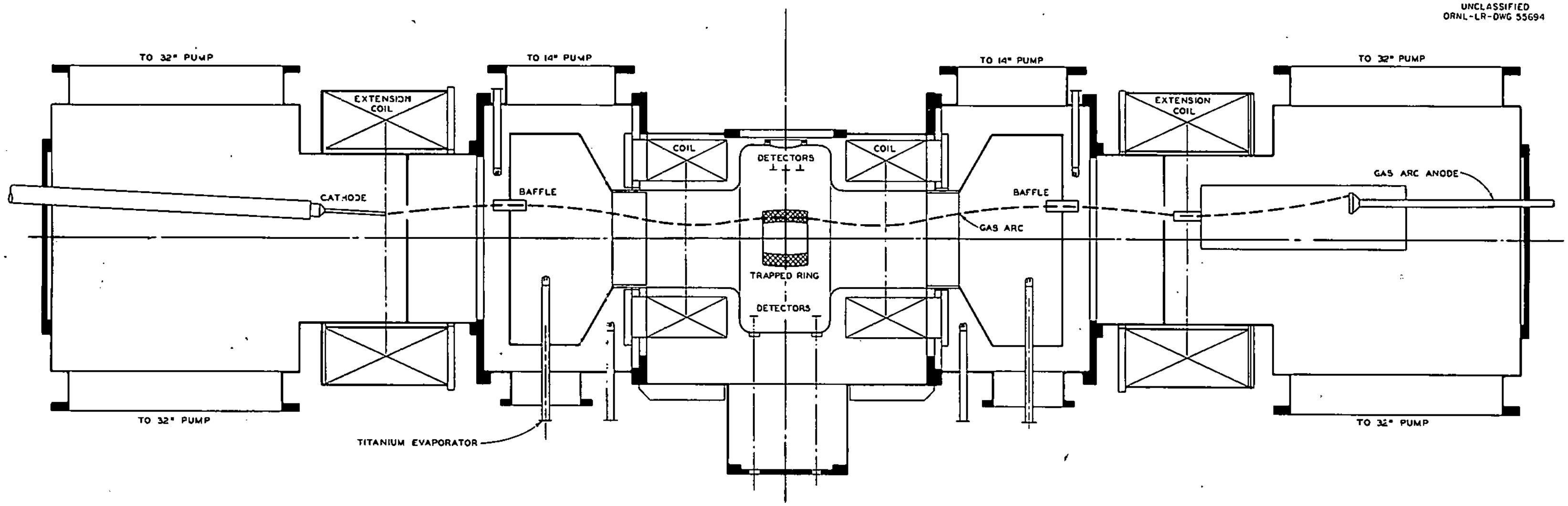

Fig. 1.15. Schematic Diagram of DCX Showing Extension Coils and Gas Arc.

With continued use, however, the copper plates apparently suffered crystalline changes, probably as the result of thermal cycling, and yielded to the pressure of the cooling water.

By use of the rotating anode, with a 4 atmospheric cc/sec deuterium gas bleed, a 200-amp arc ran at about 225 v, the liner pressure was 1 to 2×10^{-5} mm Hg, and the pressures in the outer vacuum regions were higher by factors of 5 to 10. Operation with gas flow rates much less than 4 atmospheric cc/sec resulted in almost immediate anode failure.

As indicated by these characteristics, the use of a rotating anode has not led to a usable arc. Two stationary anodes in which the arc impinges upon water-cooled tubes, arranged for vortex flow in one case and swirl flow in the other, have been fabricated. These have not yet been tested.

The high liner pressure attending operation with deuterium or hydrogen is a disturbing characteristic of these gas arcs. With 4 atmospheric cc/sec 200-amp deuterium arcs, the maximum observed ratio of tank pressure to liner pressure was 10, and the usual ratio was about 7. With a deuterium arc in operation the measured pumping speeds for a deuterium leak in the liner region were 7000 to 8000 liters/sec. Operation of the arc raised the liner pressure from a base of less than 1×10^{-6} to about 1×10^{-5} mm Hg. From the measured pumping speeds out of the liner, it appeared that arc operation produced a gas load in the liner equivalent to about 0.1 atmospheric cc/sec.

The source of this gas load is not positively known. Conductance from the higher pressure tank region is not a major factor since the combined conductance of the two isolation baffles is only 200 liters/sec *without* the arc, and is presumably less with the arc. Outgassing of the liner due to the deuterium arc is not expected to be a significant factor since the arc radiates little heat to the liner walls, and since operation with a baked liner has had little effect on liner and tank pressures measured with the arc on.

It was thought that the gas load might be due to positive ions diffusing from the arc column and being neutralized by collision with the liner baffle nearer the cathode. To check this hypothesis, an unbiased Faraday cup was inserted through the median plane probe port and the collected current was noted as the cup was advanced toward the arc. On the basis of the measured ion flux, it was not possible to account for the gas load in terms of positive ion diffusion.

The possibility exists that the neutral gas load is produced by the dissociative recombination of D_2^+ ($D_2^+ + e \rightarrow 2D^0$) and (or) radiative recombination of D^+ ($D^+ + e \rightarrow D^0$). It appears that the former process could produce the entire gas load if the arc were as much as 1% D_2^+. No analysis of the arc composition has been attempted in DCX.[4]

1.2.2 Small Carbon Arcs

It appeared that some of the objectionable features of carbon arc breakup could be alleviated by the use of an arc of smaller diameter. With a carefully focused H_2^+ beam such an arc might dissociate a reasonably large fraction of the molecular ions, and it would offer a relatively smaller target for circulating protons, so charge exchange and energy losses might be reduced.

---

[4] See, however, sec 4.3 of this report.

Two attempts were made to run small arcs in DCX-1. Each of these arcs was 120 in. long, was operated in the full magnetic field (10 kilogauss on the axis at the midplane), and was used in conjunction with a $\frac{3}{4}$-in.-diam carbon anode.

In the first run the tungsten cathode was $\frac{1}{8}$ in. OD and $\frac{1}{16}$ in. ID. With this electrode a 30-amp arc would have produced the same cathode current density as a 300-amp arc with the usual $\frac{1}{2}$-in.-OD cathode. Even with a steady flow of argon gas sufficient to keep the liner pressure at 6×10^{-5} mm Hg, it was necessary to raise the current to 90 amp to maintain the arc. After about a minute and a half, the high current density melted away a portion of the cathode and the run was terminated.

The second run was made with a $\frac{1}{4}$-in.-OD, $\frac{1}{8}$-in.-ID tungsten cathode. It was possible to operate a 110-amp, 350-v discharge with this electrode without bleeding support gas through the cathode. However, an examination of the cathode after a few minutes arc time revealed that the gas bleed hole had melted closed.

1.3 NEUTRAL BEAM APPARATUS

The motivation for this investigation was the development of a neutral beam probe for studying the DCX-1 plasma.

A diagram of the apparatus is shown in Fig. 1.16. When the pressure in the source region is raised, the three $\frac{1}{8}$-in.-diam defining apertures collimate a beam of neutrals and direct the beam into the detector region. The detector is a double Pirani gage with the resistor elements wired in a Wheatstone bridge circuit. The gage is so constructed and situated that with no directed molecular beam the bridge circuit is balanced for all detector region pressures. A directed beam, however, constitutes an additional influx of gas to half of the double gage and the bridge is unbalanced.

By using a beam of air produced by the collimating apertures, it was consistently possible to detect a flow through the apertures as low as 0.3 μ-liter/sec. The double Pirani gage detector itself is considerably more sensitive. When bleeding air directly into the gage, the limit of detection was about 0.03 μ-liter/sec.

The device had two objectionable features: (1) the detector time constant was long, in the order of several minutes; and (2) the bridge circuit galvanometer showed a continuous oscillation with a period of several minutes. In spite of these, the over-all performance of the apparatus was encouraging and a neutral beam probe for plasma work has been fabricated.

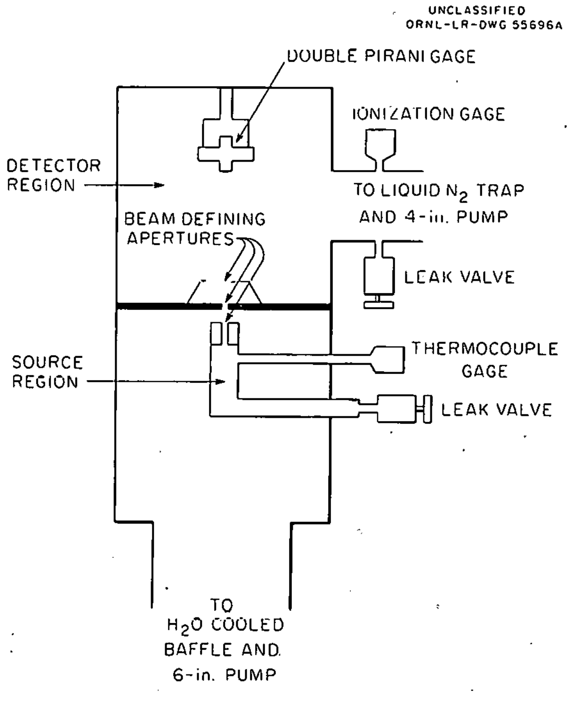

Fig. 1.16. Neutral-Beam Apparatus.

In DCX-1 the probe will be used to project a beam of neutral hydrogen through the plasma region first with and then without molecular ion injection. The detector will be used to sense the attenuation that results from ionizing and scattering collisions of the neutral beam with the trapped energetic ions. Neglecting large-angle scattering, the probability that a neutral hydrogen molecule will traverse the plasma is given as

$$P = e^{-n\sigma l v_i/v_0} ,$$

where

n = energetic ion density,

σ = cross section for ionization of neutrals by energetic ions,

l = path length through the plasma,

v_i = velocity of the energetic ions,

v_0 = velocity of the neutrals.

The cross section σ is about 1×10^{-16} cm^2/molecule and l is approximately 10 cm. A 300-kev plasma density of $2.5 \times 10^{+10}$ ions/cc would result in a P of 0.9, or an attenuation of 10%. If the sensitivity of the Pirani detector to a hydrogen beam were the same as its measured sensitivity to air, this attenuation could be measured with a total neutral beam input of about 3 μ-liters/sec. Actually the detector sensitivity should be considerably greater when using hydrogen as the probing beam, in which case densities correspondingly less than $2.5 \times 10^{+10}$ could be probed with the same total neutral beam input. The 3 μ-liters/sec input figure represents a liner pumping load of 30,000 liters/sec at 1×10^{-7} mm Hg. Since liner pumping speeds of 50,000–60,000 liters/sec have been measured[5] at 1×10^{-7} mm Hg, even lower ion densities could be probed by increasing the neutral beam input.

1.4 VACUUM EQUIPMENT

1.4.1 Tests of Redhead Vacuum Gage

Use of a Redhead vacuum gage to measure the pressure in the DCX-1 vacuum tank appeared attractive in several respects. The gage requires a magnetic field for operation and it seemed possible to make use of the natural DCX field. This would offer the advantage of mounting such gages inside the tank at the actual locations at which pressure measurements are desired. In contrast, the standard ionization gages are mounted in magnetic shields outside the vacuum tank and are connected to the desired locations through lengths of tubing. The high sensitivity of the Redhead gage allows the output signal to be read with less amplification and should permit the gage to follow more rapid pressure changes.

Some tests of a Redhead gage in DCX-1 were described in a previous report.[6] Additional performance checks were recently made on a Redhead gage mounted inside the DCX-1 tank on the median plane about 20 in. from the axis of the machine. The tests were made both with and without

---

[5] See sec 1.5, this report.

[6] *Thermonuclear Project Semiann. Rept. Jan. 31, 1960*, ORNL-2926, sec 1.2.2.

beam injection and arc operation. The gage sensitivity was evaluated by comparison with the pressure readings from a conventional ionization gage known to be dependable. The Redhead gage sensitivity was a fairly strong function of the gage anode voltage, but for a single anode voltage it was a function of the tank pressure. The sensitivity measurements as a function of voltage and pressure were not reproducible from day to day.

On the basis of the tests on this one sample it was concluded that the Redhead gage was a useful device for measuring the pressure in a strong magnetic field and for following rapid pressure fluctuations, but that it was not reliable enough to warrant replacing the conventional ionization gages on the equipment.

1.4.2 Tests of Varian Vaclon Pumps

A description of a special Vaclon pump designed for operation within the DCX-1 inner vacuum region, and test results on a pilot model were given in a previous report.[6] A large pump for operation inside the DCX-1 magnetic field has been received and partially tested. Repeated failures of insulators in the pump unit have delayed completion of these tests, but the measured pumping speeds for hydrogen gas are about 5000 liters/sec. These figures are extremely low in comparison with the design speed of 50,000 liters/sec.

Observations were presented in the last report[7] from which the inference was made that in the process of pumping a test gas a standard 250 liters/sec Vaclon pump re-emitted previously pumped gas molecules. These tests were continued and also extended to include checks of a standard 10,000 liters/sec (for hydrogen) Vaclon pump. The observations regarding re-emission from the pump elements were confirmed.

Tests on the 250 liters/sec pump indicated that with increasing concentration of a test gas, hydrogen or deuterium, the concentration of a number of heavier constituents within the pumped volume also increased in an essentially linear fashion. The mass 28 component was by far the strongest of these constituents, and considerable effort was expended in attempts to determine its origin.

It seems clear that the mass 28 constituent is not the result of an interaction of the test gas with carbon in the system since there was no mass shift in going from a hydrogen leak to a deuterium leak. It is unlikely that the constituent was bled in with the test gases since these were admitted through a palladium leak.

The usual suspects are N_2, CO, and C_2H_4. There is evidence for believing it to be the hydrocarbon resulting from breakdown of pump oil. Filling a liquid-nitrogen cold trap on the system while monitoring the mass 28 peak showed that the amplitude decreased, and the boiling point of C_2H_4 is higher than that of N_2 or CO. The Vaclon was at times operated with an oil diffusion pump, so oil vapors were present. Other hydrocarbon masses (25, 26, 29, and 31) were also noted, and though not nearly in as great abundance as the mass 28, these too increased with increased pressures.

---

[7] *Thermonuclear Project Semiann. Rept. July 31, 1960*, ORNL-3011, sec 1.1.

The more common thermal disintegration products of pump oil are reported as having masses 43, 57, 71, 84, and 97. Ions having these masses were detected in the pumped volume, but the amplitudes of their signals changed little when the Vaclon pump was turned on or off. If the PIG discharge in the Vaclon pump were breaking down the oil to produce C_2H_4, it would appear that the process must be much more selective than ordinary thermal disintegration.

Baking the Vaclon pump elements, either by prolonged high-pressure pumping or by use of a 400°C vacuum oven, did not alter the qualitative behavior of the mass 28 constituent and reduced its amplitude by less than a factor of 2. However, in each case after baking, the diffusion pump was used to lower the system to base pressure, and even though the pump was liquid-nitrogen trapped there was still the possibility of some oil contamination.

1.5 ENGINEERING MODIFICATIONS

The equipment at the high-voltage terminal of the accelerator tube has been extensively changed. A new ion source was purchased from High Voltage Engineering Corporation and has been installed. The source is of the duoplasmatron variety, as was the one it replaced. However, in the new arrangement the ion beams from the source are magnetically analyzed between the source and the accelerator tube, rather than at the base of the accelerator tube. Only the desired H_2^+ beam component is accelerated, an arrangement which minimizes the current load on the accelerator and the high-voltage power supply and also minimizes the pumping load in the vacuum tank. The new source should be capable of supplying 25 ma H_2^+ to the tube. The installation of this equipment is now complete and tests are under way to evaluate its performance in conjunction with the DCX-1 accelerator.

The increased 60-cycle power requirements of the new source and its associated equipment necessitated the construction of a three-phase isolation transformer stack to supply this power at +600 kv potential. After some initial difficulties, the transformer stack now seems to be operating satisfactorily.

The vacuum tank has also been extensively modified. The system now consists of three sections: (1) the inner liner region, which is pumped by batch evaporation from four titanium-clad tantalum filaments; (2) the intermediate region, which is pumped by seven evaporators and the two 14-in. oil diffusion pumps previously installed; and (3) the outer regions, each pumped by two 32-in. oil diffusion pumps equipped with water-cooled baffles. Isolation between the regions is achieved by passing the arc through suitably placed apertures. A section at the bottom of the tank has been modified to permit mounting a 10,000-liter/sec Varian Vaclon pump which will dispose of the undissociated portion of the H_2^+ beam. Figure 1.15 shows a diagram of the revised vacuum tank.

By using the titanium evaporators with an unbaked liner, the base pressure in the liner region was recorded as 3×10^{-8} mm Hg. For a hydrogen leak into the liner, pumping speeds of 50,000 to 60,000 liters/sec were indicated at 1×10^{-7} mm Hg. No titanium pump runs have as yet been made with an H_2^+ beam injected or with a gas arc in operation.

2. DCX-2 DESIGN AND ENGINEERING

P. R. Bell
J. S. Culver
S. M. DeCamp
J. C. Ezell
W. F. Gauster
G. G. Kelley
N. H. Lazar
R. J. Mackin
C. E. Normand
G. R. North
J. F. Potts
M. Rankin

2.1 GENERAL AND DESCRIPTIVE

2.1.1 Introduction

The last report[1] gave an introductory discussion of the DCX-2 concept and some of the design features of the machine being built to exploit it. The main features which characterize the new machine are (1) an injection scheme which provides a long path length for molecular ions in the plasma region and many passes through a trapped-ion plasma; (2) use of the ion-pumping effect of the trapped plasma, which is expected to yield pumping speeds approaching 10^6 liters/sec; (3) a magnetic field of such strength and scale as to make the mirror losses no more than those predicted by adiabatic orbit theory. It is hoped to achieve an initial plasma density in excess of 10^{11} particles/cc, using either a trapping arc or the background gas, after which the trapped plasma itself will serve as an adequate target to cause the density to build up to a point limited by mirror losses. During this report period the plasma-buildup theory has been extended by Rose[2] and Fowler[3] to take account of energy losses to the arc electrons or to the electron component of the trapped plasma. An approximate form of the theory, without energy losses, has been worked out[4] and extended to give (1) estimates of the time dependence of plasma buildup, (2) a more complete picture of buildup, using an initial arc as a trapping plasma, and (3) an estimate of the effects of impurity gases on the burnout current. A major result from this study is that an ideal carbon arc would have a density only slightly in excess of 10^{11} particles/cc. For an arc of this density there is the additional advantage that energy losses to the arc electrons are negligible.

The most promising scheme for achieving a long molecular-ion path appears to be that of injecting into a helical orbit of very fine pitch. To reduce the pitch angle below that necessary to miss the injector snout, it is planned to place the injection point in a region of reduced field. As the molecular ions move out of this region, the pitch becomes finer. The stringent requirements imposed on the magnetic field are recounted in ref 1.

Figure 2.1 shows DCX-2 in some detail. The picture is already obsolete in that the injection point has been moved into the space between the booster coil and the mirror coil, and a small "dip" coil has been added next to it.

---

[1] P. R. Bell *et al.*, *Thermonuclear Project Semiann. Rept. July 31, 1960*, ORNL-3011, pp 13–29.

[2] D. J. Rose, *Ion Energy Distribution, Energy Degradation, and Exponentiation Criteria in a Plasma Formed by Beam Trapping and Charge Transfer*, ORNL CF-60-9-112 (Sept. 30, 1960).

[3] T. K. Fowler, *Effect of Energy Degradation on the Critical Current in an OGRA-Type Device*, ORNL-3037 (Dec. 28, 1960).

[4] R. J. Mackin, Jr., *Plasma Accumulation in a Device Fed by Energetic Ion Trapping*, ORNL CF-60-11-50 (Nov. 23, 1960).

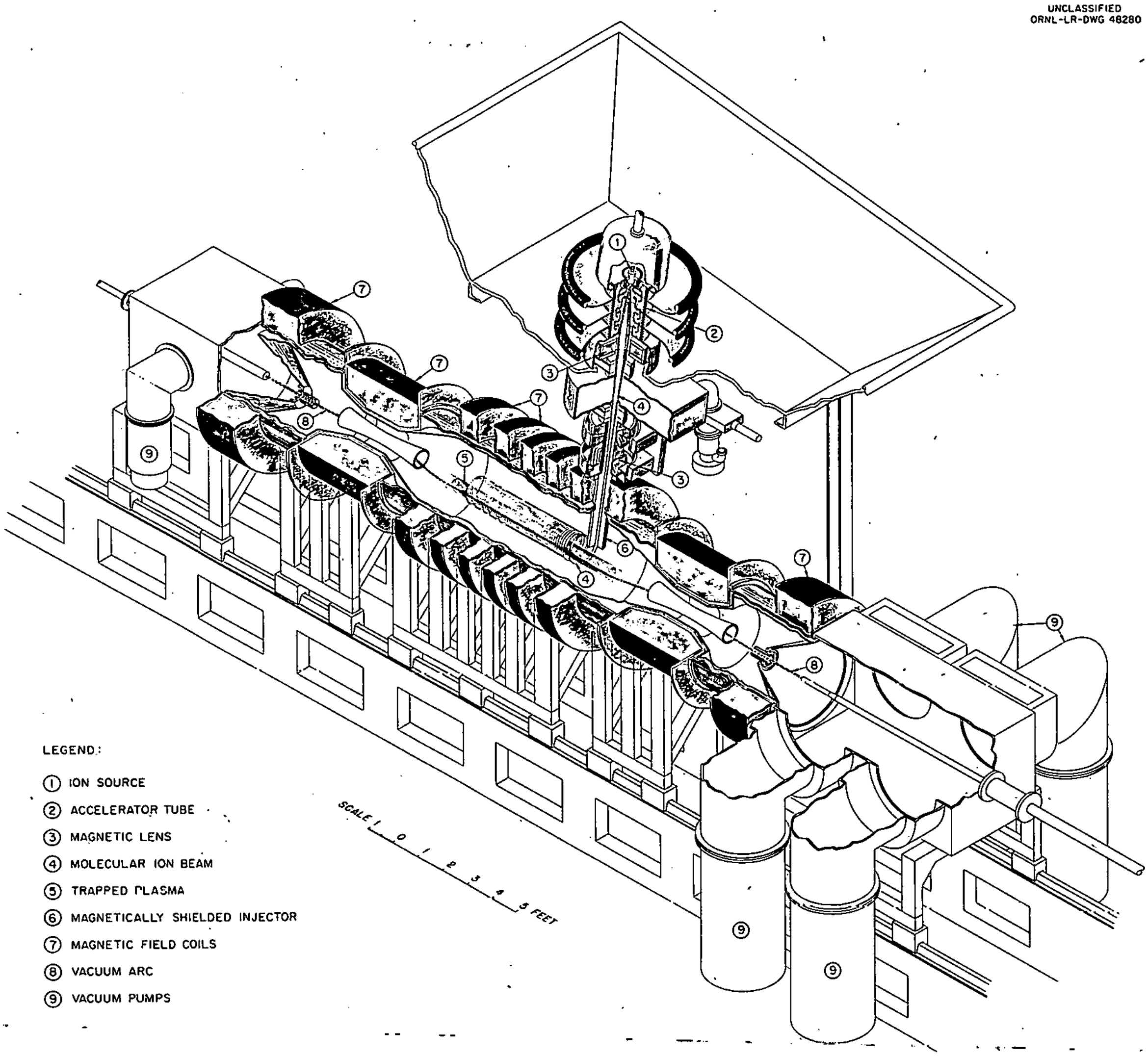

Fig. 2.1. DCX-2.

2.1.2 Orbit Calculations and Magnet Design

Considerable attention has been given to the problem of tailoring the magnetic field dip in the region of the injection snout. Certain of the orbit calculations relevant to this problem are described by North *et al.* in another section of this report.[5,6] The design of the magnet coils that will produce a magnetic field to meet the rather stringent requirements imposed by the injection considerations[1] is now complete. The calculations leading to the design are described by Gauster *et al.*[7]

---

[5] G. R. North, P. R. Bell, and R. J. Mackin, Jr., this report, sec 2.2.3.

[6] G. R. North *et al.*, this report, sec 2.2.4.

[7] W. F. Gauster *et al.*, this report, sec 8.2.

The coil assembly consists of (1) a set of outboard booster coils, whose purpose is to permit operating an arc with electrodes significantly outside the mirror coils; (2) the mirror coils themselves; (3) the inboard booster coils, whose currents will be tailored to produce an extremely uniform field in the central region; and (4) a pair of dip coils designed to produce the appropriate field dip in the region of the snout. The outboard booster coils have been built and are now in the process of being installed on an experiment to test coil design and the handling of large ion beams. The design of the mirror coils was completed in December 1960, and a contract is being negotiated for their manufacture. Delivery is expected on May 15, 1961, and May 31, 1961. Design of the inboard booster coils was completed in January 1961, and they are expected to be completed in May. The mechanical design of the magnetic coils was performed by the Engineering Group of the Thermonuclear Division.

It is expected that under extreme conditions the coils will require about 5000 gpm of cooling water. This will be divided into 656 parallel water paths. Each path will be temperature-protected by a thermal switch on the output water, set to trip at 93°C. Tripping of any switch will open the field breakers of all generators supplying the coils.

Careful tuning of the relative currents in the various coils will be necessary to obtain the uniform-field conditions in the central region of the machine. To accomplish this to first order, adjustable shunts are being designed to go across each section of the inboard booster coils. These shunts will be capable of carrying up to 5% of rated coil current. Fine control on the field will be achieved by variable-current power supplies installed across selected portions of these shunts. These power supplies will be capable of producing small changes in the magnetic field while the machine is in operation.

2.1.3 Injection System

The high-gradient 600-kv accelerator tube has been assembled and tested and found to hold full voltage. Beams up to 70 ma have been accelerated down the tube, limited by the current-handling capacity of the targets installed at the time. This work is described in more detail by Kelley *et al.*[8]

Tests on a preliminary model of the injector snout[9] have verified that the initial design will be adequate to achieve the field reduction which was required inside. Some idea of the size of the perturbations around the snout has also been acquired. The next model of the snout, now under construction, will be tested in the magnetic field provided for the high-current 600-kv beam test facility and should provide the basis for a final design.

2.1.4 Vacuum

The main features of the vacuum system were described in the previous report.[1] During the present period, the main activities in this field have consisted of consulting on the mechanical design of the vacuum system and in testing components.

---

[8] G. G. Kelley *et al.*, this report, sec 5.1.

[9] R. L. Brown, this report, sec 5.3.

Normand[10] describes elsewhere current tests on nude ion gages and on the development of an ion-beam tube with highly effective differential pumping along its length.

Barnett *et al.*[11] have conducted initial tests in DCX of a set of prototype titanium evaporators designed by Neidigh. The mechanical design appears adequate and is scheduled for use in DCX-2 without appreciable modification. Their pumping-speed results are encouraging.

2.1.5 Instrumentation

As of January 26, 1961, instrument engineering for DCX-2 is about 30% complete. This figure is based on finished drawings and does not include work still in sketch or note form.

Major components have been specified, and bills of material have been written for about 35% of the instruments. The scheduled completion date for design is March 20, 1961, and for bills of material, is March 3, 1961.

A complete description of the instrumentation is too detailed to be included in this report. Only the most significant or unusual features will be mentioned briefly below.

The penetration of the spiral beam will be monitored continuously by means of a series of calorimeters along a line parallel to the axis of the machine and intercepting the fast neutrals produced by charge exchange in the arc. Other calorimeters will measure the power returned to the injector and to the rest of the liner.

A multichannel recording means will be provided for other experimental data. The method of recording has not been decided but probably will include perhaps 14 FM tape channels for temporary storage of fast signal reading-out into chart-type recorders.

2.1.6 Engineering Design

The detailed design of DCX-2 is being carried out by the Y-12 Engineering Division and coordinated by Thermonuclear Division personnel. The first phase of this engineering is now complete. The area in which DCX-2 is to be installed has been cleared and construction is slated to start February 1, 1961. The following are included in the first phase: machine foundations and working platform; control room structure and facilities; 1000-kva, 460-v three-phase substation; cable runs and switch gear for magnet supplies; and fore-vacuum system.

Design of the major mechanical components is 80% complete, and the main tank vacuum manifolds and their supports are in the shop. The main tank section has been contracted to the MacGregor Michigan Company, Detroit, and is scheduled for shipment February 12, 1961. The 304-series stainless steel plate has been received and rolled. Welding qualification tests are about to begin, using a modified type 308 stainless steel welding rod which produces a fully austenitic, hence nonmagnetic, weld deposit. Finish-machining of the shell will be done locally if scheduling allows.

A set of hydraulic bearings has been developed which should make it possible to move the heavy tank section and coils manually along the 70-ft flat stainless steel track. In a test model,

---

[10] C. E. Normand and F. A. Knox, this report, secs 10.3 and 10.2.

[11] C. F. Barnett *et al.*, this report, sec 1.4.

oil pressure of 150 to 200 psi was found to lift and provide a virtually frictionless bearing for a 6000-lb load.

The all-copper tank liner will be constructed of Roll-Bond plate manufactured by the Olin Mathieson Chemical Corporation, East Alton, Illinois. This material has water passages formed between two metallurgically bonded sheets. Two test panels have been ordered in order to perfect assembly techniques before the rolling of the custom-designed panels for the liner.

A new support and positioning device is being designed to receive the accelerator. The structural support is an overhead aluminum bridge crane which will be purchased from an outside vendor. The positioning device has been designed to give translation along all three axes and tilting motion about the seal into the tank.

2.2 PARTICULAR ASPECTS OF DCX-2

2.2.1 DCX-2 Magnetic Field Calculations

M. Rankin

Using the Oracle code TIM,[12] a magnetic field for 600-kev H_2^+ injection into DCX-2 was designed. The following properties were imposed: (1) current densities in the three inside boosters approximately equal; (2) $H_0 \cong 12$ kilogauss; (3) mirror ratio ≈ 3.3 to 1; (4) "Mackin average" dip = 1.6% of the field; (5) dip located just outside the third inside booster; and (6) optimum homogeneity from 0 to 26 in. From power requirement considerations, the current density of the mirror coil is fixed at 7050 amp/in.^{2} and that of the outside booster at 4740 amp/in.^{2}.

A straightforward sequence of cases (described in DCX Technical Memorandum No. 32) was run to find the best geometry for meeting these requirements. The resulting coil arrangement is given in Fig. 2.2. The corresponding current densities in amp/in.^{2} are: $i_1 = 4620.9$; $i_2 = 4441.7$; $i_3 = 4577.1$; and $i_D = -1794.9$. The axial field deviates from 12 kilogauss by less than 1 gauss from 0 to 25 in. It has a dip of 122.5 gauss at 39.5 in.

Figure 2.3 is a three-dimensional representation of the magnetic field, by J. C. Jordan.

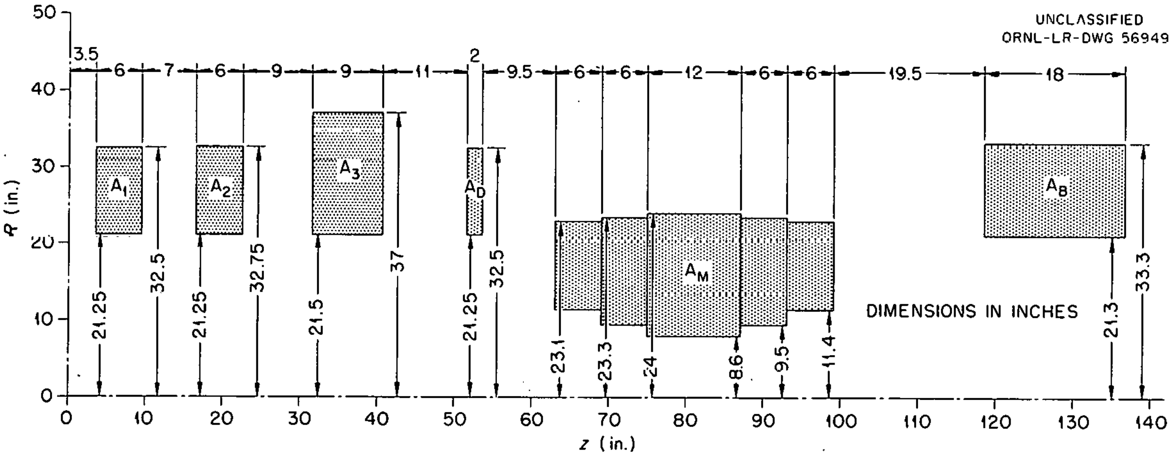

Fig. 2.2. DCX-2 Coil Geometry.

---

[12] G. R. North and M. Rankin. *Thermonuclear Project Semiann. Rept. July 31. 1960.* ORNL-3011, p 84.

UNCLASSIFIED
ORNL-LR-DWG 56950

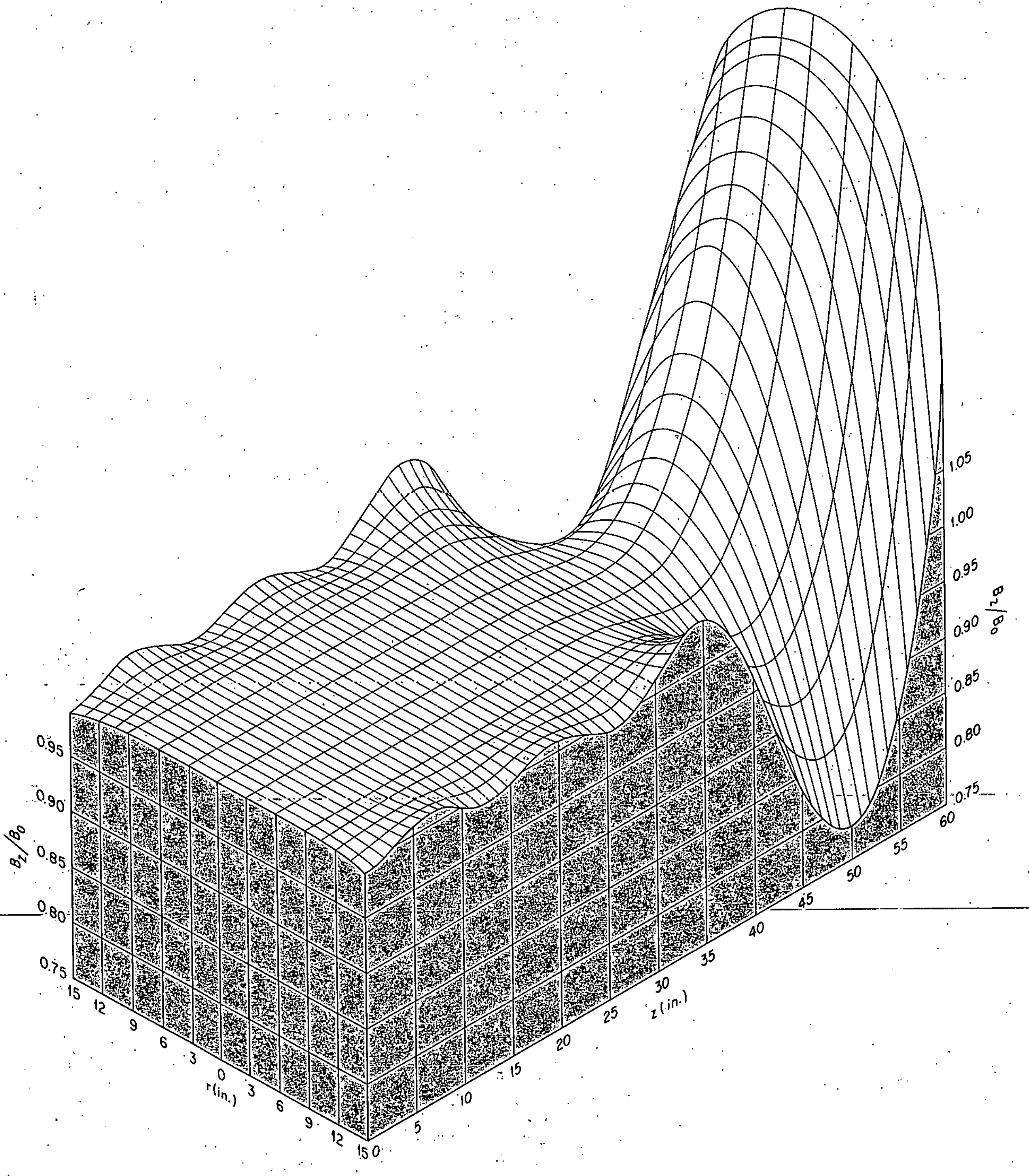

Fig. 2.3. B_z/B_0 for DCX-2 (H_2^+ Injection).

2.2.2 Absolute Containment in DCX-2

G. R. North

The equation for the containment zone of a trapped proton in DCX-2 is given by the equation[13]

$$\frac{p_\theta}{r} - \frac{e}{c} A = -p \,, \tag{1}$$

where p_θ is the canonical angular momentum, A is the magnetic vector potential, p is the total momentum of the particle, and r is the radial coordinate measured from the magnetic axis. Let us write for A:

$$A = \frac{B_0}{2} r[1 + y(r, z)] \,. \tag{2}$$

Substituting (2) into (1) gives

$$\frac{p_\theta}{p} - \frac{r^2}{2r_0} (1 + y) + r = 0 \,, \tag{3}$$

where $r_0 = cp/eB_0$. If y has little dependence on r (which is a very good approximation here), we may solve (3) to obtain

$$r = \frac{r_0}{1 + y} \left[1 \pm \sqrt{1 + \frac{2}{r_0} (1 + y) \frac{p_\theta}{p}} \right] . \tag{4}$$

Now we calculate p_θ/p for particles injected in DCX-2. Using $r \cong \frac{2}{5} r_0$, the result is readily found to be

$$(p_\theta/p)_{\mathrm{DCX\text{-}2}} \cong -\tfrac{8}{25} r_0 \,, \tag{5}$$

a result good to better than ±1% for any initial pitch less than about 6°. We now insert (5) into (4) at the mirror of DCX-2 (i.e., $y \cong \frac{5}{2}$) and find that the roots of (4) are complex, which means that this containment zone is closed.

By setting the radicand of (4) equal to zero we are able to calculate the critical value of p_θ/p:

$$\left(\frac{p_\theta}{p}\right)_{\mathrm{crit}} = -\frac{r_0}{2(1 + y)} = -\frac{r_0}{7} \,, \tag{6}$$

One may now use (6) to calculate a critical injection point such that particles would just be absolutely contained:

$$r_{\mathrm{crit}} = r_0 \left(1 - \sqrt{\tfrac{5}{7}}\right) \cong 0.39 \text{ in.} \tag{7}$$

Simple geometric considerations show that a particle must be scattered at least 14° from the injected orbit to become nonabsolutely contained. The critical angle of scatter depends on the

---

[13] T. K. Fowler and M. Rankin, *Containment Properties of DCX*, ORNL CF-59-6-32 (June 5, 1959).

position on the circle at which the particle is scattered and on the direction of scatter. An interesting case is the point at which the particle crosses the dissociating arc. At this particular point the direction of scatter makes no difference since all momentum is rotational. We write:

$$\frac{1}{r}\left(\frac{p_\theta}{p}\right)_{\mathrm{crit}} - \frac{r}{2r_0} = -\cos\alpha_{\mathrm{arc}} \,. \tag{8}$$

Inserting (6) into (8):

$$\alpha_{\mathrm{arc}} \cong 56^\circ \,. \tag{9}$$

The significance of absolute containment for the injected ions is that adiabatic containment theory is unnecessary until particles are influenced by "plasma effects." In other words, it is guaranteed that no particles will leak out the mirrors until plasma densities of the order of those in DCX-1 are established.

2.2.3 H_2^+ Orbits in the Dip Region of DCX-2

G. R. North
P. R. Bell R. J. Mackin

Several methods have been suggested for hand-tracing orbits in the DCX-2 dip-field region. The purpose of this section is to derive a helical approximation and display some results for H_2^+ ion injection. The required equations will be derived and then followed by a discussion of error. Finally, there will be a discussion of calculated orbits. See Fig. 2.4 for orbit diagram.

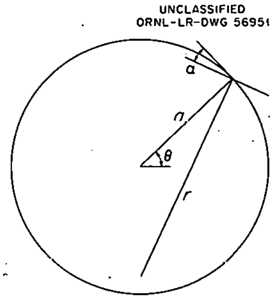

Fig. 2.4. Orbit Diagram.

The Helical Approximation. – The equation of motion in the Z direction is

$$M\ddot{Z} = \frac{e}{c} V_\theta B_r$$

$$\cong \frac{e}{c} V \cos\alpha\, B_r \text{ (for small } V_z) \,, \tag{1}$$

$$\ddot{Z} \cong a\omega^2 \cos\alpha \left(\frac{B_r}{B_0}\right) . \tag{2}$$

We shall now integrate Eq. (2) approximately, taking small arcs around the circle:

$$\dot{Z} = \dot{Z}_0 + a\,\omega^2 \int_0^t \cos\alpha \left(\frac{B_r}{B_0}\right) dt \quad (\omega \sim \text{constant}) \,.$$

For one arc segment,

$$\Delta t = \Delta\theta/\omega \,,$$

$$\dot{Z} = \dot{Z}_0 + a\omega \left[\cos\alpha\left(\frac{B_r}{B_0}\right)\right]_{\mathrm{av}} \Delta\theta \,. \tag{3}$$

The pitch angle ϕ is given by:

$$\dot{Z}/V = \sin\phi \cong \phi\ ,$$

$$\phi = \phi_0 + \left(\frac{B_r}{B_0}\right) \cos\alpha\,\Delta\theta\ . \tag{4}$$

We now write an equation for Z:

$$Z = Z_0 + a\,\phi_0\,\Delta\theta\ . \tag{5}$$

Clearly one can increment along an orbit by using Eqs. (4) and (5).

After checking a case with $\Delta\theta = 30^\circ$ and 15°, the increment was chosen to be 30°.

Discussion of Precession. – For simplicity we consider a particle which cuts the magnetic axis. From the cylindrical symmetry we have, using the Hamiltonian formulation,

$$\omega_m = \frac{eB_0}{mc}\left(\frac{A_\theta}{B_0}\right)\frac{1}{r}\ , \tag{6}$$

where ω_m is the angular velocity measured with respect to the magnetic axis, and A_θ is the magnetic vector potential. If we assume a parabolic field:

$$\frac{B_z}{B_0} = 1 - \delta\frac{r^2}{a^2} = \frac{1}{r}\frac{\delta}{\delta r}\left(r\frac{A_\theta}{B_0}\right) \quad (\text{for } \delta \text{ small})\ , \tag{7}$$

or

$$\frac{A_\theta}{B_0} = \frac{r}{2} - \frac{\delta r^3}{4a^2}\ ,$$

then we may write

$$\omega_m = \omega_0\left(\frac{1}{2} - \frac{\delta r^2}{4a^2}\right)\ . \tag{8}$$

The equation for r may be written

$$\ddot{r} = r\,\omega_m^2 - \omega_0\,r\,\omega_m\left(\frac{B_z}{B_0}\right)\ . \tag{9}$$

Using Eqs. (7) and (8) we arrive (to first order in δ) at:

$$\ddot{r} = -r\frac{\omega_0^2}{4} + \frac{\delta}{2}\omega_0^2\frac{r^3}{a^2}\ . \tag{10}$$

Clearly a first approximation to (10) is given by the circle whose equation is:

$$r_1 = 2a\sin\frac{\omega_0}{2}t\ . \tag{11}$$

Now the amount of precession in one turn is readily calculated:

$$\pi - \theta_p = \int_0^{2\pi/\omega_0} \omega_m \, dt \; . \tag{12}$$

Using the first approximation to r we obtain:

$$\pi - \theta_p = \pi - \delta\pi \; .$$

The amount $\delta\pi$ represents the precession undergone in the single turn.
Clearly then

$$\theta_p = \pi[B_z(0) - B_z(a)] \; . \tag{13}$$

A look at the DCX-2 field shows that precession should not be more than about 2° in the region of interest.

Calculations. – Several orbits have been calculated from the 12-kilogauss field in DCX-2. These H_2^+ orbits have Larmor radii of 5 in. and miss the magnetic axis by 1 in. The magnetic field used was that proposed by M. Rankin.[14]

The optimum injection point is $Z_0 = 42$ in. from the midplane. The optimum injection pitch is 7.5°. These figures were arrived at from adiabatic considerations.

The orbits were followed a few turns with the helical approximation out of the dip region. As the field began to flatten, the adiabatic formula,

$$\Delta(\phi^2) = - \Delta B/B \; , \tag{14}$$

was used. Justification is based on the first orbit calculated. The formula was used after the second, third, and fourth turns, and since the results agreed to within 5%, the rest of the orbits were followed only two turns by the helical method. After this point, one could predict the pitch in the uniform region by using the adiabatic formula.

Since the beam is an inch in diameter and slightly divergent, it was of interest to calculate the extreme rays. The results are summarized in Table 2.1.

---

[14] M. Rankin, this report, sec 2.2.1.

Table 2.1. Pitch Angles ϕ_{final} Calculated for Various Injection Points Z_0 and Various Injection Angles ϕ_0

Case	ϕ_0 (deg)	Z_0 (in.)	ϕ_{final} (deg)
1	7.5	42	2.07
2	7.5	41.5	1.4
3	7	42	Reflects
4	7.25	42.5	1.4
5	7.5	42.5	2.6

2.2.4 H_3^+ Orbits and Precession in DCX-2

G. R. North
P. R. Bell R. L. Brown R. J. Mackin

The helical approximation[15] has been used to follow H_3^+ orbits from the snout to the uniform field region. These are 900-kev orbits whose Larmor diamater is 15 in. It is to be noted that these orbits extend radially to a region where the field is not well behaved. From adiabatic approximations it was estimated that a dip in the $\langle B_z \rangle$ field should be of the order of 0.6% for a perfect mirror effect, where $\langle B_z \rangle$ represents a time average of B_z over a particle revolution. This field could be manufactured with a dip coil current of +2268 amp/m^2. Orbit studies were made with this field.

The results of the calculations showed that a $\langle B_z \rangle$ bump under the third booster was so large that when a particle got out of the dip and over this bump, its pitch would return to a larger value than the injection pitch when in a flat region (thus entirely defeating the purpose of a dip).

The solution here is to sacrifice the integrated optimum field slightly in order to take away the bump. This was done by reducing the current in the third booster by 0.6%. Hence, $\int (B - B_0)^2 \, dz$ is no longer a minimum with respect to the currents in all inboard coils. Using the helical approximation, optimum initial conditions were found to be $Z_0 = 43.5$, $\phi_0 = 4.5°$. This orbit crosses the bump with $\phi_{\text{bump}} = 0°$ and $\phi_{\text{flat}} = 4.2°$. These results show no appreciable mirror effect of the dip, but ϕ_{flat} is about 20% less than in the first case considered. It should be emphasized that ϕ_{flat} is an average in the "flat" field region. The H_3^+ orbit never sees a flat field so that the helix is continually compressing and expanding as it traverses the length of DCX-2.

Precession Calculations. – Since the large H_3^+ orbits were so sensitive to small fluctuations in the field, it was of interest to see if this property could be used advantageously. Of particular interest was the dip region at the far end of the machine. Noting that in the dip region the field has a large radial gradient, one might expect sizable precession. Only 42° of precession is necessary to miss the snout on the orbit's return path.

In order to find the precession, an approximate numerical-graphical procedure was derived. The method combines the helical approximation mentioned earlier,

$$\Delta\phi = a \cos\alpha \left(\frac{B_r}{B_0}\right) \Delta\theta \,, \tag{1}$$

$$\Delta Z = a\phi \, \Delta\theta \,, \tag{2}$$

and a formula for the radius of curvature, ρ. The helical approximation is used through a small arc $\Delta\theta$, and the radius of curvature of the orbit is calculated by using

$$\rho \cong \frac{cmV_\perp}{eB_z} = \frac{cmV}{eB_z} \cos\phi \quad (\text{for } V_z \text{ small}) \,,$$

---

[15] This report, sec 2.2.3.

or

$$\rho \cong \frac{\rho_0}{B_z/B_0}\left(1 - \frac{\phi^2}{2}\right), \tag{3}$$

with $\rho_0 = 7.5$ in. With a value of ρ one could sweep out an arc of 30° and measure the new r coordinate so as to look up the new field quantities. It is clear that one can increment along an orbit in this way with reasonable precision. This laborious procedure is the next approximation to the helical approximation alone.

Two orbits were followed in detail by using this method. The first orbit is an H_3^+ orbit beginning at the 35-in. "bump" with $\phi_0 = 1°$, $r_0 = 14$ in. The orbit has a twofold purpose: since it went directly into the snout hole (if it were there), it serves as a check on the helical approximation; total precession at the far end dip could also be estimated. It was found that precession from 35 in. in to 43.5 in. was of the order of 1°, so that the earlier work was probably very accurate. In the next part of the orbit (43.5 in. to reflection at 46.5 in.), about 15° of precession was recorded. In the round trip one might expect about 30° of precession.

From this calculation we see that we are close, indeed, to the required 42° needed to miss the snout. By making the dip "deeper," precession could be made larger. Therefore, a similar orbit was followed in the H_2^+ dip field described above. Since no precession occurs until the particle is well into the dip region, the particle was started from $Z = 39$ in. with a pitch of $\phi_0 = 8.3°$ (angle necessary to overcome the bump in this field). Computation was stopped when this particle amassed a precession angle of approximately 45°, but it was still adding more precession.

3. PLASMA PHYSICS

3.1 AN ELECTRON CYCLOTRON HEATING EXPERIMENT

R. A. Dandl R. J. Kerr
H. O. Eason M. C. Becker
F. T. May

Electron cyclotron heating experiments have been in progress during the last six months on the Physics Test Facility. The usual form of the apparatus consists of a cylindrical cavity placed in a dc magnetic mirror field. The cavity is operated in a transverse electric mode at 2.2 to 2.4 kMc. The power is fed to the cavity from a 1-kw continuous-wave Varian Associates model 802 klystron amplifier. Usually, hydrogen gas is let into the cavity, and the gas is broken down by the microwave electric field. The properties of the resulting cyclotron-heated electrons are measured by several techniques to be described.

The first experiment involved measurement of the decay time of the electron cyclotron radiation by means of a microwave dipole placed near an axial opening in the cavity. The dipole and its accompanying superheterodyne receiver were tuned to an electron cyclotron frequency higher than the heating frequency (which meant listening to radiation originating from stronger magnetic field regions). The general arrangement is illustrated in Fig. 3.1. This experiment employed a dc plasma gun (described in previous Thermonuclear Division semiannual reports) injecting axially into the microwave cavity. The cavity was operated in a TE_{015} mode. The decay times of electron cyclotron radiation after the microwave heating power was turned off were of the order of 50 msec. A

UNCLASSIFIED
ORNL-LR-DWG 53496

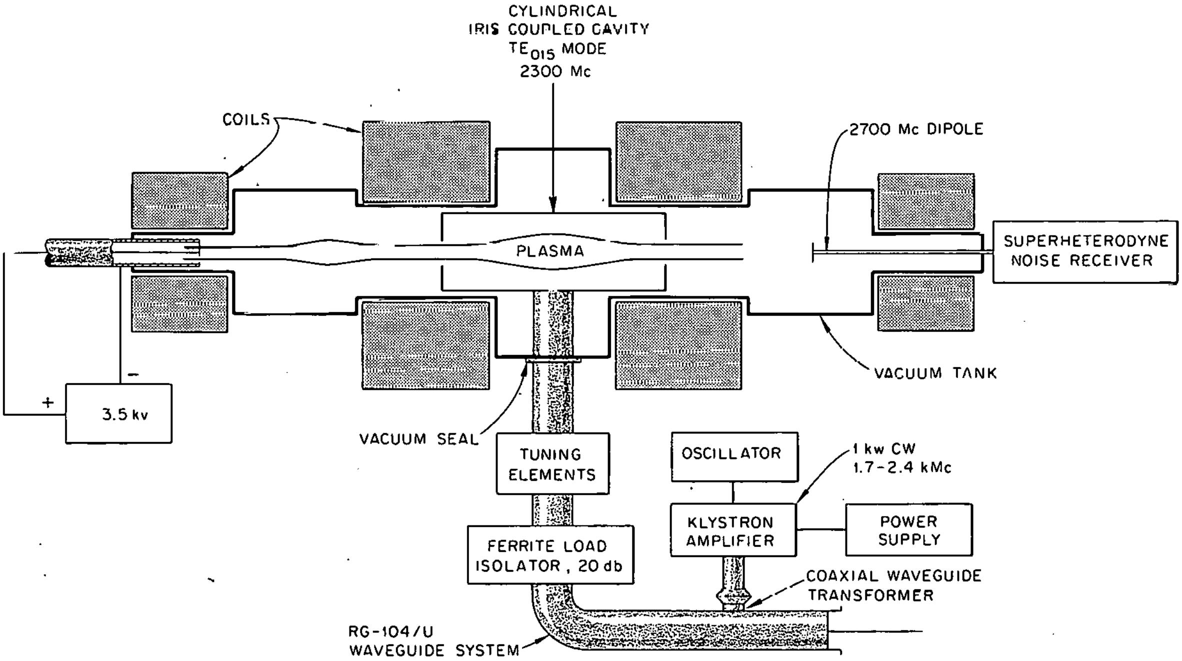

Fig. 3.1. Physics Test Facility Electron Heating Experiment.

typical photograph of such decay with the appropriate boundary parameters is shown in Fig. 3.2. The square waves at the top of the photograph indicate the plasma gun on and the microwave power on (respectively) in the positive direction. The increase in radiation just after the feed sources have been removed is attributed to anisotropic scattering processes in the presence of microwave power and to the diffusion of trapped electrons to the field region seen by the radiometer with the power off.

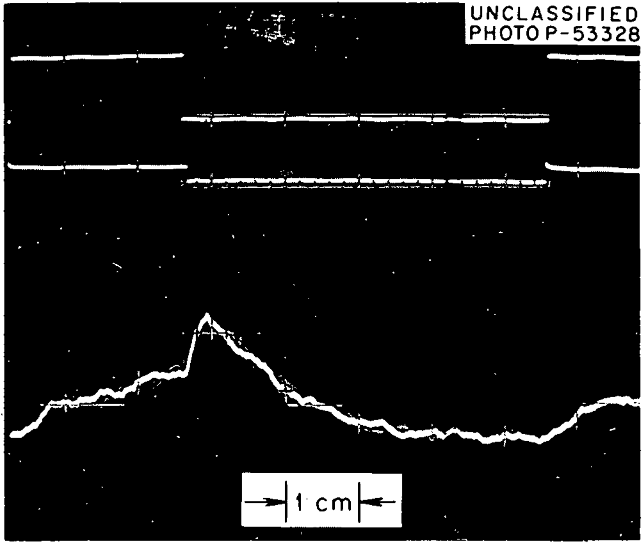

Fig. 3.2. Decay of Electron Cyclotron Radiation. Sweep speed 25 msec/cm.

Interest in electron density in this heating experiment necessarily has led to employment of techniques other than those with microwaves for density measurements. The first of these was the very simple experiment of dropping powdered metal through the plasma. In this case, molybdenum powder was dropped through the plasma and incandescence was observed, indicating considerable stored energy in the electron gas. Quantitative measurements are being considered along the lines of this experiment in an attempt to make numerical determinations. However, other diagnostic methods will probably be employed first. In order to explain the long containment time, illustrated by Fig. 3.2, electron energies of many kilovolts are necessary. This suggested that we look for bremsstrahlung radiation; it was easily found and many bremsstrahlung curves have been studied. The spectrometer technique has been refined several times, but it is still not satisfactory in terms of finally determining plasma density or plasma temperature, because the actual bremsstrahlung radiation from the gas seems to be a small part of the radiation observed. Most of it seems to be coming from impacts of hot electrons upon the walls of the cavity.

Figure 3.3 illustrates one of these bremsstrahlung curves, the data for which were taken using a sodium iodide spectrometer. The measurements were made through lead apertures with an aluminum window on the cavity. Quick estimates would indicate the electron temperature to be of the order of 10 kv. It is felt that electron densities of the order of 10^{10} or greater and temperatures of 10 kv or more are possible in this machine, and efforts are being made to optimize and determine these parameters more exactly. A neutral beam density probe is being prepared, as are other kinds of measurements, most of which are in stages too preliminary to merit description at this time.

UNCLASSIFIED
ORNL-LR-DWG 56952

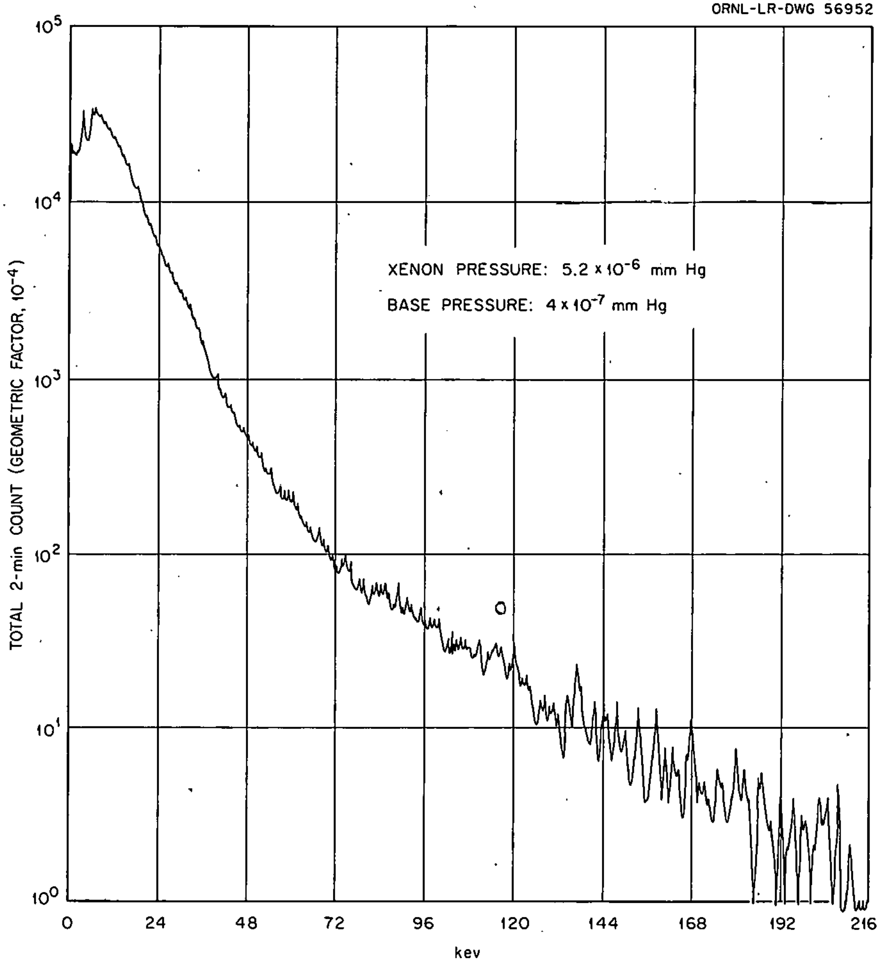

Fig. 3.3. Bremsstrahlung from Electron Cyclotron Heating. Double 1-in. lead collimators spaced 12 in. and having $\frac{1}{2}$-in. graded apertures. Axis of spectrometer in midplane.

3.2 APPARENT OBSERVATIONS OF IONIC SOUND WAVES IN AN ARC PLASMA[1]

Igor Alexeff R. V. Neidigh

3.2.1 Introduction

Oscillations have been observed in a magnetically supported cylindrical rod of plasma. This rod of plasma can be the discharge occurring in the defining aperture of a mode II, pressure-gradient arc.[2] Similar oscillations can also occur in the column of a mode I arc. These oscillations appear to be the mechanism that drives the mode II blowup phenomena.

---

[1] I. Alexeff and R. V. Neidigh, *Apparent Observations of Ionic Sound Waves in an Arc Plasma*, ORNL CF-61-2-57 (Feb. 13, 1961).

[2] R. V. Neidigh, *The ORNL Thermonuclear Program*, ORNL-2457, pp 55, 164–65 (Jan. 15, 1958); R. V. Neidigh, *The Effect of a Pressure Gradient on a Magnetically Collimated Arc*, ORNL-2288 (May 27, 1957); R. V. Neidigh and C. H. Weaver, *Proc. U.N. Intern. Conf. Peaceful Uses Atomic Energy, 2nd, Geneva, 1958* 31, 315 (1958).

An oscillation can be quite pure in frequency. Radio-frequency amplitudes can be high; more than 20 v have been found on a probe. Harmonics that are integral multiples of the fundamental frequency are observed.

The oscillation appears to be produced by a longitudinal standing ionic sound wave in the plasma column. The fundamental frequency of this oscillating system is apparently given correctly by the formula

$$F = \frac{1}{2L}\sqrt{\frac{3kT_e}{m_i}}.$$

The electron temperature, T_e, is found to be roughly equal in energy to the first excitation potential in the un-ionized gas. The frequency dependence on ion mass, m_i, and on plasma column length, L, for ions of mass 1 to 201, and for columns of 2.2 to 23.0 cm, has been investigated. The experimental frequency dependence appears to fit the theoretical predictions.

3.2.2 Properties of Ionic Sound Waves

The existence of ionic sound waves was first predicted in 1929 by Tonks and Langmuir.[3] The formula for the frequency is

$$F = \left(\frac{ne^2}{\pi m_i + ne^2 m_i \lambda^2/\gamma kT_e}\right)^{1/2},$$

where

n = number of electrons/cm^3 (since the plasma is assumed to be electrically neutral, this number is also the number of ions/cm^3),

e = charge on the electron, esu,

m_i = mass of the ion, g,

λ = wavelength of the ion wave, cm,

γ = adiabatic compression coefficient,

k = Boltzmann's constant,

T_e = electron temperature, °K.

The constant γ, referring to the adiabatic compression of the electrons, was set equal to 1 in the paper of Tonks and Langmuir. This corresponds to an isothermal ionic sound wave. If the electrons suffer scatterings, but no energy losses, during one cycle of the ionic sound wave, then γ is $5/3$. This corresponds to the case of a conventional sound wave. Spitzer[4] shows that in a sufficiently rarefied plasma, γ may be 3.

---

[3] L. Tonks and I. Langmuir, *Phys. Rev.* 33, 195 (1929).

[4] Lyman Spitzer, Jr., *Physics of Fully Ionized Gases*, p 59, Interscience, New York, 1956.

The frequency of an ionic sound wave is given by a more simple formula if the wavelength of the wave, λ, is considerably longer than the Debye cutoff length, L_D:[5]

$$\lambda >> L_D = \left(\frac{kT_e}{4\pi ne^2} \right)^{1/2} ,$$

$$F \approx \frac{1}{\lambda} \sqrt{\frac{\gamma kT_e}{m_i}} .$$

3.2.3 Model of an Oscillating Plasma Column Using Ionic Sound Waves

Assumptions Needed for the Model. – In the experiments done at the Arc Research Facility at ORNL a fixed radio-frequency oscillation was discovered in a column of plasma supported by a magnetic field. This fixed frequency is assumed to be due to a standing wave. In this case the wavelength should correspond to some dimension in the apparatus. It is assumed that the wave moves along the plasma column, parallel with the magnetic field, and that $\lambda/2 = L$, the length of the column.

The electron temperature is assumed roughly to be fixed by the first excitation potential in the un-ionized gas filling the system. Electrons having energy greater than the first excitation potential rapidly lose their energy by excitation and ionization processes. Electrons having energy below this first excitation potential lose their energy much more slowly.

During experiments with one gas, T_e should be roughly a constant despite changes in the discharge conditions. For different common gases, T_e should not vary by more than a factor of 3.5. This variation in T_e from gas to gas should also be roughly predictable.

The value of the constant γ can vary from 1 to 3. In the experiments to be discussed, the value $\gamma = 3$ fits best.

The model of the resonant system in the oscillating column of plasma is now complete. The observed oscillation is assumed to be due to ionic sound waves which move along the plasma column parallel to the magnetic field. The frequency of the oscillation is given by the following formula:

$$F = \frac{1}{2L} \sqrt{\frac{3kT_e}{m_i}} ,$$

where

F = observed frequency, cps,

L = length of the plasma column, cm,

k = Boltzmann's constant,

T_e = electron temperature, °K (T_e roughly corresponds in energy to the lowest excitation potential in the un-ionized gas),

m_i = ion mass, g.

---

[5] *Ibid.*, p 17.

Predictions of the Model. – If the above model of oscillations in the plasma column is correct, the following behavior of the frequency of oscillation should be observed:

1. The frequency is pure.
2. The frequency is not a function of the magnetic field or of the ion density. (Thus the frequency should be independent of gas density in the apparatus.)
3. The frequency is independent of plasma supply voltage and of plasma supply current.
4. Harmonics appear as integral multiples of the fundamental frequency.
5. The frequency is proportional to $(m_i)^{-1/2}$, to $(T_e)^{1/2}$, and to $(L)^{-1}$.

3.2.4 Experimental Results

Oscillations in the Defining Aperture of a Mode II Arc. – The column of plasma in the defining aperture of the mode II arc discharge was studied first. As shown in Fig. 3.4, a ring-shaped electrostatic probe was placed around the aperture exit. The probe was made ring-shaped so that radiofrequency pickup from the rotating secondary plasma would not be detected.[6] This secondary plasma occupies much of the vacuum chamber.

---

[6] R. V. Neidigh, *The ORNL Thermonuclear Program*, ORNL-2457, pp 55, 164–65 (Jan. 15, 1958); R. V. Neidigh, *The Effect of a Pressure Gradient on a Magnetically Collimated Arc*, ORNL-2288 (May 27, 1957); R. V. Neidigh and C. H. Weaver, *Proc. U.N. Intern. Conf. Peaceful Uses Atomic Energy, 2nd, Geneva, 1958* 31, 315 (1958).

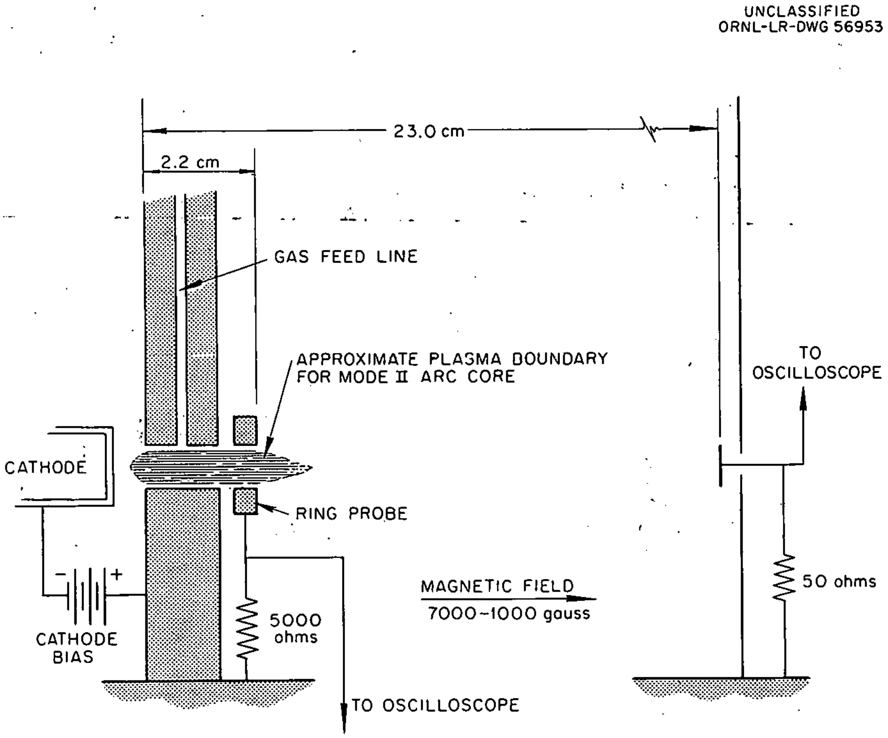

Fig. 3.4. Schematic Diagram of the Apparatus Used to Observe the Pulsation Frequency of the Plasma Boundary at the Transition from Mode I to Mode II.

An oscillation due to the plasma in the defining aperture was detected. This oscillation was studied by varying the parameters of the system, that is, gas feed, cathode voltage, cathode current, magnetic field, and type of gas. Crude but definite regularities were found in the frequency of the oscillation.

The regularities that were found are listed below. These correspond to some of the predictions of the ionic sound wave model listed above.

1. The frequency was rather pure.
2. The frequency was not a function of the magnetic field or of the gas density.
3. The frequency was not a function of cathode bias voltage or of cathode emission current.
4. The frequency, at best, was a weak function of ion mass.

Harmonics were studied next. By carefully adjusting the parameters of the system, the oscillation would abruptly change its frequency from the fundamental to the second harmonic. Figure 3.5 shows two oscilloscope traces made of oscillations in a 23.0-cm-long column of xenon plasma.

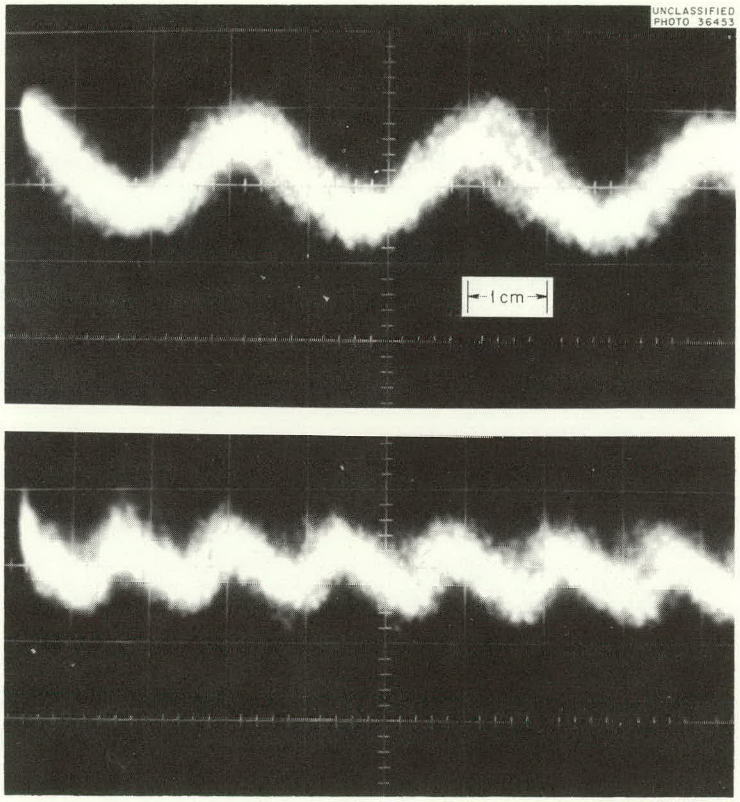

Fig. 3.5. Fundamental and Second Harmonic in a Xenon Arc. 20 μsec/cm, 0.2 v/cm.

For both traces the discharge conditions were almost identical. However, one trace shows the fundamental frequency; the other shows the second harmonic. The frequencies are related almost in the ratio 1 to 2. On occasion, harmonics up to the 5th were observed. Thus the prediction that harmonics should appear as integral multiples of the fundamental frequency is verified.

Next, the frequency dependence on ion mass was studied. The inert gases were used in the mode II arc. From the lightest to the heaviest inert gas, the lowest excitation potential, and thus the electron temperature, T_e, varies only by about 2.5. However, a variation in ion mass, m_i, of 33 to 1 is available. Thus, in going from gas to gas, the frequency change due to variations in T_e should be small compared with that due to variations in m_i.

The experimental variation of frequency as a function of ion mass is shown in Fig. 3.6. The data are represented by the group of points clustered around the line labeled "2.2-cm arc." The line is given by the theoretical formula if one assumes T_e = a constant = 17 ev. This experimental frequency dependence on ion mass agrees well with theory. The electron temperature of 17 ev seems to be a reasonable average value for the inert gases. Thus the theoretical prediction that the frequency should be proportional to $(m_i)^{-1/2}$ seems to be satisfied.

Oscillations in the Core of a Mode I Arc. – Next, the frequency dependence on plasma column length was studied. By use of a mode I type of arc, as shown in Fig. 3.7, a plasma column

UNCLASSIFIED
ORNL-LR-DWG 55149A

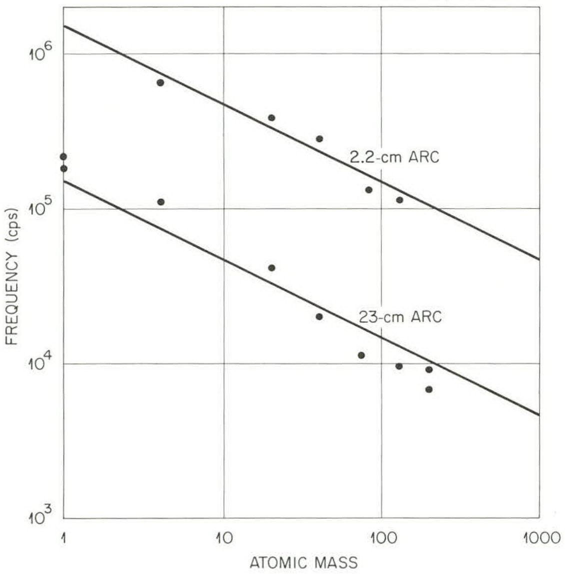

Fig. 3.6. Frequency Dependence on Ion Mass and on Length of Plasma Column.

UNCLASSIFIED
ORNL-LR-DWG 56954

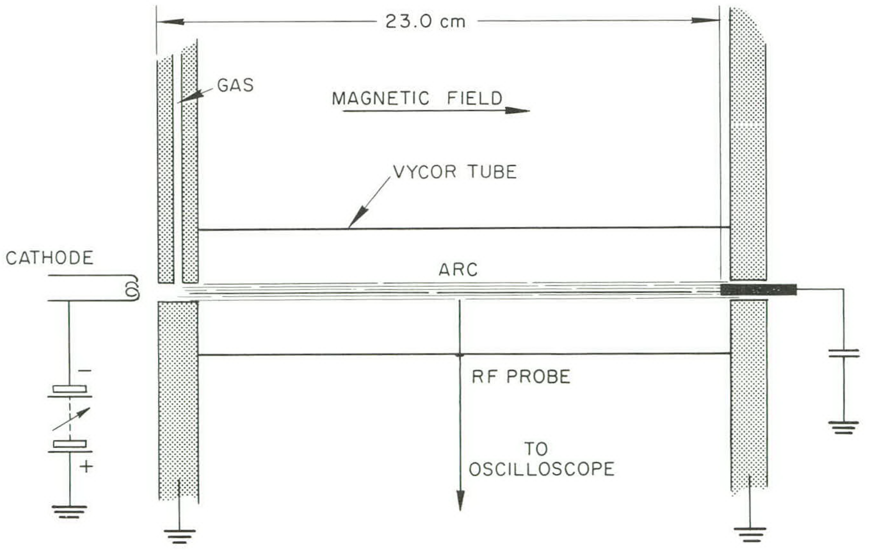

Fig. 3.7. Apparatus Used for Mode I RF Studies.

23.0 cm long was produced. As this column is now 10.5 times longer than in the previous experiment, the frequency for each of the inert gases should be 10.5 times lower. The mass scale was extended by adding mass 1, hydrogen, and mass 201, mercury.

The results of this experiment are also shown in Fig. 3.6. They are represented by the points around the line labeled "23.0-cm arc." The line is again given by the theoretical formula if one assumes T_e = a constant = 17 ev. Thus this second experiment also agrees with theory, verifying that the frequency should be proportional to $(m_i)^{-1/2}$ and to $(L)^{-1}$.

The frequency dependence on ion mass and on plasma column length was also checked for columns intermediate in length to the two columns listed above. Agreement between theory and experiment was again good.

The dependence of frequency on electron temperature has not yet been fully investigated. One difficulty is that, as Fig. 3.6 indicates, the electron temperature does not vary much. However, the departures from the straight line shown by the experimental points of the 23.0-cm arc do crudely show the expected temperature dependence. Helium and neon lie above the line, corresponding to their having excitation potentials greater than 17 ev. Argon, krypton, xenon, and mercury, correspondingly, lie below the line. Hydrogen does not fit. As it has an excitation potential of only 10 v, its points are too high. In general, the theoretical prediction that the frequency should be proportional to $(T_e)^{1/2}$ has *not* been adequately investigated.

Pulsations and Cyclotron Resonances. – Pulsations along magnetic field lines are now found in the short core of the mode II arc[6] and appear to be standing ionic sound waves, as previously discussed. The formula for the frequency,

$$F = \frac{1}{2L} \sqrt{\frac{3kT_e}{m_i}} ,$$

is applied. Here L is assumed to be only as long as the bright core of the mode II arc, which does not extend appreciably beyond the defining slot. The standing ionic sound wave appears to produce a pulsating plasma boundary which has maximum amplitude at either end of the defining slot; that is, the defining slot is equivalent to the open organ pipe, where the fundamental wavelength is twice the pipe length.

Evidence of pulsations in the core of the mode II arc is presented in Fig. 3.8. In the upper oscillogram a dual-beam oscilloscope is triggered by the signal to the anode (the lower trace). The upper two single traces are light signals from the center of the arc, but one from each side of the defining slot. Zero light intensity is at the top. It is seen that the downward light pulses are in phase. In the lower picture the oscilloscope is again triggered on the anode signal (the lower trace). The upper three single traces are from the top edge, the center, and the lower edges of the arc. The downward light pulses are in phase, showing no rotation of the plasma. The light pulses give evidence of a pulsating electron density which implies that pulsations in the plasma cause variation in the electron emission from the filament. This may be the feedback mechanism by which the oscillations are sustained.

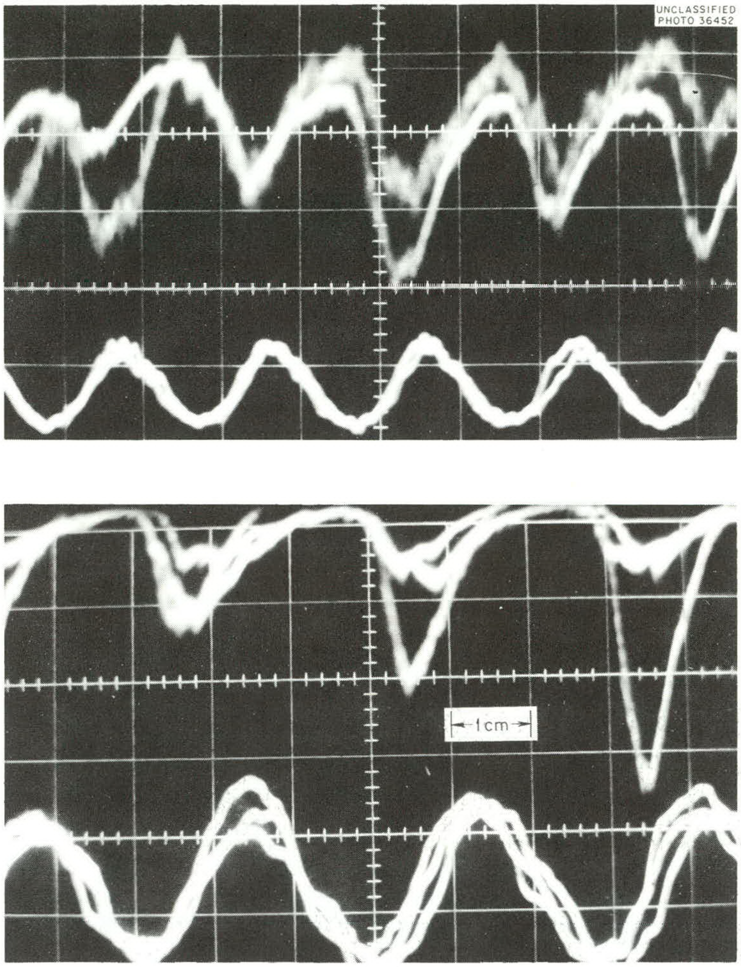

Fig. 3.8. Evidence for Pulsations in the Plasma Core in the Mode II Arc. In both pictures the oscilloscope was triggered on the anode (lower traces). In the upper picture the light pulse is from either side of the defining slot. In the lower picture the light pulses are from the top, center, and bottom edge of the arc. Note all light pulses are in phase.

When the gas is fed into the defining slot as it is in mode II, the high-pressure region is only in the vicinity of the defining slot. The region on either side is mostly sheath, and the higher sound-wave frequency permitted by this shorter arc (short "organ pipe") can be bracketed by the cyclotron frequency of the ion by adjusting the magnetic field through its permissible range. In the three experiments reported here the arc parameters (gas feed rate, cathode bias, cathode heating current) were adjusted so that an abrupt transition from mode I to mode II occurred as the magnetic field was reduced from 7000 gauss to 1000 gauss; see Table 3.1.

The appearance of the signal to a ring probe (schematic diagram and circuit shown in Fig. 3.4) is shown in Fig. 3.9. The upper trace is essentially mode I. The arc is about equal to the distance from the cathode to the anode, 23.0 cm. The ring shows only random noise. At 3750 gauss the signal becomes remarkably simple harmonic. The arc abruptly shortens to the length of the defining slot plus the ring, about 2.2 cm. Further reduction in the magnetic field (lower trace, Fig. 3.9)

Table 3.1. Transition from Mode I to Mode II; Magnetic Field Strengths for Different Atomic Masses

Gas	Magnetic Field for Transition (gauss)	Cyclotron Frequency (kc)	Sound-Wave Frequency (kc)
Argon, mass 40	3750	147	160
Nitrogen, mass 28	3000	168	181
Helium, mass 4	1100	430	520

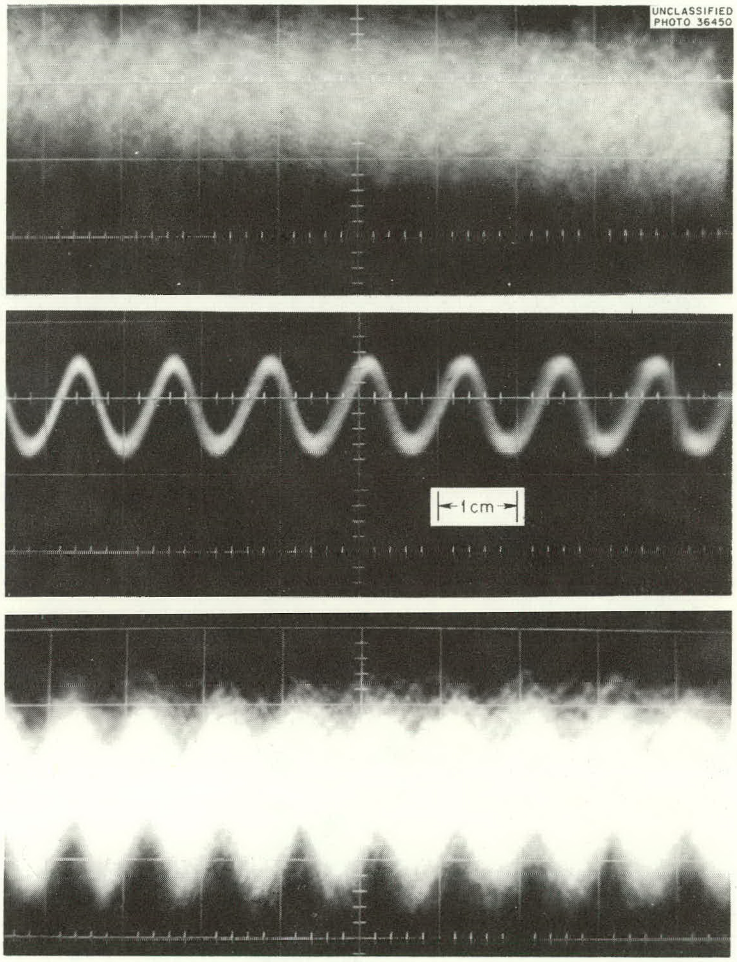

Fig. 3.9. Multiple Trace Oscillograms of the Signal to the Ring Probe When the Magnetic Field Was: (Upper) 5000 Gauss; (Middle) 3750 Gauss; (Lower) 1750 Gauss. Argon gas feed. Sweep speed, 5 μsec/cm. Vertical amplifier, 2 v/cm.

destroys some of the harmony in the signal, but energy is still being transferred to the ions, and the mode II characteristics persist.

3.2.5 Conclusions

A model describing standing ionic sound waves in a column of magnetically supported plasma has been discussed. This model is applied successfully to oscillations found in the defining aperture of a mode II pressure-gradient arc. The model also agrees well with oscillations found in a mode I type of arc.

Predictions of the model concerning the dependence of the observed frequency on ion mass, and on plasma column length, appear to fit the experimental data. Harmonics that are integral multiples of the fundamental were predicted and then found experimentally. An experimental value for the average electron temperature, T_e, has been found. This value of T_e, 17 ev, is of reasonable magnitude for the inert gases studied.

The model of an oscillator based on ionic sound waves is used successfully to predict the conditions under which the most pronounced plasma ''blowup'' occurs in the mode II, pressure-gradient arc. Apparently the best blowup occurs when the ionic sound wave is equal in frequency to the Larmor rotation frequency for positive ions in the magnetic field.

It is suggested that if ionic sound waves are really present, they may be used as a probe to measure the electron temperature, T_e, in the very hot plasmas studied in thermonuclear devices.

3.3 THEORY OF IONIC SOUND WAVES APPLIED TO RADIO-FREQUENCY PLASMA NOISE[7]

Igor Alexeff

3.3.1 Introduction

Most of the prominent spectral features in a paper by Crawford[8] can tentatively be explained in terms of standing ionic sound waves. Both the fixed low-frequency peaks and the high-frequency cutoff which varies as the square root of the anode current can be quantitatively located.

If this interpretation of the data is valid, it may be possible to find both the electron temperature, T_e, and the ion density, n, in terms of the radio-frequency noise spectrum.

3.3.2 Theory

Ionic sound waves, having a frequency as given below, were predicted for plasmas by Tonks and Langmuir in 1929[9] (see p 32 for the equation and a definition of the symbols).

---

[7] Evidence supporting the ideas of sec 3.2 of this report was found in a paper describing measurements of radio-frequency noise emitted by several mercury-vapor discharge tubes. Although the experiments were performed elsewhere, the interpretation supplements work done at ORNL. Hence, this interpretation is included here.

[8] F. W. Crawford, *Frequency Spectra of Low Frequency Fluctuations in a Plasma*, ML-762 (November 1960).

[9] L. Tonks and I. Langmuir, *Phys. Rev.* 33, 195 (1929).

In the case of a plasma, many ion wave frequencies are permitted up to the highest or cutoff frequency:

$$f_c = \left(\frac{ne^2}{\pi m_p} \right)^{1/2} .$$

This cutoff frequency is also known as the ion plasma frequency. By use of Debye's[10] sound wave theory of specific heats, one can picture the shape of the radio-frequency spectrum below the cutoff. The number of degrees of freedom in the frequency interval df is $dn = Cf^2\, df$, except possibly in the immediate region of the cutoff. Thus, one expects the radio-frequency noise spectrum to be a continuum. This continuum rises rapidly as f increases in value toward the cutoff frequency. At the cutoff, it drops to zero.

The cutoff frequency varies as $\sqrt{n}$, and n varies linearly with the anode current of the tube. Thus, the cutoff frequency is proportional to the square root of the anode current. In addition, one should be able to measure the maximum ion density in the tube by using the cutoff frequency:

$$\frac{\pi m_p f_c^2}{e^2} = n .$$

At the low-frequency end of the spectrum, one might expect to see standing waves corresponding to the lowest modes capable of being excited in the tube. It seems that the lowest modes in an oscillating system are most easily excited. These lowest modes should not vary with ion density. The formula for ionic sound waves, in the long wavelength limit, does not contain the ion density:

$$f = \frac{1}{L} \sqrt{\frac{\gamma k T_e}{m_i}} .$$

The constant L is the wavelength of the standing wave and corresponds to a physical dimension in the discharge tube.

To summarize, the ionic sound wave description of the radio-frequency noise spectrum from a plasma discharge tube might be as follows:

1. *Low-Frequency Region.* – One should find several peaks that are independent of the discharge tube current:

$$f = \frac{1}{L} \sqrt{\frac{\gamma k T_e}{m_i}} ,$$

where L corresponds to a dimension in the apparatus. If L, f, m_i, and γ are known, one can find T_e.

---

[10] F. K. Richtmeyer and E. H. Kennard, *Introduction to Modern Physics*, 4th ed., p 433, McGraw-Hill, New York, 1947.

2. *High-Frequency Region.* – One should find a continuum with a high-frequency limit. This limit should vary as the square root of the discharge tube current:

$$f_c = \left(\frac{ne^2}{\pi m_i} \right)^{1/2} .$$

This formula should be immediately useful in finding the maximum ion density, n, in the discharge (see Fig. 3.10).

UNCLASSIFIED
ORNL-LR-DWG 56955

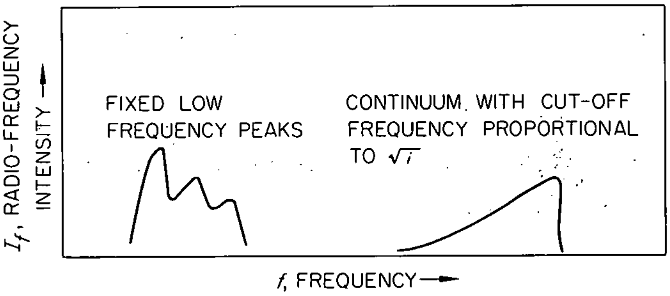

Fig. 3.10. Standing Ionic Sound Waves as a Function of Frequency. The term i is the anode current in the discharge tube.

3.3.3 Interpretation of Data

Low-Frequency Data. – Tubes I and II in Crawford's paper are geometrically simpler than tube III. Consider tubes I and II to be infinite cylinders. Standing ionic sound waves apparently do not exist along the length of the tubes. However, radial ionic sound waves do occur. The frequencies of these waves are given by the formula

$$f_{nm} = \frac{v}{2\pi R} x_{nm} ,$$

where

v = velocity of the ionic sound wave, cm/sec,
R = radius of the tube, cm,
x_{nm} = a zero of the Bessel function n.

The lowest modes are given by the following zeros: $x_{01} = 2.405$, $x_{11} = 3.832$, and $x_{02} = 5.520$.

The velocity of the sound wave is given by the formula

$$v = \sqrt{\frac{\gamma k T_e}{m_i}} ,$$

where

$m_i = 201 \times 1.67 \times 10^{-24}$ g (mercury).

Hence, the formula for f_{nm} becomes the following equation:

$$f_{nm} = \sqrt{\frac{\gamma k T_e}{m_i}}\,\frac{x_{nm}}{2\pi R} .$$

In tube I, the following frequencies are seen at 200 ma, (see Fig. 3 of ref. 8): 7.0×10^4 cps, 11.5×10^4 cps, 14.5×10^4 cps, where $R = 1.00$ cm. Let the lowest frequency be used to find T_e. Then one can see how well the other data are predicted. The constant γ is assumed to be the conventional $5/3$. A reasonable value for T_e then results:

$$T_e = 4.17 \text{ ev} .$$

One can next predict the second and third harmonic for tube I:

$f_{\text{predicted}}$ (cps)	f_{seen} (cps)
11.2×10^4	11.5×10^4
16.1×10^4	14.5×10^4

The nodal lines for these three modes are shown in Fig. 3.11. Thus the low-frequency data for tube I can be fitted very well.

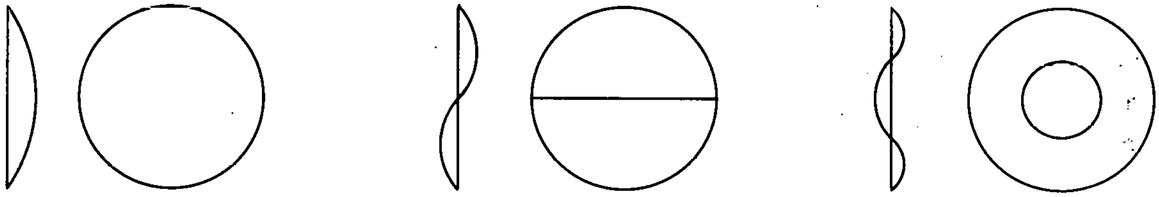

7.0×10^4 cps 11.2×10^4 cps 16.1×10^4 cps

Fig. 3.11. Nodal Lines for the Three Lowest Radial Modes in a Cylindrical Tube.

In tube II, Crawford states that he gets a strong fundamental at a frequency that varies from 7.3×10^4 cps at 100 ma, to 5.5×10^4 cps at 300 ma, where $R = 1.25$ cm. He does not give the frequencies for the higher harmonics.

By using the same value of T_e as found for tube I, one can predict a value for f:

$$f_{\text{predicted}} = 5.6 \times 10^4 \text{ cps} .$$

Thus low-frequency data given for tube II also can be fitted well.

In tube III the geometry is not sufficiently simple for one to predict a standing-wave pattern. The low-frequency data for tube III are therefore not discussed.

High-Frequency Data. – From the cutoff frequency found during a discharge, one should be able to predict the maximum ion density present in the discharge tube. However, to check the accuracy of the radio-frequency measurement, one must measure the ion density in some independent way. A Langmuir probe measurement of the plasma characteristics during a run would have been very useful. No Langmuir probe measurements were given.

Fortunately, in a discharge tube, the anode itself can be considered as a Langmuir probe operating in a saturated condition. The ion density is then given by the following formula:[11]

$$\frac{i}{A} = en\sqrt{\frac{kT_e}{2\pi m_e}} ,$$

where

i = anode current, amp,
A = anode area, cm^2,
e = electron charge, coulombs,
n = number of ions/cm^3,
k = Boltzmann's constant,
T_e = electron temperature, °K,
m_e = mass of the electron, g.

To find the ion density, one needs to know the anode current i, the anode area A, and the electron temperature T_e. The anode current is given in Crawford's paper. The electron temperature has been found from the low-frequency data. All that is needed is an estimate of the anode area.

Tube I. – Unfortunately, sufficient data are not available to estimate the anode area.

Tube II. – The anode area is 4.9 cm^2, estimated. At 100 ma, the results of the probe and the radio-frequency measurements of the ion density are compared:

$$n_{\text{probe}} = 3.5 \times 10^9 \text{ ions/cm}^3 ,$$

$$n_{\text{rf}} = 8.0 \times 10^9 \text{ ions/cm}^3 .$$

The agreement seems to be good. The value n_{rf} is greater than n_{probe}, as expected. The radio-frequency measurement yields the highest value for n; the probe yields an average value near the anode.

Tube III. – The anode area is 6.3 cm^2, estimated. At 100 ma, the results of the probe and the radio-frequency measurements are compared:

$$n_{\text{probe}} = 2.7 \times 10^9 \text{ ions/cm}^3 ,$$

$$n_{\text{rf}} = 29.0 \times 10^9 \text{ ions/cm}^3 .$$

The agreement is not too good. However, n_{rf} is greater than n_{probe}, as expected. Perhaps the more

---

[11] J. D. Cobine, *Gaseous Conductors*, 1st ed., sec 6.6, Dover, New York, 1941.

complex geometry is causing the trouble. The value for n_{rf} may correspond to a region of high ion density near the cathode.

3.3.4 Conclusions

The data in Crawford's paper seem to fit the hypothesis of ionic sound waves. Both Crawford's low-frequency and high-frequency data can be roughly described by the theory presented. In addition, using Crawford's radio-frequency measurements, rough values for the electron temperature, T_e, and the ion density, n, have been obtained. It is suggested that, if the ionic sound wave phenomenon is really the source of the radio-frequency noise, one has a new, simple method of measuring both the electron temperature and the ion density in a plasma.

4. VACUUM ARC RESEARCH

4.1 THE CARBON ARC

4.1.1 Rotational Drift of C^{2+} Ions as Affected by Arc Current in the Long Solenoid Facility

P. M. Griffin G. K. Werner

The spectrum lines emitted by carbon ions in a Luce arc exhibit a characteristic "slant" which has been reported previously.[1,2] The term "slant line" merely describes the condition in which the wavelength of the light incident on the spectrograph slit varies along the length of the slit. In this investigation, the axis of the projected image of the arc passed through the middle of the slit and was perpendicular to the slit. The Doppler-shifted wavelengths of light from different zones in the arc are consistent with the concept of an azimuthal drift of the ions about the arc axis in a sense opposite to that of the Larmor rotation of the ions. This rotational drift is probably due to the $\vec{E} \times \vec{H}$ forces resulting from a radial electric field and is superimposed on the Larmor rotation.

Figure 4.1 shows schematically the method of observation. It was assumed that there was no radial component of velocity of the ions other than that due to thermal motion. The thermal motion results in a symmetric broadening of the line, which was found to be the same at all points along the length of the line. This observation plus the fact that the line was straight was considered justification for the above assumption; these observations also indicated that either all the light was being emitted at nearly the same radius or that the angular velocity $\dot{\theta}$ was constant.

---

[1] J. R. McNally, Jr., and M. R. Skidmore, *J. Opt. Soc. Am.* **47**, 863 (1957).

[2] J. R. McNally, Jr., *J. Opt. Soc. Am.* **49**, 328 (1959).

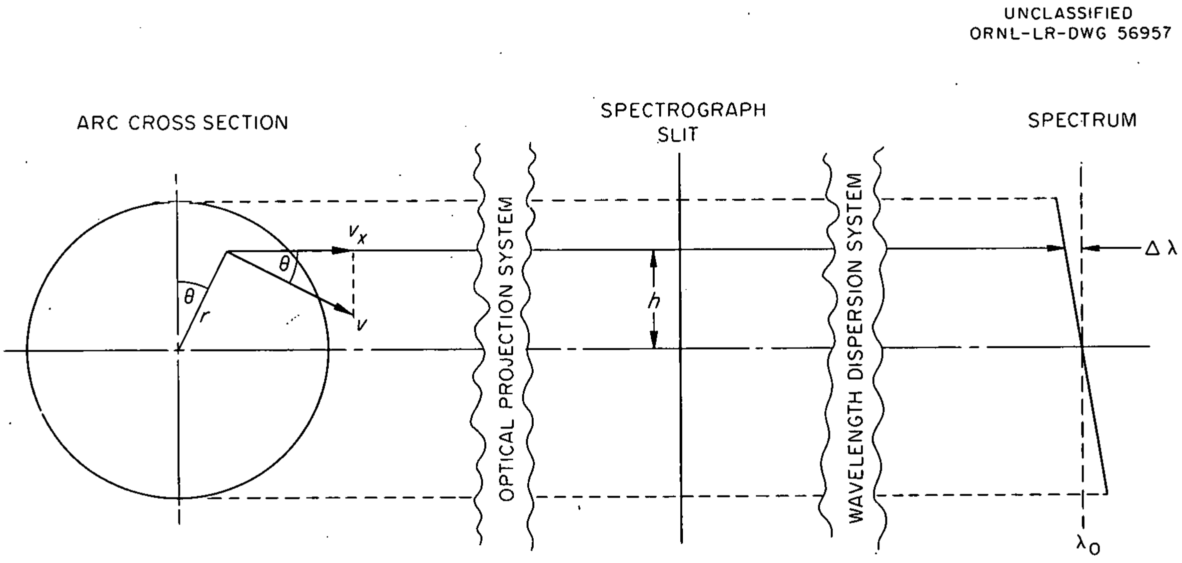

$$\Delta\lambda = \lambda_0\left(\frac{v_x}{c}\right) = \frac{\lambda_0}{c}\,(v\cos\theta) = \frac{\lambda_0}{c}\,\left(r\dot{\theta}\,\frac{h}{r}\right) = \frac{\lambda_0 h\dot{\theta}}{c}$$

Fig. 4.1. Schematic Diagram of "Slant Line" Rotational Drift Observations.

The wavelength of the line was expressed as a linear function of h of the form $\lambda = \lambda_0 + bh$. Thus, the measured Doppler shift $\Delta\lambda = \lambda - \lambda_0 = bh$ can be related to the angular velocity of the rotational drift as represented in Fig. 4.1; that is, $\lambda_0 h\dot{\theta}/c = bh$, or $\nu \equiv \dot{\theta}/2\pi = bc/2\pi\lambda_0$.

At each arc-current setting, four exposures were made, and the exposure times were increased by a factor of 3 in successive exposures. This gave line images over a wide range of photographic densities. All line images were measured and each observation was weighted by a factor w_i based on the photometric errors at that particular photographic density. Two hundred nineteen measurements, on 32 spectrograms, were made of the absolute wavelength of three C^{2+} lines (4647, 4650, and 4651 A) at different elevations h, and at eight different arc currents. The value b of the slope of a given line was determined by fitting the individual measurements of the wavelength λ_i at given elevations h_i to the expression $\lambda = \lambda_0 + bh$ by a weighted least-squares method. The resulting value of b and the probable error in b are given by:

$$b = \frac{\Sigma w_i \Sigma w_i h_i \lambda_1 - \Sigma w_i \lambda_i}{\Sigma w_i \Sigma w_i h_i{}^2 - (\Sigma w_i h_i)^2} ,$$

$$r_b = t_{0.5,n} \left[\frac{\Sigma w_i (\lambda_i - \lambda_{1\ \text{calc}})^2}{n - 2} \right]^{1/2} \left[\frac{\Sigma w_i}{\Sigma w_i \Sigma w_i h_i{}^2 - (\Sigma w_i h_i)^2} \right]^{1/2} .$$

A weighted average of all the individual determinations of b at a given arc current was calculated using a weighting factor equal to $(1/r_b)^2$. The probable error in b quoted for each arc current is

$$r_{\bar{b}} = t_{0.5,n} \left[\frac{\Sigma (1/r_b)_n^2 (\bar{b} - b_n)^2}{(n - 1) \Sigma (1/r_b)_n^2} \right]^{1/2} .$$

The results of the measurements are shown in Table 4.1 and Fig. 4.2.

The half-width as a function of arc current was reported in the previous semiannual report[3] and the results are shown in Fig. 4.3. Neither the half-width ω nor the rotational frequency ν shows a regular or even monotonic relationship in respect to the arc current I. However, the quantity ν/ω^2 shows a striking linear relationship to total arc current I, as is seen in Fig. 4.4. The significance, if any, of this linearity of ν/ω^2 in I is being investigated.

---

[3] P. M. Griffin and G. K. Werner, *Thermonuclear Project Semiann. Progr. Rept. July 31, 1960*, ORNL-3011, p 37.

Table 4.1. Rotational Frequency and Line Widths of C^{2+} Ions at Various Arc Currents

Arc length: 54 in.
Magnetic field: 2600 gauss
Larmor frequency for C^{2+}: 665 kc
Point of observation: transverse view at midplane

Arc Current (amp)	Arc Voltage (v)	Tank Pressure, Cathode End (mm Hg)	Rotational Frequency and Probable Error, $\bar{\nu} \pm r_{\bar{\nu}}$ (kc)	Average Line Half-Width and Probable Error, $\bar{\omega} \pm r_{\bar{\omega}}$ (A)	$\bar{\nu}/\bar{\omega}^2$ (kc/A^2)
		$\times 10^{-5}$			
158	97	0.9	91 ± 5	0.651 ± 0.013	215 ± 15
208	107	1.32	148 ± 4	0.577 ± 0.007	445 ± 16
256	112	1.85	171 ± 1	0.525 ± 0.004	618 ± 10
307	121	4.25	173 ± 2	0.460 ± 0.003	817 ± 14
354	127	9.75	170 ± 3	0.399 ± 0.006	1071 ± 37
405	134	13.8	162 ± 2	0.363 ± 0.003	1225 ± 25
447	140	16.0	169 ± 3	0.345 ± 0.004	1416 ± 42
475	145	18.0	183 ± 1	0.349 ± 0.002	1500 ± 19

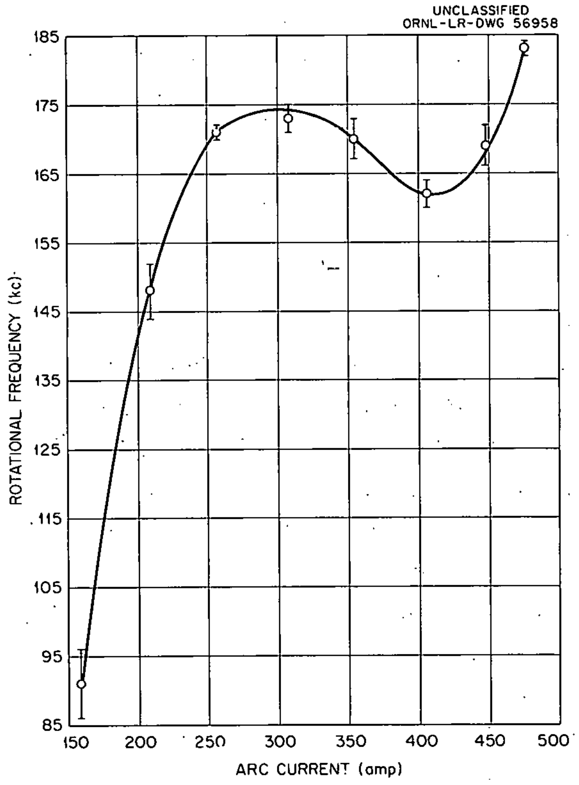

Fig. 4.2. Rotational Drift Frequency as a Function of Arc Current.

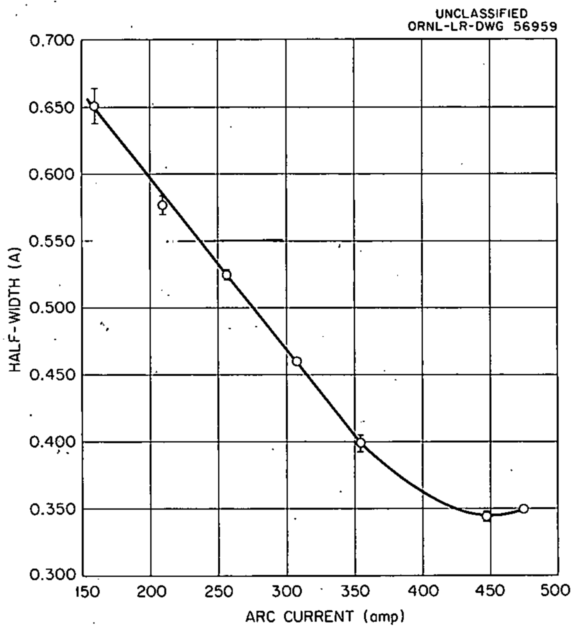

Fig. 4.3. Half-Width of the 4647-A Line of C^{2+} as a Function of Arc Current.

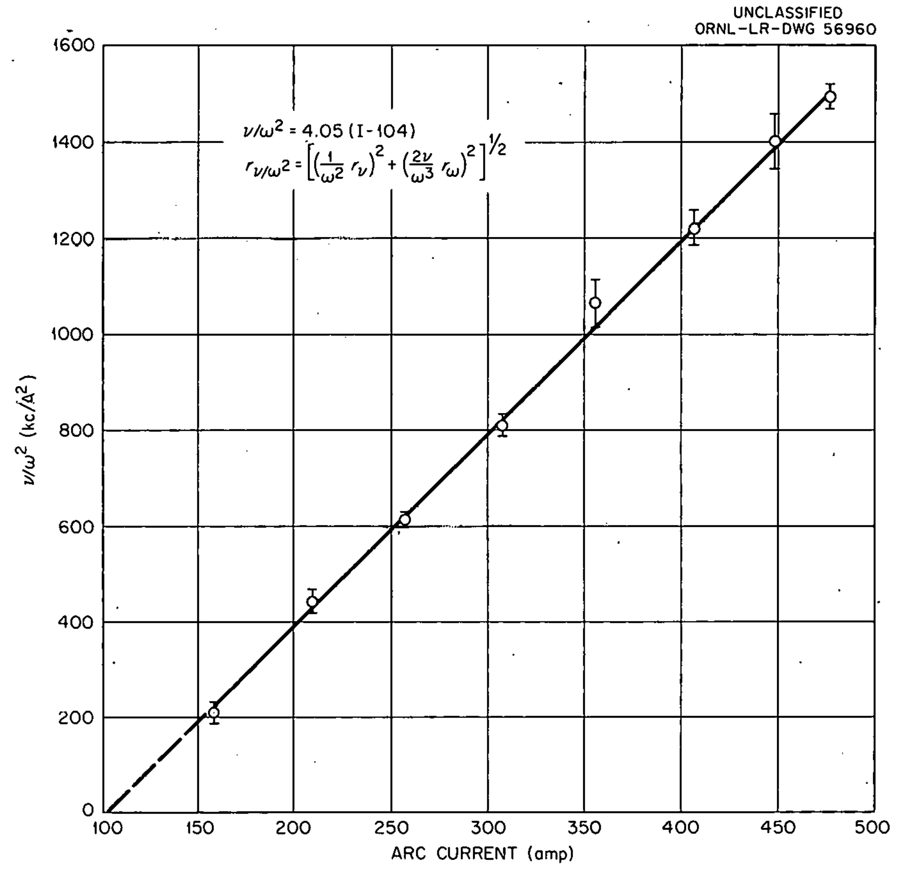

Fig. 4.4. Ratio of Rotational Frequency to Square of Half-Width as a Function of Arc Current.

4.2 THE LITHIUM ARC

4.2.1 The Lithium Arc in the Long Solenoid

J. E. Francis P. M. Jenkins
R. E. Toucey R. V. Neidigh
P. R. Bell

Initial assembly of the long solenoid (120 in.) was completed in September 1960. Since that time, it has been actively used for the study of lithium arcs.

Lithium is being studied because it is the element of lowest atomic number that forms an easily condensable vapor. In thermonuclear devices the low atomic number reduces scattering and bremsstrahlung. Lithium also requires relatively little energy to strip all orbital electrons from the nucleus so that we could hope to obtain an arc containing only Li^{3+}, from which charge exchange is impossible.

The need for high-speed pumping arrangements is reduced with lithium since any neutral lithium atoms will condense to a low-vapor-pressure solid on the walls of the equipment.

In general, the lithium arcs resemble the familiar carbon arcs. The arcs have been operated in the range from 60 to 200 amp. The voltage has been as low as 60 and as high as 250 v.

In appearance, the arc has a bright-green core, equal in diameter to the diameter of the cathode, surrounded by a sheath, approximately $1\frac{1}{2}$ to 2 in. in diameter. There is a red glow around the anode, due to excited neutral lithium, and a slight red glow around the hot free tip of the cathode. The outer sheath extends beyond the tip of the cathode back to the baffle in Fig. 4.5.

UNCLASSIFIED
ORNL-LR-DWG 56961

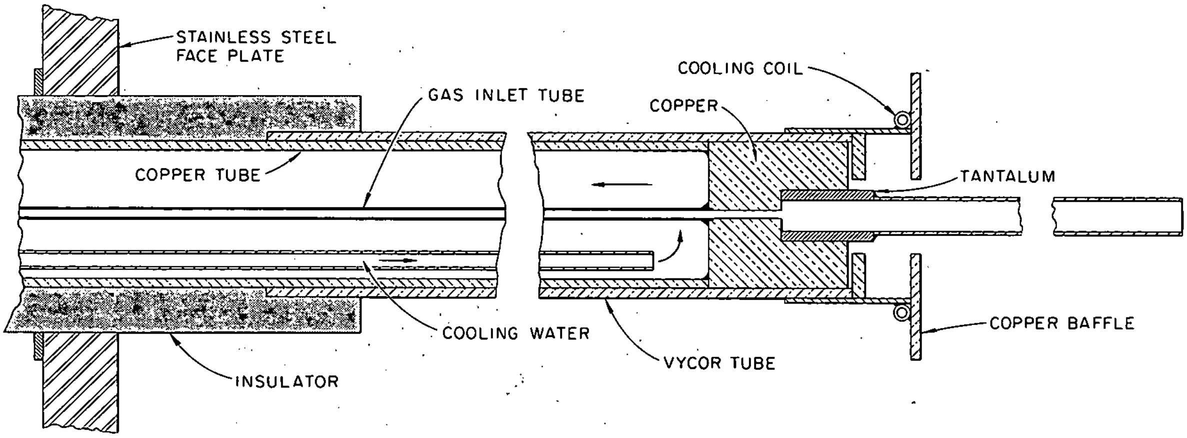

Fig. 4.5. Cathode Assembly for 120-in. Solenoid.

A considerable amount of time has been spent in the development of anodes. The early types consisted of a cooled copper cylinder, about 2 in. inside diameter, containing a number of thin disk baffles of tantalum backed up by two $\frac{1}{4}$-in.-thick tungsten plates and a central $\frac{1}{4}$-in.-diam tungsten stub. The open end of the anode was fitted with a tungsten cylinder 3 or 4 in. long, with an inside diameter of $1\frac{1}{8}$ in. Considerable difficulty was encountered with swirling of the lithium due to motor action of the arc current in a strong magnetic field. Arcs could be run for a considerable time (1 hr), but the arc was quite unstable. The addition of radial baffles and tantalum shot was unsuccessful in producing quiet arcs. Despite the instability, the Neidigh mass spectrometer frequently showed a strong indication of Li^{2+}, and upon a few occasions a trace of Li^{3+} could be seen, as is shown in Fig. 4.6.

Several quite long anode assemblies of 4-in. diameter were tried. Difficulty was encountered in restricting the arc, because the anode was too well cooled; the consequence was frequent failure of the tungsten at the back of the anode.

In order to secure better control of the lithium vapor in the anode, an anode was constructed with a separate lithium boiler (Fig. 4.7). The upper tube contains the arc. The lower tube, containing the lithium, was surrounded by a carbon strip heater such as used for calutron heaters. The most interesting result obtained with this anode was that for short periods of time a blue arc could be obtained. This was an encouraging sign since the only visible line of Li^{2+} is at 4600 A, although we have no assurance that the blue color was exclusively due to Li^{2+}. Temperature control of this anode has been difficult due to the time lag of the heaters.

UNCLASSIFIED
PHOTO 52824

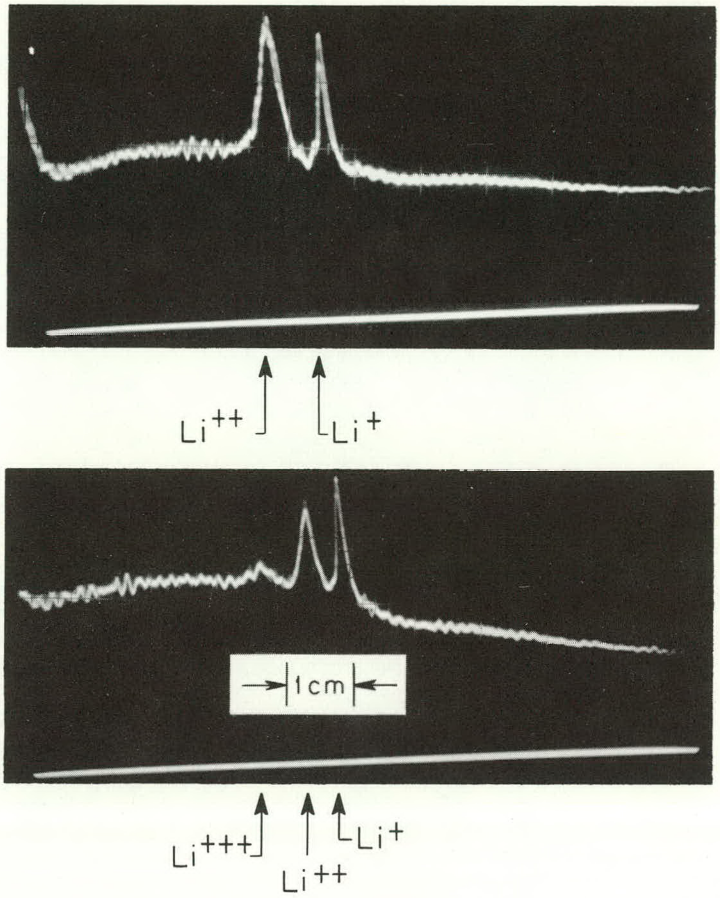

Fig. 4.6. Response of Neidigh Analyzer to Lithium Arc.

UNCLASSIFIED
ORNL-LR-DWG 56962

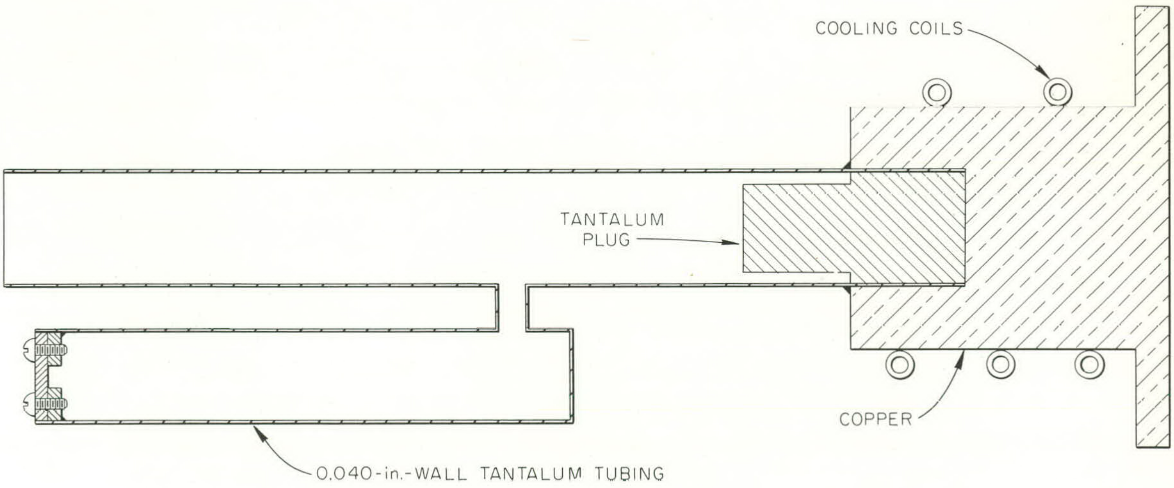

Fig. 4.7. Tantalum Boiler Assembly.

When the copper in contact with liquid lithium was not kept cool, rapid erosion of the copper occurred. To overcome this, several tantalum anodes were made (see Fig. 4.8). Some satisfactory operation was obtained with these anodes. In particular, with sufficient cooling the arc column became bluish green or blue. It has again been found difficult to control the temperature of the anodes.

To separate the lithium supply from the high heat input from the tungsten backstop, and still use the arc as the heat source for the lithium, a split anode was constructed as shown in Fig. 4.9. Operating characteristics of this anode have been very encouraging. With only a small amount of

UNCLASSIFIED
ORNL–LR–DWG 56963

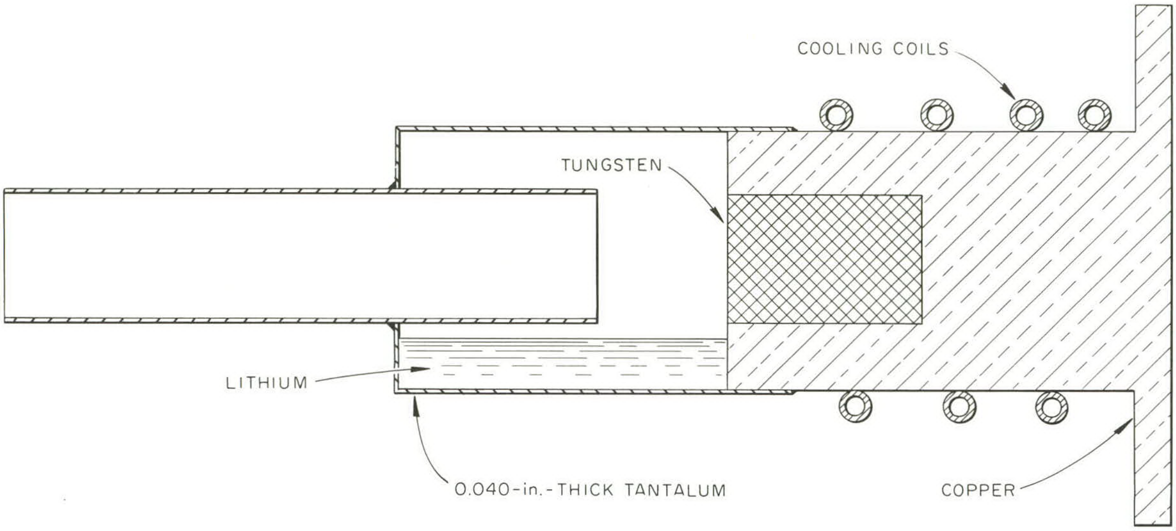

Fig. 4.8. Tantalum Anode Assembly.

UNCLASSIFIED
ORNL–LR–DWG 56964

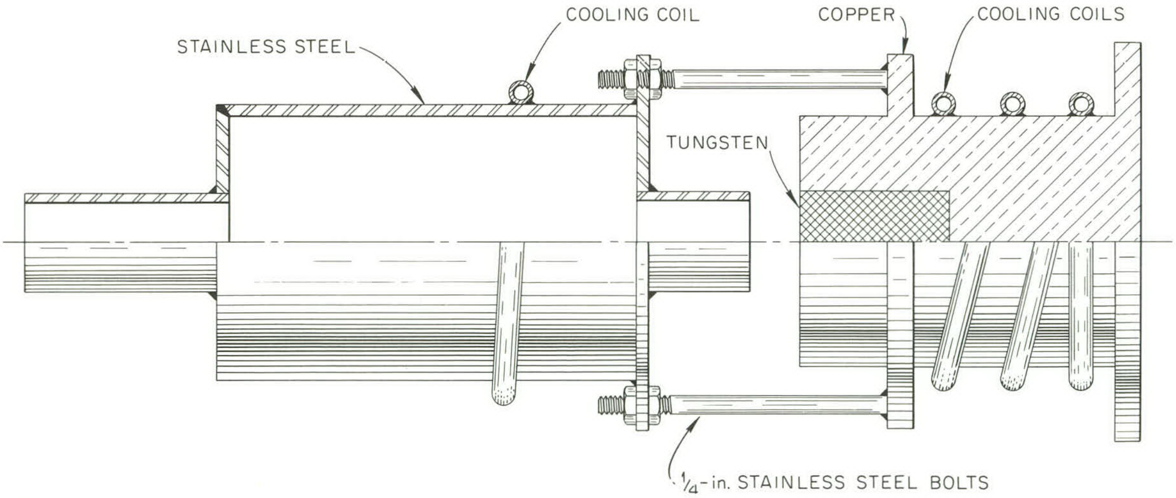

Fig. 4.9. Split Anode Assembly.

water cooling on the stainless steel pot containing the lithium, the ratio of Li^{2+} to Li^{+} is greatly increased. This increase can be seen by comparing Fig. 4.10 with Fig. 4.6. The ratio of Li^{2+} to Li^{+} could be changed (from all Li^{+} to the ratio obtained in Fig. 4.10) by varying the cooling. Wear of this anode is less than that of preceding anodes.

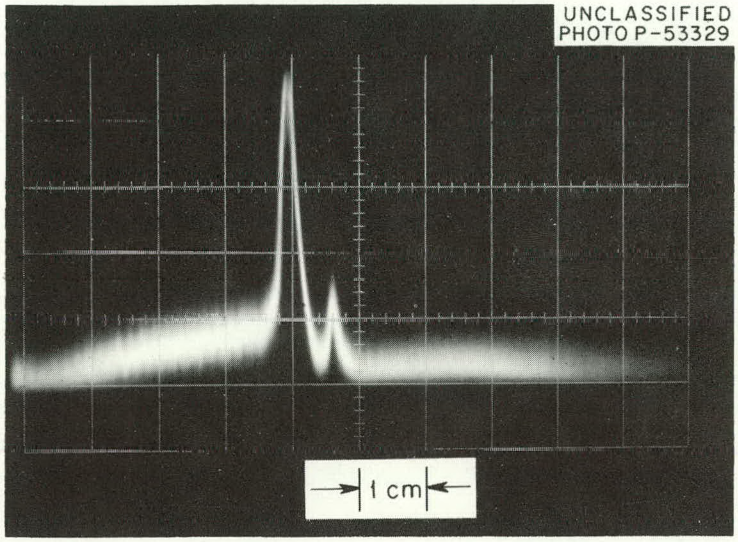

Fig. 4.10. Response of Neidigh Analyzer to Lithium Arc Using Split Anode.

Several experiments were performed in order to determine the amount of lithium transported along the arc as ions. A cathode and baffle arrangement was used as shown in Fig. 4.5. In operation, lithium is condensed on the floating, water-cooled baffle. The lithium deposit is heaviest on the inner edge, becoming very thin at 1 in. from the inner edge. Only a slight trace was visible at the outer edge of the 4-in. baffle. Some lithium was also deposited at the cool end of the cathode. The arc for these tests was approximately 112 in. long. A weighed amount of lithium was loaded into the anode. The arc was operated for a time and a record kept of the arc current. At the end of the run the amount of lithium collected on the cathode and baffle was washed off, and the resulting solution was titrated. The amount of lithium remaining in the anode was determined in the same way.

The results of the run are shown below:

Start	12 g in anode
After run	4.05 g in anode 4.59 g on cathode and baffle 7.95 g left the anode
Av current	71.6 amp
Current × time	328,430 amp-sec

If one assumes that the ion current was transported by Li^{+}, the coulomb equivalent of the lithium is (4.59/6.94) 96,500 = 63,800 coulombs. The fraction of current carried by ions is then 63,800/ 328,430 = 0.194 or 19%. If some of the current is carried by doubly or triply ionized lithium, or if some of the deposited lithium is lost, this fraction is even greater.

A rough estimate of the energy and velocity of the ions was obtained by making use of the Doppler effect. The shift in the wavelength of the 4672- and 4678-A lines emitted by excited Li^+ was measured with a Jarrell-Ash 8200 optical spectrometer. The spectrometer was calibrated against the settings obtained when looking at these lines at right angles to the axis of the arc. The lines were then measured by looking from the anode toward the cathode at a small angle to the axis of the arc. Measurements were made looking at the anode end and cathode end of the arc. The velocity of the ions was then obtained by using the formula $\Delta\lambda/\lambda = v/c$, where $\Delta\lambda$ is the the difference between the value of the line along the axis and the calibration value. The average shift for both lines at the cathode end of the image was $\Delta\lambda = 0.655 \pm 0.13$, and for the anode end of the image, $\Delta\lambda = 0.75 \pm 0.27$. This yields a velocity of $(0.42 \pm 0.08) \times 10^7$ cm/sec at the cathode end and $(0.485 \pm 0.17) \times 10^7$ cm/sec at the anode end. These velocities correspond roughly to a drift energy of 73 and 68 ev for the ions.

Measurements were made of the line width to get a rough value of the ion energy. A line width of about twice the resolution of the instrument was obtained, giving an apparent temperature of about 10 ev.

In order to study the backstreaming of the ions past the cathode, a right-angle cathode, shown in Fig. 4.11, was fabricated. This cathode was then mounted in the fifth window from the anode to

UNCLASSIFIED
ORNL–LR–DWG 56965

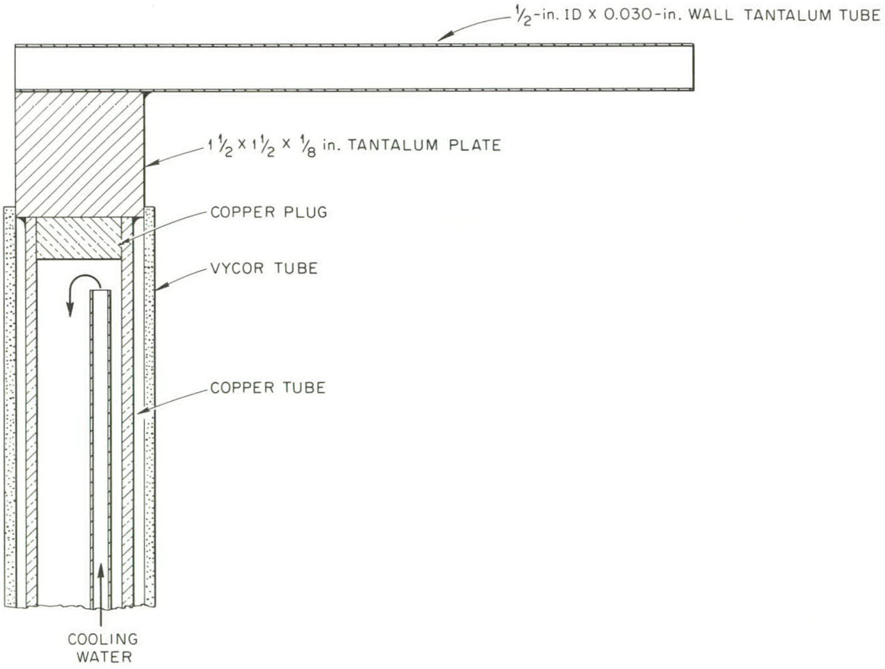

Fig. 4.11. Right-Angle Cathode.

give an arc approximately 40 in. long. The green sheath of the arc continued past the cathode until it struck an insulated baffle at the far end of the tank. In appearance the backstreaming was the same as the arc except that the green core was now absent. Neidigh's analyzer showed only Li^+ in this backstreaming. It should be noted that there was no measurement of the primary arc to indicate the amount of Li^{2+} that might have been present at that time.

The right-angle cathode was run at another position in the tank to obtain an arc 52 in. long without apparent change in the backstreaming. No particular difficulty was encountered in the operation of the right-angle cathode.

The force exerted by the backstreaming of the arc was measured by suspending an insulated tantalum plate weighing 21.7 g in the path of the backstreaming and measuring the angle of deflection of the plate, which in one experiment was 5°. The force was then calculated to be $F = (21.7) \tan 5° = 1.9$ g for an arc current of 120 amp. If the force to be expected is calculated by using the drift velocity and the amount of material carried in the arc obtained above, one obtains 7.75 g as the force to be expected from an arc current of 120 amp. The backstreaming caused a white-hot ring to appear on the surface of the tantalum, indicating the cylindrical nature of the backstreaming. In many cases holes were melted in the baffle. In most cases the baffle was swinging violently, due to fluctuations in the force. A second experiment showed 2.2 g force at an arc current of 100 amp and 160 to 175 v.

Radiometer measurements of the radiation from the arc show that the radiation decreases as the vacuum gets better. Also, placing a quartz window between the arc and the radiometer decreases the reading by more than 90%. The radiometer gave the same reading with and without a quartz window when looking at the backstreaming.

4.2.2 Anomaly in the Triplet-Singlet Ratios in the Lithium Arc

M. R. Skidmore J. R. McNally, Jr. W. F. Peed

In a system in thermodynamic equilibrium, the triplet-singlet multiplet intensity ratios approximate the ratio of statistical weights of the upper levels involved; that is,

$$\frac{I_T}{I_S} = \frac{f_T g_T \nu_T^3}{f_S g_S \nu_S^3} e^{-\Delta E/KT_e} \underset{\rightarrow}{\sim} \frac{g_T}{g_S} = 3 \, .$$

for $\Delta E < KT_e$ and $\nu_T \sim \nu_S$. There are indications that these latter conditions are well fulfilled in the lithium arc in a magnetic field. Fine structure, hyperfine structure, and isotope effects are small and are expected to introduce no gross errors in the qualitative results reported here.

Table 4.2 lists the electronic transitions, wavelengths, and the intensity ratios for the different upper energy states (see Fig. 4.12). For upper energy states having $n = 6$ or 7 there are indications in this preliminary survey that $I_T/I_S \cong 3$ and that approximate statistical equilibrium for these states may exist; however, for $n < 6$ there are increasing indications that the triplet state is much more heavily populated than the above simple model predicts even when corrected for ν and ΔE effects ($\Delta E_{\max} \sim 1$ ev, $T_e \sim 3$ ev or more). Thus, there is evidence that population of the energy

Table 4.2. Triplet-Singlet Intensity Ratio of Li^+ vs Upper-State Quantum Number

Transition	Triplets Wavelength (A)	Singlets Wavelength (A)	Intensity Ratio*
7*f* – 3*d*	2507.0	2508.9	2
7*d* – 3*p*	2402.3	2539.5	>2 (?)
6*f* – 3*d*	2728.4	2730.7	3.2
6*d* – 3*p*	2605.1	2767.1	3.4
6*p* – 3*d*	2744.9	Unknown	
6*p* – 3*s*	2330.7	Unknown	
6*s* – 3*p*	2657.3	2790.5	
5*f* – 3*d*	3195.8	3199.4	3.2
5*d* – 3*p*	3029.1	3251.1	3.6 (?)
5*p* – 3*d*	3235.7	3187.5	>24 (?)
5*p* – 3*s*	2674.4	2952.5	8 (?)
5*s* – 3*p*	3156.3	3307.4	8 (?)
4*f* – 3*d*	4671.8	4678.4	4.0
4*d* – 3*p*	4325.7	4787.5	7
4*p* – 3*d*	4842.2	4637.8	>18 (?)
4*p* – 3*s*	3684.1	4156.1	25
4*s* – 3*p*	4881.2	5038.7	12 (?)
3*d* – 2*p*	1493.1	1681.8	4
3*p* – 2*s*	1198.2	1656.0	>2
3*s* – 2*p*	1653.2	1755.5	8
2*p* – 2*s*	5484.8	9562.2	

*Uncorrected for instrumental wavelength sensitivity; such instrumental errors in the vacuum ultraviolet region would probably increase the listed intensity ratio.

states of this helium-like ion in the lithium arc may be strongly affected by a trapping of Li^+ ions in the $2s(^3S)$ metastable state, from which direct radiative decay to the ground state is strongly forbidden. This trapping in the metastable triplet state could explain the tremendous brightness in the 5484.8 line of Li^+.

Experimental gear is being assembled to measure the analogous singlet transition (9562.2 A) in the infrared to evaluate further this model. The $2s(^1S)$ metastable state may be only quasi metastable in the sense that excitation by 1 ev to the $2s(^1P)$ state permits an indirect but important mechanism for depopulating the $2s(^1S)$ state. The presence of a significant but small fraction of Li^+ ions in the $2s(^3S)$ metastable state could, because of the strong resonance character of the 2-ev transition, prevent the electrons from attaining significant energies and hence impose a limit on instability growths associated with the electron class.

UNCLASSIFIED
ORNL-LR-DWG 56956

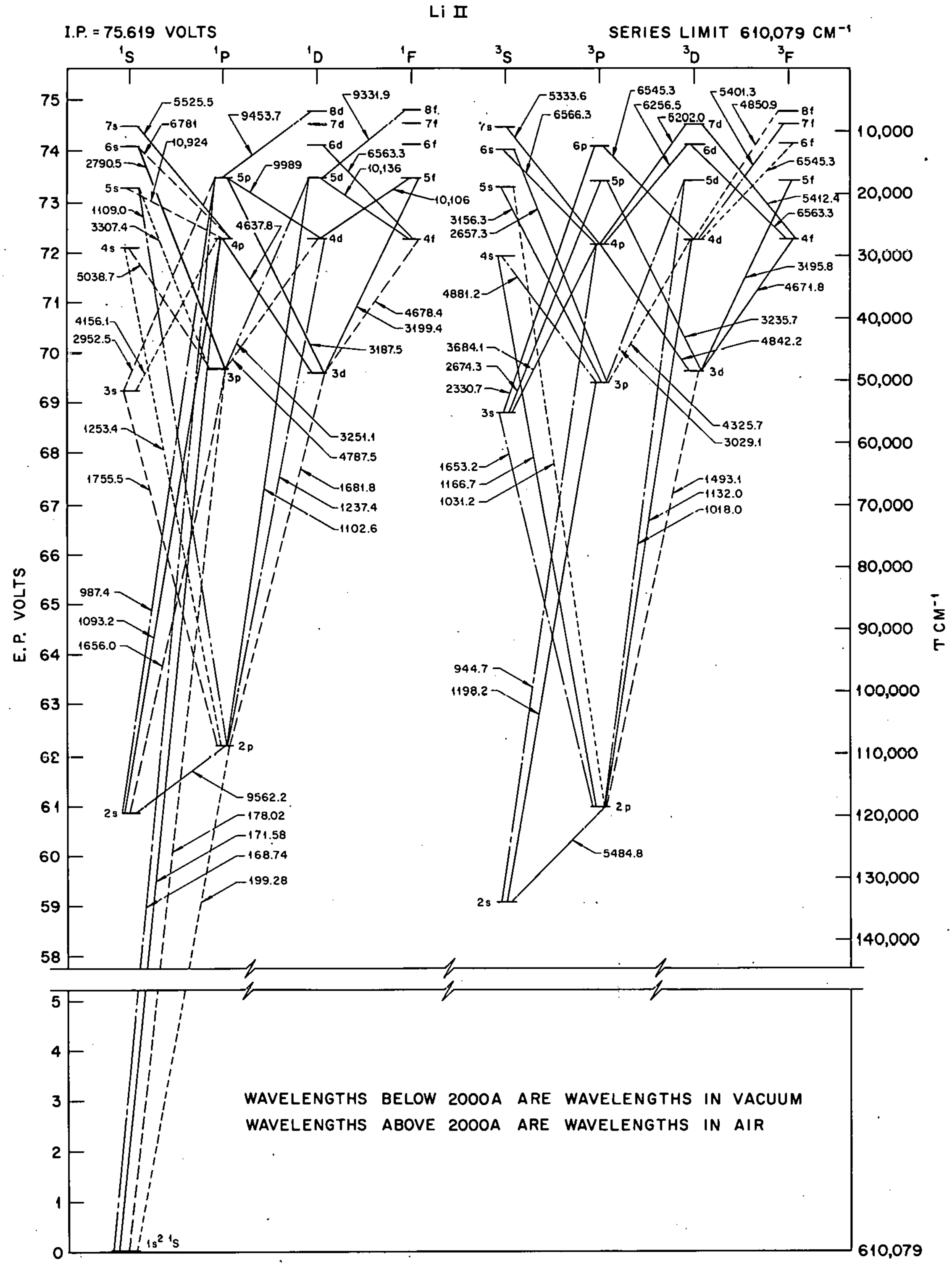

WAVELENGTHS BELOW 2000A ARE WAVELENGTHS IN VACUUM
WAVELENGTHS ABOVE 2000A ARE WAVELENGTHS IN AIR

Fig. 4.12. Grotrian Table of Lithium II.

This enhancement of low-lying triplet transitions through metastability may explain the unusually strong intensity of the λ 4650 triplet of C^{2+} lines – approximately 100 times greater than the λ 5696 singlet line.[4]

4.3 THE DEUTERIUM ARC

R. A. Gibbons R. J. Mackin, Jr. T. F. Rayburn

4.3.1 Introduction

The present deuterium-arc development program was undertaken in the summer of 1959, when it was found that charge exchange in the carbon arc was a major particle-loss process in DCX-1. The concept on which the program was based was the same as that which initially guided the deuterium arc work undertaken by Luce and Bell in 1957.[5,6] The original work very quickly departed from the initial concept and led to the development of what is now called the "hollow-cathode discharge."[6,7] The present deuterium arc is quite unlike the hollow-cathode discharge.

During the first six months of operation, the following developments took place.[8] It was demonstrated that a gas-fed arc which was an analog of the carbon arc could be operated in a multiregion vacuum system. Experiments were performed for the evaluation of the relevant system parameters necessary for the operation of such an arc. Most important among these, the quantity of gas flow necessary to sustain such an arc was ascertained, namely, about 5 cc/sec of D_2 at atompsheric pressure. The gas was fed into the anode, where it was ionized with high efficiency, and was transported along the arc column to the cathode, where it recombined. A 20-in. diffusion pump was installed on the vacuum system, which maintained the pressure in the cathode region at about a half micron in the presence of this gas throughput. The apparatus is shown in Fig. 4.13. The next task was the development of adequate arc components. The first acceptable anode is shown in ref 8, Fig. 2.25. It was found to have a 95% ionizing efficiency, and it could operate for several hours without appreciable deterioration. Following the lead of earlier work, a 1.5-cm-diam tubular tungsten cathode was used. Its only difference from a similar carbon cathode lay in the steadiness of arc operation and length of service. In particular, it did not lessen the degree of carbon contamination of the arc.

In appearance, the deuterium arc was found to be of a pale mauve color. It had a luminous hollow core region roughly equal in diameter to the cathode, surrounded by a glowing aureole whose diameter was two or three times that of the cathode. Beyond this there extended a faint

---

[4] M. R. Skidmore, J. R. McNally, and G. K. Werner, *Thermonuclear Project Semiann. Rept. Jan. 31, 1960*, ORNL-2926, p 40, Fig. 2.16.

[5] P. R. Bell and J. S. Luce, *The ORNL Thermonuclear Program*, ORNL-2457, appendix I (Jan. 15, 1958).

[6] J. S. Luce, "Studies of Intense Gaseous Discharges," *Proc. U.N. Intern. Conf. Peaceful Uses Atomic Energy, 2d, Geneva, 1958* 31, 305 (1959).

[7] C. Michelson, *Thermonuclear Project Semiann. Rept. July 31, 1959*, ORNL-2802, p 54, and *Thermonuclear Project Semiann. Rept. Jan. 31, 1960*, ORNL-2926, p 53; W. D. Getty, *MIT Quart. Progr. Rept. No. 57*, p 27 (Apr. 15, 1960); D. J. Rose and L. D. Smullin, *MIT Quart. Progr. Rept. No. 58*, p 35 (July 15, 1960).

[8] R. A. Gibbons *et al.*, *Thermonuclear Project Semiann. Rept. Jan. 31, 1960*, ORNL-2926, p 47.

UNCLASSIFIED
ORNL-LR-DWG. 48989

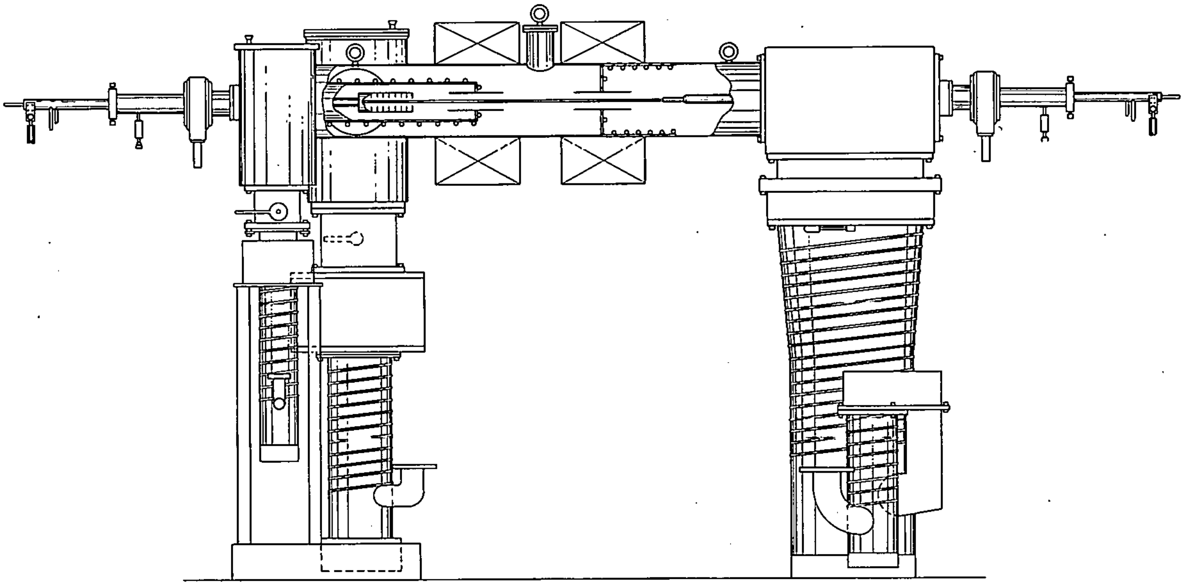

Fig. 4.13. Facility for Gas-Arc Studies.

blue aura, which has been suggested as being due to fluorescence in the surrounding gas produced by deuterium metastables. It was established that the deuterium arc acted as a strong ion pump, ionizing background gas and transporting it out of the control vacuum region. Its pumping speed for deuterium gas was found to be 75 liters/sec per centimeter of length. Typical operating parameters were 200 amp, 120 v.

The lowest pressure observed in the central region of the vacuum system was 3×10^{-5} mm Hg. The net pumping speed on this region of 4200 liters/sec, including an 800 liters/sec contribution of a diffusion pump, corresponded to pumping roughly 4% of the input deuterium gas. Measurements showed that only about 25% of this gas influx could be accounted for in terms of inleakage from the end regions, which were at higher pressure. The question of the origin of this gas will be discussed at some length below. Other properties of interest that were observed in the initial arc studied included negligible radiation to the walls, that is, less than 100 w over the entire central region. Such radiation as there was, was found to be proportional to the background gas pressure. The intensity of the 4650-A line from carbon III was found to correspond to a partial pressure of 5×10^{-7} mm of carbon monoxide.

During the second six months of operation, the widths of various spectral lines were measured. Interpretation in terms of Doppler broadening implied that the mean energies of the deuterium atoms emitting the first three lines of the Balmer series were comparable and equal to 4 or 5 ev. The mean energy of C III ions was found to be 25 ev. These data have been extended and will be reported below.

Measurements on the anode cooling water disclosed that about two-thirds of the total input power to the arc is dissipated there. From the known amount of gas being transported along the arc as ions, and with the assumption that these were practically all deuterons rather than molecular ions, it was concluded that the arc's ion current is approximately one-fourth of the total current. Somewhat more data are needed for an energy-balance analysis.

During this period the arc was moved to the axis of the machine from an initial position about 5 cm away. There were no effects which could definitely be ascribed to this change in location.

During this period the arc was operated in DCX. The minimum pressure achieved there was 1.5×10^{-5} mm Hg, apparently limited by gas influx from the ends. Subsequent experiments by the DCX group have not confirmed this finding.

The last six months were devoted mainly to diagnostic studies on the arc aimed at fully delineating its properties and forming a basis for a model by which its properties can be understood. It now appears that the arc column is a high-temperature, steady-state, 99% ionized, high-purity plasma and is susceptible to more extensive exploitation than had originally been anticipated.

4.3.2 Electrode Development

During this period, two new anode design features have been tried and found to give considerably superior performance over the original model. There are two criteria by which an anode of this type is judged. The first is that a minimal amount of the input gas escape into the vacuum system without being ionized, and the second is that the contamination of the plasma with anode material be negligible. The deep, tubular anode tends toward the accomplishment of both aims: the passage of gas through a length of arc column gives it a good chance of being ionized, and the passage of the arc through a gas column provides an energy sink for the electrons and reduces the energy which they deposit where they strike the anode surface.

In the model M anode shown in Fig. 4.14, the arc column passes a series of tungsten baffles, enters a gas chamber, and eventually follows diverging magnetic flux lines to the chamber wall. By permitting the arc column to terminate at a shallow angle of incidence on a cylindrical wall,

UNCLASSIFIED
ORNL-LR-DWG 55474A

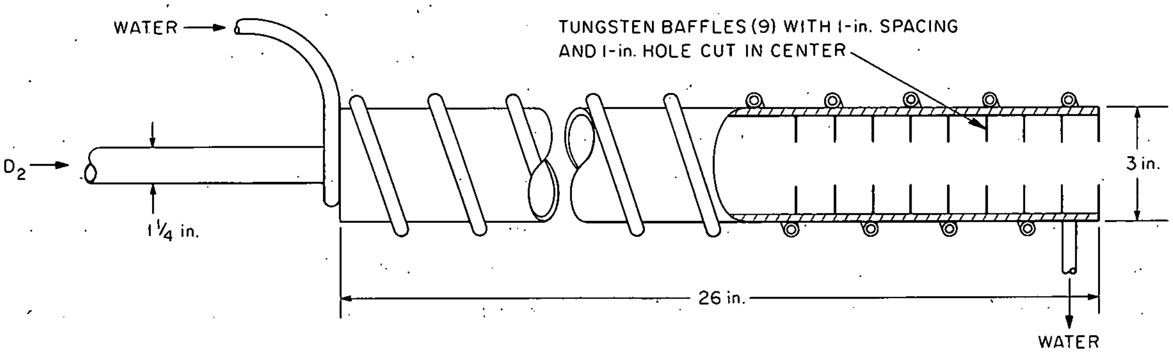

Fig. 4.14. Model M Gas-Arc Anode.

the power density was reduced to the point where it could be handled successfully with no particular attention paid to water-cooling arrangements. One model of this anode was used for about 50 hr, with modest deterioration.

With a 5 cc/sec gas flow and no arc, the pressure inside the anode was found to be 60 μ. When the arc was struck, this pressure rose to approximately 1 mm. It was measured both with a thermocouple gage and with an oil manometer. The anode's internal pressure appears to be proportional to the gas flow and, remarkably enough, is a strong function of the arc current.

This anode had an ionizing efficiency of approximately 98%. With it, it was possible to operate with deuterium flows as low as 2 cc/sec. In addition it was found possible to operate an arc with hydrogen gas. This had not been practical before. The higher mobility of hydrogen results in a lower ionizing efficiency and thus in a lower internal pressure, which previously had not given adequate protection to the surface on which the arc column terminated.

An incidental advantage of this anode was the opportunity which it presented of viewing the arc along its axis.

The model G anode is shown in Fig. 4.15. It has the strong advantage of presenting the arc with heavily water-cooled copper surfaces, and, at gas flows above 4 cc/sec, an anode of this type apparently will last indefinitely. No surface damage was detectable after 80 hr of operation. This anode was also found to have an ionizing efficiency of about 98%. The termination of the arc column was observed to be a bright ring on the end plate.

UNCLASSIFIED
ORNL-LR-DWG 55475A

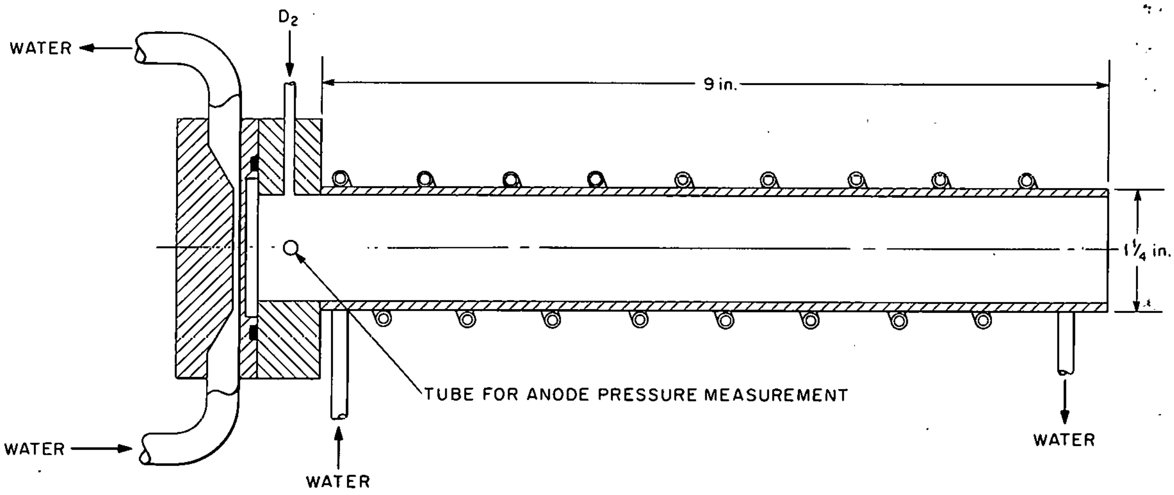

Fig. 4.15. Model G Gas-Arc Anode.

It was noted above that approximately two-thirds of the total arc power is deposited in the anode cooling water. By using separated water circuits on the model G anode, it has been found that under representative conditions two-thirds of the anode power is deposited in the end plate on which the column terminates. Reducing the inner diameter of the anode to 1 in. did not make an appreciable difference in the operation or efficiency but did result in increased difficulty of alignment. With the new anodes, the gas released into the anode region of the vacuum system was equal to or less than that released into the central region. Consequently, flexibility of operation was achieved by removing the bulkhead between the regions with only a factor-of-2 increase in the central region pressure.

One peculiarity of the model G anode is the upper limit to the gas flow which permits stable operation. For flows above about 4.5 cc/sec the arc begins to alternate between the erstwhile stable mode and one characterized by 25% higher voltage, a lower gas efficiency, and a higher pressure. The well-defined core structure is replaced by a uniformly bright column the size of the aureole. One is tempted to use the word "turbulent" to describe this mode. The alternation takes place at a rate of about 1 cps. For lower currents, the limiting gas flow is reduced.

Arcs have also been run with a model MG anode combining the best features of each of the other two. It consisted essentially of a 3-cm-ID copper tube deep enough for the arc column to impinge on the wall. Typically, it operated at 2 cc of D_2 per second, 235 v, and 120 amp. Its ionizing efficiency was 99.6%, and it also had unstable operation for a gas flow exceeding a critical value.

Following a suggestion by P. R. Bell, the cathode wall thickness near the end was reduced to 1 mm. This resulted in a 30% decrease in the operating voltage for a given gas flow. Approximately all the power reduction was accounted for in the anode cooling water.

4.3.3 Mass Analyzer Study

It was pointed out by H. Postma that the cross section for dissociative recombination of D_2^+ is adequate to account for the net gas release which sets the base pressure for the deuterium arc, if 3% of the ion flow through the arc is in the form of D_2^+. This comment motivated an experimental study of the arc halo with a mass analyzer designed by R. V. Neidigh. This analyzer is a velocity selector type and is shown in Fig. 2.6 of ref. 9. At the analyzer input, when it was located approximately 2 cm from the arc core, several mass peaks were readily discernible. The analyzer's mass scale was calibrated by the addition of a small amount of helium to the arc's gas feed. The observed peaks and their relative amplitudes are as follows:

Mass/Charge	Relative Amplitude
2	1.00
4	0.01
14	0.0025
28	0.0025

It must be emphasized at once that the relative peak amplitudes do not represent the relative fractions of the various ions present. Supplementary experiments showed that the analyzer transmission was a strongly varying function of magnetic field and thus of the ions' Larmor radius. It

---

[9] R. V. Neidigh, *Thermonuclear Project Semiann. Rept. Jan. 31, 1960*, ORNL-2926, p 31.

has not yet been found possible to make a satisfactory sensitivity calibration. As a rough estimate based on such data as were taken, it is suspected that the mass-4 peak should be multiplied by 2.

Scans of ion current as a function of radius were made over a range extending 2.5 cm outward from the edge of the aureole. In this region the ratio of the D^+ peak to the $D_2{}^+$ peak was constant, within the accuracy of the measurements. It is expected that there should be virtually no molecular ions in the hot arc core. Even so, the apparent molecular-ion density present appears to be of the right order of magnitude to account for the gas release in terms of their recombination. It is worth noting that their diffusion into the core of the arc and subsequent dissociation could also account for this amount of gas release. They thus represent a gas source even if dissociative recombination is eventually shown to be negligible.

Believable scans of ion density as a function of radius cannot be satisfactorily made with this instrument until its sensitivity has been measured as a function of magnetic field and of field gradient.

One measurement was made in order to get a rough idea of the history of the molecular ions which were observed. The feed gas was converted to a mixture of hydrogen and deuterium in equal parts. It was supposed that if the molecular ions represented molecules which managed to get through the anode without appreciable interaction and which were ionized near the exit, the only new mass which would appear would be $H_1{}^+$ with $H_2{}^+$ being buried under the D^+ peak. The results showed a mass-3 peak, presumed to be HD^+, twice as large as the $D_2{}^+$ peak, the value expected from simple combination of the ion species in the ratio present.

We are indebted to R. V. Neidigh for the use of the mass analyzer.

4.3.4 Spectroscopic Studies on the Deuterium Arc

Radial Distribution of Spectral Line Intensities. – A Jaco 8200, 0.5-m Ebert-type scanning spectrometer has been used to measure the spatial variation of intensity of several spectral lines in a direction transverse to the arc. The spectrometer was mounted with its slit parallel to the arc axis, and an image of the arc was focused on the slit. A slit width of 100 μ was used, which produced flat-topped spectral lines. The spectrometer was mounted on a platform which could be moved perpendicular to the arc axis. In each case the spectrometer was set to register the peak intensity of the line. Because of the arc's high degree of stability, the readings were quite steady and reproducible over a period of hours. The radiation recorded by the spectrometer at any position was that emitted over an entire chord of the arc column. The observed distribution was therefore converted into a radial distribution function by means of an Abel inversion.[10] In each of the figures which present the data, the scan is shown on the left side of the center axis and the radial distribution of emission on the right.

Figure 4.16 shows the D_α (6561 A) scan. The D_β (4860 A) distribution is almost identical.

---

[10] W. J. Pearce, *Plasma Jet Temperature Study*, Missile and Space Vehicle Dept., Rept. No. R59SD440, General Electric Co., Philadelphia, Pa. (1959).

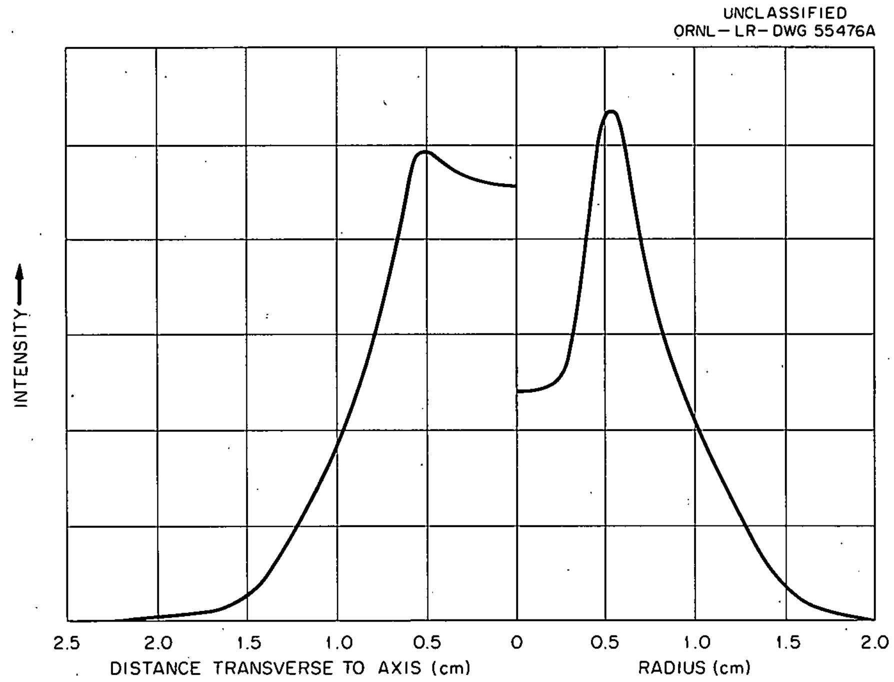

Fig. 4.16. Spatial Distribution of the D (6561 A) Line. On the left is the variation of the spectrometer reading with position; on the right is the inferred radial distribution function.

Figure 4.17 shows scans of the 4922- and 4713-A lines of neutral helium, made when helium was used to raise the helium partial pressure to 3.9×10^{-5} mm (gage reading). These lines correspond respectively to the transitions $4^1D - 2^1P$ and $4^3S - 2^3P$. The excitation functions for their production have been measured and form the basis for an estimate of the electron temperature. As performed by Cunningham,[11] the analysis consisted of integrating the two measured cross sections over Maxwellian energy distributions and determining the ratio as a function of temperature. The result[12] was: T_e (ev) = 18 $I(4922)/I(4713)$, for 5 ev $\leqq T_e \leqq$ 70 ev.

The electron temperature, as indicated by this technique, is plotted with the radial intensity distribution on the right half of Fig. 4.17. The estimate of the intensity ratio in the region within the cylinder corresponding to peak intensity is particularly susceptible to the magnification of statistical errors by the Abel inversion process and to effects of departures from cylindrical symmetry. The accuracy of the technique itself is subject to question, and the curve is regarded as being only indicative.

There now appear to be better data than those used by Cunningham, and their use would eliminate the strongest objections to the method. It is hoped that an experimental comparison with other temperature-indicating techniques can soon be made. In the observed range, the temperature results should not, however, be particularly sensitive to slight deviations from a Maxwellian distribution.

---

[11] S. P. Cunningham, *Livermore Conference on Thermonuclear Reactions, 1955,* WASH-289, p 279 (1956).

[12] This form was communicated by M. S. Jones and E. B. Meservey.

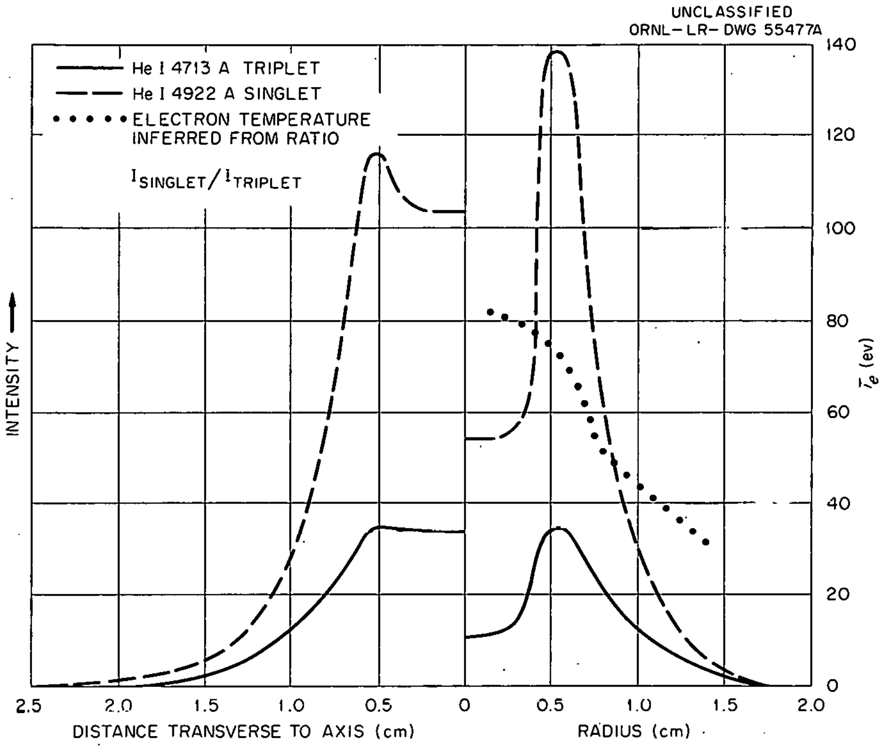

Fig. 4.17. Distribution of Two Lines from Neutral Helium. Included on the right is an electron temperature distribution inferred from the ratio of their intensities.

Explicitly, the electrons which are involved are just those in the general region of the apparent mean energy. The cross section for the 4713-A line peaks at 35 ev and that of the 4922-A line at 45 ev. If the cross sections are correct even roughly, this method should give a more accurate result than those in which a temperature is deduced from the energy distribution in a region many times above the mean electron energy.

Figure 4.18 shows a comparison of lines from neutral and ionized helium. The sharply peaked radial distribution appears to be typical of ion lines. Figure 4.19 compares lines of singly and doubly ionized carbon and indicates that the degree of sharpness goes up with the degree of ionization (or the height of the excited level). We have not yet found a way to separate, with any confidence, the electron temperature effects on these curves from the electron and ion density effects. The depression of the singly ionized carbon inside the arc core is readily understandable in terms of its depletion by ionization to higher levels.

Two points should be borne in mind in the interpretation of these data: first, that the relative amplitudes of the two carbon lines are entirely arbitrary; second, that some departure from circular symmetry was evidently present, based on the comparison of the data above and below the arc center (not shown), and that this would have a marked effect on the results of the Abel inversion inboard of the peak of the distribution. The present results must be considered as quite preliminary.

UNCLASSIFIED
ORNL-LR-DWG 55478A

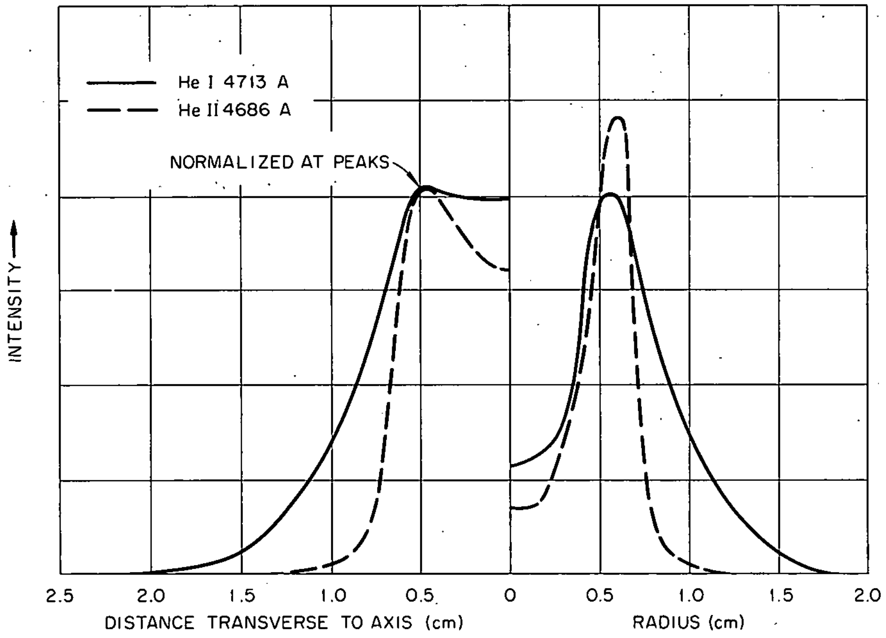

Fig. 4.18. Distribution of Lines from Neutral and Ionized Helium.

UNCLASSIFIED
ORNL-LR-DWG 55479A

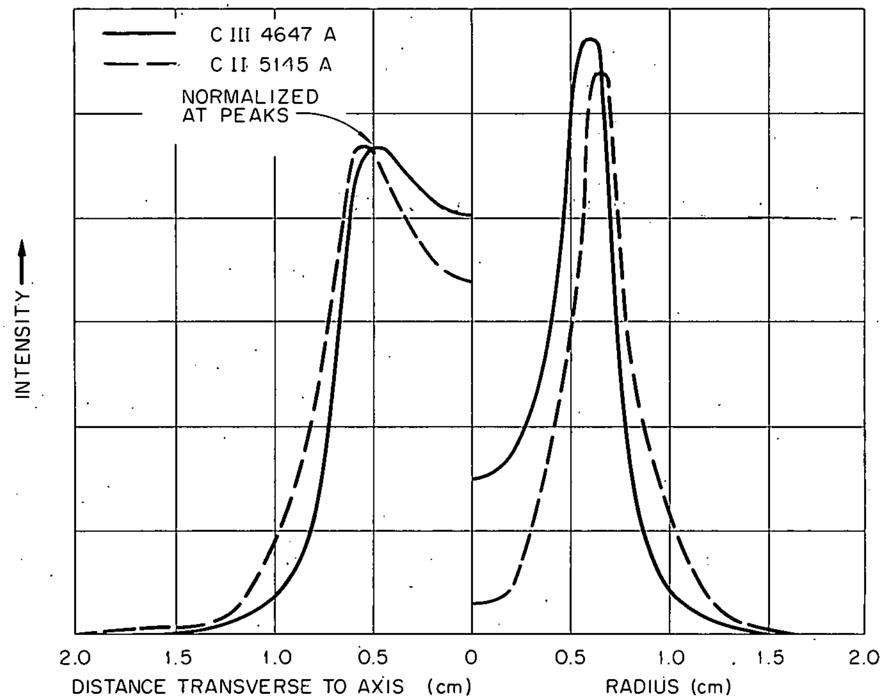

Fig. 4.19. Distribution of Lines from Singly and Doubly Ionized Carbon.

Line-Width and Impurity Studies. – The Jaco 8200 scanning spectrometer has been used with 5-μ slits for studies of spectral line widths. The resolution with these slits was found to be about 0.34 A. The spectrometer slits were aligned perpendicular to the arc column, so that the measured widths are weighted averages of a quantity which possibly has a spatial variation.

After correction for the spectrometer resolution, the widths of the first four Balmer lines are shown in Table 4.3, column 2. Interpreted as Doppler broadening, the D_α broadening corresponds to a mean energy of the emitting atoms of 3 ev. The apparent systematic increase in fractional broadening as one goes to the higher members of the series is the effect one would expect from Stark (density-dependent) broadening. In the third column, the Doppler width corresponding to 3-ev atoms is tabulated. In the region of highest density (about 10^{14}, based on microwave transmission to be presented below), Stark broadening should begin to contribute detectably to the width of the D_β line.[13] An estimate of the Stark width is made by assuming (incorrectly) a Gaussian form and subtracting. The result is shown in the last column of the above table.

Table 4.3. Width of Balmer Lines in Deuterium Arc

Line	Line Width (A)	Doppler Contribution (A)	Stark Contribution (A)
D_α	0.52 ± 0.4	0.52	
D_β	0.52 ± 0.03	0.38	0.35
D_γ	0.50 ± 0.06	0.34	0.37
D_δ	0.60 ± 0.07	0.32	0.51

The deuterium atom energies are just those which would be expected following the dissociation of deuterium molecules. The Franck-Condon principle[14] requires that the dissociation take place by initial excitation of an electron into an excited state of the molecule which is unstable to dissociation. In general, such states are located at energy levels such that there is an excess reaction energy of several electron volts which must be taken up in a kinetic energy of the atoms. This excess energy has only been evaluated explicitly when both atoms are in the ground state. It is possible that the states leading to different lines would yield different excess energies, so that the Stark-effect estimate above is doubly vitiated.

To the extent that the deuterium arc column is free from large electric fields, it is reasonable to expect that all ions present will have the same temperature. In a plasma whose density is 10^{14} cm^{-3} the mean time for equipartition of energy between two different ion types is of the order of a microsecond, corresponding to a drift length of about a centimeter.

---

[13] Hans Griem, A. C. Kolb, and K. Y. Shen, *Phys. Rev.* 116, 4 (1959).

[14] H. S. Massey and E. H. S. Burhop, *Electronic and Ionic Impact Phenomena*, pp 221 ff., 229 ff., Oxford Press, 1956.

The data on other plasmas with which the arc might be compared are conflicting. In the Zeta toroidal discharge, Hughes *et al.*[15] report equal Doppler temperatures for F VI and B IV. Zaidel,[16] however, studying a nominally identical discharge in Alpha, finds Doppler broadening which goes up with increasing ionic charge. He has points for O II–O VI, N I–N V, C III, and C IV.

To clarify this problem we compared a series of line widths in the deuterium arc both from impurities naturally present and from impurities which were added. The results are shown below in the form of apparent ion temperatures based on the assumption that all broadening is Doppler broadening. To within the accuracy of the measurements all ion temperatures seem to be the same:

Ion	Temperature (ev)
He II	15
C II	16
C III	16
O II	14
O III	17
Average	16

It seems likely that the deuterons of the plasma have the same temperature.

In the course of these measurements, an indication of the role of impurities was sought. Carbon monoxide was bled into the system until the 4647-A line had increased in intensity by a factor of 10. Its line width was then measured and found to be unchanged. It is inferred that the impurities normally present have no effect on the particle temperatures in the arc. This result was the same when the gas was bled into the anode, thus supporting the idea of rapid equipartition of energy.

The partial pressure of carbon-containing gas during this experiment was measured by the method described earlier of comparing the carbon light increase with the pressure increase in the chamber. The result was 4×10^{-7} mm Hg. The same procedure, using an oxygen line, gave half this value, suggesting that the carbon is contained in equal parts of CO and an organic vapor, such as CH_4. The CO gas inflow into the anode to double the carbon light intensity was measured to be 0.04% of the deuterium input. Since the drift velocity in the arc must be the same as that of the deuterons, the implied heavy ion impurity level is of the same order as the sum of the carbon and oxygen throughput: 0.06%. This degree of plasma purity has only recently been equaled in the model Etude Stellarator[17] by prolonged discharge cleaning of the walls (2 million pulses). The difference lies in the enormous difference in gas throughput, of course. The low throughput of "endless" machines is, in this regard, a disadvantage that can only be overcome by a successful "divertor."

---

[15] T. P. Hughes, S. Kaufman, and R. V. Williams, to be published (1960).

[16] A. N. Zaidel *et al.*, *Zhur. Tekh. Fiz.* 30, 1422 (1960).

[17] M. S. Jones, Jr., and L. G. Smith, *Bull. Am. Phys. Soc.* 5, 314 (1960), paper D13.

Studies with High-Resolution Spectrograph (R. A. Gibbons, G. Lockhart,[18] R. J. Mackin, Jr., W. F. Peed, and T. F. Rayburn). – Previous studies of spectral line widths have been made with the Jaco 8200 instrument, whose best resolution is about a third of an angstrom. This is approximately one-half to one-third of the line widths which were actually measured, which lessens one's confidence in the accuracy of the results. For more precise studies an echelle instrument is being utilized. The original aims of the experiment were: (1) the actual measurement of line shapes for the succession of lines in the Balmer series for comparison with Stark broadening theory to give a measure of arc density; and (2) the detection of so-called "slant" effect in the observed spectral lines which would indicate the extent of ordered motion of the particles emitting light.

Aside from the extremely high resolution of the instrument, the experiment was found to possess a number of difficulties. First, the arc is such a dim source that it seems unlikely that there will be sufficient light for measurements of Balmer lines higher in the series than D_γ. Second, in spite of the considerable care which was taken in the tedious process of calibrating the film's sensitivity to various spectral lines, the scatter in the results suggests that the observed spectral line shapes cannot be followed over much more than one decade of intensity and that even over that range the uncertainties are such as to make an Abel inversion unprofitable.

Only preliminary results of the measurements are available at this time. Foremost, and independent of the difficulties of the photometric method, no slant was observed in the hydrogen atom lines, indicating an effect less than 0.03 A, which corresponds to an ordered velocity less than 2×10^5 cm/sec. The line widths for D_α, D_β, and D_γ were measured for observations at various distances from the arc axis. There was a fairly large scatter of values but only a hint of the systematic variation with position that would be expected from a density effect. In general, the average widths were not appreciably different from those measured with the Jaco. It now appears that the entire line shape must be studied for any Stark effects to make themselves shown.

It seems likely that dissociative recombination of molecular ions would, because that reaction is exothermic, predominantly produce one atom in the second excited state. If a few additional electron volts are available, the third and higher excited states would be produced. To the extent that the Balmer light in the arc halo is produced by such a process, there should be a broadening in that region characteristic of the initial molecular ion motion as well as the kinetic energy of the atoms resulting from the residual reaction energy. The absence of such an effect suggests strongly that no significant amount of the light so observed is the result of molecular ion recombination.

---

[18] Consultant, University of Tennessee.

4.3.5 Microwave Experiments

H. O. Eason R. J. Mackin, Jr.
R. A. Gibbons T. F. Rayburn
J. D. Tillman[19]

Microwave transmission measurements were made at 2 and 4 mm in order to get a rough idea of the arc density. The microwave method and equipment used are described in ref 20. It was found that 4-mm waves were attenuated 20 db by the presence of the arc column. The arc was thus essentially opaque to the 4-mm waves, consistent with a maximum density in excess of 6×10^{13} electrons/cc. The same attenuation was found for microwaves beamed through a hydrogen arc. These measurements were made with a type M anode. A substantial variation in the attenuation was observed as the arc current and input-gas feed were varied. These results are shown in Fig. 4.20. Their interpretation in terms of density variation is obscured by the possibility of refractive effects, since the arc was a cylindrical structure. In this connection one should note the remarks made in connection with a similar experiment on a carbon arc.[21] An unsuccessful search was made for 4-mm waves reflected at 90° in the plane perpendicular to the axis.

Two-millimeter microwaves were transmitted through a 150-amp deuterium arc with only 3 db of attenuation. The variation of attenuation with arc current is shown in Fig. 4.21.

These measurements suggest that the electron density in the arc is of the general order of 10^{14} electrons/cc and that it varies in the expected sense with arc current and with gas feed.

---

[19] Consultant, University of Tennessee.

[20] H. O. Eason, Jr., *Thermonuclear Project Semiann. Rept. Jan. 31, 1959*, ORNL-2693, pp 37–39.

[21] H. O. Eason, Jr., *Thermonuclear Project Semiann. Rept. July 31, 1959*, ORNL-2802, p 46.

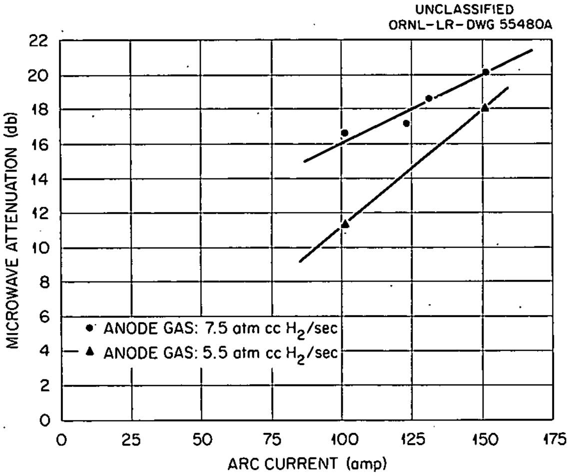

Fig. 4.20. Variation of 4-mm Microwave Attenuation in Hydrogen Arc with Current and Gas Feed.

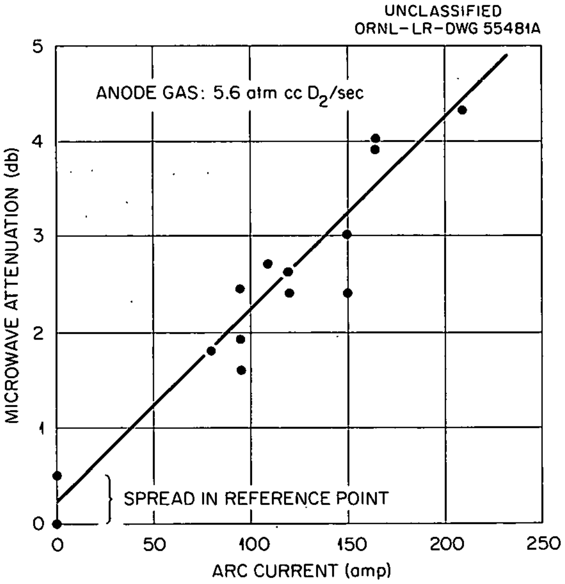

Fig. 4.21. Variation of 2-mm Microwave Attenuation in Deuterium Arc with Current.

5. ION PRODUCTION, ACCELERATION, AND INJECTION

5.1 HIGH-CURRENT ION BEAM INJECTION

R. C. Davis
R. R. Hall
G. G. Kelley
N. H. Lazar
R. F. Stratton
E. C. Moore
O. B. Morgan

5.1.1 High-Current Accelerator[1]

Because of the occurrence of discharges between adjacent corona shields on the accelerator tube above 450 kv, in an air atmosphere, a vinyl-plastic cover was made for the tube and corona shields to permit the use of electron-attaching gases. The cover was partially inflated with Freon-12 and then fully inflated with nitrogen. A very small nitrogen flow into the cover was maintained in order to compensate for small leaks. It was possible under these conditions, after cleanup, to maintain 630 kv for times up to 1 min. The breakdowns then were external to the vinyl-plastic cover and seemed to take place between the corona balls and the platform at the 600-, 450-, or 300-kv corners. It was possible to maintain the accelerator tube at 600 kv for as long as 15 min. Lucite sheets $\frac{1}{2}$ in. thick were laid on the floor and the sloping sides of the platform to insulate the platform from the corona balls. This was only moderately successful, as the breakdowns seemed now to seek out the cracks between the Lucite sheets. A new high-voltage lead arrangement described below is expected to reduce the breakdown problem.

Two different types of targets were used for stopping the ion beam. The first was a $\frac{5}{16}$-in.-thick copper sheet with parallel grooves milled to a depth of $\frac{3}{16}$ in. on 0.364-in. centers so that $\frac{3}{8}$-in. copper tubing with Inconel-ribbon turbulence promoters could be laid in and hard-soldered for heat transfer. The target was canted at 60° to effectively double the area hit by the beam. With a water flow of 100 to 150 gpm, this target was expected to permit a beam power density of 15 kw/in.^{2}. The source was operated at 26 ma and 450 kv for about 10 min before a hole melted through the copper into the water line.

A second type of target, made of $\frac{3}{8}$-in. copper sheet with $\frac{1}{8}$-in. rifle-drilled holes on $\frac{1}{4}$-in. centers, was used with a similar water flow. This target was operated at 70 ma and 540 kv for about 5 min and again at 70 ma and 570 kv for about a half hour before a hole was melted into it. The melting seemed to accompany a high-voltage breakdown.

Other targets have been constructed but are, as yet, untried. One consists of a flat array of parallel $\frac{3}{8}$-in. copper vortex tubing on $\frac{7}{16}$-in. centers. The array is canted at 60°. A rotating target is also being made.

Preliminary beam-profile measurements were made by moving a $\frac{1}{8}$-in.-diam tungsten rod through the ion beam while operating at 15 ma and 550 kv. A Polaroid camera was used to record the oscilloscope traces of the ion current on the target as a function of the position of the tungsten rod in the beam. The beam is approximately the expected diameter at a distance of 24 in. below the

---

[1] *Thermonuclear Project Semiann. Progr. Rept. July 31, 1960,* ORNL-3011, p 59.

center of the solenoid lens. Figure 5.1 shows pictures of the beam profile under two conditions of current in the solenoid lens. Quantitative analysis of the results is difficult and has not been made as yet.

Experiments were halted about November 15 in order to raise the accelerator tube and platform to permit installation of the DCX-2 outboard booster coils underneath. While shut down, the new high-voltage lead arrangement mentioned above is being installed. This new system, shown in Fig. 5.2, will eliminate three corners where breakdowns can occur, and the new positioning of the conductors should provide a more suitable electric field between the conductors. In addition, the

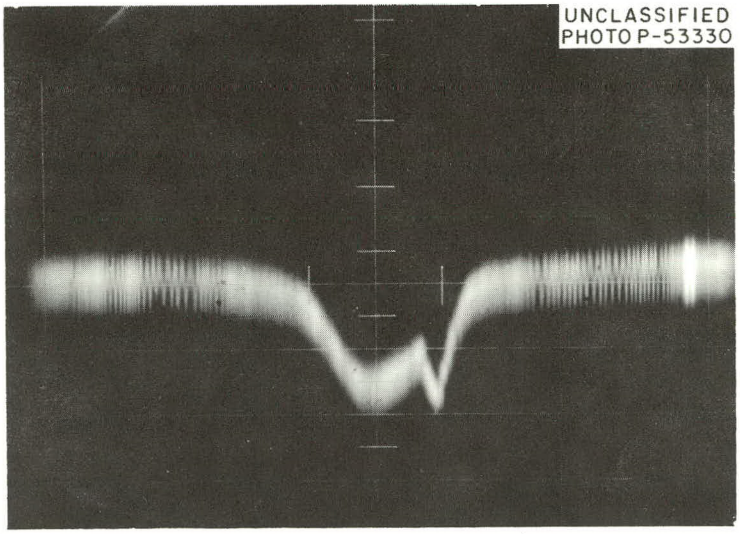

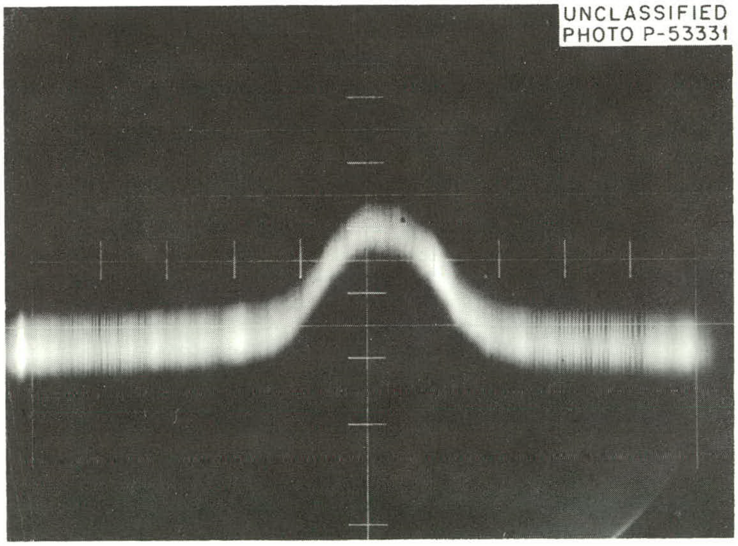

Fig. 5.1. Oscilloscope Traces Showing Variation of Ion Current on the Target as a $\frac{1}{8}$-in. Tungsten Rod Is Swept Across the Beam 24 in. Below the Center of the Solenoid Lens. Extracted ion current was 15 ma at 550 kv. Top picture was taken with the mass 1 component of the beam in focus, and the bottom picture shows all the components unfocused. One centimeter of abscissa represents $\frac{5}{8}$ in. of tungsten rod travel.

UNCLASSIFIED
ORNL-LR-DWG 56967

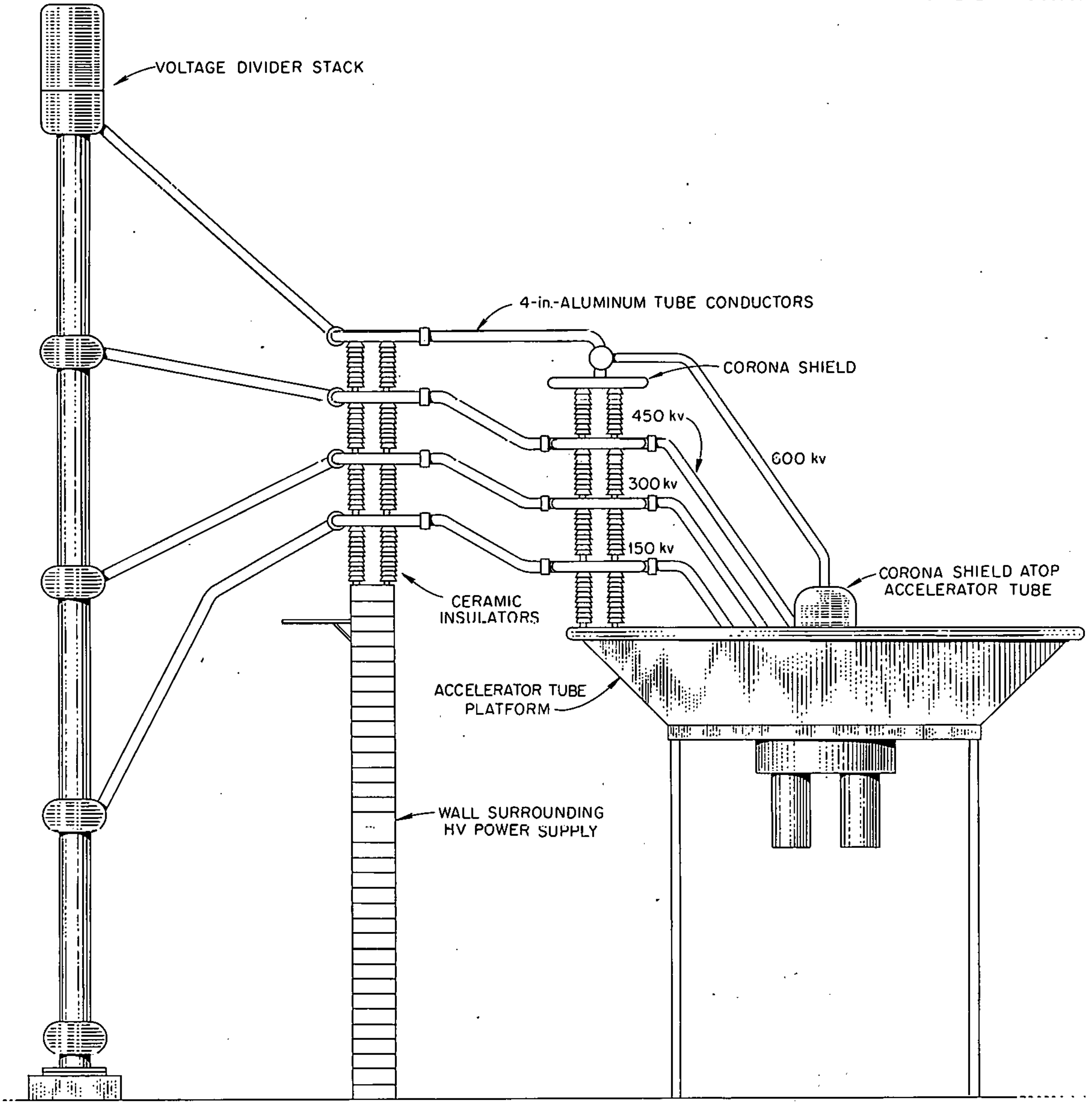

Fig. 5.2. Drawing of the New High-Voltage Lead Arrangement.

new arrangement is integrated with a scheme worked out by P. F. Galle for switching of the high-voltage supply to two other stations. Raising of the platform is due to be completed by the middle of February.

With the platform raised, a 72-in.-long by 28-in.-diam tank will be used vertically so that beam-profile measurements can be made up to a distance of 100 in. from the center of the solenoid lens magnet. After work on the magnetic shielding for the injection snout has been completed by R. L. Brown of the magnetics group, the 72-in. tank will be positioned horizontally beneath the platform and used in conjunction with the DCX-2 outboard booster coils to perform ion injection experiments.

UNCLASSIFIED
ORNL-LR-DWG 56968

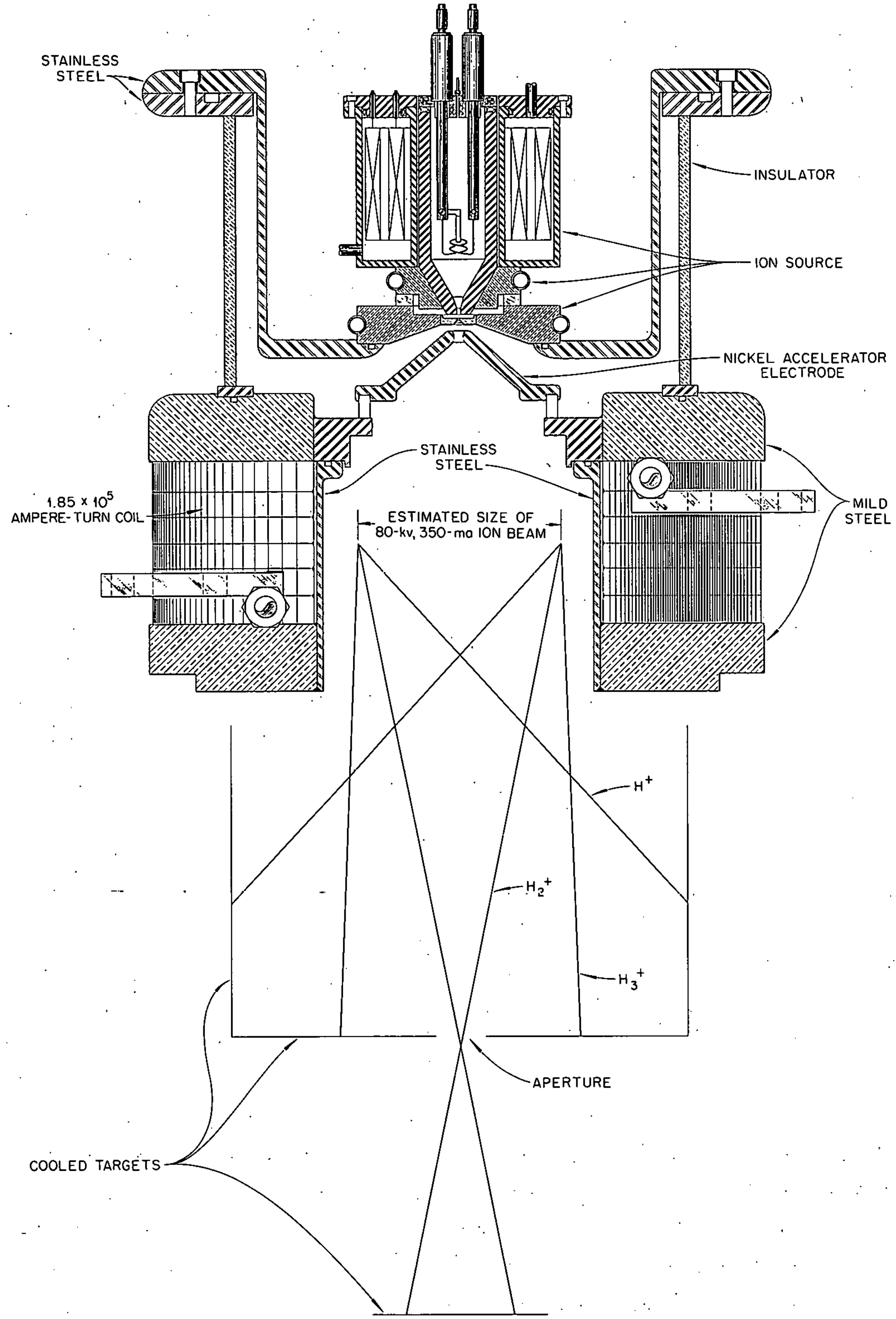

Fig. 5.3. Electromagnetic Analyzer Showing Beam Envelopes with H_2^+ Focused at the Aperture.

5.1.2 Ion-Source Test Facilities

Ion currents have been obtained with the modified von Ardenne source which are the right order of magnitude (340 ma) to be used with the DCX-2 injector system. Two factors remaining to be studied in this high-current range are beam composition and divergence. Analysis of ion beams with electrostatic lens systems has been limited to 100 ma or less by beam divergence in the lens causing a portion of the beam to strike the lens parts.[2]

Electromagnetic focusing by means of a solenoid lens had been ruled out previously because the dependence of focal length on mass made it impossible to separate the beam components emerging from the lens in a transverse magnetic analyzing system. However, utilizing the mass dependence of focal length of the solenoid lens and passing the desired beam component through a small aperture (Fig. 5.3), it seems possible to perform a high-current beam analysis with only a small and correctable error. A lens for this type of analysis has been built and is ready for testing as soon as the necessary 7000-amp rectifiers have been installed.

The 1.85×10^5 ampere-turn coil for the lens was designed in conjunction with R. L. Brown. The lens has a 6-in. inside diameter, a 13-in. outside diameter, and a length of 6.5 in. The maximum central field is 9 kilogauss, which corresponds to a minimum focal length of ≈ 2.5 in. for H_2^+ ions at 80 kev. The lens was made strong, permitting an object distance of only 4.75 in., to minimize space-charge spreading above the lens aperture.

This lens system will also be utilized in efforts to extract ion currents in excess of 340 ma. Other projects that are being considered for the facility are neutralized beam experiments and the development of methods for handling very high power densities from ion beams on cooled surfaces.

5.2 BEAM INJECTION

C. W. Blue	A. C. England	R. L. Knight	O. D. Matlock	O. Sharp
E. L. Earley	H. C. Hoy	J. S. Luce	V. J. Meece	W. L. Stirling

5.2.1 Electrostatic Ion-Beam Deflection

In multiple-pass DCX machines, it is possible to express plasma losses on the injection snout in terms of a "limiting mirror ratio" for the machine.[3] However, the injection snout will not become the limiting factor until the dissociating arc is turned off and breakup proceeds on the trapped plasma.

One method of increasing this limiting mirror ratio is by electrostatic deflection of the molecular ion beam prior to plasma dissociation. It is clear that any physical object used as a deflector electrode will deflect the beam so that the orbit center will be about one Larmor radius from the electrode. In EP-B, this condition is equivalent to moving the orbit center at most by one snout radius. Such a deflection, in principle, could nevertheless increase the limiting mirror ratio to a value close to that determined by the mirror field.

---

[2] *Ibid.*, p 61.

[3] T. K. Fowler, *Loss of Plasma on the Injector*, DCX-2 Technical Memo No. 27.

The above possibility was first suggested by the observation that a beam of approximately $\frac{1}{2}$ amp of ions could be deflected across a magnetic field of several thousand oersteds by a cylindrical deflecting electrode (whose axis coincided with the field) biased at a high negative potential.

This type of deflection only affected particles which passed in the immediate vicinity of the cylinder. The ion beam could pass at a distance several diameters from the cylinder without being deflected, but a small decrease of the separation between the cylinder and the beam could cause a sudden shift in the ion-beam trajectory. These observations indicated the apparent existence of a sheath some distance from the cylinder.

More recent experiments have been aimed at the practical utilization of this effect. The object of these experiments has been to find an electrode configuration such that the ion beam would not be seriously defocused. Figure 5.4 shows the best shape found to date for this purpose. This configuration utilizes floating shields at the edges of the deflector in an attempt to provide a comparatively uniform electric field over the region of the deflection. All experiments used a calutron grid ion source with a 21-kev He^+ ion beam in a magnetic field of about 2600 oersteds. The grid source was $\frac{1}{2}$ in. in height, while the slit in front of the target was $\frac{1}{8}$ in. in height. It was found possible to move the beam about 2 in. with a deflector potential of −7 kv.

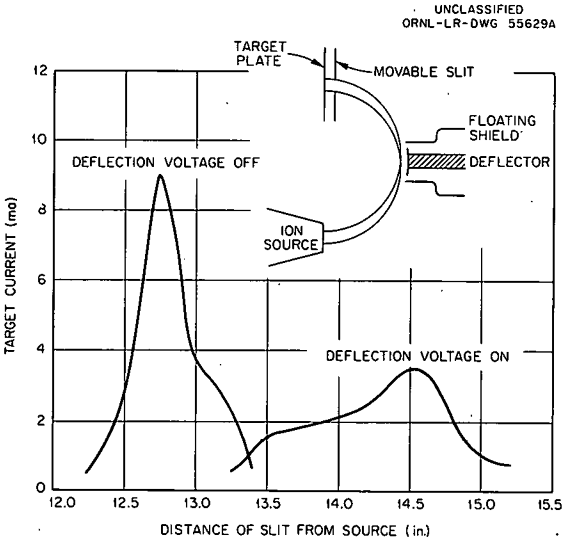

Fig. 5.4. Electrostatic Beam Deflection Shielded Curved Deflector.

Care must be exercised in applying a scaling law to this experiment in order to indicate possible application to a 600-kev D_2^+ or H_2^+ ion beam. Sheath formation at higher voltages, high magnetic fields, and lower pressures may be governed by parameters not studied in these experiments. Also, the location of the deflector electrode at the 90° focal point (as used here) would intercept the trapped plasma. Preliminary calculations (subject to the above limitations) indicate that the deflection of a 600-kev D_2^+ ion beam by 2.8 in. (the approximate snout radius) with a reasonable electrode length would require voltages on the order of −100 kv on the deflector.

Further experimentation is in progress to study the sheath formation near the deflection electrode and to consider other possible electrode configurations.

5.2.2 Neutralized-Beam Injector

The principle of neutralized-beam injection has been discussed in the preceding semiannual report[4] and will not be reviewed here. Useful application of these principles is being made in two

---

[4] *Thermonuclear Project Semiann. Progr. Rept. July 31, 1960,* ORNL-3044, chap. 3.

devices. One is a 600-kev neutralized ion beam accelerator and the other a 100-kev high-energy plasma accelerator. The purpose of the 600-kev model is to deliver a high current ($\frac{1}{2}$ amp), 600-kev H_2^+, and/or H_3^+ space-charge-neutralized beam into DCX-EP-B. The 100-kev model is being designed to deliver a beam of ions and electrons of equal velocity and density. As discussed in the preceding semiannual report,[4] the density of the beam must be sufficiently high for "polarization" to take place so that the beam will cross the 5000-gauss field of DCX-EP-A or the 12,000-gauss field of DCX-EP-B.

Figure 5.5 shows the three methods of electrical connections used when testing the prototype for these two accelerators. Accelerating voltages between 5 and 15 kv have been used when only the electron-gun arc is on. Higher acceleration voltages will be possible when the electrode configuration can be more favorable than that existing in the Sherwood Tank Facility.

UNCLASSIFIED
ORNL LR DWG 55724R

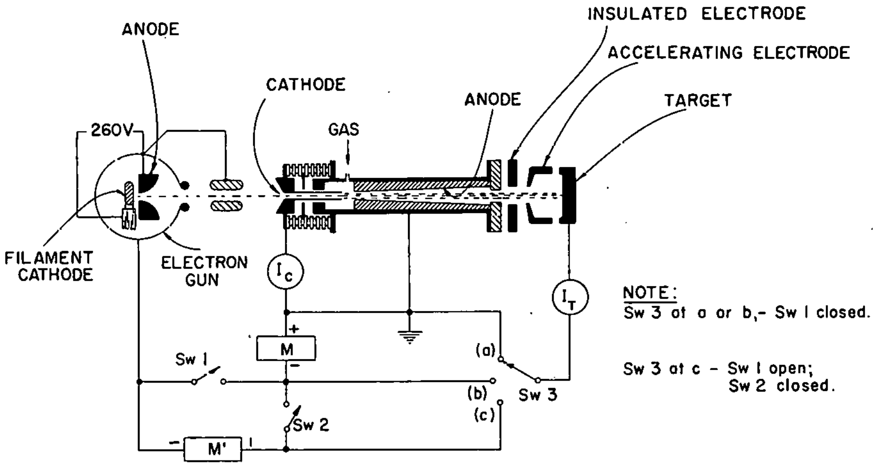

NOTE:
Sw 3 at a or b,- Sw 1 closed.

Sw 3 at c - Sw 1 open;
Sw 2 closed.

Fig. 5.5. Neutralized Electron-Ion Source.

In position *a* (see Fig. 5.5), the ratio of the target current I_T to the ion-source cathode current I_C has been as high as 100 ma to 1 ma. The inner diameter of the ion-source cathode is 0.250 in., and the inner diameter of the electron-gun anode is 0.190 in. For a high current ratio, the alignment of the electron gun and the ion source is critical and is complicated by the nonuniform field in the Sherwood Tank Facility.

When the unit is connected as shown in *b* of Fig. 5.5, the ratio of I_T to I_C drops to a value between $\frac{1}{2}$ and $\frac{1}{3}$ for acceleration voltages below 15 kv. Figure 5.6 shows a typical curve for the current distribution on the target. This curve was taken for an acceleration voltage of 8 kv. Since the electron-gun arc drop was 280 v, the position of the current peak indicates an energy loss of 500 to 600 ev for the electron beam. Calculated scattering losses predict an energy loss of only 70 to 100 ev. The low-energy region of the curve is questionable, as indicated by the dashed line.

Figures 5.7 and 5.8 show typical curves for the currents I_T and I_C, respectively, as a function of the voltage difference (M') between the acceleration potential and deceleration potential. These data were taken with the unit connected as in *c* of Fig. 5.5.

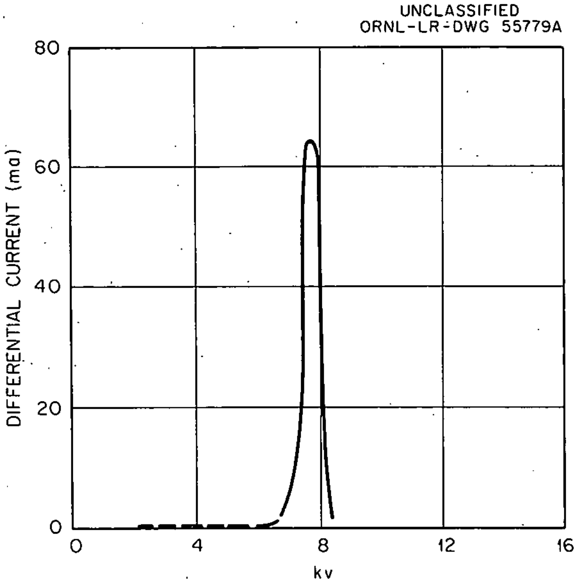

Fig. 5.6. Energy Spectrum for 8-kv-acceleration Electron Gun.

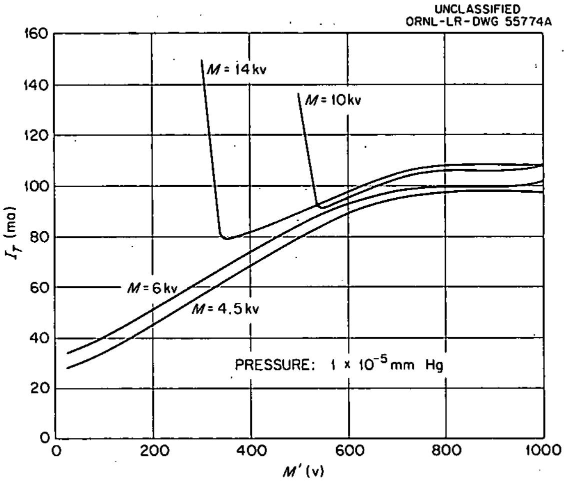

Fig. 5.7. Variation of Accelerating Voltage with Electron Current on Target.

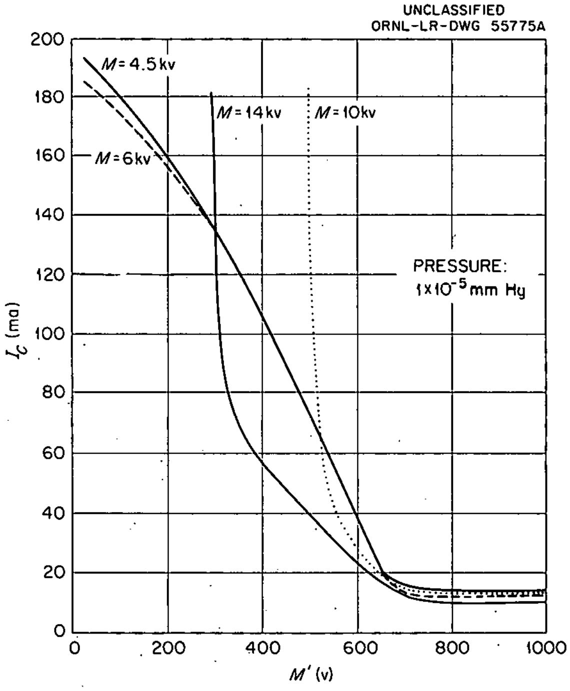

Fig. 5.8. Variation of Accelerating Voltage with Electron Current on Ion Source Cathode.

For values of the M' voltage above 700 v, the currents I_T and I_C are constant; between 600 and 700 v, the current I_T (I_C) decreases (increases) independent of pressure from 5×10^{-6} mm Hg to 1.1×10^{-5} mm Hg and of magnetic field from 2200 gauss to 2800 gauss. The rapid rise in both currents at low abscissa values is dependent on both acceleration voltage and pressure. No measurements of this rapid current increase have been made as a function of magnetic field. It has been ascertained that the rise in both currents is due to thermionic emission of the ion-source cathode. This phenomenon is not completely understood. Meaningful tests are difficult to make because of the large pressure changes which occur when the cathode reaches emission. This in turn changes the stable range of operation insofar as applied voltages are concerned. At a current ratio I_T/I_C equal to 100/1, this rapid current increase is virtually eliminated. In this case, power dissipation on the ion-source cathode is insufficient to cause emission. The data also indicate that the slope of the curve of I_T between 0 and 700 v is a function of acceleration voltage for $I_T/I_C \cong 100/1$.

A more versatile unit is being assembled to study this energy loss behavior in detail. The existence of such a phenomenon in the accelerator is not undesirable. On the contrary, it will contribute to the oscillatory electrons needed for neutralization in the ion accelerating gap, as described in ref 4.

Investigation is under way to determine the behavior of the system when both the electron gun and ion arcs are on. It is not possible to raise the acceleration voltage (M in c of Fig. 5.5) above 3 kv due to the low current-handling capacity of the power supply presently available at the Sherwood Tank Facility. Typical current readings without electron injection are I_T = 1 amp (ion current) and I_{AE} (current on accelerating electrode) = 1.7 amp. With electron injection, I_{AE} falls 100 to 200 ma and the electrode is visibly cooler; I_T shows no significant change. However, a meter reading is meaningless since ions and electrons are both collected on the target, and observation is difficult in the present configuration.

Attempts so far to measure power dissipated on the target have been unsuccessful. A new nonradiative target is being built in order to make calorimetric measurements.

Figure 5.9 is an assembly drawing of the 100-kev high-energy plasma accelerator being assembled on DCX-EP-A. Problems of magnetic field shape and alignment mentioned earlier will be virtually eliminated. Thus more meaningful results will soon be forthcoming.

5.2.3 Beam Disposal with Rotating Titanium Target

Two problems associated with the injecting and trapping of a beam of high-energy particles in a magnetic volume are (1) the immediate removal of the untrapped portion of the beam from the system so that it does not contribute to the gas pressure in the reacting volume, and (2) dissipating the energy of this part of the beam. These problems are common to all DCX machines and become more difficult with increase of input beam current. An input current of 500 ma of H_2^+ is equivalent to a leak of 10^6 liters/sec at a pressure of 10^{-7} mm. The rotating-target titanium pump appears to be a means of solving both problems simultaneously.

The rotating anode (Fig. 5.10), developed for arc experiments in DCX-EP-A and described elsewhere,[5] has proved effective as a target of the rotating-can type. It has successfully dissipated 58 kw of power when operating as an anode for an arc ¾ in. in diameter. It has been shown by O. C. Yonts that a beam of H^+ ions from a calutron-type ion source may be "pumped" by a titanium target. If the surface of the rotating target is covered with titanium it may also be used as a pump. In operation, the pumping surface is continuously replaced by a titanium evaporator on the side of the target opposite the ion beam. Proper shielding of the evaporator prevents titanium contamination of the rest of the system. Such a target-pump arrangement has been operated

---

[5] O. D. Matlock, p 8 *et seq.* in *A Compilation of Material Presented by the Exploratory Physics Group at the Thermonuclear Project Meeting, June 1, 1960,* compiled by J. S. Luce, ORNL CF-60-6-96 (June 21, 1960).

UNCLASSIFIED
ORNL-LR-DWG 55778A

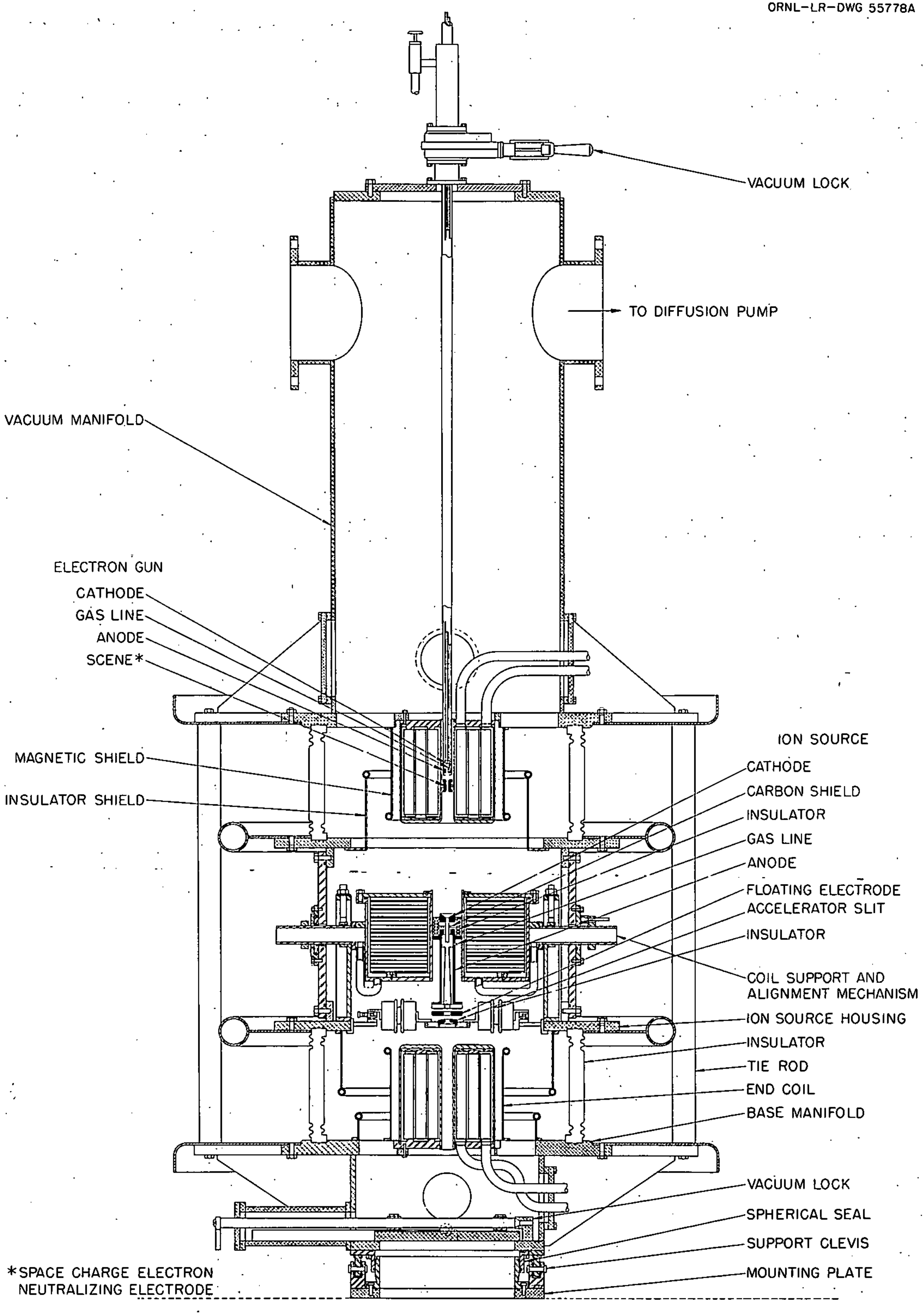

Fig. 5.9. The 100-kev High-Energy Plasma Accelerator.

in the Sherwood Tank Facility with a 600-ma, 25-kev beam of H^+ ions (see Fig. 5.11). The ion beam was moved from the coated section of the target to the uncoated section by changing the magnetic field. The resulting increase of pressure was compared to a leak rate of hydrogen into the system, which gave the same pressure change. Typical results are: $I(H^+) = 0.6$ amp $= 3.78 \times 10^{18}$ particles/sec; leak rate $= 3.69 \times 10^{18}$ particles (atoms)/sec. Motion of the beam over the target area prior to turning on the titanium evaporator in no way affected the base pressure. Before

UNCLASSIFIED
ORNL-LR-DWG 49111A

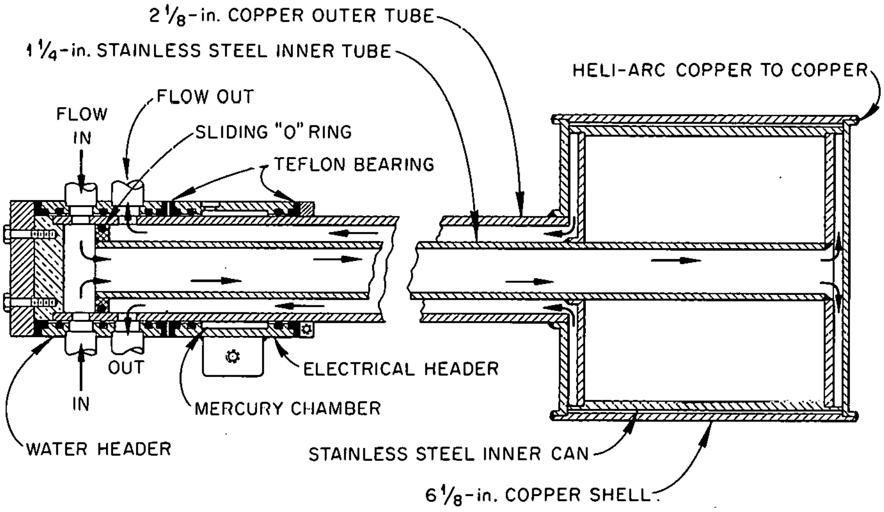

Fig. 5.10. Rotating Anode Assembly with Water and Electrical Headers.

UNCLASSIFIED
ORNL-LR-DWG 55776A

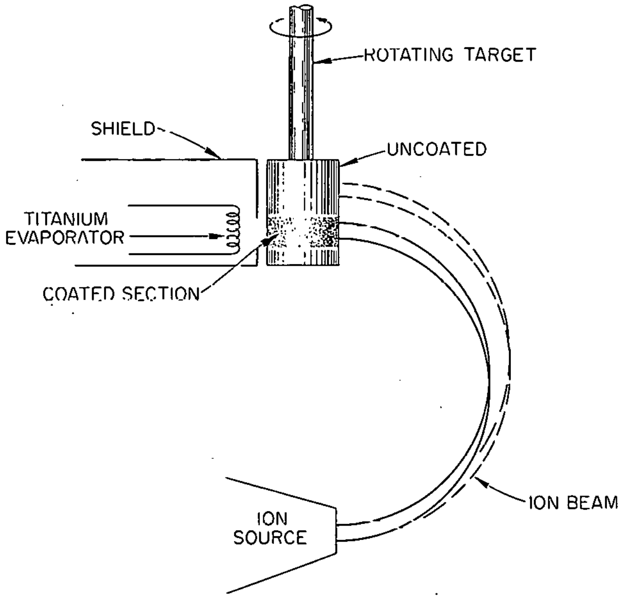

Fig. 5.11. Rotating Target Titanium Pump.

the section of the target had been coated with titanium, moving the ion beam by change of the magnetic field had given no change of the pressure.

A similar installation (see Fig. 5.12) has been made in DCX-1 and will be tested when operation is resumed.

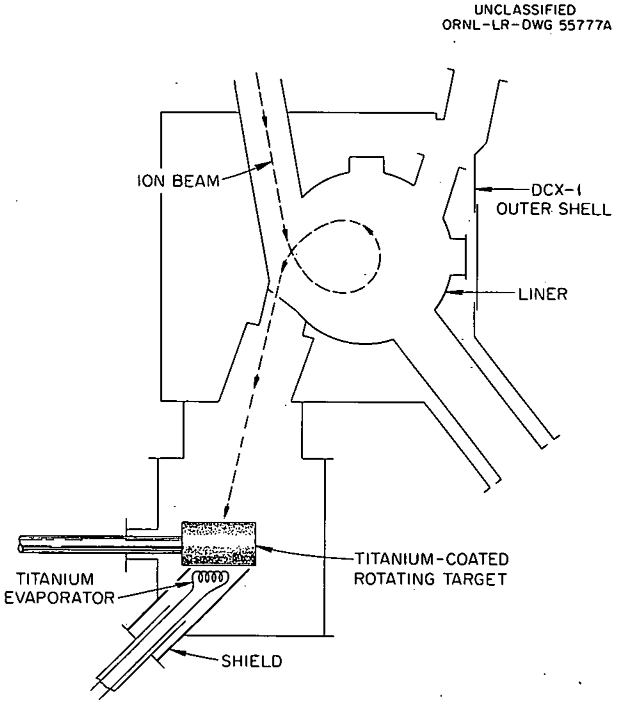

Fig. 5.12. Titanium Pump in DCX-1.

6. THEORY AND COMPUTATION

6.1 INSTABILITIES DUE TO ANISOTROPIC VELOCITY DISTRIBUTIONS

Philip Burt[1] E. G. Harris[2]

An instability which may occur in DCX has previously been investigated.[3] This instability arises when the ions have large velocities perpendicular to the magnetic field and a very small spread in the distribution of $v_{||}$, the component of velocity parallel to the field. The theory predicted that unstable oscillations would occur when $\omega_{pe} > \omega_{ci}$, where ω_{pe} and ω_{ci} are, respectively, the electron plasma and ion cyclotron frequencies. For DCX this gives a critical density of 3×10^6 cm^{-3} above which unstable oscillations should occur. The theory also predicted that the unstable oscillations would have frequencies which are integral multiples of the ion cyclotron frequency. This calculation assumed an infinite homogeneous plasma in a uniform magnetic field.

In order to investigate instabilities in a plasma which more closely resembles that in DCX, we have assumed the following plasma configuration. The plasma is bounded by two cylindrical shells of radii R_1 and R_2. The ions move in circular paths about the axis of the cylinder and they all have the same angular velocity ω_{ci}. The electrons are "cold" (i.e., have zero velocity). The cylinder is infinite in the direction of the magnetic field, which is parallel to the axis. This configuration is illustrated in Fig. 6.1.

UNCLASSIFIED
ORNL-LR-DWG 55451

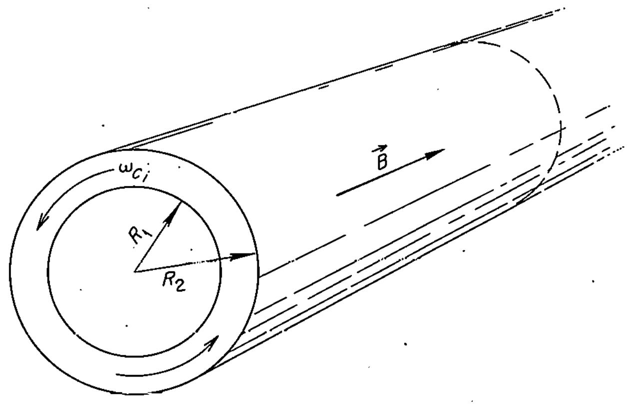

Fig. 6.1. Plasma Configuration.

Perturbations of the ion density of the form

$$n_i(r, \theta, z, t) = Z(r)e^{i(l\theta + k_z z + \omega t)}$$

were assumed. Similar perturbations in the other quantities were assumed. Solution of the differential equations led to a dispersion relation giving ω as a function of l, k_z, ω_{pe}, ω_{pi}, ω_{ce}, and ω_{ci}. This relation is extremely complicated and will not be given here. We shall discuss the results which we have been able to extract from it.

---

[1] Now at the University of Tennessee.

[2] Consultant, University of Tennessee.

[3] E. G. Harris, *Unstable Plasma Oscillations in a Magnetic Field*, ORNL-2728 (June 5, 1959).

A perturbation of the charge density of the plasma can be represented schematically, as in Fig. 6.2. For very low densities the perturbation is carried along with the ions; so the frequency of this mode is approximately $\omega = l\omega_{ci}$. Now, superimposed upon this, there is an ion plasma oscillation which can be resolved into two waves; one of these propagates in the direction of the ion motion, giving a frequency $\omega = l\omega_{ci} + \omega_{pi}$; the other propagates in the opposite direction, giving a frequency $\omega = l\omega_{ci} - \omega_{pi}$. In addition to these two oscillations there is an oscillation of the electrons parallel to the magnetic field. This is at the electron plasma frequency

$$\omega_{pe} = \left(\frac{4\pi n e^2}{m}\right)^{1/2} .$$

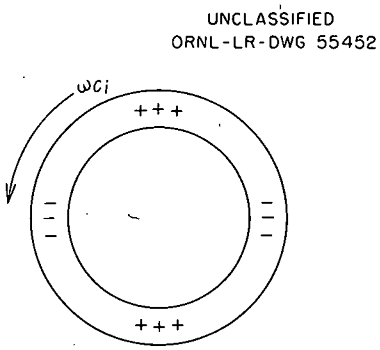

Fig. 6.2. Perturbation of the Plasma Corresponding to $l = 2.9$.

As the particle density, n, is increased, ω_{pe} increases and approaches $l\omega_{ci} - \omega_{pi}$. When the two frequencies become equal, a strong resonance occurs; for still higher densities, ω becomes complex, indicating an instability. A mode with a given l becomes unstable when

$$\omega_{pe} > l\omega_{ci} , \qquad l = 1, 2, 3, \ldots .$$

The real part of ω for the unstable modes is very close to $l\omega_{ci}$.

These results for the bounded plasma are essentially the same as those found for the infinite plasma; that is, as the density is increased, the plasma first becomes unstable when $\omega_{pe} > \omega_{ci}$. Modes corresponding to higher l values become unstable when $\omega_{pe} > l\omega_{ci}$. These unstable modes have frequencies which are very nearly (but not exactly) equal to integral multiples of ω_{ci}.

The amplitude to which these unstable oscillations grow must be determined by some nonlinear effect. We have estimated the amplitude on the assumption that it was limited by the requirement that the particle densities could not become negative. We estimate that for a particle density of 10^7 cm^{-3} the oscillations would grow to an amplitude of only about 20 v. This is a very modest amplitude in comparison with the DCX injection energy of 300 kv. Our calculation indicated that the amplitude should grow linearly with the density and, hence, with the beam current.

6.2 EXACT RELATIVISTIC FOKKER-PLANCK COEFFICIENTS FOR A PLASMA

Albert Simon

In the previous semiannual report, we gave the exact solution of the pair-correlation equations for a plasma by a generalization of the method of Lenard and Balescu.[4] This solution was for the case of a plasma of electrons and infinitely massive ions which, in zero order, was infinite and uniformly distributed in space, was static, and had an isotropic distribution of velocities. In addition, there were no external fields, and the radiation field was taken to be absent in zero order.

---

[4] A. Lenard, *Ann. Phys. (N.Y.)* 10, 390 (1960); R. Balescu, *Phys. Fluids* 3, 57 (1960).

These results have now been generalized in three ways. First, the requirement that the radiation field be absent in zero order was found to be unnecessary. The result obtained is independent of this. Second, the distribution of velocities may now be entirely arbitrary. Third, the ions need no longer be taken as infinitely massive. Instead we can handle an arbitrary mixture of electrons and ions.

The first two generalizations have been incorporated into a general paper which is to appear in the *Physics of Fluids* shortly.[5] A short note on the third point has been written up and is to be submitted to the same journal.[6] Calculations on that most important generalization, the inclusion of an external magnetic field, are well under way.

6.3 A KINETIC EQUATION FOR A RADIATION FIELD OSCILLATOR

E. G. Harris[7]

An equation similar to the Fokker-Planck equation has been derived for $f(q_\lambda, v_\lambda)$, the distribution function for a radiation field oscillator. The derivation followed the approximation scheme of Klimontovich[8] rather than the Simon-Harris[9] generalization of the Rosenbluth-Rostoker expansion.[10]

For a plasma whose ions and electrons are in thermal equilibrium at temperature T the equation for $f(q_\lambda, v_\lambda)$ becomes

$$\frac{\partial f}{\partial t} + v_\lambda \frac{\partial f}{\partial q_\lambda} - \omega_\lambda^2 q_\lambda \frac{\partial f}{\partial v_\lambda} = \omega_p^2 q_\lambda \frac{\partial f}{\partial v_\lambda} + \frac{\omega_p^2 KT}{\omega_\lambda^2} \frac{\partial^2 f}{\partial q_\lambda \, \partial v_\lambda} , \tag{1}$$

where $\omega_\lambda = kc$ is the free space frequency of the oscillator and ω_p is the plasma frequency. This equation has a number of interesting properties. We note that the first term on the right-hand side can be combined with the last term on the left-hand side to give

$$\omega^2 q_\lambda \frac{\partial f}{\partial v_\lambda} , \tag{2}$$

with

$$\omega^2 = \omega_\lambda^2 + \omega_p^2 = k^2 c^2 + \omega_p^2 . \tag{3}$$

If we define $\bar{q}_\lambda$ and $\bar{v}_\lambda$ by

$$\bar{q}_\lambda = \int q_\lambda \, f(q_\lambda, v_\lambda) \, dq_\lambda \, dv_\lambda \tag{4}$$

---

[5] See also Albert Simon, *Exact Relativistic Fokker-Planck Coefficients for a Plasma*, ORNL-3040 (Jan. 10, 1961).

[6] This will also appear as ORNL-3066.

[7] Consultant, University of Tennessee.

[8] Yu L. Klimontovich, *Soviet Phys. JETP* **36**, 999 (1959).

[9] Albert Simon and E. G. Harris, *Phys. Fluids* **3**, 245 (1960).

[10] N. Rostoker and M. Rosenbluth, *Phys. Fluids* **3**, 1 (1960).

and

$$\bar{v}_\lambda = \int v_\lambda \, f(q_\lambda, v_\lambda) \, dq_\lambda \, dv_\lambda \, , \tag{5}$$

then we find that these average values satisfy

$$\frac{d}{dt}\bar{q}_\lambda = \bar{v}_\lambda \tag{6}$$

and

$$\frac{d}{dt}\bar{v}_\lambda = -\omega^2 \bar{q}_\lambda \, . \tag{7}$$

Therefore $\bar{q}_\lambda$ and $\bar{v}_\lambda$ oscillate with the frequency $\left(k^2 c^2 + \omega_p^2\right)^{1/2}$ which is expected for a wave in a plasma.

If we define

$$U_\omega = \int \left(\tfrac{1}{2} v_\lambda^2 + \tfrac{1}{2} \omega^2 q_\lambda^2 \right) f \, dq_\lambda \, dv_\lambda \, , \tag{8}$$

we find from Eq. (1) that

$$\frac{d}{dt} U_\omega = 0 \, . \tag{9}$$

Note that this is not true for

$$U_{\omega_\lambda} = \int \left(\tfrac{1}{2} v_\lambda^2 + \tfrac{1}{2} \omega_\lambda^2 q_\lambda^2 \right) f \, dq_\lambda \, dv_\lambda \, .$$

We find that

$$f(q_\lambda, v_\lambda) = e^{-(v_\lambda^2 + \omega_\lambda^2 q_\lambda^2)/2KT}$$

is a time-independent solution of Eq. (1).

In deriving Eq. (1) we found additional terms of the right-hand side which could be interpreted as the result of the emission of Cerenkov radiation by plasma particles moving with velocities greater than the velocity of light. In a relativistic theory there would be no such particles, of course, so these terms were dropped.

6.4 EXCITATION OF THE FIRST EXCITED STATE OF HYDROGEN

R. G. Alsmiller, Jr.

In a recent publication, Gryzinski[11] has introduced a formalism for calculating the ionization and excitation of atoms by charged particles. In several cases tested by Gryzinski the calculated results were found to agree very well with experiment. To test the theory further, the cross section for the excitation of the first excited state of hydrogen by electrons has been calculated and compared with the experimental cross section. To carry out the calculation it is necessary to specify

---

[11] M. Gryzinski, *Phys. Rev.* 115, 374 (1959).

the electron velocity distribution in the ground state of hydrogen. If we assume the electron velocity distribution, $N(v)$, to be given by (this approximation has been used by Gryzinski with good results)

$$N(v) = \delta\left(v - \frac{e^2}{\hbar}\right) ,$$

we obtain the cross-section values shown in Table 6.1. Also shown in the table are the experimental values of the cross section for the excitation of the $2p$ state of hydrogen.[12] From the table it can be seen that the results are quite poor, the experimental values being somewhat larger than the calculated values over most of the energy range considered.

Table 6.1. Cross Section for the Excitation of the First Excited State of Hydrogen

E in Units of $\frac{1}{2}m(e^4/\hbar^2)$	σ (Calculated) in Units of πa_0^2	σ (Experimental, see ref 12) in Units of πa_0^2
0.75	0	0
1.0	0.337	
1.75	0.502	0.5
3.0	0.374	0.7
4.0	0.319	0.7
8.0	0.203	0.55
10.0	0.188	0.5

In order to test the validity of the approximate velocity distribution used above, the cross section was calculated at one energy using the exact velocity distribution. Using the exact distribution we obtain $\sigma(E = 8) = 0.198$, while using the approximate distribution we obtain $\sigma(E = 8) = 0.203$. Thus the two distribution functions give approximately the same result, and the poor agreement between theory and experiment indicated in Table 6.1 is not due to the approximate velocity distribution used.

6.5 CODE TO CALCULATE PARTICLE ENERGY DISTRIBUTIONS

T. K. Fowler Mozelle Rankin

Several changes in the code, discussed previously,[13] for solving coupled, steady-state Fokker-Planck equations to obtain the energy distribution of ions and electrons in DCX have led to preliminary success. A revised code has been completed to treat one species. Terms representing particle loss by scattering and a monoenergetic source are included, and the iteration procedure

---

[12] W. P. Fite and R. T. Brackmann, *Phys. Rev.* 112, 1151 (1958).

[13] T. K. Fowler and Mozelle Rankin, *Thermonuclear Project Semiann. Rept. Jan. 31, 1960*, ORNL-2926, sec 4.4.

used in solving the nonlinear equation has been shown to be convergent. Figure 6.3 gives solutions, arbitrarily normalized, for several values of the leak rate, L, taken independent of E for test purposes. As one would expect with our monoenergetic source, for very large L, $f(E)$ is sharply peaked at the source energy, E_0, while for successively smaller L, the distribution relaxes nearer and nearer to a Maxwell distribution with $kT = \frac{2}{3}E_0$.

The one-species code is now being amended to include interaction with a second species with given, fixed energy distribution, and the leak term is being altered to include in a self-consistent way effects of any electrostatic field which may develop to restrain electron escape.

UNCLASSIFIED
ORNL-LR-DWG 56969

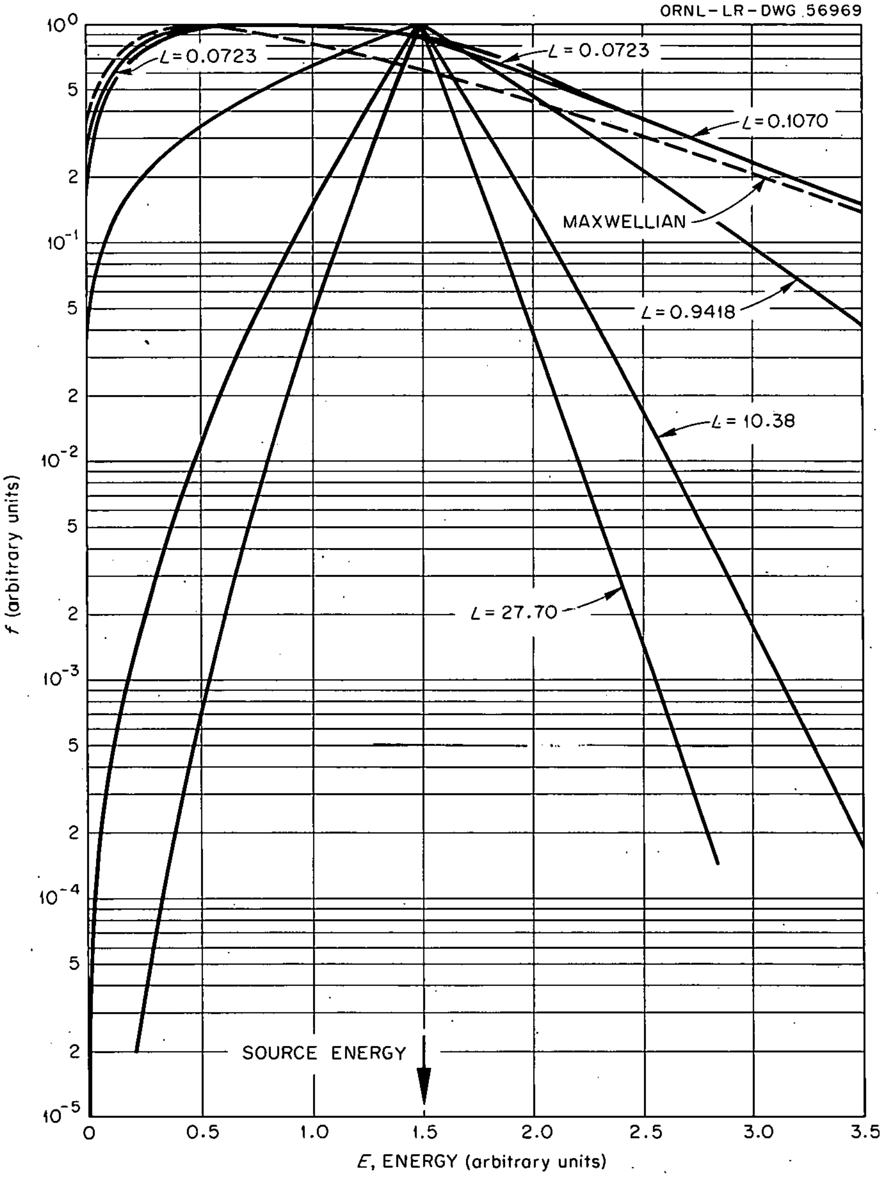

Fig. 6.3. Steady-State Energy Distributions for Various Loss Rates, L.

6.6 EFFECT OF ENERGY DEGRADATION ON THE CRITICAL CURRENT IN AN OGRA-TYPE DEVICE[14]

T. K. Fowler

Simon's calculation[15] of the critical injection current required to achieve a high ion density in an OGRA-type device has been extended. The new calculation includes the effect, neglected by Simon, of the degradation of trapped ion energy due to energy transfer to the continuous flux of cold electrons released in the ionization of the neutral background. In summary, our calculation provides the charge-exchange cross section, averaged over the ion-energy distribution, to be used in Simon's calculation of the critical current.

Figure 6.4 gives revised "S-curves," the relation between injection current and ion density achieved. We plot only the low-density portion where charge exchange is the dominant loss mechanism. The bend in the curve defines the critical injection current, I_{crit}, beyond which the density

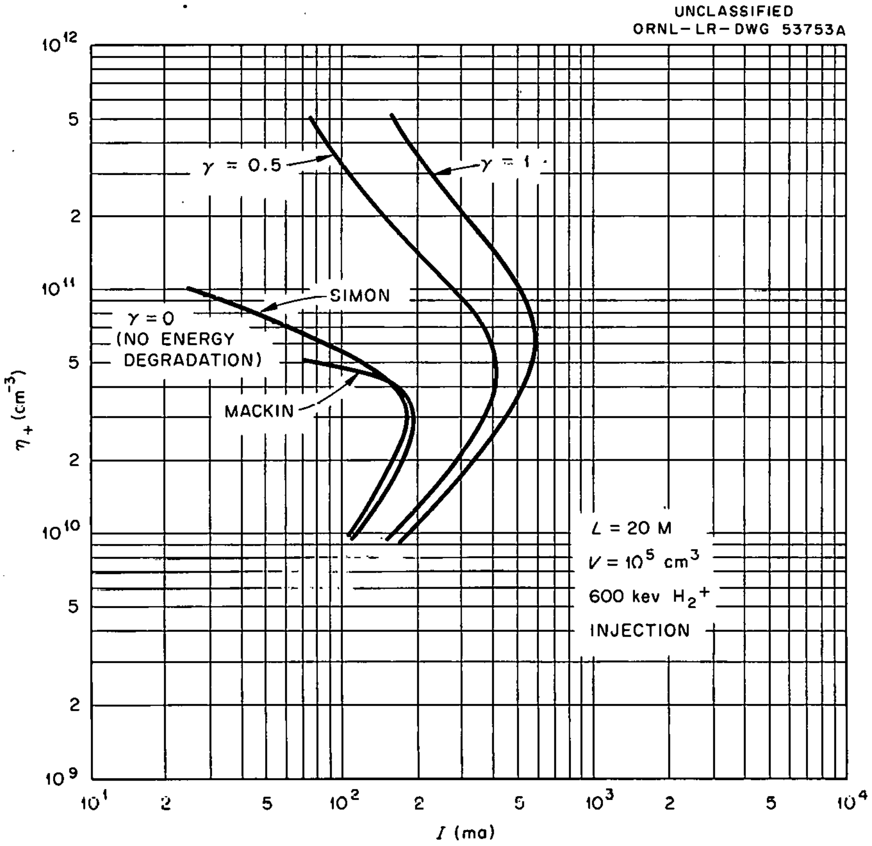

Fig. 6.4. Comparison of S-Curves for Several Values of γ, the Rate of Energy Transfer from Ions to Electrons Relative to the Rate if the Electron Distribution Is Maxwellian.

---

[14] Abstract of published report: *Effect of Energy Degradation on the Critical Current in an OGRA-Type Device*, ORNL-3037 (Dec. 28, 1960).

[15] Albert Simon, *Critical Current for Burnout in an OGRA-Type Device*, ORNL-2831 (Oct. 23, 1959); *J. Nuclear Energy: Pt. C* 1, 215 (1960).

is not limited by charge-exchange losses. We give results for two assumptions about the energy transfer rate (cases $\gamma = 1$ and 0.5), and, for comparison, Simon's result neglecting energy transfer ($\gamma = 0$), together with an approximation due to Mackin. Figure 6.5 compares I_{crit} for various injection energies.

UNCLASSIFIED
ORNL-LR-DWG 53751A

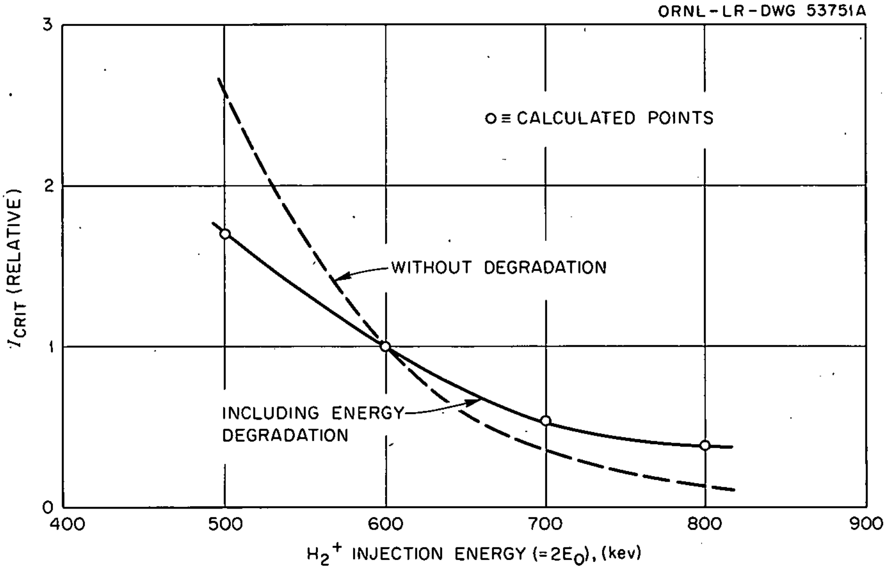

Fig. 6.5. Critical Current vs Injection Energy.

6.7 CONSIDERATIONS OF PHASE SPACE AVAILABLE FOR BEAM INJECTION IN THREE DIFFERING CASES

D. W. Kerst[16] T. H. Ohkawa[17]

In this section general considerations such as have been useful in accelerator design are applied to the injection and trapping of beams in arrangements of interest for controlled fusion.

6.7.1 Injection of a Beam of Neutral Atoms Which Dissociates on Trapped Plasma at Steady State

The fundamental notion we use is that the volume of phase space occupied by the system of ion plus electron in the form of an atom in a beam is the same as the phase volume of the pair after dissociation (assuming a Hamiltonian dissociation process):

$$\left[(\Delta p_i)^3(\Delta q_i)^3(\Delta p_e)^3(\Delta q_e)^3\right]_{\text{beam}} = \left[(\Delta p_i)^3(\Delta q_i)^3(\Delta p_e)^3(\Delta q_e)^3\right]_{\text{mirror}} , \quad (1)$$

where $(\Delta p_i)^3$ represents the spread of momentum space occupied per ion, $(\Delta q_i)^3$ the volume occupied by one ion, and the terms with the subscript e are corresponding spread and volume for the

---

[16] Consultant, General Atomic Division, General Dynamics Corp.

[17] General Atomic Division, General Dynamics Corp.

electron. For an injection ion beam (Fig. 6.6) of the momentum p_i, very small angular spread θ, and momentum magnitude spread δp_i we have

$$(\Delta p_i)^3_{\text{beam}} = \pi p_i^2 \theta^2 \delta p_i$$

and

$$(\Delta q_i)^3_{\text{beam}} = \frac{1}{n_i},$$

UNCLASSIFIED
ORNL-LR-DWG 56970

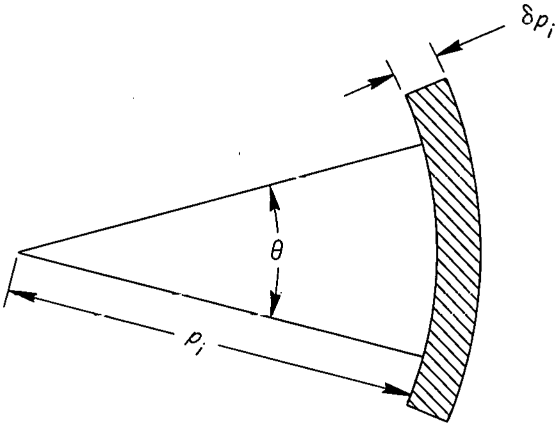

Fig. 6.6. Ion Beam Momentum Distribution.

where n_i is the ion density in the beam. The bound electron fills a phase volume of magnitude $\hbar^3$; thus the left side of (1) is

$$V_{\text{beam}} = \frac{\pi p_i^2 \theta^2 \delta p_i \hbar^3}{n_i}, \tag{2}$$

for the 12-dimensional phase volume. The phase volume of the ions in the mirror *before* equipartition collisions have changed $|p_i|$ but after the mirror walls have mixed directions is

$$V_i = \frac{4\pi p_i^2 \delta p_i}{n},$$

where n is the ion (or electron) density in the mirror confinement volume. If the electron left the ion with the same velocity and direction, we would have

$$V_e = \frac{4\pi p_e^2 \delta p_e}{n},$$

with $p_e = (m/M)p_i$. (Note that this unperturbed departure of the electron is not correct if the quantum uncertainty in p_e is greater than the inherent beam spread δp_e. Another type of calculation is needed for the latter case.)

We now form the 12-dimensional phase volume in the mirror for one particle pair:

$$V_{\text{mirror}} = \frac{16\pi^2 p_i^4 \delta p_i^2}{n^2} \left(\frac{m}{M}\right)^3 . \tag{3}$$

Equating (2) and (3) we have

$$n^2 = \left(\frac{m}{M}\right)^3 \frac{16\pi p_i^2 \delta p_i n_i}{\hbar^3 \theta^2} \tag{4}$$

for the square of the upper limit on particle density in a mirror with an injector characterized by

n_i, δp_i, and θ. For example, if we have 1 amp/cm^2 of 300-kev deuterons,

$$n_i = 10^{10} ,$$

$$p_i = 1.8 \times 10^{-15} ,$$

$$\delta p_i = 1.8 \times 10^{-18} \text{ (0.1\% momentum spread)} ,$$

$$\theta = 0.01 \text{ radian} ,$$

$$\hbar = 10^{-27} ;$$

then $n = 1.5 \times 10^{20}$ particles/cm^3 (this includes ions and electrons) as the upper limit for this injector.

But we must quickly add that Eq. (4) is wrong for this example because the momentum space shell thickness δp_e due to the original beam energy spread has the value

$$\delta p_e = \frac{m}{M} \delta p_i = 10^{-21} ,$$

which is much less than

$$\delta p_{e(\text{quantum})} = \frac{\hbar}{a} = \frac{10^{-27}}{10^{-8}} = 10^{-19} ,$$

where a is the Bohr radius and $\delta p_{e(\text{quantum})}$ is the quantum spread of the momentum shell expected. That is, on dissociation the δp_e amounts to several volts ($\sim 10^{-19}$) and the δp_e from the beam is an underestimate of the space in which dissociated electrons find themselves. Thus, for our example,

$$V_e = \tfrac{4}{3}\pi \left(\frac{\hbar}{a}\right)^3 \frac{1}{n_e} ,$$

and (4) becomes, with $n_e = n$,

$$n = \frac{4}{\theta} \sqrt{\frac{\pi n_i}{3a^3}} . \tag{5}$$

For our example, $n = 4 \times 10^{19}$ as a limit. Note that the final density in (4) and in (5) is proportional to the square root of the beam intensity when the quantum of phase space is brought in by the bound electron.

These estimated limits are maximal with no collisions. The limits may not be possible to attain in real cases. With collisions the limit can rise because the particles move into other regions of phase space, depleting that into which they are injected. For example,

$$V_i \text{ would be } \frac{\tfrac{4}{3}\pi p^3_{i(\text{thermal})}}{n}$$

with a similar volume for electrons which would be very large when the electrons warm up from a few volts to a few kilovolts by equipartition.

6.7.2 Molecular Ions Dissociating to Neutral Atoms and Ions

In this case,

$$V_{\text{beam}} \text{ per bound molecular ion} = \frac{\theta^2 \pi p_M^2\, \delta p_M}{n_M} \hbar^3 ,$$

where n_M is the density of molecular ions in the beam, and since the neutrals will continue in a beam of divergence angle θ,

$$V_{\text{mirror}} \text{ per free ion–neutral pair} = \frac{\theta^2 \pi p_n^2\, \delta p_n}{n_n}\, \frac{4\pi p_i^2\, \delta p_i}{n_i} .$$

But $p_n = p_i$ and $\delta p_n = \delta p_i$; $n_M = n_n$ of outgoing neutral beam; $p_M = 2p_n$ and $\delta p_M = 2\delta p_n$; so

$$n_i = \frac{\pi}{2}\, \frac{p_i^2\, \delta p_i}{\hbar^3} . \tag{6}$$

In our example,

$$n_i = \frac{\pi (1.8 \times 10^{-15})^2 (1.8 \times 10^{-18})}{2 \times 10^{-81}} = 10^{34} .$$

So molecular dissociation has the possibility of much higher limits than neutral-atom dissociation, but both limits are sufficiently high to allow thermonuclear possibilities. Actual densities will be depressed by leakage since Liouville's theorem has given steady-state densities with no leak. A background of neutrals provides particles in phase space where they can recombine with thermalized ions to leak out and depress the density.

6.7.3 Two Oppositely Charged Neutralizing Beams

For the first case we assume that the edges of the mixed beam of electrons and ions of equal velocity are charged by the polarization process so that the internal electric field provides a force which cancels the magnetic force:

$$\frac{\vec{E} \times \vec{B}}{B^2} = \vec{v} .$$

The edges of the beam thus act as an electrostatic inflector which pipes the beam into the center of the confining magnetic field. The trapping process is then just like that in an accelerator, where beam optics govern. Forming the phase volume for a pair of unbound particles traveling with the same speed and with the same optics:

$$V_{\text{beam}} = \frac{\pi p_i^2 \theta^2\, \delta p_i}{n_i}\, \frac{\pi p_e^2 \theta^2\, \delta p_e}{n_e} ,$$

while the phase space they go into in the mirror before particle collisions alter the magnitude of the momentum, but after the magnetic scattering randomizes the directions,

$$V_{\text{mirror}} = \frac{4\pi p_i^2\, \delta p_i\; 4\pi p_e\, \delta p_e}{n^2}.$$

Equating, we get

$$n = \frac{4\sqrt{n_i n_e}}{\theta^2} = \frac{4}{\theta^2} n_{\text{beam}}\,, \tag{7}$$

which is also the answer for a single beam.

The usual parameters of an injecting accelerator's beam are θ and radius or focal length in the system of the injector. They are connected by the relation

$$r = \frac{\theta\lambda}{2\pi},$$

where λ is twice the focal length. Thus

$$n_{\text{beam}} = \frac{N}{\pi r^2} = \frac{4\pi N}{\theta^2\lambda^2},$$

where N is the number of particles per centimeter of beam length. So (7) becomes

$$n = \frac{16\pi N}{\theta^4\lambda^2}, \qquad \text{or} \qquad n = \frac{4N}{\pi\theta^2 r^2}. \tag{7'}$$

After thermalization (if the mirror holds the particles that long),

$$V_{\text{mirror}} = \frac{\tfrac{4}{3}\pi p^3_{i(\text{thermal})}\cdot \tfrac{4}{3}\pi p^3_{e(\text{thermal})}}{n^2_{\text{thermal}}},$$

with

$$p^2_{i(\text{thermal})} = \frac{\tfrac{1}{3}p_i^2}{2} = \left(\frac{M}{m}\right)^2 p_{e(\text{thermal})} \qquad \text{and} \qquad p_e = \frac{m}{M}p_i\,.$$

We get

$$n_{\text{thermal}} = \frac{1}{9}\sqrt{\frac{2}{3}}\,\frac{1}{\theta^2}\,\frac{p_i}{\delta p_i}\, n_{\text{beam}}\,. \tag{8}$$

Thus while our example of injector optics [Eq. (7)] would give

$$n = \frac{4}{10^{-4}}\,10^{10} = 4\times 10^{14}\ \text{particles/cm}^3\,,$$

we find that with equipartition [Eq. (8)] we get

$$n = \frac{10^{10}}{9(10^{-4})} \sqrt{\frac{2}{3}}\, 10^3 = 9 \times 10^{15} \text{ particles/cm}^3 .$$

It is interesting to see that the total number of ions possible in the whole mirror can be determined if we add the rate of leak to the steady-state computation. The total rate of leak is

$$\frac{n^2 V}{2n\tau_{\text{escape}}} ,$$

where V is the complete plasma volume and $n\tau_{\text{escape}}$ = a constant $\approx 5 \times 10^{13}$. Combining with (7′), we find for the total number of particles in the volume

$$nV = \frac{10^{14}}{4} \pi \theta^2 r^2 v = 10^{18} , \tag{9}$$

where v, the beam velocity, is taken as 10^8 cm/sec in our example of the injector that furnishes 1 amp/cm^2 of 300-kev deuterons.

Without equipartition

$$V = \frac{10^{18}}{4 \times 10^{14}} \approx 3000 \text{ cm}^3 . \tag{10}$$

Thus this injector can fill only a 3-liter volume to the Liouville limit. Bigger volumes will leak more and will require more injectors.

Another way is to introduce an escape factor, ϵ, in (7′); then (7′) and (9) become

$$n = \epsilon \frac{4N}{\pi \theta^2 r^2}$$

and

$$n = \frac{10^{14} \pi \theta^2 r^2 v}{4V\epsilon} .$$

Multiplying these together,

$$n = 10^7 \sqrt{\frac{vN}{V}} \approx \frac{2 \times 10^{16}}{\sqrt{V}} .$$

Thus, if

$$V = 10^6 \text{ cm}^3 ,$$

then

$$n = 2 \times 10^{13} .$$

We see the beam quality is not dominant in case the injector is not able to keep up with the leak.

The requirements on beam quality from the injector are just as severe as they are for an inflector in a standard accelerator. Factors of the perfection of phase-space filling may differ between different methods, but the limits determined by Liouville's theorem govern.

An additional case of the two neutralizing beams is that of no straight moving core to the polarized beam but, rather, the possibility pointed out by Rose[18] that the looping trajectories of oppositely charged particles drift together across the magnetic field, as shown in Fig. 6.7*a*.

The same double-beam treatment of the phase-space limit, Eq. (7), holds in this case too.

Further comments can be made on the detailed behavior of injection processes which may limit the attainable density very drastically to values far below the Liouville limit. For example, Rose pointed out what might happen to neutralizing oppositely charged beams if they strike a conductor. Suppose this conductor is an already captured plasma in a mirror. Then the beam splits and passes around and out of the mirror, as shown in Fig. 6.7*b*.

In the dense core case also, the core can split and pass around, as shown in Fig. 6.7*c*.

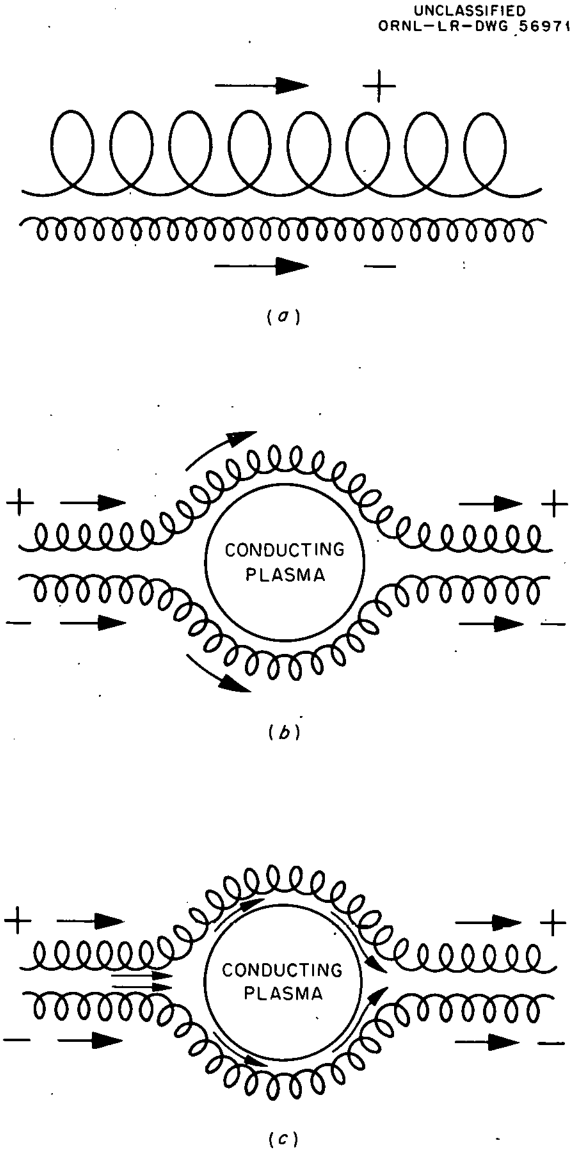

(*a*)

(*b*)

(*c*)

Fig. 6.7. Trajectories of Oppositely Charged Particles Across a Plasma in a Magnetic Field.

This type of flow is unstable, but densities within the plasma would be limited to about the same value as densities in the beam.

---

[18] D. J. Rose, *Thermonuclear Project Semiann. Rept. July 31, 1959*, ORNL-2802, p 99.

7. INSTRUMENTATION

7.1 THERMOSWITCHES FOR MAGNET COIL HIGH-TEMPERATURE DETECTION

R. L. Brown

The magnet coils of DCX-2 will have 946 water coolant paths. The malfunction of any one of these could result in serious damage and costly delays while making repairs. DCX-2 design specifies that one bimetallic thermoswitch be located at the end of each water coolant path. It is to be mounted directly on the copper conductor. This switch will automatically shut down DCX-2 at any time the temperature rises above 95°C.

A test section was constructed using the same size conductor that is used in DCX-2 outboard coils. Provisions were made for simultaneous testing of four switches as shown in Fig. 7.1. A total of eight switches were tested.

The test section was heated with a current up to 14,000 amp dc, and the temperature was controlled by regulating the water flow in the tube. Increasing the temperature in increments of 1 to 2°C over an extended length of time caused the normally closed switches to open at the specified

UNCLASSIFIED
ORNL-LR-DWG 56972

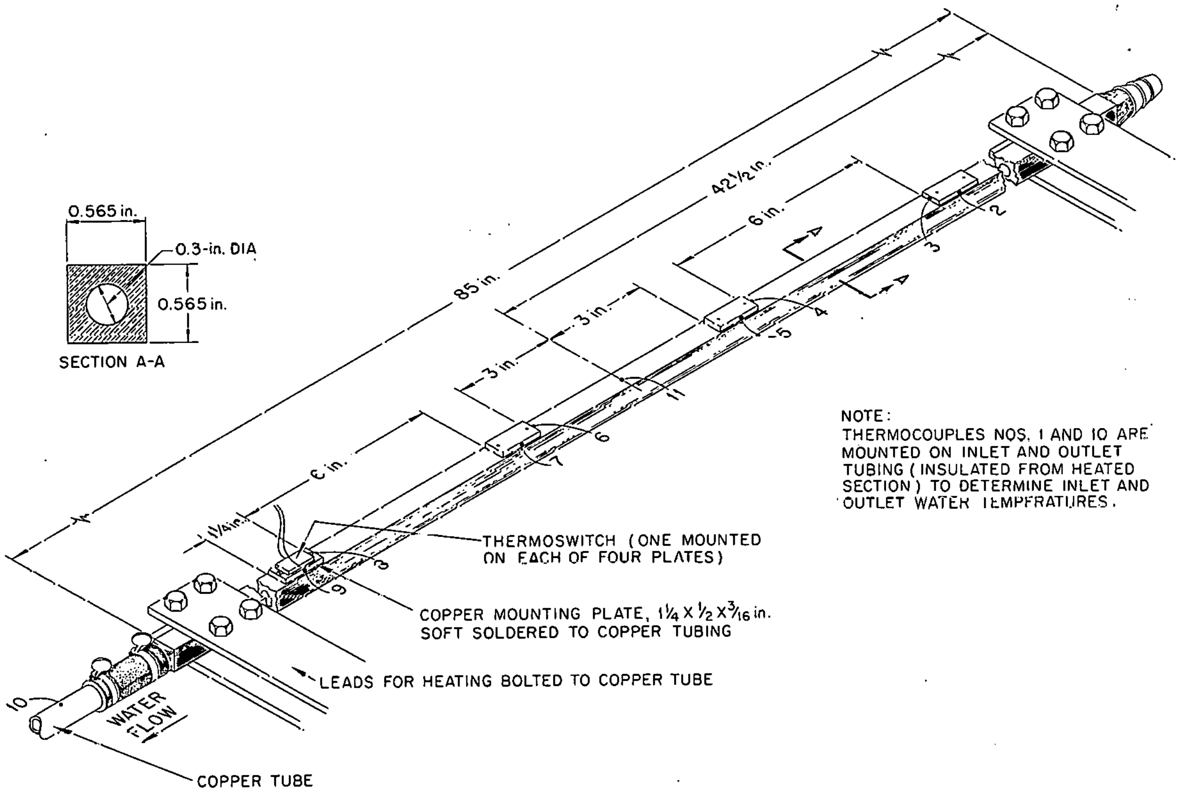

NOTE:
THERMOCOUPLES NOS. 1 AND 10 ARE MOUNTED ON INLET AND OUTLET TUBING (INSULATED FROM HEATED SECTION) TO DETERMINE INLET AND OUTLET WATER TEMPERATURES.

Fig. 7.1. Test of Thermal Switch Prototypes for DCX-2.

95°C. Setting the current at 4000 amp, approximately the current in DCX-2, and increasing the temperature rapidly causes the switches to operate at an average copper temperature of 112 ± 2°C (corresponding water temperature still safely below boiling). The average time delay was 19.5 sec.

Since the switch will be in the stray magnetic field of DCX-2, tests were run to determine what effect this may have on the operation of the switches. It was found that the temperature at which the switch operates is shifted upward about 2.5°C when in a field of 6 kilogauss. This is calculated to be the maximum field in which any switch will be located. This effect is considered to be insignificant.

8. MAGNETICS

8.1 DESIGN OF MAGNETIC MIRROR FIELDS WITH EXTREMELY HOMOGENEOUS CENTRAL ZONES

D. L. Coffey　　　J. E. Simpkins

The previous report[1] described the design of magnetic mirror fields with central zones (approximately 250 liters volume) homogeneous to about 0.1% in field strength, and computational codes developed for this and related purposes.

This report will describe further developments of these techniques, and show in some detail the application of the principles in the design of DCX-EP-B.

The design of the coil system for DCX-EP-B was limited by the following requirements:

1. total coil power must not exceed 12 Mw,
2. maximum outside diameter of the mirror and inside booster coils must not exceed 48 in. (to fit vacuum tank),
3. reasonable access must be provided for vacuum and diagnostics,
4. outside boosters must be outside main tank, and have radial access for gas arc operation,
5. maximum field homogeneity must be achieved while maintaining 3.5 mirror ratio for hydrogen injection and 2.5 for deuterium.

Field homogeneity near the axis is a strong function of the inside radius of the coils near the region of interest. Therefore, within the available power and feasible current densities, the inside radius of the booster coils was maximized.

To achieve the best possible field shape, a computer code, originally written by the Electronuclear Division of ORNL,[2] was modified for our purposes. This revised code provides for a least-squares fit of the magnetic field strength at points on or off the axis and with or without weighting factors. Of the several possible methods of using this least-squares code, the following four were studied in some detail:

1. axial minimization – involving only axial field points in the solution,
2. off-axis minimization – a solution using only field points at a fixed radial distance off-axis,
3. a combination of methods 1 and 2 – using both off-axis and on-axis points,
4. average minimization – whereby the "average field"[3] experienced by the injected molecular ions was minimized.

While these methods made possible the design of a very homogeneous central zone, they were of little help in shaping the required "field dip region." This field dip, necessary for proper ion injection, was designed by use of the "superposition theorem" of Gauster.[4] The use of this theorem permitted shaping the field dip while maintaining the homogeneous central zone.

---

[1] D. L. Coffey, W. F. Gauster, and J. E. Simpkins, *Thermonuclear Project Semiann. Progr. Rept. July 31, 1960*, ORNL-3011, p 80.

[2] B. D. Williams and G. L. Broyles, personal communication.

[3] D. L. Coffey, W. F. Gauster, and J. E. Simpkins, *op. cit.*, p 81.

[4] W. F. Gauster, this report, sec 8.2.

Figure 8.1 shows the coil system evolving from these calculations, a useful field shape, and the resultant ion trajectories.[5] Since the ions must make one full revolution before again arriving in the vicinity of the injection snout, it is clear that if beam spreading effects are not too great both the H_2^+ and H_3^+ ions will miss the snout. The split outboard booster coil system is designed to facilitate gas arc operation.

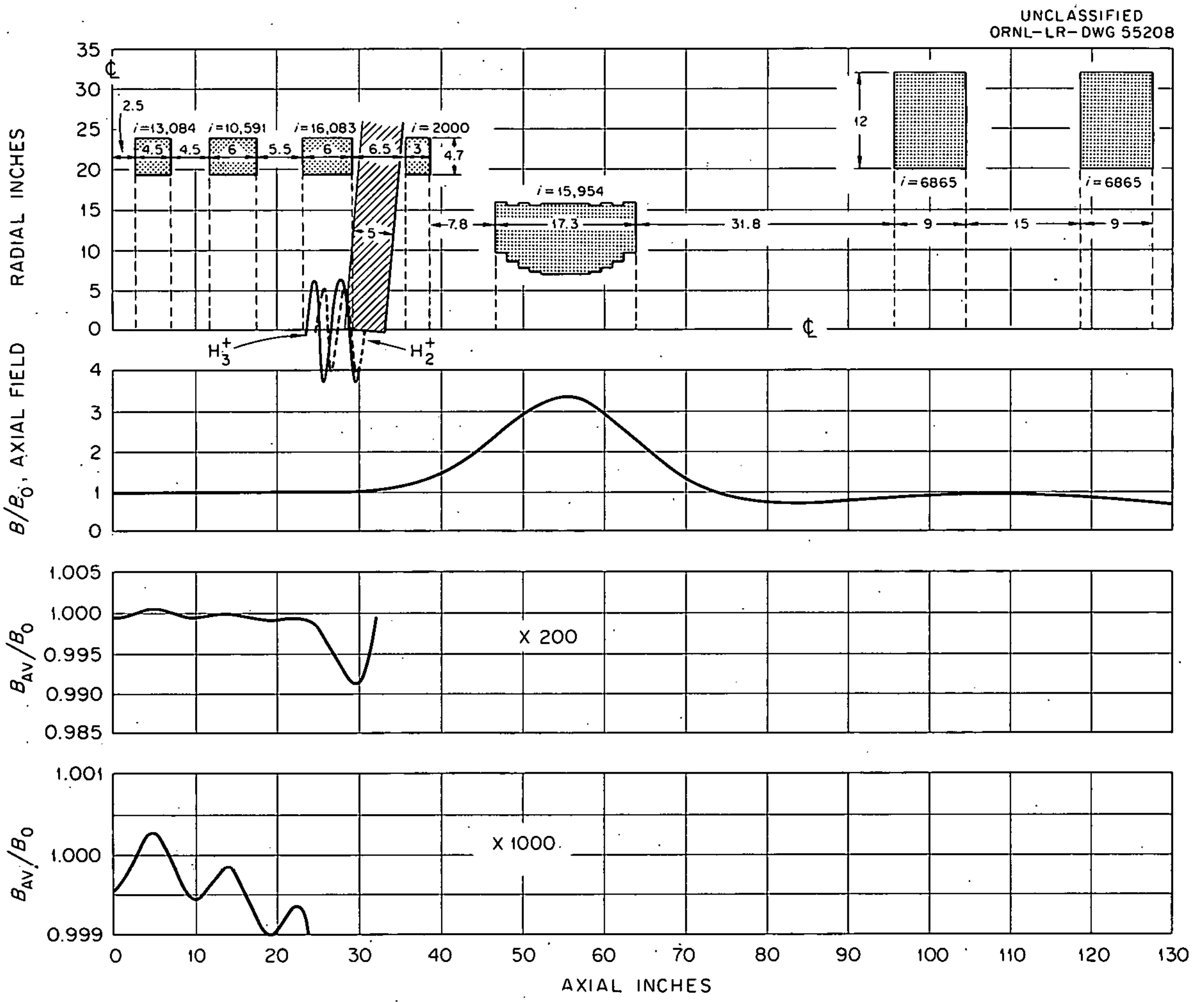

Fig. 8.1. A Possible Field for Hydrogen Injection in DCX-EP-B.

The nominal field strength, B_0, is 12,000 gauss for hydrogen ion injection and 17,000 gauss for deuterium ion injection.

Figure 8.2 illustrates a magnetic field solution for deuterium ion injection. In this mode of operation the mirror ratio is 2.5. The current densities of the inside booster coils are somewhat higher to provide the 17,000-gauss field, but the field shape is very similar to that for hydrogen ion injection.

---

[5] Ion trajectory calculations by G. R. North; sec 2.2.3, this report.

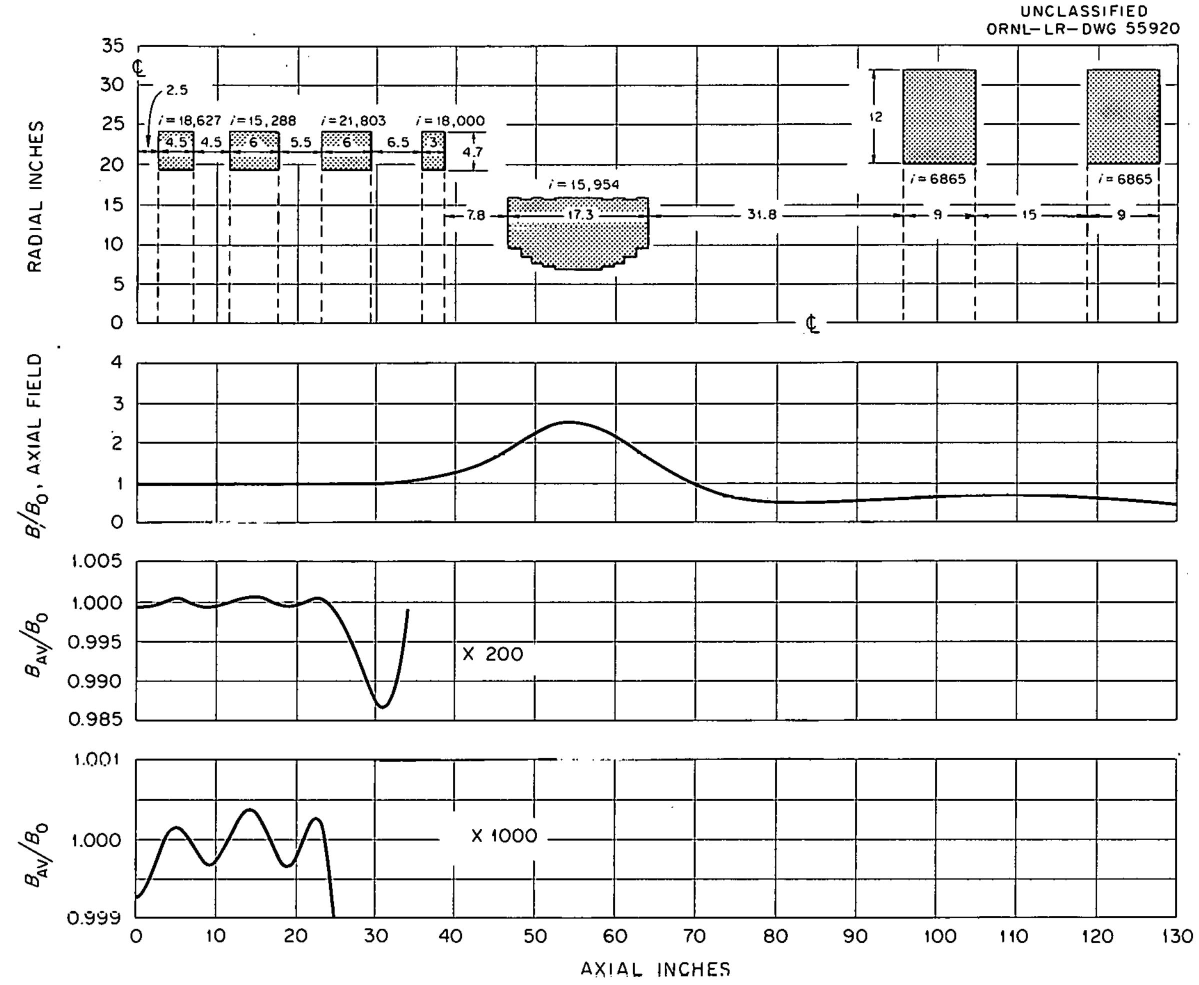

Fig. 8.2. A Possible Field for Deuterium Injection in DCX-EP-B.

8.2 FIELD OPTIMIZATION BY SUPERPOSITION OF OPTIMIZED MAGNETIC FIELDS

W. F. Gauster

Thermonuclear research facilities for high-energy ion injection which are using the multiple pass concept (DCX-2 and DCX-EP-B) call for magnetic mirror fields with extremely homogeneous central zones. Furthermore, an appropriate "field dip" near the injection snout has to be provided. Previously a mathematical method has been described,[6] which gave very good results for the homogeneous central zone. It seemed to be possible to obtain the field dip as a by-product of the optimization of the current densities of the three inside coil pairs without providing a special dip coil for this purpose. Detailed studies demonstrated, however, this assumption as being too optimistic, and showed the difficulties associated with achieving the final goal by intelligently guessing the

---

[6] D. L. Coffey, W. F. Gauster, and J. E. Simpkins, *Thermonuclear Project Semiann. Progr. Rept. July 31, 1960*, ORNL-3011, p 80.

shape and current density of a dip coil. It was only by applying the following superposition theorems that satisfactory results could be easily realized.[7]

8.2.1 Field Optimization with Known Central Magnetic Field Strength B_0

In DCX-2 the magnetic field is produced by the following coil pairs:

1. Magnetic mirror coils and outside booster coils, both with known current densities. The field produced by these coils is designated $B_a(z)$.
2. One pair of dip coils with a current density i_D, which is variable in order to change the shape of the dip. The field produced by this coil pair with any arbitrarily assumed current density $i_D^{\star}$ is designated $B_D^{\star}(z) = i_D^{\star}\, b(z)$. The field produced by the eventually selected current density i_D is $B_D(z) = i_D\, b(z)$.
3. Three pairs of inside booster coils with current densities i_k, where $k = 1, 2, 3$. The field produced by these coils is designated

$$B_c(z) = \sum_{k=1}^{3} i_k\, f_k(z) ,$$

where $f_k(z)$ is the flux density produced at the magnetic axis by coil pair number k in the distance z from the center, with the unit current density in the coil pair concerned.

The total magnetic field produced at the axis is

$$B_z(z) = B_a(z) + i_D\, b(z) + \sum_{k=1}^{3} i_k\, f_k(z) . \qquad (1)$$

This field is called "optimized" if the current densities in the inside booster coils i_k assume such values that for the "homogeneous" zone, that is, $-L \leqq z \leqq L$, the flux density $B_z(z)$ approaches the constant value B_0 as well as possible. Therefore

$$K = \int_0^L (B_z - B_0)^2\, dz = \min \text{ (ref 6)} \qquad (2)$$

and

$$\frac{\partial K}{\partial i_l} = 2 \int_0^L \left[B_a(z) + i_D\, b(z) + \sum_{k=1}^{3} i_k\, f(z) - B_0 \right] f_l(z)\, dz = 0 , \quad l = 1, 2, 3 . \qquad (3)$$

Introducing the abbreviations

$$\begin{aligned} \int_0^L f_l(z)\, dz &= F_l , \\ \int_0^L f_k(z)\, f_l(z) &= F_{kl} , \\ \int_0^L B_a(z)\, f_l(z)\, dz &= G_l , \\ \int_0^L b(z)\, f_l(z)\, dz &= H_l , \end{aligned} \qquad (4)$$

---

[7] Mozelle Rankin, this report, sec 2.2.1; G. R. North *et al.*, this report, sec 2.2.3.

Eq. (3) yields the following three linear equations for i_k:

$$\sum_{k=1}^{3} F_{kl} i_k = B_0 F_l - G_l - H_l i_D , \qquad l = 1, 2, 3 . \tag{5}$$

Instead of solving these equations directly, new quantities i_{ak}, i_{bk}, and i_{ck} are introduced as the solutions of the following systems of equations:

$$\left.\begin{aligned} \sum_{k=1}^{3} F_{kl} i_{ak} &= -G_l , && (6) \\ \sum_{k=1}^{3} F_{kl} i_{bk} &= -i_D^{\star} H_l , && (7) \\ \sum_{k=1}^{3} F_{kl} i_{ck} &= B_0^{\star} F_l , && (8) \end{aligned}\right\} \qquad l = 1, 2, 3 ,$$

where $i_D^{\star}$ and $B_0^{\star}$ are arbitrary values. The linear form

$$i_k = i_{ak} + \frac{i_D}{i_D^{\star}} i_{bk} + \frac{B_0}{B_0^{\star}} i_{ck} , \qquad k = 1, 2, 3 , \tag{9}$$

is a solution of Eq. (5).

Equations (6), (7), and (8) can be interpreted as follows:

1. The inside booster coil pairs energized with the current densities i_{ak} together with the regularly energized mirror and outside booster coils produce on the axis a field

$$B_a'(z) = B_a(z) + \sum_{k=1}^{3} i_{ak} f_k(z) , \tag{10}$$

so that

$$\int_0^L [B_a'(z)]^2 \, dz = \min . \tag{11}$$

That means $B_a'(z)$ approaches for $-L \leqq z \leqq L$ as well as possible the value zero. $B_a'(z)$ is shown in Fig. 8.3*a*.

2. The inside booster coil pairs, energized with the current densities i_{bk}, together with the dip coil, energized with the arbitrary current density $i_D^{\star}$, produce on the axis a field

$$B_b'(z) = i_D^{\star} \, b(z) + \sum_{k=1}^{3} i_{bk} \, f_k(z) , \tag{12}$$

so that

$$\int_0^L [B_b'(z)]^2 \, dz = \min . \tag{13}$$

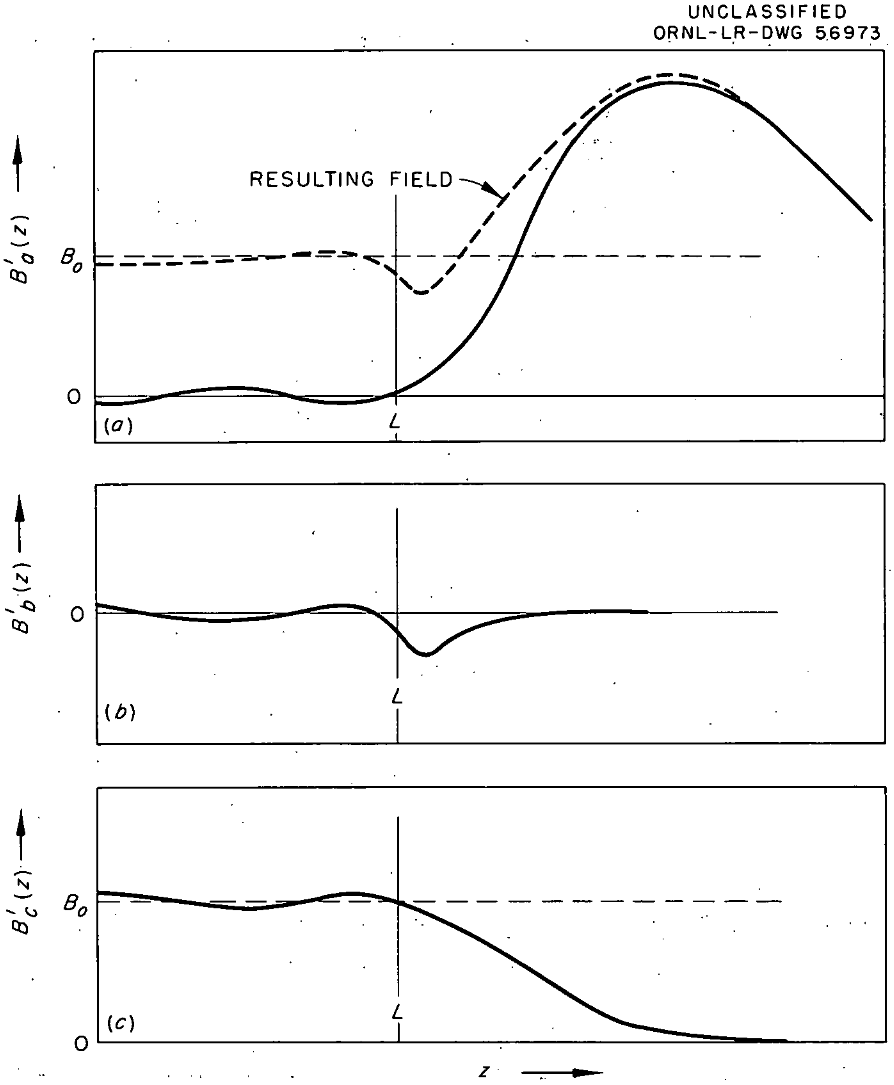

Fig. 8.3. Component Fields (not to Scale, in Order to Show More Clearly the Field Deviation in the "Homogeneous" Zone and the Dip Region).

Therefore $B'_b(z)$ likewise approaches as well as possible the value zero for $-L \leqq z \leqq L$. $B'_b(z)$ is shown in Fig. 8.3*b*.

3. The inside booster coil pairs energized with the current density i_{ck} produce alone on the axis a field

$$B'_c(z) = \sum_{k=1}^{3} i_{ck} f_k(z) , \tag{14}$$

so that

$$\int_0^L [B'_c(z) - B_0^*]^2 \, dz = \min . \tag{15}$$

$B'_c(z)$ approaches for $-L \leqq z \leqq L$ as well as possible the constant value B_0^*. $B'_c(z)$ is shown in Fig. 8.3*c*.

The component fields $B'_a(z)$, $B'_b(z)$, and $B'_c(z)$ are "optimized" fields since they deviate for $-L \leqq z \leqq L$ as little as possible from zero and B_0^*, respectively. To find the optimized field $B_z(z)$ by means of superposition of the optimized component fields has the advantage that for different values of i_D and of B_0 the field shape can be easily found without the necessity to repeat each time the whole procedure for each selected value of B_0 and i_D. The influence of changing the numerical values of B_0 and i_D on the resulting optimized field shape can easily be seen on the changed component fields.

8.2.2 Field Optimization When B_0 Is Not Known

In Eqs. (2) and (3) B_0 can be considered as a variable. Then a fourth equation

$$\frac{\partial K}{\partial B_0} = -2 \int_0^L \left[B_a(z) + i_D\, b(z) + \sum_{k=1}^{3} i_k\, f(z) - B_0 \right] dz = 0 \tag{16}$$

has to be used to find i_k and B_0. This procedure allows a check on whether the distance between the mirror coils is well chosen. Field optimization is not very sensitive with respect to the exact value of B_0. With larger deviations of the "natural" value of B_0 [which follows from Eqs. (3) and (16)], however, only relatively poor homogeneity can be achieved in the central zone $-L \leqq z \leqq L$.

It can be shown in a similar way, as previously described, that field optimization by superposition of optimized magnetic fields is possible also in this case. The system of linear equations is

$$\begin{aligned} &\sum_{k=1}^{3} F_{kl}\, i_k - F_l B_0 = -G_l - H_l i_D\,, \qquad l = 1, 2, 3\,, \\ &\sum_{k=1}^{3} F_k i_k - L B_0 = -\int_0^L B_a(z)\, dz - i_D \int_0^L b(z)\, dz\,, \end{aligned} \tag{17}$$

which can be treated by solving the two systems of linear equations

$$\begin{aligned} &\sum_{k=1}^{3} F_{kl}\, i_{1k} - F_l B_1 = -G_l\,, \qquad l = 1, 2, 3\,, \\ &\sum_{k=1}^{3} F_k i_{1k} - L B_1 = -\int_0^L B_a(z)\, dz\,, \end{aligned} \tag{18}$$

and

$$\begin{aligned} &\sum_{k=1}^{3} F_{kl}\, i_{2k} - F_l B_2 = -H_l i_D^*\,, \qquad l = 1, 2, 3\,, \\ &\sum_{k=1}^{3} F_k i_{2k} - L B_2 = -i_D^* \int_0^L b(z)\, dz\,. \end{aligned} \tag{19}$$

The inside booster coils energized with the current densities i_{1k} produce, together with the regularly energized mirror and outside booster coils, a magnetic field which is optimized in the central zone for a constant flux density B_1. The inside booster coils, with current densities i_{2k}, and the dip coil, energized with the arbitrary current density i_D^*, produce a field which is optimized for another constant flux density B_2. The current densities i_k and the optimum flux density B_0 are determined by

$$i_k = i_{1k} + \frac{i_D}{i_D^*} i_{2k} , \qquad k = 1, 2, 3 , \tag{20}$$

and

$$B_0 = B_1 + \frac{i_D}{i_D^*} B_2 . \tag{21}$$

Also in this case the influence of a change of the numerical value i_D can be easily observed without the necessity of repeating the optimization procedure for each numerical value of i_D.

8.3 SOME GEOMETRICAL PROPERTIES OF ION TRAJECTORIES

W. F. Gauster

8.3.1 Curvature of a Particle Orbit in Space

The trajectory of a charged particle (rest mass m_0, charge q), moving with the velocity $\bar{v}$ (velocity of light = c) through an electromagnetic field (electric field strength $\bar{E}$, magnetic flux density $\bar{B}$), is determined by Lorentz' equation:

$$\frac{d}{dt} \frac{m_0 \bar{v}}{[1 - (v^2/c^2)]^{1/2}} = q(\bar{E} + \bar{v} \times \bar{B}) . \tag{1}$$

The unit vectors in the directions of $\bar{v}$, of the principal normal, and the binormal of the trajectory are:

$$\bar{e}_v = \frac{\bar{v}}{v} , \qquad \bar{e}_\rho = \frac{\bar{\rho}}{\rho} , \qquad \bar{b} = \bar{e}_v \times \bar{e}_\rho , \tag{2}$$

where $\bar{\rho}$ is a vector point from the particle position P to the center of curvature Q of the trajectory (see Fig. 8.4). Frenet's first formula yields

$$\frac{d\bar{v}}{dt} = \bar{e}_v \frac{dv}{dt} + \bar{e}_\rho \frac{v^2}{\rho} . \tag{3}$$

UNCLASSIFIED
ORNL-LR-DWG 56974

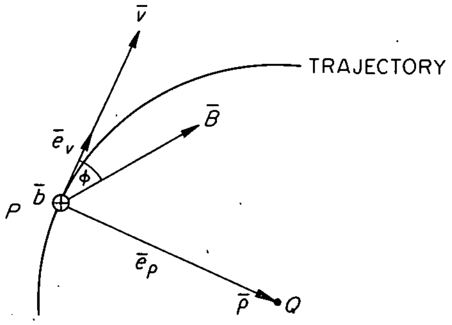

Fig. 8.4. Trajectory and Principal Unit Vectors $\bar{e}_v$, $\bar{e}_\rho$, and $\bar{b}$.

This equation applied to Eq. (1) leads to[8]

$$\frac{m_0}{[1-(v^2/c^2)]^{3/2}}\frac{dv}{dt}\bar{e}_v+\frac{m_0}{[1-(v^2/c^2)]^{1/2}}\frac{v^2}{\rho}\bar{e}_\rho=q(\bar{E}+\bar{v}\times\bar{B})\,. \tag{4}$$

The vector

$$\frac{q}{m_0}(\bar{E}+\bar{v}\times\bar{B})=\bar{w} \tag{5}$$

can be split into two perpendicular components:

$$\bar{w}=\bar{w}_v+\bar{w}_\rho\,, \tag{6}$$

where

$$\bar{w}_v=\left(\frac{\bar{w}\cdot\bar{v}}{v^2}\right)\bar{v}\,,$$

$$\bar{w}_\rho=\bar{w}-\left(\frac{\bar{w}\cdot\bar{v}}{v^2}\right)\bar{v}\,.$$

Then from Eq. (4)

$$\frac{1}{[1-(v^2/c^2)]^{1/2}}\frac{v^2}{\rho}\bar{e}_\rho=\bar{w}_\rho \tag{7}$$

or

$$\begin{aligned}\frac{1}{[1-(v^2/c^2)]^{1/2}}\frac{v^2}{\rho}&=|\bar{w}_\rho|=w_\rho\,,\\ \bar{e}_\rho&=\frac{\bar{w}_\rho}{w_\rho}.\end{aligned} \tag{8}$$

Finally

$$\bar{\rho}=\frac{v^2}{[1-(v^2/c^2)]^{1/2}}\frac{\bar{w}_\rho}{w_\rho{}^2}\,. \tag{9}$$

At this place it should be remembered that a curve in space is determined by the initial tangent and principal normal (or binormal) directions, and the two scalar functions curvature $1/\rho(s)$ and torsion $1/\tau(s)$. To know for any point of the space curve the curvature $1/\rho$ and the direction of the principal normal, that is, $\bar{\rho}$ as given by Eq. (9), is, of course, likewise sufficient to determine the orbit.

---

[8] Compare: W. Glaser, p 124 in *Encyclopedia of Physics*, vol 33, Springer, Berlin, 1956.

In a purely magnetic field

$$\bar{E} = 0\,,$$

$$\frac{dv}{dt} = 0\,;\quad v = \text{constant}\,, \tag{10}$$

$$\bar{\rho} = \frac{m_0 v^2}{q[1 - (v^2/c^2)]^{1/2}} \cdot \frac{\bar{v} \times \bar{B}}{(\bar{v} \times \bar{B})^2}\,.$$

In this special case, the introduction of the normalized quantities

$$\rho^\star = \frac{m_0 v^2}{q[1 - (v^2/c^2)]^{1/2}\,B_0}\,,$$

$$B^\star = B/B_0 \tag{11}$$

(B_0 arbitrary) yields

$$\rho = \frac{\rho^\star}{B^\star \sin\phi}\,. \tag{12}$$

Here ϕ denotes the angle between $\bar{v}$ and $\bar{B}$ (see Fig. 8.4).

8.3.2 Trajectory Code

The possibility to find the center of curvature for any point of a particle trajectory by means of Eq. (9) can be used to set up a special trajectory computer code which will be described in the following for a nonrelativistic particle movement in a stationary field for simplicity reasons.

Lorentz' equation (1) assumes now the form

$$\frac{d\bar{v}}{dt} = \frac{q}{m}(\bar{E} + \bar{v} \times \bar{B})\,. \tag{13}$$

Introducing cylindrical coordinates r, θ, z,

$$\bar{v} = \bar{e}_r \dot{r} + \bar{e}_\theta r\dot{\theta} + \bar{e}_z \dot{z}\,,$$

$$\frac{d\bar{v}}{dt} = \bar{e}_r(\ddot{r} - r\dot{\theta}^2) + \bar{e}_\theta(r\ddot{\theta} + 2\dot{r}\dot{\theta}) + \bar{e}_z \ddot{z}\,, \tag{14}$$

and therefore

$$\ddot{r} = r\dot{\theta}^2 + \frac{q}{m}(E_r + r\dot{\theta}B_z - \dot{z}B_\theta) = f_1(r, \theta, z, \dot{r}, \dot{\theta}, \dot{z})\,,$$

$$\ddot{\theta} = \frac{1}{r}\left[-2\dot{r}\ddot{\theta} + \frac{q}{m}(E_\theta + \dot{z}B_r - \dot{r}B_z)\right] = f_2(r, \theta, z, \dot{r}, \dot{\theta}, \dot{z})\,, \tag{15}$$

$$\ddot{z} = \frac{q}{m}(E_z + \dot{r}B_\theta - r\dot{\theta}B_r) = f_3(r, \theta, z, \dot{r}, \dot{\theta}, \dot{z})\,.$$

This system of second-order differential equations can be approximately solved by means of Runge-Kutta's method. Starting with known values r_k, θ_k, z_k and $\dot r_k$, $\dot\theta_k$, $\dot z_k$ for $\tau = \tau_k$, new values r_{k+1}, θ_{k+1}, z_{k+1}, for $\tau_{k+1} = \tau_k + \tau$ are calculated in a specific way.[9] This procedure involves besides other steps to evaluate the functions f_1, f_2, and f_3 [see Eq. (15)] for four different sets of values of r, θ, and z and $\dot r$, $\dot\theta$, $\dot z$. In this operation the greatest amount of calculation work goes in evaluating the field quantities $\bar{B}$ and $\bar{E}$ for the four different locations concerned. The special method by Nyström[10] reduces the necessary number of evaluations of the field quantities to three-quarters of those when the regular Runge-Kutta method is applied.[11]

The leading idea of the new code is not to use one fixed coordinate system only, but to introduce for each step from τ_k to τ_{k+1} a new auxiliary cylindrical coordinate system. Its origin Q_k is obtained by proceeding from the particle position P_k to the end point of the vector $\bar\rho_k$ [see Eq. (9)]. The z_k axis has the direction of the binormal $\bar b_k$ (see Fig. 8.5); the angle θ_k is measured from the zero direction $-\bar\rho_k$. In this coordinate system

$$\begin{aligned} r_k &= \rho_k & \qquad \dot r_k &= 0 \\ \theta_k &= 0 \qquad \text{and} & \dot\theta_k &= \frac{v_k}{\rho_k}\,. \qquad (16) \\ z_k &= 0 & \dot z_k &= 0 \end{aligned}$$

The movement from position k to $k + 1$ is in first approximation a circular movement and the Runge-Kutta procedure yields with some chosen τ a relatively very accurate result. It is expected that this advantage surpasses sensibly the computer work for the coordinate transformations. This computer code is being programmed at this time.

UNCLASSIFIED
ORNL-LR-DWG 56975

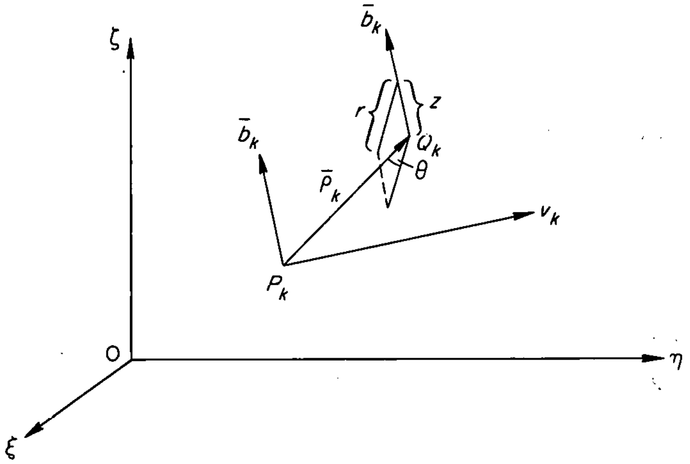

Fig. 8.5. Auxiliary Coordinate System r, θ, z. Any kind of stationary coordinate system can be used. Here a Cartesian coordinate system is shown.

8.3.3 Projection of a Trajectory on a Stationary Plane

Graphical methods use the projections of trajectories on a stationary plane A.[12] The radius of curvature of such a curve can be found in a very simple way for the case of the nonrelativistic

---

[9] See for instance: L. Collatz, *Numerische Behandlung von Differentialgleichungen*, Springer, Berlin, 1951.

[10] E. J. Nyström, *Acta Soc. Sci. Fennicae* 50(13), 1–15 (1925).

[11] The author thanks Walter Gautschi of the Mathematics Panel for advice and useful discussion in this matter.

[12] P. R. Bell *et al.*, this report, sec 2.2.4.

movement of a charged particle in a magnetic field with $\bar{E} = 0$. The Lorentz equation is now

$$\frac{d\bar{v}}{dt} = \frac{q}{m} (\bar{v} \times \bar{B}) \, . \tag{17}$$

The stationary plane A is supposed to be perpendicular to a unit vector $\bar{e}$. The subscripts $\perp$ and $\parallel$ refer to the direction of this unit vector.

The radius of curvature $\rho_\perp$ of the projection curve is in a simple relation to the line element $ds_\perp$ and the contingence angle $d\phi_\perp$ (see Fig. 8.6):

$$\rho_\perp \, d\phi_\perp = ds_\perp \tag{18}$$

or

$$\rho_\perp \frac{d\rho_\perp}{dt} = \frac{ds_\perp}{dt} = v_\perp$$

and

$$\frac{1}{\rho_\perp} = \frac{1}{v_\perp} \frac{d\phi_\perp}{dt} \, . \tag{19}$$

From Fig. 8.6 follows

$$d\phi_\perp = \frac{|\bar{v}_\perp \times (\bar{v}_\perp + dv_\perp)|}{|\bar{v}_\perp| \cdot |\bar{v}_\perp + dv_\perp|} \, . \tag{20}$$

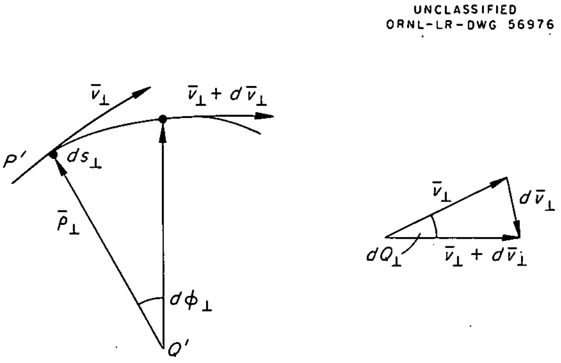

Fig. 8.6. Projection of a Trajectory on a Stationary Plane.

Therefore

$$\frac{d\phi_\perp}{dt} = \frac{|\bar{v}_\perp \times (d\bar{v}_\perp / dt)|}{v_\perp^2} \, . \tag{21}$$

For the projection of $\bar{v}$ on a stationary plane

$$\frac{d\bar{v}_\perp}{dt} = \left(\frac{d\bar{v}}{dt} \right)_\perp \, . \tag{22}$$

From (17), (19), and (21) follows

$$\frac{1}{\rho_\perp} = \frac{q}{m v_\perp^3} \, |\bar{v}_\perp \times (\bar{v} \times \bar{B})_\perp| \, . \tag{23}$$

This can be written in the form

$$\frac{1}{\rho_\perp} = -\frac{qB_\parallel}{m v_\perp} \left[1 - \frac{v_\parallel (\bar{v}_\perp \cdot \bar{B}_\perp)}{v_\perp^2 B_\parallel} \right] . \tag{24}$$

For $\bar{B}_{\perp} = 0$, $\bar{B}_{\parallel} = \bar{B}$, that is, magnetic flux density perpendicular to the plane A, the well-known relation

$$\frac{1}{\rho_{\perp}} = -\frac{qB}{mv_{\perp}} \tag{25}$$

results. The minus sign indicates negative sense of rotation for positively charged particles.

For a rotationally symmetrical magnetic field, a cylindrical coordinate system r, θ, z is used in the conventional way. For the projection of a trajectory on a plane perpendicular to the z axis,

$$\frac{1}{\rho_{\perp}} = -\left[\frac{qB_z}{m\sqrt{v_r^2 + v_\theta^2}}\right]\left[1 - \left(\frac{v_r v_z}{v_r^2 + v_\theta^2}\right)\left(\frac{B_r}{B_z}\right)\right] . \tag{26}$$

This expression is useful for discussing the accuracy of graphical methods for determining ion orbits.

8.3.4 Trajectory of the r-z Movement

In the case of a rotationally symmetrical magnetic field and $\bar{E} = 0$, the r-z motion is independent of the $\theta(\tau)$ motion[13] which is determined by

$$v_\theta = r\dot{\theta} = \frac{1}{m}\left(\frac{P_\theta}{r} - qA\right) , \qquad P_\theta = \text{constant} . \tag{27}$$

A trajectory of the r-z movement is of course not the projection of the actual trajectory (in space) on the r-z plane.

It is easy to find the radius of curvature ρ of the r-z movement trajectory. The starting point is the well-known formula

$$\frac{1}{\rho} = \frac{d^2z/dr^2}{[1 + (dz/dr)^2]^{3/2}} . \tag{28}$$

Introducing the derivatives with respect to time,

$$\frac{1}{\rho} = \frac{\dot{z}\ddot{r} - \ddot{z}\dot{r}}{(\dot{r}^2 + \dot{z}^2)^{3/2}} \tag{29}$$

is obtained. The velocity vector of the r-z movement is

$$\begin{gathered} \bar{u} = \bar{e}_z v_z + \bar{e}_r v_r , \\ u^2 = v^2 - v_\theta^2 . \end{gathered} \tag{30}$$

---

[13] M. Rankin and T. K. Fowler, *Thermonuclear Project Semiann. Rept. Jan. 31, 1959*, ORNL-2693, pp 18–21.

Its angle with the z axis is α (see Fig. 8.7). From Eqs. (14) and (15) follows

$$\begin{aligned}
\dot{r} &= v_r = u \sin \alpha \, , \\
\dot{\theta} &= \frac{v_\theta}{r} \, , \\
\dot{z} &= v_z = u \cos \alpha \, , \qquad (31) \\
\ddot{r} &= \frac{v_\theta^2}{r} + \frac{q}{m} v_\theta B_z \, , \\
\ddot{z} &= -\frac{q}{m} v_\theta B_r \, .
\end{aligned}$$

UNCLASSIFIED
ORNL-LR-DWG 56977

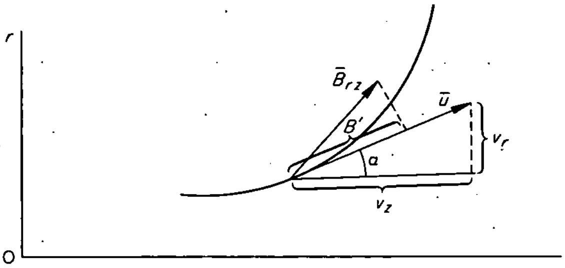

Fig. 8.7. Trajectory of the r-z Movement.

These values substituted in Eq. (29) yield

$$\frac{1}{\rho} = \frac{1}{u^2} \left[\frac{v_\theta^2}{r} \cos \alpha + \frac{q}{m} v_\theta \left(B_z \cos \alpha + B_r \sin \alpha \right) \right] . \qquad (32)$$

From Fig. 8.7 it follows that the projection of the vector

$$\bar{B}_{rz} = \bar{e}_z B_z + \bar{e}_r B_r \qquad (33)$$

on the direction of $\bar{u}$ is

$$B' = B_z \cos \alpha + B_r \sin \alpha \, . \qquad (34)$$

Therefore

$$\frac{1}{\rho} = \frac{v_\theta^2}{v^2 - v_\theta^2} \left(\frac{\cos \alpha}{r} + \frac{qB'}{mv_\theta} \right) . \qquad (35)$$

An auxiliary quantity ρ' is introduced by

$$\rho' = -\frac{mv_\theta}{qB'} \, , \qquad (36)$$

which applies to a circular movement around the z axis. Then Eq. (35) can be written as

$$\frac{1}{\rho} = -\frac{v_\theta^2}{v^2 - v_\theta^2} \left(\frac{1}{\rho'} - \frac{\cos \alpha}{r} \right) . \qquad (37)$$

This relation allows a simple graphical determination of the r-z movement trajectory. It must be noted, however, that graphical methods directly connected with the actual movement in space should give in general better results. This follows from the fact that a spatial trajectory with little change in curvature corresponds to an r-z movement with rapidly changing ρ if the trajectory passes near the z axis.

8.4 FORCE CALCULATIONS FOR AXIALLY SYMMETRICAL COIL SYSTEMS

P. A. Thompson

The first step toward the ultimate determination of the total effects of electromagnetic forces in such large machines as DCX-2 is the calculation of the mutual forces between pairs of coils. If the actual field produced by one coil at the center of gravity of the cross section[14] of another coil is known (from computer results, for instance), an approximation of this mutual axial force can be derived from $dF_z = IB_r\,dl$. If the B_r produced by the first coil is expressed in gauss, the radius of the second coil replacement loop in inches, and the current in ampere-turns, the force in tons is given by

$$F_z = 1.7956 \times 10^{-9}\,(NI)_2 a_2\, B_r(z, a_2)\,.$$

On the other hand, if this field is not known, it also can be approximated by a single loop effect. Calling B_r^* the r component of the field normalized to B_0 (the field at the center of a single loop), the expression in tons for the force is

$$F_z = 4.44 \times 10^{-10}\,(NI)_1\,(NI)_2\,\frac{a_2}{a_1}\,B_r^*\left(\frac{z}{a_1}, \frac{a_2}{a_1}\right),$$

where z = axial separation of the replacement loops. The B_r^* values are usually obtained from a special 6 × 4 ft graph made by the Engineering Science Group; or, if slightly more accuracy is desired, the tables prepared by Nancy Alexander of the Mathematics Panel may be employed.

It would be assumed that replacement of coil cross section with several loops instead of just one would yield more accurate results – especially if a large number of loops (approaching the number of actual windings in the coil) were used. It has been previously noted that a single loop replacement in some cases gave results about 20% too high[15] and could, therefore, be used if conservative results with attendant simplicity of calculation are desired. Comparison of one and two loop per coil replacement for a pair of like coils with tall, narrow cross section reveals that, if the separation is about the same as the inside radius, two loops give forces almost 40% *lower* than one loop. If the coil separation is then increased by a factor of 10, the two-loop method yields results 7% *higher* than the one-loop method. In the calculations for DCX-2 the forces for two adjacent inboard booster coils (Nos. 1 and 2) were made (*a*) replacing each coil by a single loop, (*b*) replacing each coil by two loops, and (*c*) replacing one coil by 12 loops and using computer data for the field produced by the other coil. Assuming (*c*) to give the most nearly correct results, (*a*) leads to a figure about 7% too high (conservative), while (*b*) gives a force 8% too low. The oscillatory nature of the force as a function of number of loops used to represent the cross section indicated that further study should be made of this type of approximation, using as parameters shape and relative size

---

[14] For a discussion of the slightly better approximation resulting from the application of Lyle's theorem, see W. F. Gauster, H. Mott, and C. E. Parker, *Thermonuclear Project Semiann. Progr. Rept. July 31, 1960*, ORNL-3011, p 88.

[15] J. N. Luton, Jr., *Long Solenoid Technical Memo No. 1*, p 7 (July 7, 1960).

and separation. An Oracle code using an existing elliptical integral field code[16] is now being prepared for this study.

To a very good approximation the sum of the forces on the individual replacement loops in either of a pair of coils may be thought of as the total mutual electromagnetic force. The distribution of this total force along the radial dimension of the coil, however, is not constant. In such an extreme case as that of the tall, thin dip coil and the adjacent large, low mirror coil in DCX-2 this distribution of force can be a major factor in mechanical design (see Fig. 8.8). In the more typical case represented by the inboard boosters the variation is noticeable only for small values of normalized Z (Fig. 8.9), and in almost all cases of coils in lumped-solenoid arrangement the center of force is near the cross-section center.

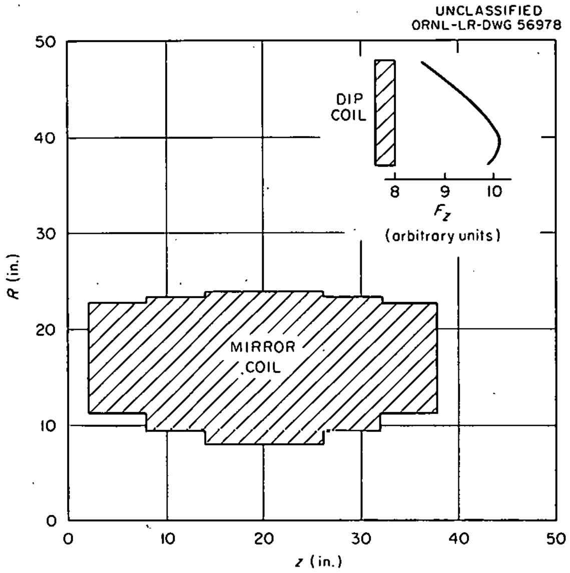

Fig. 8.8. Contour of Axial Force Along Radial Dimension of Dip Coil in DCX-2.

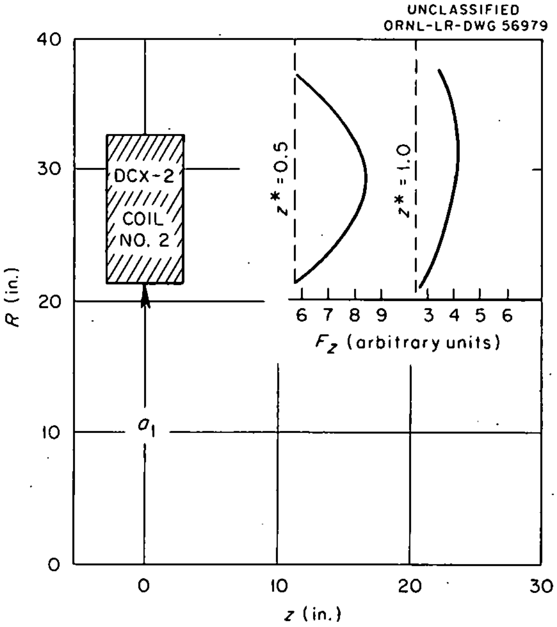

Fig. 8.9. Radial Contours of Axial Forces for Coil Elements Along Typical Z^* Planes Where $Z^* = Z/a_1$.

Assuming now that a sufficiently accurate method has been used to calculate the mutual electromagnetic forces between all coil pairs in a system for a given mode of operation, the total resultant electromagnetic force on each coil of the system must next be obtained. This, of course, is simply the sum of the mutual pair forces on one side of the coil in question minus the sum of those on the other side. Table 8.1 gives the total electromagnetic forces on each coil of one-half of DCX-2 (the system being symmetrical about the midplane) for a central field of 17 kilogauss and dip coil current reversed.

---

[16] M. Rankin, *Thermonuclear Project Semiann. Rept. Jan. 31, 1959*, ORNL-2693, p 11.

Table 8.1. **Total Electromagnetic Force on Each Coil**

(DCX-2 geometry as of Oct. 12, 1960)

(+ forces toward midplane; – forces outward)

Coil	Force (tons)	Coil	Force (tons)
F_{outboard}	+97.5	$F_{\text{inboard No. 3}}$	+73.9
F_{mirror}	–10.8	$F_{\text{inboard No. 2}}$	–8.4
F_{dip}	+0.3	$F_{\text{inboard No. 1}}$	–3.1

For the purposes of design engineering one now calculates the necessary reaction forces which must be supplied by mechanical members to keep the coils from moving. The simplest scheme here is to begin at one end of the system and observe that an additional force equal to the total electromagnetic force on the end coil must be supplied by the first mechanical member (between it and the second coil). This member in turn will exert an equal and opposite force on the second coil which, together with the electromagnetic force on this coil, must be counteracted by the next mechanical member, etc. Typical reaction forces (all compressional) to be withstood by mechanical members in DCX-2 for the case listed in Table 8.1 are 98 tons between mirror and outboard booster, 63 tons between the two innermost inboard boosters, $\frac{1}{3}$ ton between dip coil and adjacent inboard booster, etc.

In order to include enough safety factor in the mechanical design, recalculations should next be made for possible fault conditions, such as mirror and outboard booster at one end of the machine not being energized. In this case the force between the dip coil and adjacent inboard booster instead of being $\frac{1}{3}$ ton is 85 tons at the end away from the de-energized coils, and between the like pair at the other end of the machine there is an expansion force of some 12 tons.

All the above considerations have been for axial forces, only since calculations show that radial forces are of relatively small importance in DCX-2.[17] This is in contrast to some dc coil systems, especially to certain pulsed coils, where the tendency to explode radially is of primary concern.

A final element in force calculations for DCX-2 should be mentioned: The injection "snout" will contain a relatively large amount of ferromagnetic material in the form of a Hyperco beam shield. It is extremely difficult to determine analytically the force to be experienced by this material due to the magnetic field of the machine. Scale model tests have therefore been scheduled for the near future.

---

[17] R. N. Lyon and W. F. Gauster, *DCX-2 Technical Memo No. 42* (Jan. 31, 1961).

8.5 APPLICATIONS OF A FIELD ANALOG FOR AXIALLY SYMMETRICAL COIL SYSTEMS

P. A. Thompson

The resistance network analog device for representing axially symmetrical magnetic fields used so extensively at Project Matterhorn has been widely reported in the literature.[18–20] Previous semiannual reports of the Thermonuclear Division have mentioned the analog machine adapted from Wakefield's ideas and built by the Engineering Science Group.[21,22] The basic soundness of the design of the present device has recently been reconfirmed by comparisons with computer data for single loops. However, an attempted use of the "board" for studying possible cusp-geometry fields led to a substantial change in its operation and suggested a novel "display" function for the apparatus.

In order to produce a cusp field it is necessary to use coils which buck each other, that is, the currents flow in opposite directions. Wakefield recommends feeding the coil representations on the analog board with alternating current 180° out of phase;[23] the direction of the magnetic field is then determined by associating the detected board voltage with the feed of the appropriate coil. In actual use the phase of the detected signal was completely ambiguous, varying continuously over the whole 180°. Although this difficulty has apparently not been reported previously, the problem is not surprising, since the large size (5 × 5 ft) of the device naturally leads to appreciable capacitive reactance. In order to overcome the reactance effects of ac, the use of dc with its attendant problem of contact potential was attempted. By comparing ac and dc feeds for such simple configurations as single loops it was discovered that dc field intensity values (computed from readings of ∇V on the board) were rather unpromising. However, equipotential lines, although not of the same value, were almost identical in shape for both ac and dc. It was therefore decided to abandon attempts at calculating actual B values and to concentrate instead on the more qualitative indications of field line plots (represented by the board's equipotentials). By the use of a Moseley X-Y recorder with point plotter attachment it is possible to make field plots rather quickly. Changes in current ratio and coil shape, placement, and relative size for the cusp field arrangement were represented on the analog board with ease and some speed.

Here then was a logical use for the analog board: obtaining quick approximations of field line shapes, rather than actual field intensity values. (The latter can easily be calculated by a computer as soon as the coil arrangement is determined. It would, however, be very tedious and in

---

[18] K. E. Wakefield, *A Resistance Analogue Device for Studying Axially Symmetric Magnetic Fields*, PM-S-23, NYO-7313, Project Matterhorn (revised Nov. 28, 1958).

[19] U. Christensen, *Resistance Values of Axially Symmetric Analog Boards*, Tech. Memo No. 71, Project Matterhorn (Apr. 3, 1959).

[20] K. E. Wakefield, "The Use of Analog Computers in the Design of Magnetic Field Systems," p 61 in *Proceedings of Symposium on Magnetic Field Design in Thermonuclear Research, Gatlinburg, Tenn., Dec. 11–12, 1958*, ORNL-2745 (Oct. 7, 1959).

[21] W. F. Gauster, *Thermonuclear Project Semiann. Rept. Jan. 31, 1959*, ORNL-2693, p 104.

[22] W. F. Gauster, *Thermonuclear Project Semiann. Rept. July 31, 1959*, ORNL-2802, pp 105,134.

[23] K. E. Wakefield, *A Resistance Analogue Device for Studying Axially Symmetric Magnetic Fields*, PM-S-23, Project Matterhorn, p 8 (Dec. 13, 1956).

complicated cases hopeless to try to find appropriate coil arrangements by means of computer calculations.) Pursuing this line of reasoning, it was obvious that even more speed and flexibility would be desirable. To plot only a few field lines from board readings with the X-Y recorder takes about an hour; to be really useful in this mode of operation the board should be able to show the effects of parameter changes almost instantaneously. For this purpose a constant display system for the analog has been designed and it is now being built.

In essence the system consists of a method of sampling in turn the potential of each of the board's junction points by means of a 30-rps mercury-jet switch (which sweeps up in the r direction) and a high-speed multibank stepping switch (which indexes the sweep in the z direction) and of an arrangement for displaying the position of the preset potential in each vertical column on a large-screen long-persistence kinescope tube, which has a vertical sweep synchronized with the mercury-jet switch. In actual operation several equipotential lines (representing magnetic field lines) will be displayed simultaneously as a series of dots, and the entire board will be sampled at a rate better than once every 2 sec.

While the rather complex switching elements have been in construction, the board has been used with further refinements to find the necessary current ratios for the coils in the DCX-EP-B design to produce a linear field gradient. A typical "linear" field line was chosen, and where this line passed through network junction points (there were four), connections were made with a switching arrangement to a digital voltmeter. Points between these connections were checked by an interpolation potentiometer. The scaled current to each coil representation on the board was monitored by an appropriate milliammeter, which was marked to indicate the maximum current density the coil could handle. The solutions obtained in this manner were checked on a computer, the results being given elsewhere in this report.[24]

8.6 DESIGN OF AN ION INJECTION SNOUT

R. L. Brown

As reported in the last report,[25] DCX-2 and DCX-EP-B require compact ion injection snouts which are field-free on the inside and do not disturb the external field.

A model compensating coil using copper sheets as current-carrying conductors was constructed and tested. Magnetic field measurements made in a Beta tank indicate that the concept of snout injection is sound. However, the inability of the Beta tank to simulate the exacting demands of DCX-2 and DCX-EP-B rendered the results of the test inconclusive. Therefore a new test will be made in which the snout will be placed in the field of the outboard coils for DCX-2. The DCX-2 coils will produce a strong (12 kilogauss), very uniform, and well-regulated field. A new snout coil design is being constructed using hollow copper conductors. The conductors are initially round tubes; they are then flattened and bent in the peculiar shapes as required for a special cosine coil. Figure 8.10

---

[24] D. L. Coffey and J. E. Simpkins, this report, sec 8.1.

[25] *Thermonuclear Project Semiann. Progr. Rept. July 31, 1960*, ORNL-3011, pp 24, 93.

shows two coil turns and Fig. 8.11 is a pictorial view of the snout model. High current density necessitates that each turn of the coil be individually cooled. Table 8.2 shows the anticipated coil specifications using the flattened copper conductors.

UNCLASSIFIED
PHOTO 35608

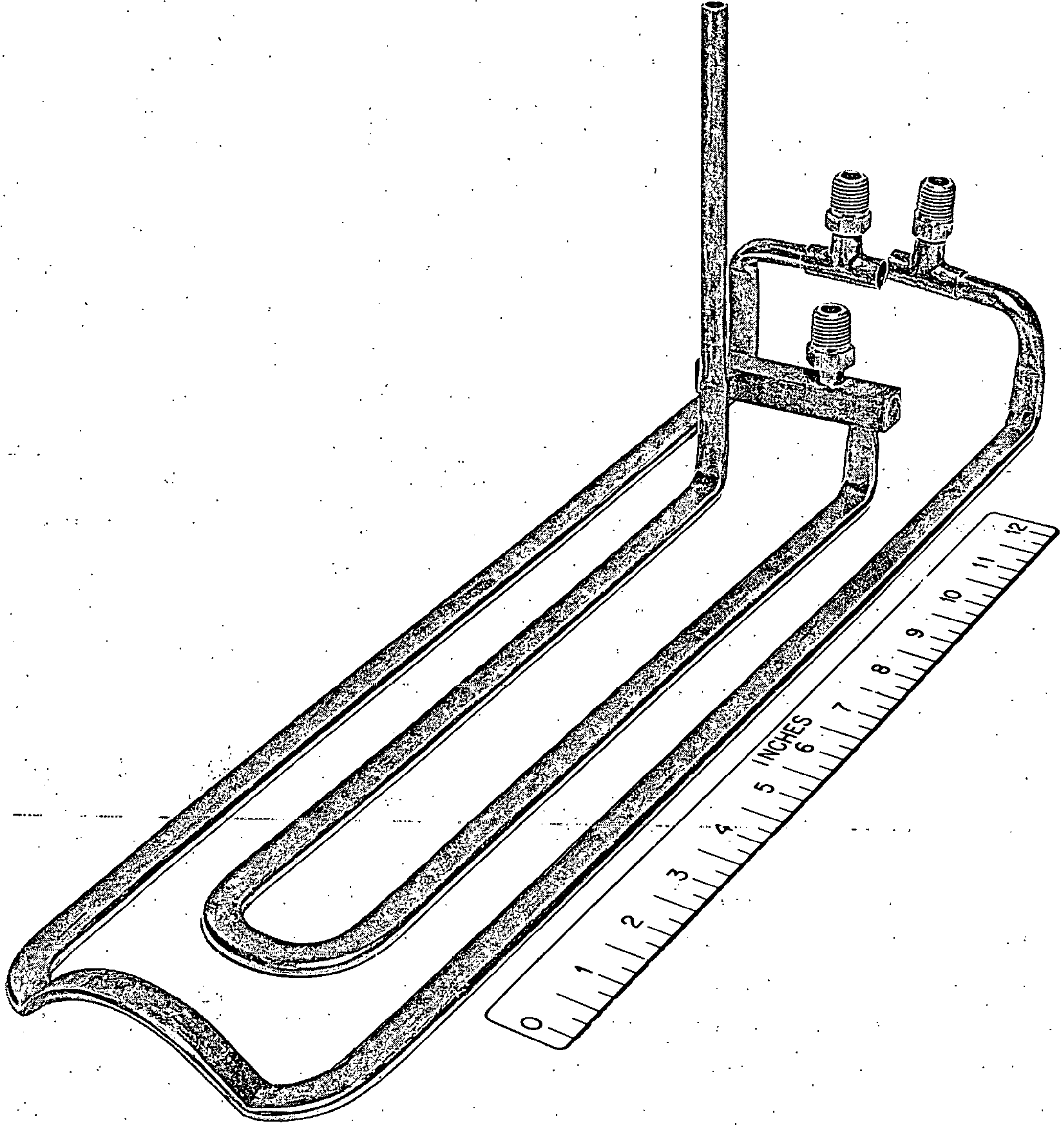

Fig. 8.10. Two Turns of Snout Model Coil.

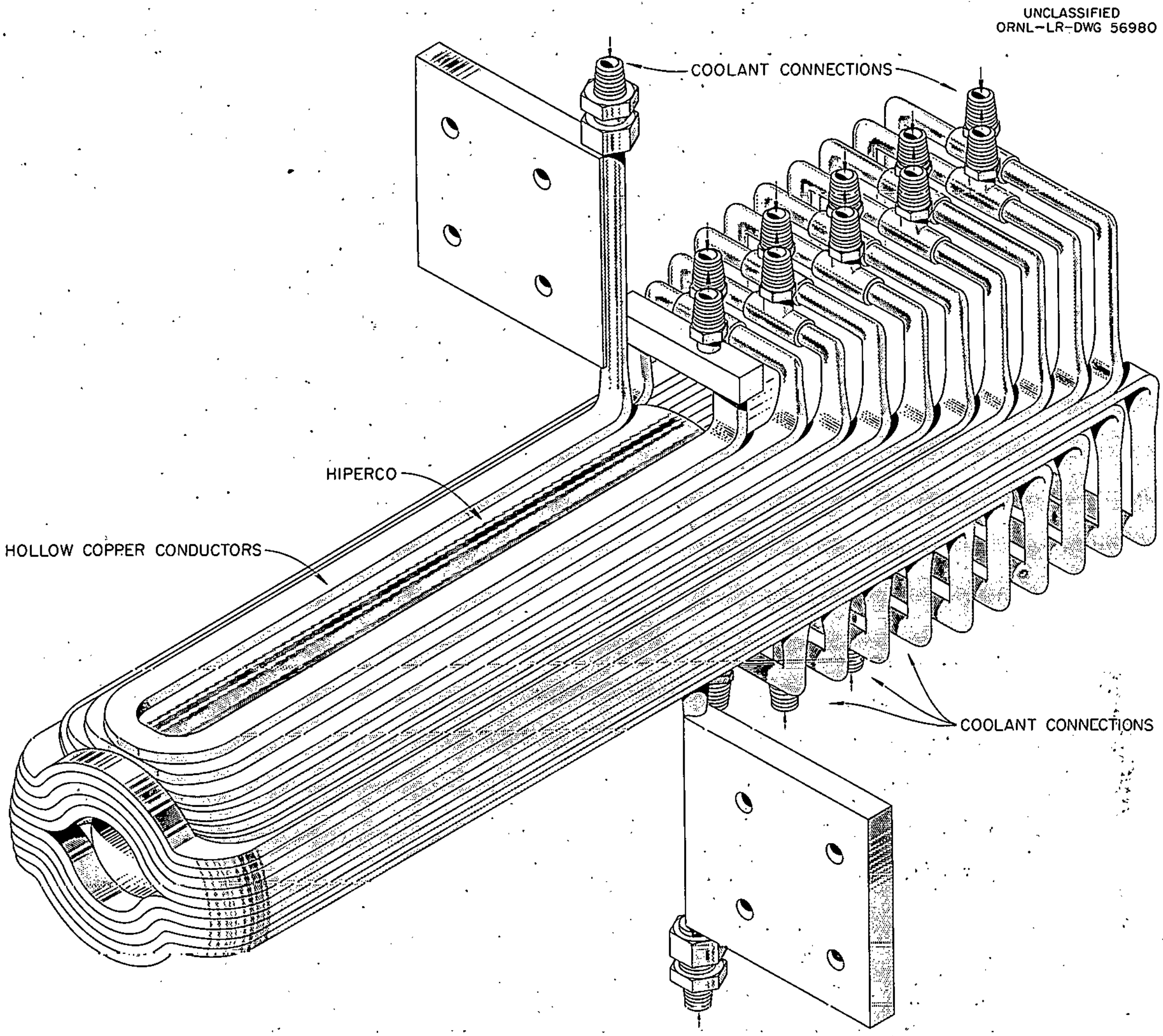

Fig. 8.11. Ion Injection Snout Model.

Table 8.2. Snout Coil Specifications

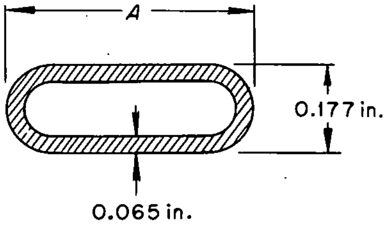

CONDUCTOR CROSS SECTION

	Model	DCX-2 and DCX-EP-B	
		Case I	Case II
OD of conductor before flattening, in.	3/8	3/8	1/2
Dimension *A*, in.	0.485	0.485	0.683
Total conductor length, ft	78	158	158
Number of turns	22	22	22
Conductor resistance, microhms/ft	150	150	115
Total resistance, ohms	0.012	0.024	0.018
Current, amp	6000	6000	6000
Current density, amp/in.^{2}	95,200	95,200	68,200
Potential, v	72	145	110
Power, kw	430	870	655
Ambient water temperature, °C	30	30	30
Water flow, gpm	55	110	85

9. CROSS-SECTION MEASUREMENTS

9.1 DEVELOPMENT OF CROSSED-BEAM APPARATUS

D. P. Hamblen L. A. Massengill Herman Postma

Apparatus is being developed for the purpose of measuring the dissociation cross section for H_2^+ in collision with other ion species – electrons[1] and protons.

In order to measure the dissociation of H_2^+ in collision with electrons, a 20-kev H_2^+ beam of 0.2 ma/cm^2 current density is crossed at right angles with a 13.4-ev electron beam of current density 3 ma/cm^2 in a region where the background-gas pressure is 1×10^{-6} mm Hg. The electron beam is modulated at 50 cps to distinguish the effect of the target electrons from the background gases. Ivash[2] has calculated the dissociation cross section, and this permits an estimate of the expected currents. For the choice of present energies and intensities, a cross section of 10^{-16} cm^2 gives a modulated current of 10^{-12} amp of H^+ arising from electron dissociation of H_2^+ and a dc current of 10^{-8} amp of H^+ arising from breakup on the background gas. Amplification of the 50-cps signal by a narrow-band amplifier[3] and rejection of the dc background permits distinguishing the signal from the background noise. The amplifier has an intrinsic noise of 2×10^{-13} amp for this frequency. However, several rather elusive difficulties had to be resolved in order to realize the application of this amplifier to this purpose. First, a 50% 120-cps current modulation of the H_2^+ beam caused the background signal to be modulated at 120 cps. This periodic variation resulted in the amplifier exceeding its dynamic range and blocked further reception of the desired 50-cps signal due to the electron beam. By suitable filtering and regulation of the high-voltage accelerating supply and the rf ion source supplies, this was reduced to a more tolerable level of ¼%. Second, the reduction of the 120-cycle ripple brought evidence of other longer-term (1-sec) random variations of beam current of 2% which made detection difficult because of the violent jumping of the base signal. While a complete cure of this difficulty has not been effected, reduction to 0.5% has been made. The order of difficulty in curing voltage fluctuations is appreciated by realizing that in our configuration a 1-v variation in 20 kv changes the beam current by 1%.

Armed with some experience of the difficulties of crossed-beam techniques, it has become possible to examine one of the tenets of DCX-2 – the dissociation cross section of H_2^+ in collision with H^+. Apparatus has been built and tested which will permit measurement of this cross section. Using the duoplasmatron source and power supplies from DCX-1 and other equipment loaned by the ion source group, a beam of 20 ma of H^+ of 50 kev energy has been obtained within a spot size of ½-in. diameter. Adapter plates permit the installation of this apparatus on one end of DCX-1 where the axial magnetic field confines the proton beam to movement along the axis. In the midplane, the 600-kev 10-ma H_2^+ beam will cross the protons at right angles, and suitably placed ion

---

[1] D. P. Hamblen *et al.*, *Thermonuclear Project Semiann. Progr. Rept. July 31, 1960*, ORNL-3011, p 105.

[2] E. V. Ivash, *Phys. Rev.* 112, 155 (1958).

[3] F. T. May and R. A. Dandl, "An Active Filter Element and Its Application to a Fourier Comb," to be published in *Rev. Sci. Instr.*

collectors will permit detection of the dissociated products. For an estimated cross section of 10^{-16} cm^2, the anticipated currents will be (for 10 ma of H_2^+ and 10 ma of H^+) 10^{-8} amp for background and 10^{-10} amp from the modulated proton beam.

Apparatus is being tested to measure the dissociation of H_2^+ by intense electric fields.[4]

Installation of a 600-kv power supply for acceleration of ions to permit a continuation of the program of high-energy cross-section measurements is nearing completion.

---

[4] J. R. Hiskes, *Dissociation of Molecular Ions by Electric Fields*, UCRL-9182 (1960).

10. VACUUM SYSTEMS AND TECHNIQUES

C. E. Normand   R. V. Neidigh   R. A. Strehlow[2]
F. A. Knox   R. E. Clausing[1]   J. D. Redman[2]

10.1 INTRODUCTION

Vapor-deposited metal film pumping studies have continued to be of greatest concern to the vacuum systems staff. The evaluating of other vacuum system components has proceeded with studies of ionization gage calibrations, so-called "nude" ion gages, a variety of instruments applicable to the 0.2 to 100 μ pressure range, and isotherms in diffusion-pump jet streams.

10.2 EVAPORATIVE PUMPING

10.2.1 Large-Scale Pump Test

Previously there was reported[3] a large-scale pump test. This system uses a large (30,000 cm^2) surface covered with a vapor-deposited titanium film as the primary pump, with a 6-in. diffusion-pump system as an essential auxiliary. A detailed description of the apparatus was given and the method of operation described. Data which described the pumping characteristics of the system for hydrogen during both continuous and batch evaporation of the titanium were also presented. This apparatus and similar operating procedures have now been used to investigate the ability of such films to adsorb other gases.

Figure 10.1 presents the results of these additional experiments. The parameter S plotted as the ordinate is defined as the gas leak rate into the system in liter-atmospheres per second divided by the system pressure in atmospheres. For this system the value of S can be referred to as the speed of the system (uncorrected for base-pressure effects) for values of S below approximately 150,000 liters/sec for H_2 and perhaps 50,000 or 30,000 liters/sec for gases of mass 28 or 44, respectively. Values as high as 120,000 liters/sec for mass 28 and 90,000 liters/sec for mass 44 are probably not seriously in error, but values greater than these have meaning only as a qualitative measure of rates of adsorption onto the titanium film.

Helium, argon, and methane are very poorly pumped by the film, if at all. Indeed, the measured speeds are what would be obtained with the 6-in. diffusion-pump system alone.

The curve for hydrogen is the same as that appearing in the previous report[4] except that no base pressure correction has been applied to the data. Speeds as high as 140,000 liters/sec for hydrogen at a pressure of 10^{-6} mm Hg have been attained during runs with high evaporation rates after large amounts of titanium had been evaporated.

The curve for oxygen is similar to that for hydrogen. Argon as an impurity in the oxygen used in these experiments would have the effect of reducing the S values somewhat and might

---

[1] Metallurgy Division.

[2] Reactor Chemistry Division.

[3] C. E. Normand *et al.*, *Thermonuclear Project Semiann. Progr. Rept. July 31, 1960*, ORNL-3011, p 118.

[4] *Ibid.*, p 121.

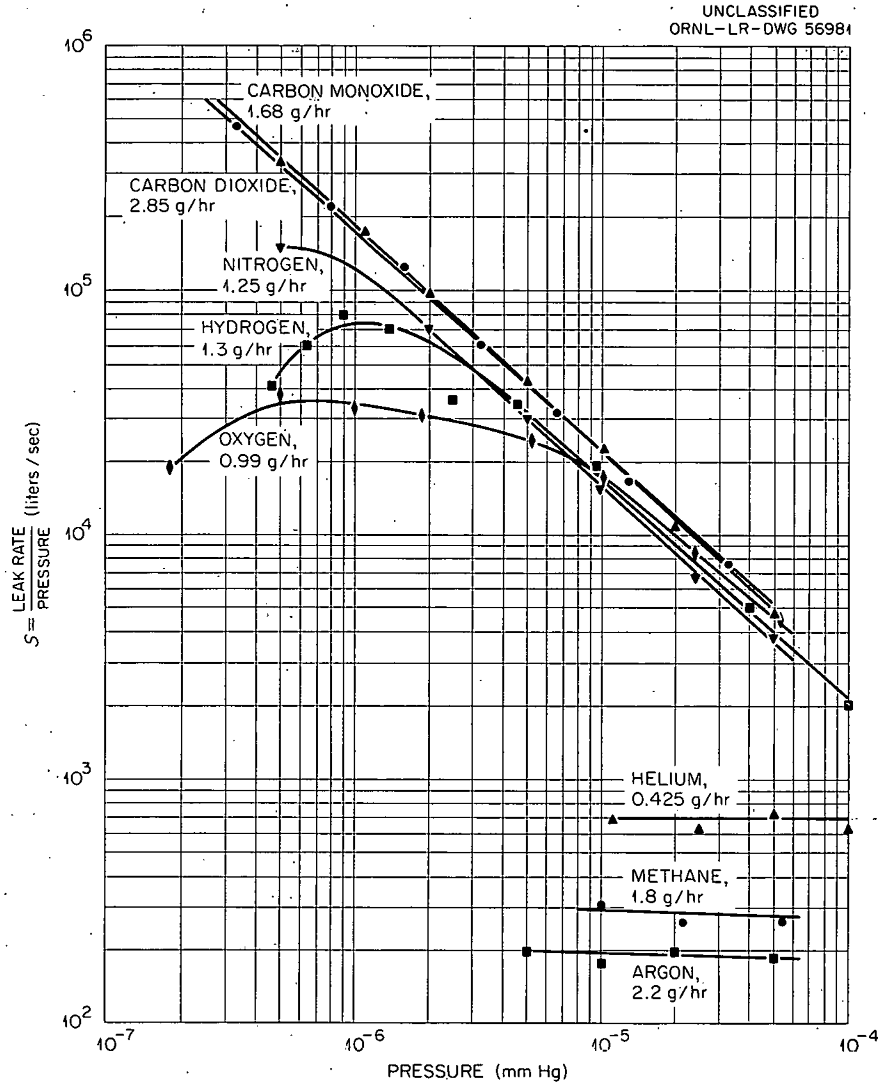

Fig. 10.1. Pumping Characteristics of the Large-Scale Pump Test for Hydrogen During Continuous and Batch Evaporation of Titanium.

alter the shape of the curve. Relatively high speeds were obtained, however, and ratios of titanium atoms per oxygen molecule between 2 and 6 were obtained during continuous evaporation. Subsequent to a batch evaporation of 5.36 g of titanium, the oxygen adsorption proceeded at about 20,000 liters/sec and slowly fell to 15,000 liters/sec after 50 atmospheric cm^3 of oxygen had been adsorbed ($Ti/O_2 \approx 50$) at pressures between 2 and 8×10^{-7} mm Hg.[5] Speed continued to fall as more oxygen was admitted, until, after 240 cm^3 of O_2 was admitted ($Ti/O_2 \approx 7$), the speed was 750 liters/sec and the pressure was 1×10^{-4} mm Hg. By comparison with previous experiments with hydrogen, very little titanium was available to the oxygen. Moreover, after the determination

---

[5] A 1% argon impurity could account for this entire pressure.

with oxygen, a measured hydrogen speed of only 1100 liters/sec was obtained, indicating that the remaining titanium was reactive to neither the oxygen nor the hydrogen.

Nitrogen, carbon monoxide, and carbon dioxide all behaved much alike. All had adsorption rates which were nearly independent of pressure and were governed primarily by the titanium evaporation rate. All had titanium-atom-to-gas-molecule ratios between 1 and 2 throughout the pressure range investigated. All had high sticking factors, probably above 0.3, and, for some unknown and perhaps fortuitous reason, the curves are essentially straight lines even at low pressures where S must be strongly influenced by the geometric configuration of the system.

Adsorption of nitrogen, carbon monoxide, and carbon dioxide on films produced by batch evaporation was similar to that reported above for oxygen. The initial adsorption rates were high but fell rapidly. Only a small percentage of the titanium in the film was available to the gas, and the adsorption of relatively small amounts of these gases on the evaporated film reduced its subsequent hydrogen adsorption rate markedly. Summarizing, oxygen, nitrogen, carbon monoxide, and carbon dioxide are readily pumped by the titanium film during continuous evaporations, while argon, helium, and methane are pumped to effectively no extent.

10.2.2 Beam-Tube Facility

A facility has been assembled for determining the effectiveness and limitations of evaporated titanium in providing the differential pumping needed between the accelerator tube (at relatively high pressure) and the plasma-containing region (at much lower pressure) of a DCX-like device.

The facility, shown in Fig. 10.2, consists of two chambers, 10 and 12 in. in diameter by 20 in. long, connected by a prototype beam tube. Chamber 1, corresponding to the accelerator tube, is equipped with liquid-nitrogen trap, ionization gage, and gas-inlet line. Chamber 2, corresponding to the plasma volume, also has an oil diffusion pump with baffle and valve. The beam tube consists of three identical "cells," each 6 in. in diameter, 8 in. long, and closed at both ends by thin metal diaphragms having central, circular apertures of 10 cm^2 area. Each cell has a side

UNCLASSIFIED
ORNL-LR-DWG 56982

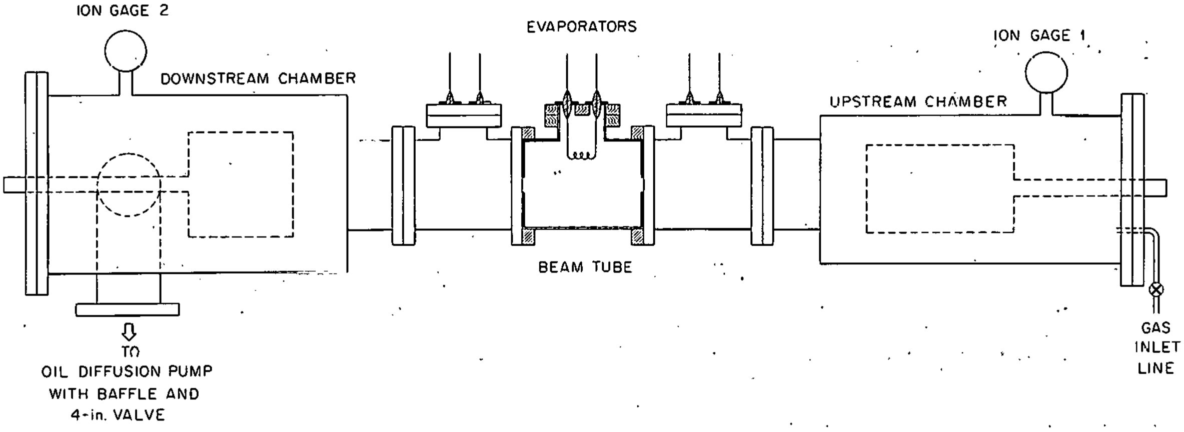

Fig. 10.2. Beam-Tube Test Facility.

port through which a titanium evaporator may be installed, and water cooling coils soldered to the cell wall.

The evaporators consist of open spirals wound from about 16 in. of 0.045-in. titanium-tantalum alloy wire (80% Ti–20% Ta). The three evaporators were operated in series from a Powerstat. Titanium evaporation was found to begin at a heating current of about 17 amp, and the filaments softened to the point of sagging under their own weight at 20 amp or less. Thus, the practical operating range for these evaporators was quite narrow. The filaments were generally operated at about 18 amp. Average filament life was about 24 hr, and the average rate of evaporation, as determined from weight loss, was approximately 18 mg/hr per filament.

The effectiveness of a differentially pumped system of the type here investigated can be expressed in many ways. It does appear, however, that the most pertinent question that can be asked about such a system is this: What fraction of the gas that enters the tube at its upstream end emerges from its downstream end? An answer to this question is a direct measure of the tube's effectiveness in doing what it was designed to do. Once such an answer has been found, however, a second and almost equally important question arises. This is: Under what conditions and within what limitations is this performance realized? The facility and the experiments carried out in it were designed to give answers to these two questions.

Preliminary Measurements. – Prior to the evaporation of any titanium in the assembled system, it was evacuated by the diffusion pump to its base pressure, and the characteristics of the system were measured. The characteristics are listed below:

Base pressure, no liquid nitrogen
    Chamber 1 (upstream): $p_1 = 2.0 \times 10^{-6}$ torr
    Chamber 2 (downstream): $p_2 = 7.5 \times 10^{-7}$ torr

Average pumping speed for H_2, $Q = 0.3$ to $11.0\ \mu$/sec
    From chamber 1: $S_1 = 60$ liters/sec
    From chamber 2: $S_2 = 250$ liters/sec

Effective conductance for H_2
    Chamber 1 to chamber 2: $C = 79$ liters/sec

Note: Throughout this work the factor 2.15 has been used to convert ion-gage readings to equivalent H_2 pressure.

After these constants of the system had been determined, the evaporators were outgassed by heating at a series of increasing filament currents. The onset of titanium evaporation was clearly indicated by the system pressure dropping well below the initial base values. With evaporation continued, at a presumably constant rate, pressures continued to drop in an exponential-like manner for several hours. The time required to attain a new pressure equilibrium is determined in part by system conductances, but much more, in our system, by the rate of titanium evaporation.

If evaporation is continued until pressures become essentially constant in the system, and H_2 is then introduced at some constant rate into chamber 1, resulting pressure rises are observed in both chambers 1 and 2.

If Q_1 is the measured rate at which H_2 is introduced, Δp_1 is the observed pressure rise in chamber 1, and Δp_2 the pressure rise in chamber 2, it follows that:

(*a*) $Q_1/p_1 = S_1$, the speed of pumping from chamber 1;

(*b*) $S_2 \times \Delta p_2 = Q_2$, the rate at which H_2 enters chamber 2; and

(*c*) Q_2/Q_1 is the desired beam tube "transmission factor" for H_2.

Under conditions that can be reproduced, the speed of pumping from chamber 1 is found to be 300 to 320 liters/sec (compare with 60 liters/sec before titanium evaporation); also, the tube transmission factor is 0.002 to 0.003; that is, only 0.2 to 0.3% of the H_2 entering the beam tube finds its way into chamber 2.

In order to attain and maintain this level of performance, two conditions must be satisfied.

1. Cell surfaces must be adequately coated with freshly evaporated titanium prior to the introduction of H_2 into the system. Unless this is the case, the pumping speed from chamber 1 will be lower, and the tube transmission factor will be higher than indicated above.

What constitutes adequate coating can be roughly estimated on the following basis: The rate of titanium evaporation from one of our filaments is about 18 mg/hr, and the coated surface area of a cell is about 1350 cm^2. Some 3 hr of evaporation is required to give near optimum performance. This gives an average coating density of some 5×10^{17} atoms/cm^2, which is equivalent to only a few atomic layers.

2. The second condition has to do with the ability of the system to maintain a high level of performance. For a given rate of titanium evaporation, there is an upper limit to the quantity of H_2 that can be pumped per second without having performance deteriorate with time.

Again, a very crude estimate can be made of the relation of the critical H_2 throughput to the rate of titanium evaporation. Taking the evaporation rate to be 18 mg/hr per filament (54 mg/hr for three filaments), one obtains 2×10^{17} as the number of titanium atoms emitted per second. In our measurements, the critical H_2 throughput appeared to be (very roughly) 2.5 liter-microns/sec, which is equivalent to 0.8×10^{17} H_2 molecules/sec. No significance is attached to these numbers beyond the fact that they are of the same order of magnitude.

Present plans call for an evaluation of the tube's performance with heavy-duty evaporators. With these larger evaporators one expects longer filament life and a higher rate of titanium evaporation. Higher evaporation rate should reduce the period of prepumping evaporation and increase the gas-handling capacity of the system. It does not appear likely, however, that the transmission factor of the three-cell tube will be significantly reduced.

A bakable beam-tube prototype (Fig. 10.3), constructed with five cells each of 6-in. diameter and 4-in. height, with 20.3-cm^2 apertures, has also been tested by using a filament arranged axially through the apertures as a titanium source. The filament was constructed of stranded tantalum and titanium wires kept under tension by a weight. The evaporation was continued until filament failure occurred. The pressure in an upper chamber (4 × 8 × 10 in.) at the top of the beam tube was monitored by an ion gage (gage 1). This chamber, which had one opening to the larger vacuum region through the beam tube, was at the lower pressure during the test. The assembly was placed in a

UNCLASSIFIED
ORNL-LR-DWG 56983

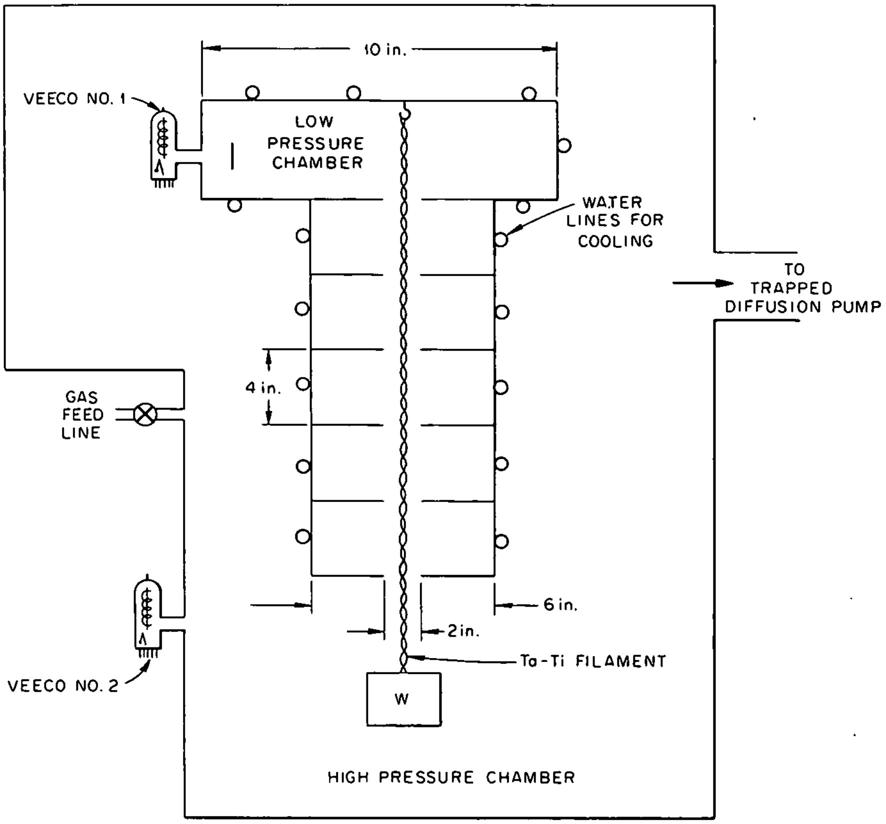

Fig. 10.3. Bakable Beam-Tube Prototype.

large vacuum chamber metered by a second ion gage (gage 2). During the experiment this larger region was pumped continuously by conventional means. The pressure was brought to 2×10^{-6} torr by adjusting the leak rate of hydrogen gas.

At the end of the pumpdown, bakeout, and titanium evaporation the pressure in the low-pressure chamber (gage 1) was about 2×10^{-8} mm Hg. After 2.5 hr the pressure had risen to 2.4×10^{-8} torr. Thus, more than 98% of the 2-liter-micron/sec hydrogen flux to the tube was removed. Figure 10.4 shows the time behavior of this assembly. All pressures recorded are corrected for gage sensitivity.

10.2.3 Pumping by Other Vapor-Deposited Metal Films

Table 10.1 lists data showing maximum pumping speeds observed for a variety of metals in a cylindrical chamber of about 1500 cm^2. The chamber (6 in. in diameter by 11 in. high) was initially evacuated with an MCF 300 oil-diffusion pump which operated continuously during the evaporations. Because of vapor pressure limitations, zirconium, niobium, and tantalum proved difficult to evaporate by means of either a resistance-heated filament or basket source. It will be seen from the table that with the dependable evaporation sources, titanium yields the greatest net increase in

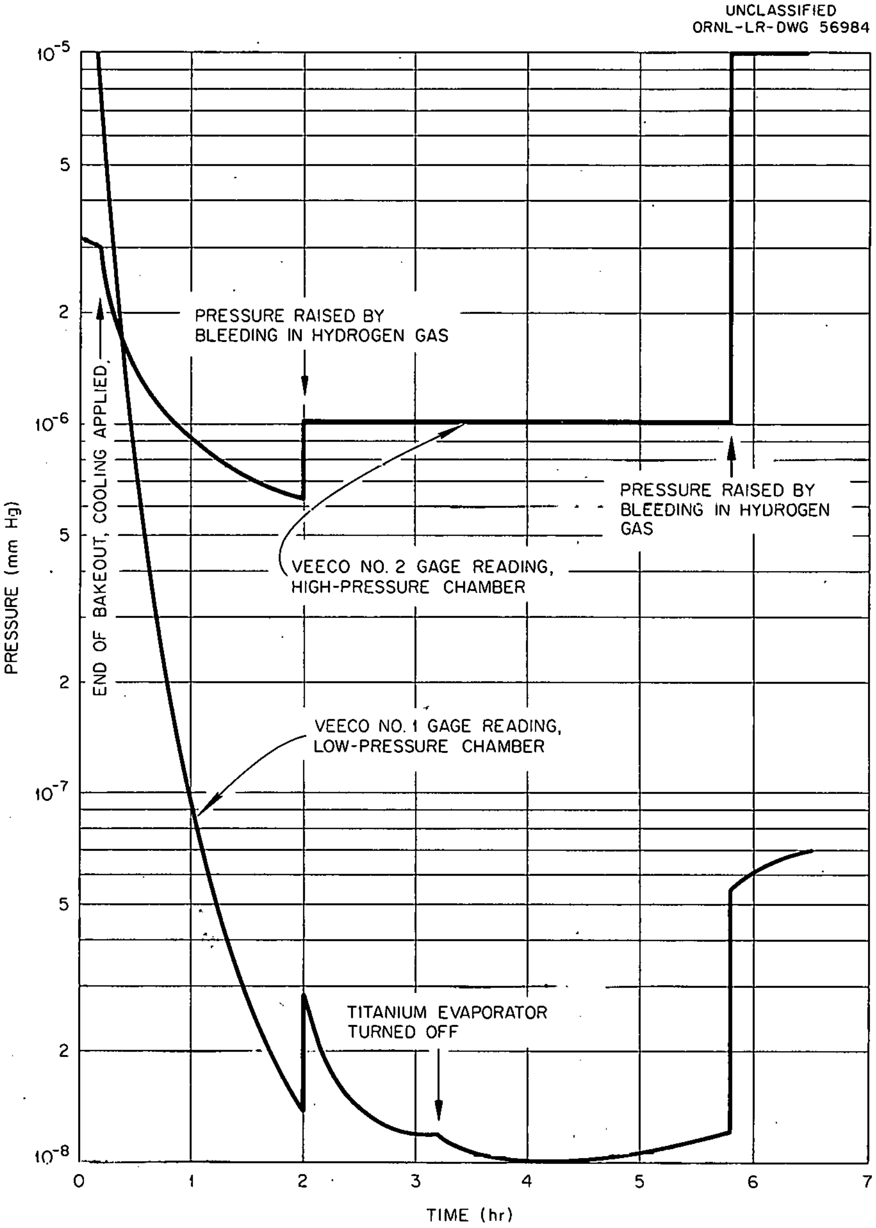

Fig. 10.4 Bakable Beam-Tube Prototype. Pressure at ion source end (Veeco No. 2) and pressure at reaction chamber end (Veeco No. 1) as a function of time.

pumping speeds beyond the base speed provided by the conventional pump. Development of other source designs may, of course, significantly alter these results.

In the studies summarized in Table 10.1, a background pumping speed for H_2 was measured after a stabilization of base pressure before each evaporation or evaporation attempt. Following evaporation, the test chamber was cooled and the base pressure was allowed to stabilize before measuring the postevaporation pumping speed. The listed decrease in speed with increasing pressure is probably a function of the degree of saturation of the metal with hydrogen. Between

Table 10.1. Summary of Pumping Speed Measurements, Using Various Vapor-Deposited Metal Films

Metal Evaporated	Weight of Metal Evaporated (g)	Net Pumping-Speed Increase (liters/sec)	Capacity for H_2 (cc)	Approximate Temperature of Evaporation (°C)	Evaporation Source	P_{base} at Various Times	P_{base}	Pumping Speed for H_2 (liters/sec) – Corrected for Sensitivity						
								4×10^{-7}	8×10^{-7}	4×10^{-6}	8×10^{-6}	4×10^{-5}	8×10^{-5}	4×10^{-4}
Titanium	0.419	7200	330	1340	Polystranded helix of Ti and Ta	Background	1.5×10^{-6}			287	278	288	290	215
						Postevaporation	1.5×10^{-7}	7450	6850	5830	5410	4800	4300	2470
						After H_2 saturation	2×10^{-6}			385	430	360	360	240
						After overnight pumping	6×10^{-7}			297	278	278	278	215
Titanium	0.324	7200	535	1340	Alloy – 80% Ti in Ta	Background	1.6×10^{-6}			262	275	270	270	215
						Postevaporation	7×10^{-8}	7450	6540	4170	4050	4300	3070	1710
						After 455 cc H_2	7×10^{-7}			319	319	310	310	247
						After H_2 saturation	7×10^{-7}			279	289	289	292	239
						After overnight pumping	1.4×10^{-6}			254	255	270	263	216
Molybdenum	0.594	730	6	2240	Mo helix around W core	Background	1.4×10^{-6}			277	277	275	275	215
						Postevaporation	2×10^{-7}	1100	720	593	465	330	307	
						After H_2 saturation	6×10^{-7}		475	395	342			
Zirconium	0.05	430		2400	Chunks in W basket	Background	2×10^{-6}			262	277	281	286	216
						Postevaporation	1×10^{-7}	705	645	508	375	360	309	216
Chromium	5.6	200		1125	Chunks in W basket	Background	3×10^{-6}				274	269	268	215
						Postevaporation	5×10^{-7}	465	294	245	267	305	268	215
Tantalum	0.07	100		2450	Ta helix around W core	Background	4×10^{-6}			268	290	286	268	226
						Postevaporation	1.6×10^{-7}	378	395	312	330	306	306	
Lithium	0.56	None		600–700	Chunks in Ta boat				No improvement in P_{base} or pumping speed					
Zirconium	0.01	None		630	Wire around W core				W failed as Zr melted					
Niobium	0.01	None		2400	Wire on W core				As Nb melted, the filament failed					

each of the speed measurements for any of the evaporations, however, the base pressure was found to be essentially unchanged. Only after a longer period of time did the base pressure rise significantly.

10.2.4 Effect of Arc Radiation on Pumping Speed of Titanium

An attempt was made to answer the question of whether the pumping speed of a titanium surface would be affected by radiation from a carbon arc. The apparatus (Fig. 10.5) was essentially a liner evacuated to about 10^{-8} mm Hg by baking it out and then depositing titanium on the inner surface. A 200-amp carbon arc was struck just outside of a hole in the liner so that radiation from the arc

UNCLASSIFIED
ORNL-LR-DWG 56985

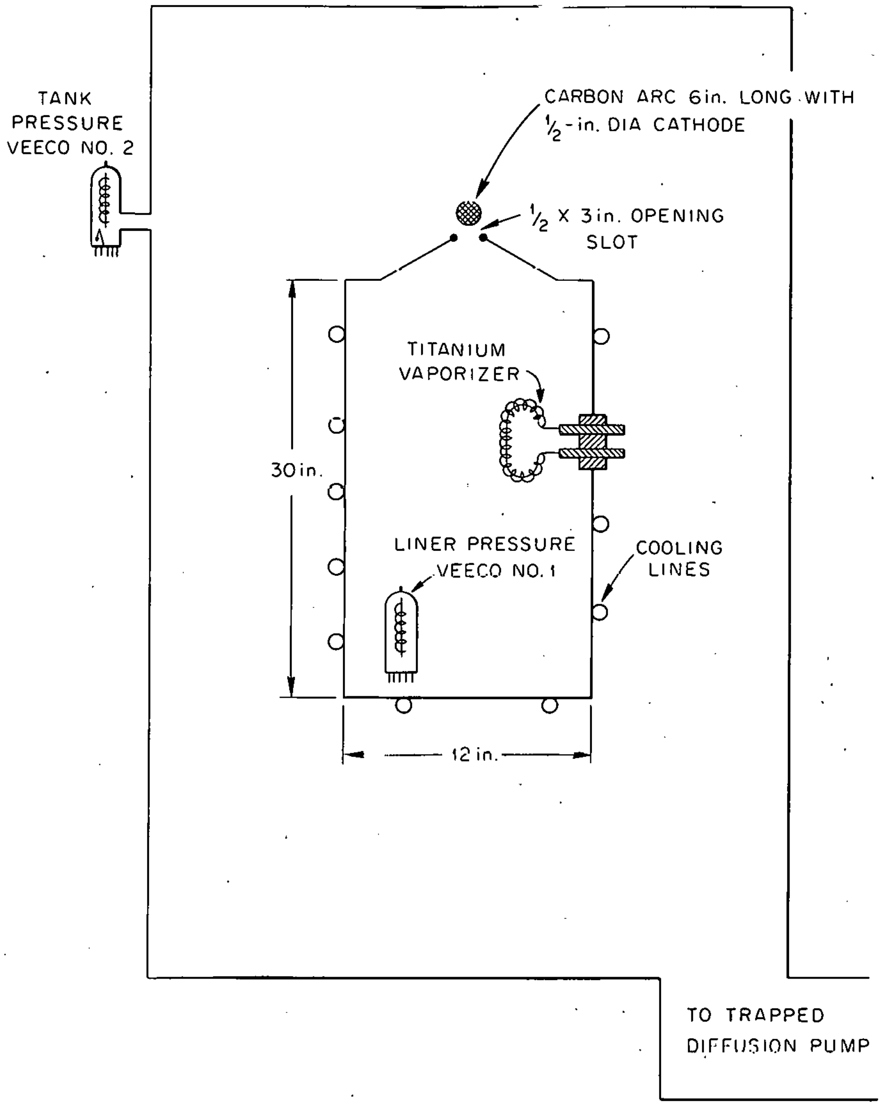

Fig. 10.5. Schematic Diagram of Apparatus to Test the Effect of Carbon Arc Radiation on the Pumping Speed of a Titanium Surface.

entered through a raised slot ½ by 3 in. About 90% of the surface coated by titanium received direct radiation from the arc. The behavior of the liner vacuum and the tank vacuum was followed on recorders.

The liner vacuum is plotted as a function of the tank vacuum in Fig. 10.6. This curve was determined before the arc was struck but with the titanium vaporizer on. The lowest point on the curve represents the base pressures in the liner and in the tank. Air was then bled into the outer vacuum system at a fixed rate and both systems allowed to come to equilibrium. This established the next point. The other points were similarly determined. Air was bled into the system through the arc cathode to simulate outgassing from the arc electrodes when the arc was running. If the arc radiation causes the pumping speed in the liner to decrease, the points representing the new equilibrium condition would be above the curve.

The arc was struck mechanically, and successive pressure readings are indicated by the numbered points. The initial pressures are indicated by 1, and the points are separated by 2-min intervals. After 12 min with the arc running at 200 amp, the pressures were down to the equilibrium values obtained with the arc off (point 7). They remained there for an additional 2 min and appeared to be steady at this point. The titanium vaporizer was then turned off. The pressure rose along the equilibrium curve for 2 min (point 8). The arc was then turned off and the experiment terminated.

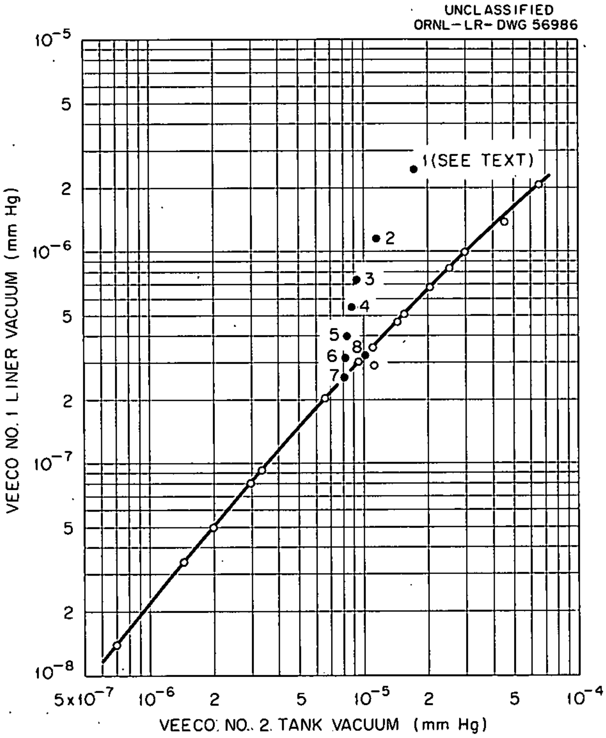

Fig. 10.6. Carbon Arc Radiation Test. Liner vacuum as a function of tank vacuum, before, during, and after striking the carbon arc.

Conclusions. – Only preliminary conclusions can be drawn from this one experiment, but it appears that the previously deposited titanium surface is adversely affected by the initial burst of gas coincident with striking the arc. As titanium metal continues to be deposited the surface apparently recovers its pumping ability after some minutes and then behaves as though no radiation were falling upon it.

About 10% of the surface of the liner did not receive the direct radiation. A portion of the surface was as far as 35 in. from the arc. Within these limitations the titanium surface appears to be unaffected by the carbon arc radiation.

10.3 VACUUM INSTRUMENTATION

10.3.1 Ionization-Gage Calibrations

The gage-test facility described in the last semiannual report has been in continuous use throughout this report period. In addition to "spot" calibrations of a number of individual gages, two prolonged series of tests have been run.

Constancy of Gage Calibration. – This series of tests was planned to show how an ionization gage maintains its calibration from day to day and throughout its service life. Three new Veeco RG-75 gages were installed for testing on August 15, and are still in operation. One of them (No. 4) has been operated continuously, except for a few outage periods of a few hours each. The other two were also operated continuously for the first nine weeks but have been operated intermittently with outage periods varying from a few weeks to a month or more since that time. All gages were powered by Veeco power supplies and operated at the recommended 10-ma electron current. They were checked, usually each working day, for calibration for air over the pressure range 10^{-4} to 10^{-6} torr, and average "calibration factors"[6] were determined.

On the basis of the average calibration factors obtained, the following observations are made:

(*a*) All three of the gages used in this series of tests read higher than true pressure ($k < 1$). This is not true of all RG-75 gages, however, for low-reading gages of this type have been found.

(*b*) Calibration factors vary slightly (usually less than 3%) from day to day. This variation can be attributed, in part, to experimental error, but there is also evidence of variation with ambient temperature.

(*c*) Except for these small, random day-to-day variations, the calibration factors for all three gages have remained remarkably constant for both continuous and intermittent operation.

(*d*) The calibration is not changed by degassing the gage, provided that time is allowed for attaining equilibrium after degassing.

Average calibration factors for the three gages at three widely spaced time intervals are tabulated in Table 10.2.

---

[6] Calibration factor is here defined as the ratio of true pressure change to gage response: $k = \frac{\Delta p(\text{true})}{\Delta p(\text{gage})}$.

Table 10.2. Typical Calibration Factors: RG-75 Gages

	Average Calibration Factor		
	Gage 1	Gage 2	Gage 4
August 24–31	0.86	0.91	0.96
November 1–8	0.85	Not operating	0.93
January 5–12	0.87	0.91	0.95

Conclusions. – (*a*) Individual gages of the same type may have distinctly different calibration factors; (*b*) except for small random variation, the calibration factor for a given gage remains practically constant throughout its service life.

Whether or not the above relations hold for gages of other types has not been determined, nor has any investigation been made of the possible effects on gage calibration of such factors as trapped vs untrapped systems.

"Nude" Ionization Gage Calibrations. – Many users of nude ionizations gages have reported discrepancies between these and conventional ones when both are applied to the same system. Generally, these discrepancies have been left unresolved. To permit investigation of this problem, the gage-test facility was modified by the addition of a 3-in. port in the test chamber through which a nude gage might be mounted for calibration.

Tests have been run on three nude gages, each test extending over a period of three to four weeks. During these tests, the calibration factors for the nude gage and for two RG-75 gages were simultaneously determined each working day.

All three of the nude gages were of the Bayard-Alpert type. Gages 1 and 2 were Vactronic type VAC-NIG, and gage 3 was a Veeco type RG-75 from which the glass envelope had been removed.

Throughout the series of tests the calibration factors for the two conventional RG-75 gages remained essentially constant. This was by no means true, however, for the three nude gages.

To illustrate the changes observed in the calibration, Table 10.3 lists the calibration factors found at eight-day intervals.

Table 10.3. Calibration Factors for Nude Gages

Days of Operation	Vactronic VAC-NIG No. 1	Vactronic VAC-NIG No. 2	Veeco RG-75 Nude
1	1.55	1.62	1.21
8	22.9	11.4	5.15
16	52.9	32.4	9.20
24	87.0 (21 days)	29.7	21.0

Certain facts not reflected in Table 10.3, but indicative of the unreliability of these gages, should be mentioned.

(*a*) After two weeks of operation the calibration factor for gage 1 had risen to 86, but was reduced to 23 by thorough outgassing. During the next four days, however, values of 41, 53, 70, and 87 were observed. A second outgassing at this time reduced k to 37, but it was again 87 three days later.

(*b*) Similar but less pronounced reductions in the calibration factor of gage 2 were observed following outgassing.

(*c*) Three successive calibrations of gage 2 on its 14th day of operation yielded calibration factors of 7, 20, and 21.

Conclusions. – *(a)* The three nude gages that have been tested are completely unreliable, at least under conditions existing in our test system. The pressures indicated are too low by anywhere from 20% to almost two orders of magnitude; *(b)* the reasons for this unreliability are not known, but additional experiments are planned to shed light on this question.

10.3.2 Pressure Measuring in the 0.2 μ to 100 mm Hg Range

A comparison of four gages of different types was undertaken to meet a current need in the region of intermediate to low vacuum. The instruments used were:

1. A mercury absolute pressure gage. Care was taken to drive off gases from this closed-end manometer.
2. A Stoke-McLeod gage, 0 to 700 μ range, No. 276-B (Flosdorf modification).
3. A Wallace and Tiernan absolute pressure gage. This gage is actuated by a capsule similar to an aneroid barometer mechanically coupled to a pointer across an external scale.
4. A Multi-Station Autovac Pirani gage, type 3294-B. Four Pirani tubes at four locations may be read by the gage individually by operating a selector switch. Two scales are available, one below 100 μ and the other above. The instrument will switch itself automatically from one scale to the other and indicate the scale in use by a light. An external relay may also be activated as the scale is switched. Separate individual controls are provided for zero point adjustment and for circuit resistance. A single sensitivity control and an adjustment for the scale switching pressure are provided.

A conventional 2-in. diffusion pump and mechanical forepump were operated in order to maintain low pressure in a 5-in.-diam by 17-in.-long manifold to which were attached the various pressure-measuring devices. The mercury absolute gage was carefully made in order to exclude air and was found to have a zero reading at high vacuum. It compared well with the McLeod gage at 700 μ (although it was somewhat difficult to read at this pressure). The McLeod gage was used as calibrated by the manufacturer. The Wallace and Tiernan gage had no external adjustment.

An adjustment of all of the controls of the Multi-Station Pirani gage was made before the final testing. The four Pirani gages were attached with rubber vacuum tubing, with a minimum exposure of the tubing. Procedures for these adjustments are given in CVC Instruction Bulletin No. 9-25-A. After setting each Pirani tube circuit to its rated resistance, the pressure was held at 100 mm Hg on the mercury absolute pressure gage, while all four tubes were set at this maximum reading value by using a combination of the sensitivity and gage position controls. One hundred millimeters of mercury pressure was used rather than atmospheric pressure in order to provide a narrower calibration range. The zero controls were then used to set each tube reading at zero pressure. Rechecks were made at 100 mm Hg pressure. Fifteen minutes was the length of time needed for the readings to stabilize at the high pressures, with less time required at lower pressures. A slight drift in pressure readings was observed.

The various types of gages were tested with air and with deuterium. Since the pressure indication of the Pirani gage is dependent upon the thermal conductivity of the gas present, it showed a different reading for one gas as compared to the other at the same absolute pressure. After an initial evacuation of the system, gas was admitted to 100 mm pressure as indicated on the absolute pressure gage. Readings of all gages were taken. The pressure was then lowered and readings taken until the whole pressure range had been covered. For deuterium at pressures of less than 100 μ, the entire volume of gas present was pumped out and then refilled from a deuterium supply in order to minimize effects from outgassing. This ensured that the pressure reading was that due to deuterium.

The mercury absolute pressure gage and the McLeod gage being subject to direct standardization are the most reliable, and their operating characteristics are well known. The Wallace and Tiernan aneroid gage was found to have a fast response (over the range 0 to 50 mm), was easily readable, was accurate to within 2% at higher pressures, and showed pressure variations of 0.1 mm. For air the Pirani gage readings were a little higher than those of the McLeod gage over the whole range. The ratio of pressures indicated was 1.16 for the 0 to 100 μ range, 1.22 for 100 to 350 μ, and decreasing to 1.01 at 1000 μ. With deuterium the ratio was larger, being 1.6 over the 0 to 100 μ range, and 1.62 to 1000 μ. Above 2.5 mm absolute pressure, with deuterium, the Pirani gage readings were much larger and by 4.5 mm absolute showed readings of 100 mm. Below 2.5 mm, pressures of deuterium could be successfully read and interpreted.

10.4 DIFFUSION PUMPS

10.4.1 Isotherms in Diffusion-Pump Jet Streams

Information has been obtained on the shape and flow of the vapor stream of a diffusion pump by inserting into that stream a temperature-sensing device such as a thermocouple and measuring the temperature that it attains. While the real significance of the temperature thus measured at a point may be somewhat in doubt, this procedure does give relative information regarding the conditions at that point.

In a vapor stream of high density there is no method for the direct measurement of static temperature. The temperature indicated by a thermometer so used is higher than the static temperature.

There exists a concentration gradient in the jet ranging from densities corresponding to pressures close to 1 mm Hg down to that of the vacuum system itself, close to 1×10^{-7} mm Hg. This concentration gradient results in quite a different rate of heat accumulation on any temperature-sensing element positioned at various points in the gradient.

In this study of the shape and flow patterns of diffusion-pump jets, it is probable that the temperatures measured provide a very good indication of the total amount of energy and therefore concentration of vapor existing at the various points. Isotherms may be considered to be isobars as well. It has been found that the temperature change due to radiation, with respect to the cold exterior walls and the pump or the hot central stack, is quite small.

The measurement of temperatures in diffusion-pump jet streams has been accomplished in a modified 20-in. pump with a 36-in.-diam test dome. A rod carrying a thermocouple was used to survey the area or volume occupied by the vapor jet. The survey area is the surface of a cylinder which intersects the volume of the vapor jet. Positioning of the thermocouple is done on points measured radially in the dome. Plotting the points on a plane surface then gives the cross-sectional picture of the temperature found in the jet. Using this technique it is possible to study any of the usual variables which enter into diffusion pump design (oil-vapor temperature, jet-orifice area, nozzle shape and angle, cooling-surface position, etc.).

Thus far no startling differences have been found in any of the jets tested. (The original modification of the replacement DPI jets for the Westinghouse 20-in. pump appears to be one of the best.) Figure 10.7 shows a typical set of isotherms obtained.

UNCLASSIFIED
ORNL-LR-DWG 56987

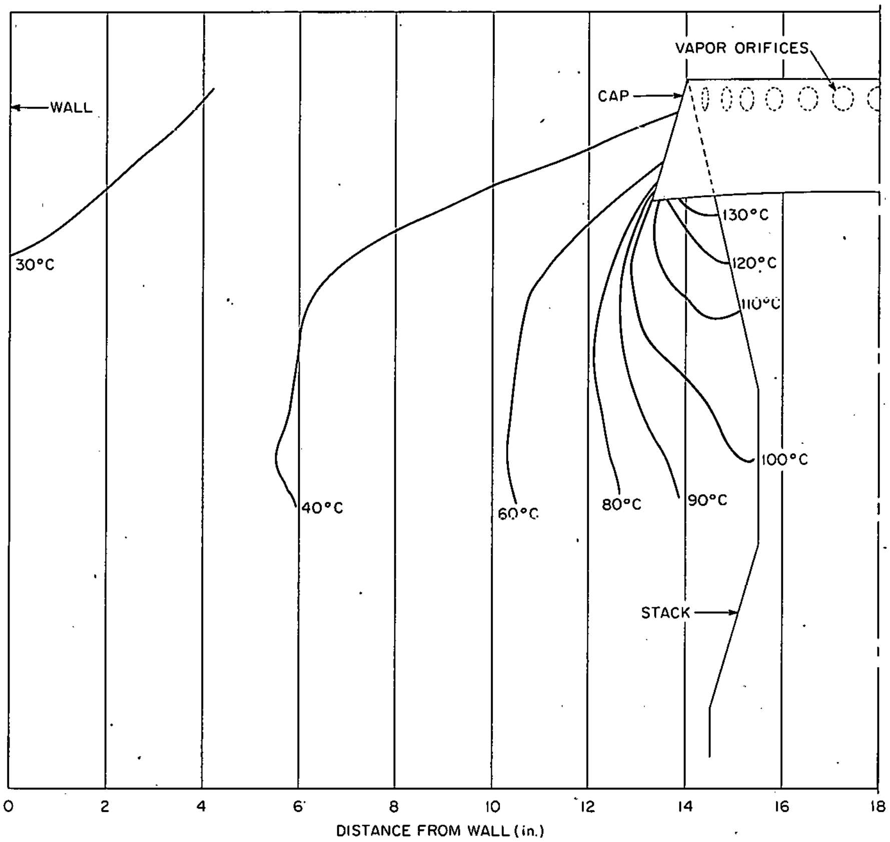

Fig. 10.7. Isotherms in Diffusion-Pump Jet Streams.

11. STATUS OF BALL-LIGHTNING STUDY

J. R. McNally, Jr.

A summary of a preliminary survey of observations of ball lightning was reported earlier.[1] This summary presented very general information abstracted from 110 possible ball-lightning observations reported by ORNL monthly-roll personnel. Since that time a survey of all Union Carbide Corporation personnel in Oak Ridge has been completed, with over 500 reports from a statistical sample of 15,923 individuals.

A summary of the observations suggests that lightning balls (1) usually occur as the result of lightning discharge; (2) originate randomly in space, although they are often initially associated with wires or structures; (3) are frequently air-borne or air-borne part time; (4) move randomly in space or along conductors and oftentimes exhibit a rolling or spinning motion; (5) are usually about 10 in. in diameter; (6) are usually spherical; (7) are very rarely green or violet but are frequently multicolored (the white and blue-white balls are usually very hot and brilliant and sometimes cause considerable damage); (8) have a median duration of about 3 to 4 sec; (9) frequently decay quite suddenly (sometimes explosively); (10) generally do not affect the observer's vision unless of the white or blue-white category and close to the observer. In numerous cases other supporting witnesses were on hand and are said to have given essentially the same details.

The statistics compiled agree in general with other observations reported in the literature.[2–6] There is no doubt that some of them fall into the category of "St. Elmo's fire," "Jacob's ladder," and other discharges involving conductors or a conductor and the atmosphere. However, there is a surprisingly large number of the individual, air-borne, free-floating type (144 instances plus 90 which were air-borne part time) to which Kapitza's postulate of standing electromagnetic waves[7] may not apply, according to Tonks.[8] No reports of beaded or rosary lightning were made.

The fact that 62 observations of doughnut or ring configurations and 50 observations of surface-type glow distributions were reported suggest the possibility of an excited ring or surface. It is possible, of course, that psychological factors inherent in the question that was asked may have led observers to make such reports on the glow distribution ("Was it a surface, volume, doughnut, or ring type of glow?). It is also possible that multicoloring of the ball due to internal temperature variations may account for such a glow distribution. Although no question was asked specifically on the internal motion of the lightning ball, 46 individuals reported a rolling, spinning, or tumbling

---

[1] J. R. McNally, Jr., *Thermonuclear Project Semiann. Progr. Rept. July 31, 1960*, ORNL-3011, p 134.

[2] B. L. Goodlet, *J. Inst. Elec. Engrs. (London)* 81, 1 (1937) estimates 4 to 11 megajoules for an actual fireball the size of which was reported to be that of a large orange.

[3] W. Brand, *Der Kugelblitz*, Hamburg, 1923.

[4] W. J. Humphreys, *Proc. Am. Phil. Soc.* 76, 613 (1936).

[5] M. Rodewald, *Z. Meteorol.* 8, 27 (1954).

[6] See also H. Nauer, *Umschau Fortschr. Wiss. u. Tech.* 56, 75 (1956); J. C. Jensen, *Physics* 4, 372 (1933).

[7] P. L. Kapitza, *Proc. Acad. Sci. USSR* 101, 245 (1955).

[8] L. Tonks, *Nature* 187, 1013 (1960), estimates 0.36 megajoule total radiation for a particular idealized case (10 cm diameter).

type of motion suggesting rotational plasma or mass flow and the possibility of an internal ring current. A ring-current model for ball lightning has been proposed by Shafranov.[9]

Preliminary results on a subsequent second survey of the 515 observers indicate that approximately one-third of them describe the internal motion as characterized by rolling, swirling, or rotating. (No leading question on possible internal motion was asked.) Many cases reported in the literature ascribe a similar rotational property to the ball. For example, a ball-lightning observation reported by L. B. Loeb to Humphreys[4] included the statement, "It has been my impression in thinking of it that the so-called ball was internally in rapid rotation of some sort or there was a vortex which gave it its shape."

The possibility of a naturally stable plasma configuration at thermonuclear energies raises penetrating questions regarding the whole aspect of thermonuclear reactions. A preliminary review of the ball lightning survey is available and it is hoped to publish more complete results as an ORNL report as soon as possible.

---

[9] V. D. Shafranov, *Soviet Phys. JETP* 33, 710 (1957); translation in *Soviet Phys. JETP* 6, 545 (1958).

12. DESIGN AND ENGINEERING

J. F. Potts, Jr.

The activities of the Engineering Services Group are generally integrated with the research efforts of other groups in the Thermonuclear Division. The group executes or coordinates engineering design, shop fabrication, building operations, and maintenance.

Engineering Services Group design activities are summarized as follows:

Jobs on hand 8-1-60 on which work had not started	18
New jobs received	120
Total jobs	138
Jobs completed	111
Jobs in progress	13
Backlog of jobs 1-31-61	14
Total drawings completed for period	299
Overtime (draftsmen, man-days)	40

During this interval a significant part of the design activity was concentrated on electromagnet coils, cans, and supports for DCX-2 and EP-B. Other phases of engineering design for these two projects were supplied by Y-12 and by the ORNL Engineering and Mechanical Division, this group providing only a measure of coordination.

Shop fabrication for the period is summarized as follows:

Jobs requiring 16 man-hours or less	291
Jobs requiring up to 1200 man-hours	567
Jobs requiring up to 2000 man-hours	2
Jobs of miscellaneous character in plating, carpenter, electrical, and millwright shops	250
Jobs by outside contractors	2

The average shop manpower to accomplish the above work consisted of 22 machinists, 15 fabricators, and 6 welders in the Y-12 shops and 7 craftsmen in the ORNL shops.

The Thermonuclear Division relocation to Building 9201-2 is complete. Efforts are still under way to complete the installation of a 5-Mw ac-dc motor-generator set, a second 600-hp motor-generator set, and additional 460-v and 2300-v ac distribution transformers. Also under way are modifications to the pumps, demineralizers, and filters to improve the capacity and resistivity of the building demineralized water.

PUBLICATIONS

OPEN LITERATURE

Author(s)	Title of Article	Journal or Book
E. G. Harris and A. Simon	Coherent and Incoherent Radiation from a Plasma	*Phys. Fluids* 3, 255 (1960)
A. Simon	Critical Current for Burnout in an OGRA-Type Device	*J. Nuclear Energy: Pt. C, Plasma Phys.* 1, 215–29 (1960)
O. C. Yonts and D. E. Harrison	Surface Cleaning by Cathode Sputtering	*J. Appl. Phys.* 31, 1583–84 (1960)
J. R. McNally, Jr.	The Direct-Current Experiment (DCX) and High-Temperature Measurements in the Carbon Arc	*Optical Spectrometric Measurements of High Temperatures* (ed. by P. J. Dickerman), pp 70–94, University of Chicago Press, 1961.

ORNL REPORTS

Author(s)	Title	Number	Date
J. A. Ray	Measurements of the Energy Distribution of Energetic Particles Escaping DCX	CF-60-5-141	8-22-60
D. J. Rose*	Ion Energy Distribution, Energy Degradation, and Exponentiation Criteria in a Plasma Formed by Beam Trapping and Charge Transfer	CF-60-9-112	9-30-60
R. J. Mackin, Jr.	Plasma Accumulation in a Device Fed by Energetic Ion Trapping	CF-60-11-50	11-10-60
H. Postma and D. P. Hamblen	Dissociation of H_2^+ by Hydrogen	ORNL-2966	11-28-60
T. K. Fowler	Effect of Energy Degradation on the Critical Current in an OGRA-Type Device	ORNL-3037	12-28-60
A. Simon	Exact Relativistic Fokker-Planck Coefficients for a Plasma	ORNL-3040	1-10-61
I. Alexeff and R. V. Neidigh	Apparent Ovservations of Ionic Sound Waves in an Arc Plasma	CF-61-2-57	2-13-61

---

*Consultant, MIT.

THIS PAGE

WAS INTENTIONALLY

LEFT BLANK

ORNL-3104
UC-20 – Controlled Thermonuclear Processes
TID-4500 (16th Ed.)

INTERNAL DISTRIBUTION

1. I. Alexeff
2. R. G. Alsmiller
3. C. F. Barnett
4. P. R. Bell
5. D. S. Billington
6. E. P. Blizard
7. C. W. Blue
8. G. E. Boyd
9. R. L. Brown
10. C. E. Center (K-25)
11. R. A. Charpie
12. R. E. Clausing
13. R. S. Cockreham
14. D. L. Coffey
15. F. L. Culler
16. J. S. Culver
17. R. A. Dandl
18. R. C. Davis
19. S. M. DeCamp
20. J. L. Dunlap
21. H. O. Eason
22. R. S. Edwards
23. A. C. England
24. J. C. Ezell
25. J. L. Fowler
26. T. K. Fowler
27. J. E. Francis
28. J. H. Frye, Jr.
29. W. F. Gauster
30. J. H. Gibbons
31. R. A. Gibbons
32. P. M. Griffin
33. W. R. Grimes
34. E. Guth
35. C. S. Harrill
36. C. C. Harris
37. G. R. Haste
38. A. Hollaender
39. A. S. Householder
40. H. C. Hoy
41. R. P. Jernigan, Jr.
42. R. G. Jordan (Y-12)
43. W. H. Jordan
44. C. P. Keim
45. M. T. Kelley
46. G. G. Kelley
47. R. J. Kerr
48. R. L. Knight
49. P. Lafyatis
50. J. A. Lane
51. N. H. Lazar
52. G. F. Leischsenring
53. S. C. Lind
54. R. S. Livingston
55. J. R. McNally, Jr.
56. R. J. Mackin
57. W. D. Manly
58. E. R. Mann
59. O. D. Matlock
60. K. Z. Morgan
61. O. B. Morgan
62. J. P. Murray (K-25)
63. R. V. Neidigh
64. J. H. Neiler
65. M. L. Nelson
66. J. Neufeld
67. C. E. Normand
68. G. R. North
69. C. E. Parker
70. W. F. Peed
71. D. Phillips
72. J. F. Potts
73. M. Rankin
74. H. Postma
75. J. D. Redman
76. R. G. Reinhardt
77. P. M. Reyling
78. M. T. Robinson
79. P. W. Rueff
80. W. K. Russell
81. H. E. Seagren
82. E. D. Shipley
83. A. Simon
84. M. R. Skidmore
85. M. J. Skinner
86. A. H. Snell
87. W. L. Stirling
88. R. F. Stratton, Jr.
89. R. A. Strehlow
90. J. A. Swartout
91. E. H. Taylor
92. P. A. Thompson

93. R. M. Warner
94. H. L. Watts
95. A. M. Weinberg
96. E. R. Wells
97. T. A. Welton
98. G. K. Werner
99. G. C. Williams
100. C. E. Winters
101. W. L. Wright
102. O. C. Yonts
103. W. P. Allis (consultant)
104. D. Alpert (consultant)
105. W. B. Ard, Jr. (consultant)
106. J. F. Bailey (consultant)
107. W. H. Bostick (consultant)
108. W. R. Chambers (consultant)
109. E. Creutz (consultant)
110. J. W. Flowers (consultant)
111. M. W. Garrett (consultant)
112. O. G. Harrold (consultant)
113. E. G. Harris (consultant)
114. R. Hefferlin (consultant)
115. D. E. Harrison (consultant)
116. G. W. Hoffman (consultant)
117. V. W. Hughes (consultant)
118. D. W. Kerst (consultant)
119. E. D. Klema (consultant)
120. G. B. Lockhart (consultant)
121. E. W. McDaniel (consultant)
122. M. R. C. McDowell (consultant)
123. J. E. Mott (consultant)
124. W. B. Pardo (consultant)
125. H. K. Reynolds (consultant)
126. F. F. Rieke (consultant)
127. H. S. Robertson (consultant)
128. D. J. Rose (consultant)
129. L. P. Smith (consultant)
130. H. S. Snyder (consultant)
131. P. M. Stier (consultant)
132. C. H. Weaver (consultant)
133. J. D. Tillman (consultant)
134. Thermonuclear Library
135. Sherwood Reading File (V. Glidewell)
136. Biology Library
137. Reactor Division Library
138-140. Central Research Library
141-165. Laboratory Records Department
166. Laboratory Records, ORNL RC
167-168. ORNL – Y-12 Technical Library, Document Reference Section

EXTERNAL DISTRIBUTION

169. E. P. Gyftopoulos, Massachusetts Institute of Technology
170. S. C. Brown, Massachusetts Institute of Technology
171. M. B. Gottlieb, Princeton University
172. J. M. B. Kellog, Los Alamos Scientific Laboratory
173. A. C. Kolb, Naval Research Laboratory
174. J. A. Phillips, Los Alamos Scientific Laboratory
175. R. F. Post, University of California, Lawrence Radiation Laboratory
176. Lyman Spitzer, Jr., Princeton University
177. E. Teller, University of California, Lawrence Radiation Laboratory
178. C. M. Van Atta, University of California, Lawrence Radiation Laboratory
179-180. Division of Research and Development, AEC, ORO (1 copy each to H. M. Roth and R. B. Martin)
181-182. Controlled Thermonuclear Branch, AEC, Washington, (1 copy each to A. E. Ruark and H. S. Morton)
183. Oak Ridge Operations Office
184-791. Given distribution as shown in TID-4500 (16th ed.) under Controlled Thermonuclear Processes category (75 copies – OTS)